Development of terahertz photomixer technology at telecommunications wavelength

Reshma Anamari Mohandas

Submitted in accordance with the requirements for the degree of
Doctor of Philosophy

The University of Leeds
School of Electronic and Electrical Engineering

April 2016

The candidate confirms that the work submitted is her own, except where work which has formed part of jointly-authored publications has been included. The contribution of the candidate and the other authors to this work has been explicitly indicated below. The candidate confirms that appropriate credit has been given within the thesis where reference has been made to the work of others.

<u>Devices fabricated in Chapter 2 of this thesis appeared in publications as follows:</u>

H. Nong, S. Pal, S. Markmann, N. Hekmat, R. A. Mohandas, P. Dean, L. Li, E. H. Linfield, A. Giles Davies, A. D. Wieck, and N. Jukam, "Narrow-band injection seeding of a terahertz frequency quantum cascade laser: Selection and suppression of longitudinal modes," *Applied Physics Letters,* vol. 105, pp. -, 2014

The THz QCL used for the measurements were fabricated by myself. Other authors were responsible for the measurements, analysis, QCL growth and supervision of the work.

D. R. Bacon, J. R. Freeman, R. A. Mohandas, L. Li, E. H. Linfield, A. G. Davies, and P. Dean, "Gain recovery time in a terahertz quantum cascade laser," *Applied Physics Letters,* vol. 108, p. 081104, 2016.

THz QCL used for the measurements were fabricated by myself. Other authors were responsible for the measurements, analysis, QCL growth and supervision of the work.

<u>Devices fabricated in Chapter 4 of this thesis appeared in publications as follows:</u>

R. A. Mohandas, J. R. Freeman, M. C. Rosamond, O. Hatem, S. Chowdhury, L. Ponnampalam, M. Fice, A. J. Seeds, P. J. Cannard, M. J. Robertson, D. G. Moodie, J. E. Cunningham, A. G. Davies, E. H. Linfield, and P. Dean, "Generation of continuous wave terahertz frequency radiation from metal-organic chemical vapour deposition grown Fe-doped InGaAs and InGaAsP," *Journal of Applied Physics,* vol. 119, p. 153103, 2016.

Work including fabrication, characterization, data gathering, analysis was carried out by me under the supervision of Dr. Joshua R Freeman. Other authors were responsible for electron-beam lithography, design, growth of the wafer and supervision of the work.

In loving memory of my father,
- Late. Mr. Mohandas K

Acknowledgements

First and foremost, I would like to express my sincere gratitude and thanks to my supervisors Dr. Paul Dean and Prof. Edmund H Linfield for giving me an opportunity to do a PhD at the University of Leeds. It was indeed an honour to be a PhD student under their guidance and I would like to thank them for all the help, care, advice and support throughout these years. Thanks are due to Prof. Giles A Davies and Prof. John E Cunningham for all the valuable comments during the supervision meetings.

I would like to give special thanks to Dr. Joshua R Freeman for all the support and help throughout the past three years. Although one of the busiest persons, he had the patience to answer all my questions. He offered help with experiments involving photomixers, QCLs, the list is never ending!. Thanks a lot for the patience and the confidence you have shown. It was a great experience working with you, Josh.

Another person who needs special mention is Dr. Mark C Rosamond. He had always been prompt in fabricating samples and was extremely helpful. I am also grateful to Dr. Alex Valavanis for all the cryogenics and QCL characterization experiments and the numerous trainings. I would like to thank Dr. Lianhe Li for providing the QCL wafers.

I would like to make a special note of my colleagues in the fourth floor office, Dr Jay Keeley, Dr. Iman Kundu, Dr. Divyang Mistry, Dong Rui, Dr. Viktor Doychinov, Dr. Julie Zhu, Pierluigi Rubino and Manoj Kumar, it was you guys who made the long office hours enjoyable and thanks for all moments and fun we had. Also I am indebted to my supervisory meeting colleagues, David Bacon and Dr. Siddhant Chowdhury for all the support and also allowing me to speak first, everytime.

I would like to express my special thanks to Dr. Nic Hunter. He is such a nice companion and friend, and very supportive. I am thankful to other members of the group, Dr. Andrew Burnett, Dr. Chris Wood and Dr. Chris Russell. I am grateful to Geoff Butterworth, Dr. Li Chen, Jordan and Chris Day for the cleanroom training and prompt help.

Special thanks to Louise Redmonds, Sue Hobson and Clair Atkinson for the administrative help and support. I would like to thank all the members and staff of School of Electronic and Electrical Engineering department.

I am thankful to my friends, Sam and Becci for the lively house environment and making me feel at home.

Coming from a traditional Malayali family, the decision to do a PhD was not an easy one and for that, I would like to take this opportunity to thank my family for all the love and support throughout. Thanks are due to my mother for the courage and strength she has shown and standing with me by my decisions. Thanks are due to my niece, Nandhu and my sister, Resmi for the unconditional love and affectionate conversations. I would like to thank my cousins, Resna and Sasi for the weekend chats.

I would have never aspired to do a PhD, unless my father had nurtured in me the values of education from an early age. I hope, I have made him proud.

For all the companionship, love, care, support, criticism, trust, confidence, comments, motivation, and everything else, I am grateful to you, my dearest Vineeth.

Thanks to God Almighty for all the strength and courage.

Abstract

Terahertz (THz) region is one of the least developed regions of the electromagnetic spectrum. Lack of compact and high power sources and detectors in this wavelength range has limited its use for various key applications. In this thesis, three different approaches adopted for the generation of THz radiation are discussed, quantum cascade lasers (QCLs), photoconductive emitters and photomixers and emphasis is given to photomixing.

Photomixers generate continuous wave THz radiation by beating two independent laser beams on a semiconductor material. Beat frequency between the laser beams determines the emission frequency. In this work, two different materials, iron (Fe)–doped indium gallium arsenide (Fe:InGaAs) and Fe–doped indium gallium arsenide phosphide (Fe:InGaAsP) is used for THz photomixing at telecommunications wavelength. Characterizing the materials gave an idea about its intrinsic properties. With a standard antenna design, exemplar performance in terms of bandwidth (>2.4 THz) and output power was obtained from these materials.

In order to improve the THz power from photomixers, two different electrode designs with nanometre dimensions were attempted on Fe:InGaAsP wafer. The spectral bandwidth and power from the emitters were studied at different bias orientations and polarizations. Mapping the emitters gave an insight into the geometrical dependence of the emission mechanism. The design was tested in a THz time domain system to confirm the results.

Using photomixers, a 2.0 THz QCL was injection locked to a heterodyne source. The emission frequency of the QCL was locked over ~20 MHz. QCL voltage modulation was monitored for different emitter modulation frequencies. Locking experiment was performed at different injected signal strengths and QCL biases. QCL emission frequency was monitored at the injection locked frequency and Fabry-Perot modes.

Contents

List of publications

The work described in this thesis has been reported in a number of journal and conference publications, as summarised below.

Journal Publications

- R. A. Mohandas, J. R. Freeman, M. C. Rosamond, O. Hatem, S. Chowdhury, L. Ponnampalam, M. Fice, A. J. Seeds, P. J. Cannard, M. J. Robertson, D. G. Moodie, J. E. Cunningham, A. G. Davies, E. H. Linfield, and P. Dean, "Generation of continuous wave terahertz frequency radiation from metal-organic chemical vapour deposition grown Fe-doped InGaAs and InGaAsP," *Journal of Applied Physics,* vol. 119, p. 153103, 2016.

- D. R. Bacon, J. R. Freeman, R. A. Mohandas, L. Li, E. H. Linfield, A. G. Davies, and P. Dean, "Gain recovery time in a terahertz quantum cascade laser," *Applied Physics Letters,* vol. 108, p. 081104, 2016.

- H. Nong, S. Pal, S. Markmann, N. Hekmat, R. A. Mohandas, P. Dean, L. Li, E. H. Linfield, A. Giles Davies, A. D. Wieck, and N. Jukam, "Narrow-band injection seeding of a terahertz frequency quantum cascade laser: Selection and suppression of longitudinal modes," *Applied Physics Letters,* vol. 105, pp. -, 2014.

Conference Publications

- Reshma A. Mohandas, Joshua R. Freeman, Mark C. Rosamond, Osama Hatem, Siddhant Chowdhury, Lalitha Ponnampalam, Martyn Fice, Alwyn J. Seeds, Paul J. Cannard, Michael J. Robertson, David G. Moodie, John E. Cunningham, A Giles Davies, and Edmund H. Linfield, and P. Dean, "Generation of continuous wave terahertz frequency radiation from MOCVD grown Fe-doped InGaAs and InGaAsP " *Oral Presentation,* 40th Infrared Millimetre WavesTerahertz Conference, Hong Kong, 2015.

- Siddhant Chowdhury, Joshua R. Freeman, Mark C. Rosamond, Reshma A. Mohandas, Manoj Kumar, Lianhe Li, Paul Dean, A Giles Davies, and. Edmund H. Linfield, "Study of the effect of annealing temperatures on low-temperature-grown-GaAs photomoxers " *Poster Presentation,* UK semiconductors, Sheffield, UK, 2015.

- Siddhant Chowdhury, O.Hatem, Paul Dean, Reshma A. Mohandas, Lianhe Li, Paul Dean, A Giles Davies, and. Edmund H. Linfield, "Terahertz emission and detection using Fe-doped InGaAs and low-temperature grown-GaAs photoconductive switches " *Poster Presentation,* UK semiconductors, Sheffield, UK, 2013.

- Hanond Nong, Shovon Pal, Sergej Markmann, Negar Hekmat, Reshma A. Mohandas, Paul Dean, Lianhe Li, Edmund H. Linfield, A. Giles Davis, Andreas D.Wieck and Nathan Jukam, “Selection of Longitudinal Modes in a Terahertz Quantum Cascade Laser via Narrow-band Injection Seeding”, *Oral Presentation*, CLEO conference, USA, 2015.

- Sergej Markmann, Hanond Nong, Shovon Pal, Negar Hekmat, Paul Dean, Reshma A. Mohandas, Lianhe Li, Edmund. H. Linfield, A. Giles Davis, Andreas D.Wieck and Nathan Jukam, “Investigation of Time-resolved Gain Dynamics in an Injection Seeded Terahertz Quantum Cascade Laser”, *Oral Presentation*, CLEO conference, USA, 2015.

- Sergej Markmann, Hanond Nong, Shovon Pal, Negar Hekmat, Reshma A. Mohandas, Paul Dean, Lianhe Li, Edmund. H. Linfield, A. Giles Davis, Andreas D. Wieck and Nathan Jukam, “Observation of Time-resolved Gain Dynamics in an Injection Seeded Terahertz Quantum Cascade Laser”, *Oral Presentation,* 40th Infrared Millimetre WavesTerahertz Conference, Hong Kong, 2015.

Abbreviations

AWG	Arbitrary waveform generator
BTC	Bound-to-continuum
CW	Continuous wave
DBR	Distributed Bragg reflector
DFB	Distributed feedback
DI	De-ionised
DSN	Double sided nanostructure
EDFA	Erbium doped fibre amplifier
EO	Electro-optic
ESA	Electrical spectrum analyser
FTIR	Fourier transform infrared
FWHM	Full width half maximum
GHz	Gigahertz
HEB	Hot electron bolometer
IF	Intermediate frequency
IR	Infrared
IPA	Iso-propyl alcohol
LIV	Light-current-voltage
LPE	Liquid phase epitaxy
LT	Low-temperature
MBE	Molecular Beam epitaxy
MHz	Megahertz
MOCVD	Metal organic chemical vapor deposition
NS	Nanostructure
NSG	Nanostructure grating
OSA	Optical spectrum analyser

PC	Polarization control
PoC	Polished connection
PM	Polarization maintaining
PMMA	Polymethyl methacrylate
QCL	Quantum cascade laser
RBW	Resolution bandwidth
RTA	Rapid thermal annealer
SI	Semi-insulating
SISP	Semi-insulating surface plasmon
SP	Surface plasmon
SSN	Single sided nanostructure
TD	Time domain
THz	Terahertz

List of figures

List of tables

Chapter 1 Introduction

1.1 Terahertz radiation

The terahertz (THz) frequency region spans between 100 GHz (3 mm) and 30 THz (10 μm) in the electromagnetic spectrum (Figure 1.1) [1]. This area lies between microwave frequencies and mid-infrared frequencies. Due to a previous lack of compact sources and detectors, it has been one of the least developed regions of electromagnetic spectrum and has thus been referred to as the 'terahertz gap' [2]. However, significant advances made in the past twenty years have developed emitters and detectors to be used for several key applications.

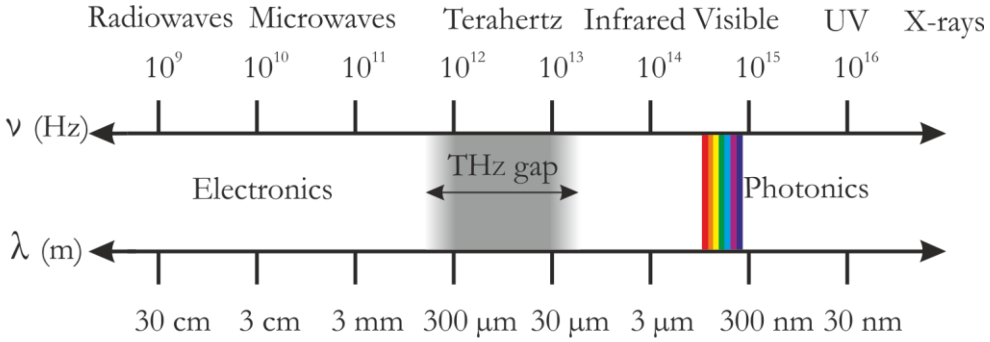

Figure 1.1: Electromagnetic spectrum showing the THz gap. Image modified from ref [3].

For example, astronomers and meteorologists are interested in the THz field due to spectral features in the interstellar dust cloud [4]. The abundance of various chemicals, which result in ozone layer depletion, have emission in the THz region [5]. Also, the composition of earth's atmosphere leading to climate change and pollution can be monitored as well [6]. This has caught the widespread attention of atmospheric chemists [7]. The emission from interstellar dust provide information about the composition, star formation in our galaxy and the cosmic abundance of various elements [8, 9]. Applications have also been reported in other fields such as imaging [10, 11], security screening [12, 13] and drug spectroscopy [12, 14-16].

An advantage of using THz radiation for imaging materials is that it is non-ionising in nature. Many chemical species have characteristic vibration spectra in the THz frequency range. The inter- and intra-molecular modes can be accessed allowing retrieval of information about not only the chemical species but also its crystallographic structure and packing [16]. Since many non-metallic and non-polar materials are transparent to THz radiation, they can be used for illicit materials detection and non-destructive evaluation [14]. This technique enables the reliable detection of drugs hidden in paper, plastics and cardboard. The detection of concealed weapons, ideal for security applications in the airport, can also be carried out using THz radiation [12, 13, 17].

Unlike X-rays [18], THz radiation is non-ionizing due to its low photon energy. Due to the high concentration of water in human tissue, THz radiation typically does not penetrate further than several millimetres before complete absorption. THz radiation can be used for the *ex vivo* imaging of cancerous tissues [19]. This research was carried out in a laboratory environment. The same group later demonstrated *ex vivo* and *in vivo* imaging of biological tissues (basal cell carcinoma) [20] in a hospital environment. THz radiation has been used for imaging human breast cancer tissues [21] and colon cancer detection [22]. Furthermore, there have been applications demonstrated including wireless telecommunications [23], dark-field imaging [24] and dental cavity diagnosis [25]. There have been several review articles over a wide range of topics [1, 3, 4, 26-30] and several books published [31-35] on the development of THz radiation and its potential application in a wide range of fields.

1.2 Terahertz sources

The lack of high power, room-temperature and efficient sources of THz radiation has hindered its impact in industrial applications. The majority of the high power THz sources available today either require cryogenic temperature operation [36] or expensive laser sources to excite them [37]. In this section, a brief outlook at the different methods adopted for THz generation is given.

The first demonstration of the generation of THz radiation dates back to the 1920s [38], using a Hertzian dipole. Although this demonstration was a significant step in bridging the electrical and optical region of the spectrum, there was no significant advancement in the field over the next sixty years. Black body temperatures in the range of 14–140 K [4] lie in the THz range. However, the radiation is weak and incoherent and thus cannot be detected efficiently. For many THz applications, a high power coherent source is required. Vacuum tube sources (VTS) such as the gyrotron produce THz radiation by electrons spiralling in a strong magnetic field and electromagnetic radiation is emitted when resonance is achieved [39] and can produce THz power in the milliWatt range [4]. In the 100–200 GHz frequency range, output power of ~1 MW has been obtained from gyro-oscillators [40]. Backward wave oscillators (BWO) generate THz radiation through the modulation of electrons using a magnetic field spiralling in the opposite direction [41] and are the most advanced among the tube sources. Power levels of ~50 mW at 300 GHz have been reported [42]. Although these VTS generate high power radiation, they require higher magnetic fields, ~tens of Tesla [43].

Since the THz region lies between the electrical and optical wavelengths, possible methods for generating THz include the up-conversion of signals at electrical frequencies or the non-linear down-conversion from optical frequencies. Frequency multipliers and doublers generate THz radiation by multiplying the source frequency in a non-linear device [44]. The reported power levels using this technique are low and proved to be inefficient at higher frequencies. For example, GaAs-based planar Schottky diodes (using multiplier chains at 600 GHz at 120 K) produced a power level of ~15 μW at 1.7 THz [45]. The negative differential resistance property of resonant tunnelling diodes (RTDs) can be used to generate and amplify THz radiation. There has been reported power levels of ~23 μW at 342 GHz and ~0.6 μW at 1.02 THz from a GaInAs/AlAs RTD [46]. Other solid-state sources currently used include impact avalanche transit time (IMPATT) diodes and tunnel injection transit time (TUNNETT) diodes [35]. The electronic up-conversion process is subjected to parasitic and transit time effects, resulting in a high frequency roll-off.

One method of generating THz from the down-conversion of optical frequencies is through optical rectification in non-linear crystals. This is achieved by exciting the crystals with an ultrafast femtosecond source, usually in the visible or near IR region. This method has been used to generate radiation between 0.18–5.27 THz from a GaSe crystal [47], with ~1 mW average power; and between 0.4 THz and 3.5 THz from quasi-phase-matched-GaAs [48]. The process of optical rectification requires phase matching between the incident optical field and THz field, restricting crystal choices and dimensions. Another means of generating THz radiation is through use of a THz wave parametric oscillator. This employs a non-linear crystal placed in a Fabry-Pérot cavity, excited with an ultrafast laser [49]. Optically pumped gas lasers have also been studied. In this instance, the gas within the cavity determines the wavelength of the emitted radiation. Methanol is a common choice as it possesses a lasing transition at 2522.78 GHz. Power levels are of the order of 1–20 mW using ~100 W excitation power [35]. However, their energy consumption is high and the apparatus is quite bulky.

Free electron lasers (FEL) can also be used for THz generation; here electrons are accelerated within an alternating magnetic field. They can produce high powered, tunable THz radiation [50], but possess several drawbacks in that they are typically very large, expensive and require strong magnetic fields (~10^5 T).

A significantly different approach to generate THz radiation is with the use of a hot hole germanium laser. In this case the lasing frequency is dependent on the hole transition between two Landau levels in the presence of electric and magnetic fields [32]. Several μW of power were reported at a heat sink temperature of 15 K at 0.42 T [51]. Another approach used strained Ge layers and the lasing transition was engineered to be between light hole and heavy hole valence subbands and have power levels of ~10 mW [52]. While these sources are easily tunable and have reported emission between 2.5 and 10 THz, and output power of ~10 mW, they require a continuous flow of liquid helium to make them operational.

Photoconductive THz emission (PCE) using semiconductors does not require cryogenic temperature for its operation and is broadband. This was first demonstrated in 1984 [53] and is now a well-established area of research. Initially, this technique was demonstrated for pulsed THz emission and later for continuous wave (CW) emission. This technique and the ‘photomixer’ sources [54] will be discussed in detail in Chapter 3 of this thesis. Consequently, power levels as high as ~2 mW have been reported [37]. More recently, a major breakthrough in THz laser research was the invention of quantum cascade laser (QCL) in 1994 [55]. Initially developed for emission in the mid-infrared (IR) region, it was later developed for THz frequencies, with the first THz QCL reported in 2002 [56]. QCLs will be discussed in Chapter 2.

In this work, two different methods are adopted for THz generation, THz QCLs (Chapter 2) and photoconductive emission (Chapter 3, Chapter 4 and Chapter 5). Both techniques can be used for the generation of pulsed (Chapter 2 and Chapter 5) and continuous wave (Chapter 2, Chapter 3, Chapter 4 and Chapter 5) THz radiation.

1.3 Structure of this thesis

Chapter 2 gives a brief introduction to the history and operation of THz QCLs. It also describes the fabrication and characterization of THz QCLs in detail. The performance parameters of a fabricated device are presented and this is used for injection locking experiment in Chapter 6.

Chapter 3 presents a study of the theory of photomixing and the development of a fibre based photomixing system, operating at 1550 nm. Emphasis is given to the emission mechanism behind photomixing and various factors affecting the emitter performance are explained. The performance of a photomixer system is optimised using the commercial TOPTICA emitter.

Two new different materials adopted for photomixing at 1550 nm, Fe doped InGaAs and Fe doped InGaAsP are discussed in Chapter 4. Photoluminescence experiments used for confirming the bandgap energy of both materials, are discussed in detail, together with the fabrication steps applied to both wafers. The performance of photomixers are compared in terms of bandwidth and output power and the Fe doping levels are varied to observe the effect this has on both single gap and interdigitated active region designs. The dependencies on bias and optical power for the two material are investigated and explained.

Chapter 5 presents the different methods applied to improve the CW THz power. This is predominately focused on enhancing the emitted and detected signal at 2 THz. Resonant antennas with dual-dipole dual-slot elements are discussed. Designs fabricated on a

Fe:InGaAsP wafer are characterized in the fibre-coupled photomixing system. Two different designs, encompassing electrodes with nanometre spacing and a two-turn antenna are adopted. The fabrication and characterization of the emitters is discussed. Mapping of the emitters as a function of excitation spot, performed at various polarizations, biases and frequencies, is explained to understand the geometrical dependence of the THz emission. In order to validate the results, the experiment was repeated in a time-domain system and to confirm the results, the experimental details performed on a three-turn antenna are also presented.

The injection locking of a THz QCL to a heterodyne photomixer source is presented in Chapter 6. Different methods adopted for locking QCLs are provided and a brief introduction into injection-locking of lasers is given. A comparison of the various photomixers discussed in the Chapter 3 and 4 is performed, in order to find the most suitable source. The injection locking setup is explained and the experiment is performed at different injected power levels and QCL bias. The effect that this has on the QCL output spectrum is presented and discussed.

Chapter 7 summarises the major achievements and results from this work and suggests topics for future work.

Chapter 2 Terahertz quantum cascade lasers

This chapter gives an overview of one of the most advanced THz sources, quantum cascade lasers. The first section gives an introduction to the historical advances that led to the development of THz QCLs. The theory behind the emission mechanism is described in the second section, discussing the different active region designs. In the third and fourth sections, QCL fabrication and characterization procedures are explained. The characterization results from a fabricated QCL are explained, including the current–voltage relationship and spectral performance.

2.1 Introduction

The first laser was demonstrated in 1960 by Theodore Maiman [57]. This device, with a ruby gain medium had an emission wavelength of 649.3 nm. Soon after the invention of the first laser, a semiconductor laser was demonstrated by two groups in 1962 [58, 59] and they demonstrated stimulated emission from a GaAs p–n junction. The invention of the first quantum well laser was only in 1975 [60]. GaAs–$Al_{0.2}Ga_{0.8}As$ heterostructures were grown on GaAs substrates and emission reported at 822 nm (1.509 eV). The gain medium and the population inversion mechanism is extremely different in each case and is briefly discussed here.

In any laser having a solid-state [57], liquid dye [61] or gas [62] as the gain medium, lasing occurs due to electron transition between two discrete energy levels, as shown in Figure 2.1 (a). The emission wavelength is determined by the energy difference between the two energy levels, $E_{21} = E_2 - E_1$ and thus each material has its own characteristic wavelength. Population inversion, necessary for lasing, is achieved by populating the upper laser level with more electrons compared to the lower laser level. In order to initiate lasing by stimulated emission, an external pump source is used. The energy of the incident photons is absorbed by the electrons and they are raised to an upper level, emitting a photon to subsequently reach the lower level by stimulated emission. Emitted photons will be coherent, which implies they have identical frequency and phase.

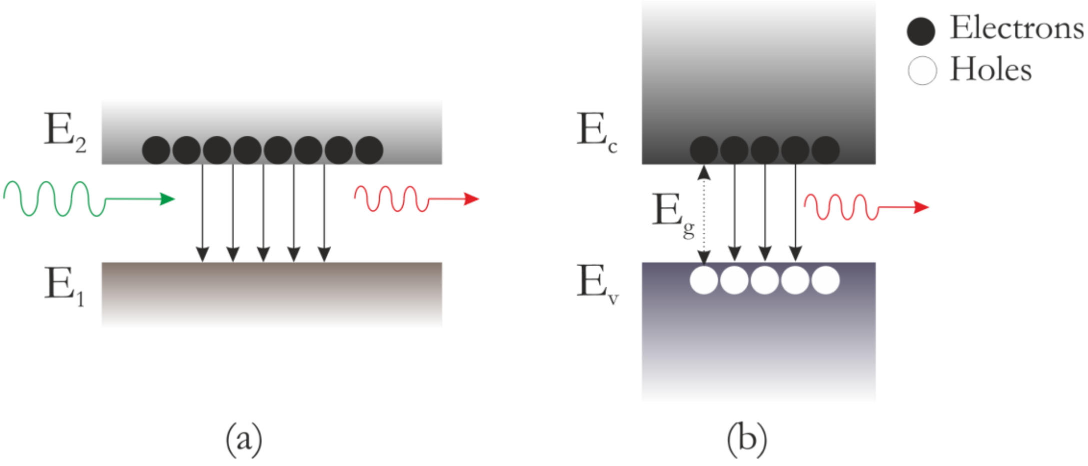

Figure 2.1: Schematic of the lasing transitions in (a) a solid-state laser and (b) a semiconductor laser. The lasing wavelength (red line) is determined by the energy difference between E_2 (upper lasing level) and E_1 (lower lasing level) and an external pump source (green line) is used for achieving population inversion. For a semiconductor laser, the lasing wavelength (red line) is ≥ bandgap (E_g).

In a semiconductor laser [59], the lasing transition takes place between the conduction band (CB) and the valence band (VB) edge. The bandgap of the semiconductor determines the maximum emission wavelength. The emission wavelength is determined by the characteristic wavelength, $E_g \geq E_c - E_v$, where E_c and E_v are the conduction and valence band edges respectively. The electron recombines with a hole and emits a photon, as shown in Figure 2.1 (b). Population inversion is achieved by either electrical or optical pumping. Quantum well (QW) lasers on the other hand have heterostructures of different semiconductor layers. A narrow bandgap material is placed between two wide bandgap materials to form a quantum well. Owing to the small thicknesses of these layers, quantum confinement effects appear resulting in the formation of bound states in the well (the multiple energy levels in a quantum well are called subbands). The emission wavelength is determined by the thickness of the quantum well [63]. The energy difference between two discrete levels, E_n in an infinite potential well is given by,

$$E_n = \frac{h^2 n^2}{8m^* L^2} \tag{2.1}$$

where h, m^* and L represent the plancks constant, electron effective mass inside the well and the well width, respectively. However, no barrier is infinitely thick and the wavefunction penetrates through the barrier.

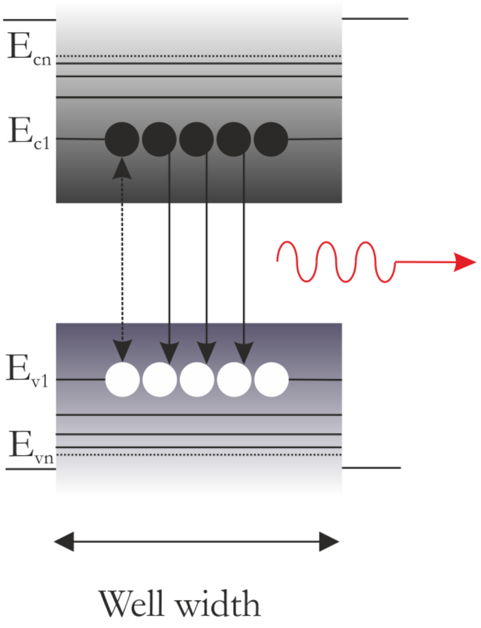

Figure 2.2: Schematic diagram showing the lasing transition in a quantum well laser. The laser transition occurs between the lowest occupied energy level in CB, E_{c1}, and the highest unoccupied energy level in VB, E_{v1}. The emission wavelength (red line) will be thus greater than the bandgap energy.

The lasing transition occurs when an electron in a bound state in the CB, E_{c1}, makes a transition to another bound state in the VB, E_{v2}, as represented in Figure 2.2. Tuning the lasing wavelength can be achieved by alternating the well thickness, since it creates a change in energy level. The emitted photon energy is greater than the bandgap energy.

Due to the involvement of two different charge types, electrons and holes, semiconductor lasers are ‘bipolar’.

A similar approach for generation of THz wavelengths between 1 mm to 100 μm has been impossible until recently due to the lack of a sufficiently small-bandgap semiconductors. A different approach for light amplification in semiconductors was proposed by Kazarinov and Suris in 1971 [64]. They suggested a possible amplification of light in intersubband transitions. Intersubband transitions occur between the different energy levels in the CB of a QW itself (i.e. holes are not involved). This can result in an emission at wavelengths smaller than the bandgap energy of the semiconductor, since valence band energy levels are not involved in optical transition.

It was Jerome Faist *et al.* [55] who demonstrated the first quantum cascade laser. It had an $Al_{0.48}In_{0.52}As/Ga_{0.47}In_{0.53}As$ superlattice grown on an InP substrate. It involved sophisticated band-structure engineering of semiconductor heterostructures leading to lasing due to intersubband transitions. They reported an emission wavelength of 4.2 μm (71 THz) and 8 mW of output power at cryogenic temperature.

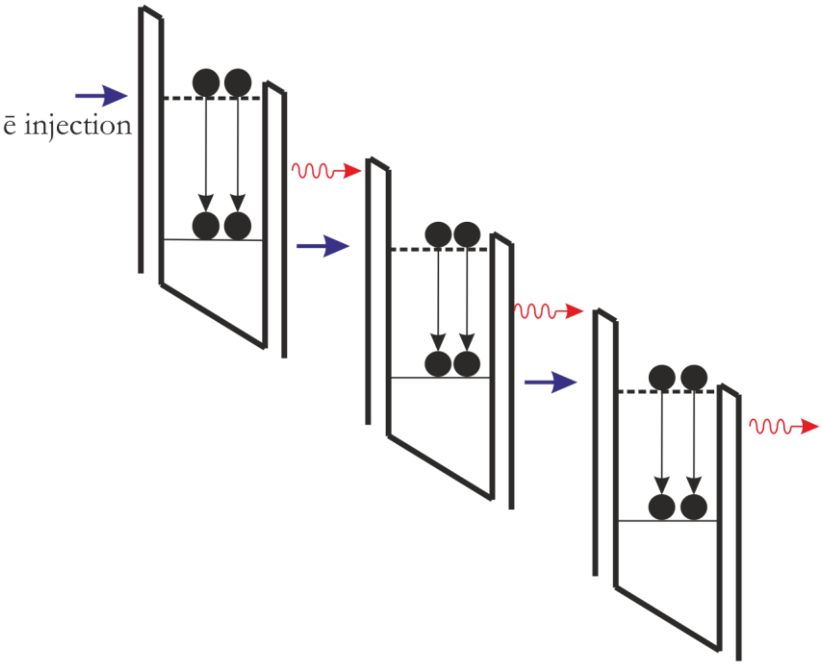

Figure 2.3: Schematic diagram showing the lasing transition in a QCL at an applied bias. Electrons are injected via an injector miniband or state (blue arrows) into the upper lasing level (dotted line) in the quantum well, transits to the lower lasing level (solid line) emitting a photon (red lines). The electrons are extracted into the upper lasing level of the next period and the process repeats. A cascade of photons is emitted.

The principle behind the QCL is different from that of a QW laser or bulk semiconductor laser. It consists of a series of heterostructure layers forming quantum wells and barriers to form a 'superlattice'. As a result of overlapping multiple energy levels from different quantum wells, 'minibands' are formed. The overlapping of energy levels results in faster scattering of electrons. These minibands can serve both as an injector or an extractor. The electron is injected to the upper lasing state from the injector region at an applied bias. Population inversion is attained between the upper lasing level and lower lasing level. The electron in the upper lasing level will transit into the lower subband with the emission of a photon with THz energy. On reaching the lower subband, coupled to the extractor state, the electrons tunnel to the next quantum well which contains the upper lasing level in the next period, will emit a photon and move to the lower subband. Thus, a single electron can produce a cascade of photons resulting in a coherent emission and hence the name quantum cascade lasers, as shown in Figure 2.3. These lasers are 'unipolar' as they involve only one type of charge carrier for lasing. Changing the lasing frequency is achieved by changing the layer thickness due to the change in energy level.

Several factors affect the lasing conditions. Population inversion between the upper lasing level and lower lasing level, is affected due to thermal backfilling of electrons and phonon scattering (thermally activated). Thermal backfilling of the lower lasing level occurs when electrons gain energy due to thermal absorption and move to a higher energy state, thus not contributing to lasing transition. Thermal phonon scattering is when electrons in the upper lasing level transit to the lower subband by emitting a longitudinal optical (LO) phonon.

Similar to any laser, in a QCL the gain in the cavity should overcome the losses. The losses in QCL arise due to several factors, a) mirror losses from the two output coupling facets, b) free carrier absorption losses due to the n+ doped semiconductor layers, and c) resonant intersubband transition losses. The threshold current density, J_{th}, defined as the current density required for the lasing to initiate [65], is given as

$$J_{th} = \frac{\alpha_w + \alpha_m}{g\Gamma} \tag{2.2}$$

where α_w, α_m, g and Γ represent the waveguide loss, mirror loss, modal gain and overlap factor between the optical field and the active region, respectively. It is desirable to have J_{th} as low as possible, corresponding to less current to operate the device, which can be accomplished by low loss and high gain.

The continuous wave (CW) operation of a mid-IR QCL was reported in 1996 [66] and room temperature operation in 1997 [67] by the same group. Power levels of 3.4 W has been achieved from the mid IR QCLs CW mode at room temperature [68].

2.2 Terahertz quantum cascade lasers

Soon after the invention of mid-IR quantum cascade lasers, many attempts were made to operate the laser in the terahertz region. In the 1–5 THz region, the photon energy (~4–25 meV) is lower than the LO phonon (lattice vibration) energy (~36 meV in GaAs) [69, 70]. There are other contributing factors due to electron-electron scattering, electron-impurity scattering, interface-roughness scattering and phonon scattering. In addition, the required spacing between the intersubband energy levels in the THz region is much smaller than in the IR region, making it more difficult to selectively depopulate the lower lasing level, thus the LO phonon cannot be used for population inversion. Another constraint in achieving THz QCL was waveguiding. The free carrier absorption losses are quite high, which is proportional to the square of the wavelength [71].

The first demonstration of a THz QCL was only a decade later by Köhler *et al.* [56]. It was a GaAs/AlGaAs chirped superlattice active region, (which is discussed in the next subsection) QCL having a single plasmon waveguide (explained in Section 2.2.1) and emitted at a single mode frequency of 4.4 THz and 2 mW output power and had a maximum operating temperature of 50 K in pulsed operation.

A range of active region designs were developed to improve the emission frequency, efficient removal of the electrons from lower subbands and efficient injections. THz QCL active regions can be classified into four principal design schemes: a) chirped superlattice (CSL), b) bound-to-continuum (BTC), c) resonant phonon (RP) and d) hybrid design, as shown in the Figure 2.4.

a) Chirped superlattice (CSL)

The wavefunctions of the different quantum wells and barriers in the active region couple to form minibands and thus the lasing transition takes place between a pair of minibands. As shown in Figure 2.4 (a), the lasing transition takes place between the lower state of the upper miniband and the upper state of the lower miniband. Here, the population inversion is due to scattering of electrons in the various coupled minibands. The electron relaxation from the upper state of the lower miniband takes place due to elastic scattering. This design has the advantage of low threshold current density and the disadvantage is thermal backfilling which limits its operation at higher temperatures [56].

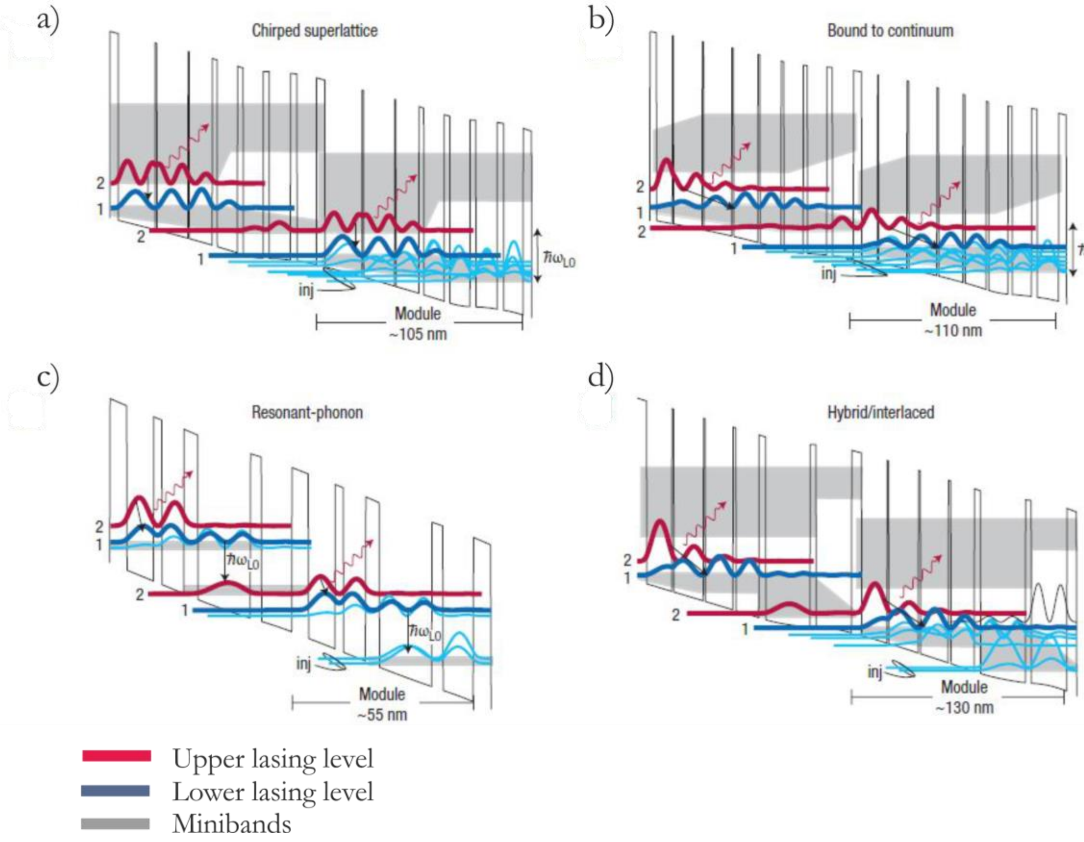

Figure 2.4: Schematic diagram representing commonly used active region designs in THz QCLs, (a) Chirped superlattice, (b) Bound-to-continuum, (c) Resonant-phonon and (d) Hybrid, showing energy levels and lasing transitions. Image reproduced from ref [69].

b) Bound to Continuum active region

Very similar to the CSL design, the upper lasing miniband is replaced by a bound state which forms an isolated state adjacent to the injection barrier. Lasing takes place between the bound state and the miniband and depopulation involves elastic scattering within the minibands. The radiative transition is more diagonal (from one well to another well) in real space compared to the CSL design. Due to less thermal backfilling, better operating temperatures and power performances [72] can be achieved.

c) Resonant phonon active region

The collector and injector barrier energy level differs from the lower lasing state by the energy of a LO phonon, E_{LO}=36 meV in GaAs [70], which enhances the efficient depopulation of the lower lasing state by emitting LO phonon. Minibands are not involved in the lasing transition and thus it is possible to selectively depopulate the lower lasing state compared to the previous two active region designs. Electrons reaching the upper lasing level emits a photon and reaches the lower lasing level. The collector, then emits LO phonon, which is in a tunnelling resonance with the excited energy level in the adjacent quantum well. Electrons are efficiently removed from the lower level to the upper level which reduces the lower state lifetime. The upper state has little overlap with the injector state and has better lifetime compared to the lower state. The only disadvantage is higher threshold current [73], required for the alignment of different energy levels (LO phonon energy ~36 meV).

d) Hybrid design

This design is actually a compromise between the BTC and RP designs. Here the upper lasing state remains a bound state as in the BTC design and the lower miniband is at a LO phonon energy difference from the injector well. The direct coupling between the upper level and the extractor well is relaxed. Also the alignment at the extraction well is relaxed as the alignment can take place over a miniband with respect to a particular level. The RP design has the greatest disadvantage of requiring high threshold current for alignment of the energy levels (upper lasing level, lower lasing level and the injector level) for lasing. However, for a BTC design, optical transition occurs at a very low threshold current. Both designs are combined to produce this hybrid design [74]. Also a new design termed scattering assisted injection was also demonstrated in 2010 [75].

2.2.1 Waveguiding in THz QCLs

For waveguiding in THz QCLs, two different methods are employed a) semi-insulating surface plasmon (SISP) [56] and b) metal-metal or double metal (DM) waveguide [76]. In a SISP waveguide, the mode is confined between top metal layer and the bottom n^+ layer which acts as a quasi-metallic layer, as shown in Figure 2.5 (a). The n^+ layer between the active region and the substrate acts as both an optical confinement layer and electrical contact layer. The electromagnetic mode is confined due to the overlap of the modes with the surface plasmon modes beneath the top metal layer, see Figure 2.5 (b) and the bottom n^+ layer. In the case of DM waveguide, the bottom n^+ layer is replaced with a second metallic layer, resulting in better mode confinement and thus reducing the losses. The processing complexity and growth requirements had made SISP devices favourable. In fact, the tighter mode confinement in DM QCLs results in a divergent beam compared to SISP QCL.

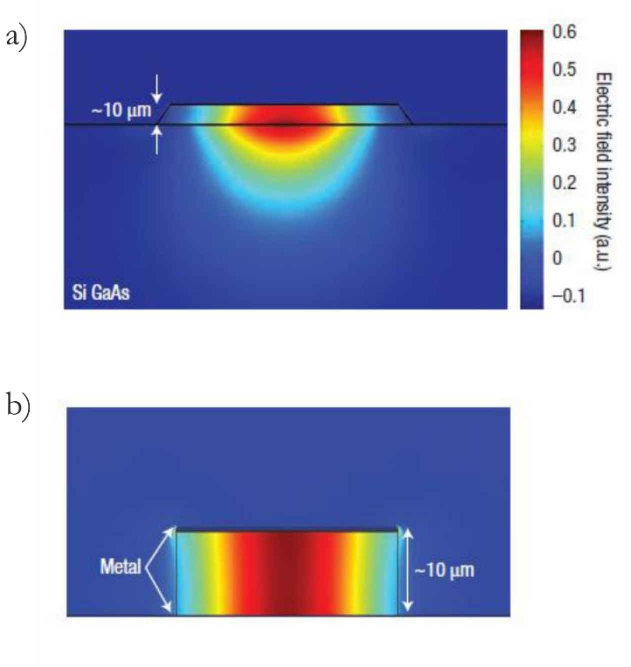

Figure 2.5: Electric field intensity pattern observed in the two commonly used waveguide design, (a) SISP and (b) double metal. Image reproduced from ref [69].

2.2.2 THz QCL advances to date

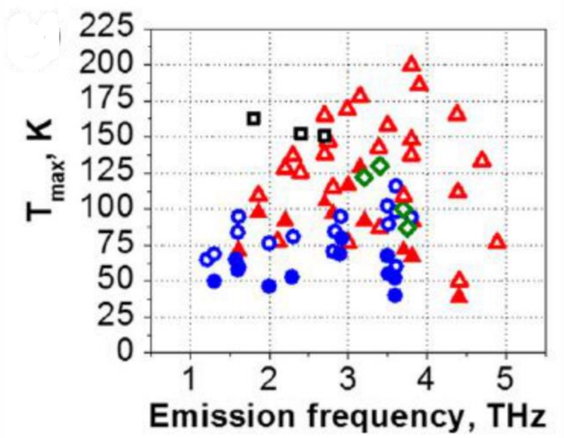

Figure 2.6: Summary of the THz QCL performance at different maximum operating temperatures and the corresponding lasing frequency. Image reproduced from ref [77]. Red triangles correspond to RP design, black squares are scattering-assisted design, blue circles are BTC design and green diamond correspond to material system other than GaAs/AlGaAs.

Ever since the first demonstration of THz QCL in 2002 [56], there have been several reports to improve the operating temperature in both pulsed and CW mode [78-83]. The maximum operating temperature attained is ~200 K [84] in pulsed mode and ~129 K [85] in CW mode, without the presence of any external magnetic field, see Figure 2.6. Maximum operating temperatures as high as 225 K [86] have been obtained using magnetic field (B), since the presence of magnetic field can reduce non-radiative scattering between energy levels. The range of frequencies achieved with QCLs is between 1.2 THz [87] and ~5 THz [88]. The maximum power levels obtained to date are ~1 W in pulsed mode [36] and ~138 mW in CW mode [89]. A recent review of THz QCL performance in terms of maximum operating temperature and frequencies is also provided in ref [77].

In this chapter, fabrication of a BTC QCL with a SISP waveguide is demonstrated as it will be used for injection locking, which will be discussed in Chapter 6. Fabrication procedure is the same for varying active region QCLs with a SISP waveguide.

2.3 Fabrication of THz QCLs

The active region of a QCL encompasses hundreds of periods of GaAs/AlGaAs [56] layers, grown on a lattice matched semiconductor, SI-GaAs substrate. The growth process is usually carried out in a molecular beam epitaxy (MBE) machine. MBE growth is preferred over other growth techniques due to the uniformity and improved surface quality. The growth is performed under vacuum and precursors used are of high purity.

The active region of the QCLs used in this work had a GaAs/AlGaAs heterostructure and was grown on SI-GaAs substrate. The wafers were grown by Dr. Lianhe Li in the MBE machine at The University of Leeds and were processed in the Wolfson nanotechnology cleanroom. A standard SISP waveguide THz QCL fabrication procedure carried out in the group was followed and can be found in these references [90-92]. The different steps involved in the fabrication process are discussed in detail in the following subsections.

2.3.1 Defining the fabrication window

Initially, a 8 mm×6 mm piece was cleaved from the 2-inch wafer. The wafer size was chosen to match the dimensions of the photolithography mask, to be used in the subsequent steps. The sample was cleaned using acetone and isopropyl alcohol (IPA) to remove any dust or debris. The sample was left in acetone for 5 min in a beaker and placed in a 20% power ultrasonic bath (Bandelin Sonorex Digital 10P) and this was followed by repeating the same in IPA. The sample was blow dried using dry nitrogen (N_2). However, to ensure the removal of any sort of organic waste, the sample was left in a plasma asher, Emitech K1050X at 85 W power for 5 min.

It was then spun with Shipleys S1813® photoresist in a spin coater at a rate of 4000 rpm for 30 s. This ensured a resist thickness of 1.2–1.4 μm. The resist was then baked using a hotplate at 115 °C for 1 min to remove any excess solvent on the sample surface. The first photolithography step was to remove the edge beads that might have arisen due to resist build-up, from the four corners of the sample. If they are not removed, it can affect the subsequent fabrication steps. The sample was exposed using a UV mask aligner at an incident wavelength of 310 nm at 10 mWcm^{-2} for 6 s. The exposed sample was developed in Microposit MF 319 developer for 75 s. Following this, sample was cleaned using de-ionised (DI) water for 1 min and blow dried using dry N_2.

2.3.2 Defining laser ridge

The active region of QCL (multiple periods of GaAs/AlGaAs layers) is sandwiched between two highly doped n$^+$ layers which is intended for applying bias. The top n$^+$ layer is for top contact and the bottom n$^+$ layer is for bottom contact. All the layers are grown uniformly in the MBE machine and a mesa etching has to be carried out to define the laser ridge of required length and width. The laser ridge is defined by photolithography followed by a mesa etching process to expose the active region.

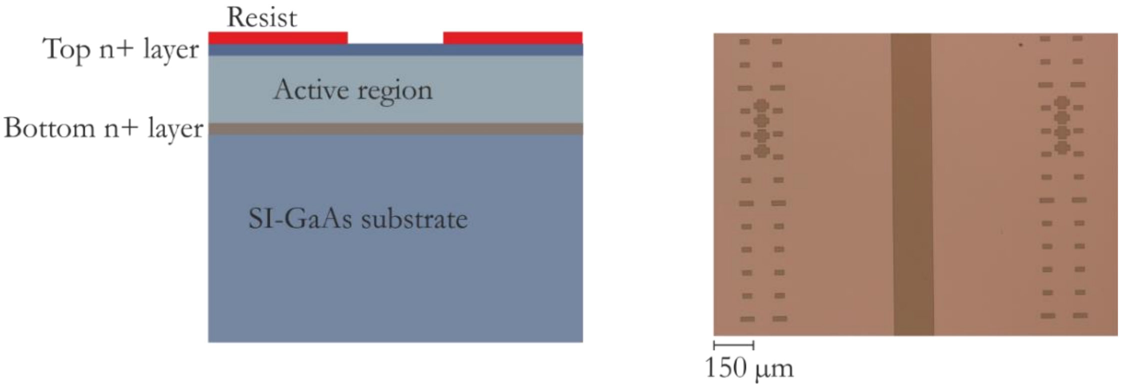

Figure 2.7: Schematic representation (left) and optical image (right) of the ridge definition lithography step. Different layers are marked in the schematic diagram and with the resist (red) layers after development. In the optical image, laser ridge is in the centre and the small rectangle shapes on both sides are alignment marks.

With the edge beads removed, the sample was exposed by a second photolithography step. A chrome-on-glass mask was used for this purpose. The sample was exposed using the same mask aligner used for edge bead removal at similar power levels, with an exposure time of 3 s[1]. The exposed sample was developed in MF 319 for 75 s followed by a quick wash in DI water. Figure 2.7 shows a schematic representation and photographic image of the top surface soon after lithography. The mask has ridge widths ranging between 90 μm and 200 μm, in the present work the ridge width is 150 μm, unless stated. The alignment marks were defined on both sides of the ridge to help identify the right design for further lithography steps.

A wet chemical etch was carried out for the mesa etch. For that, the sample was initially stuck to a glass plate using S1813 and soft baked at 115 ºC for 1 min. The wet chemical etching solution comprised of concentrated Sulphuric acid (H_2SO_4), hydrogen peroxide (H_2O_2) and water (H_2O), i.e., H_2SO_4: H_2O_2: H_2O in a 1:8:40 ratio. The prepared solvent was left for 10-12 minutes at 25 ºC to have a uniform etch rate. The required etch depth depends upon the active region design and usually ranges between 12–15 μm. Special care was taken to ensure that the sample was not overetched, as overetching the sample may lead to removal of the bottom n^+ layer, thus rendering it useless. To confirm the etch depth, an Alpha step D-500 surface profiler was used. Figure 2.8 shows the sample after the etching process, both schematic and photographic images.

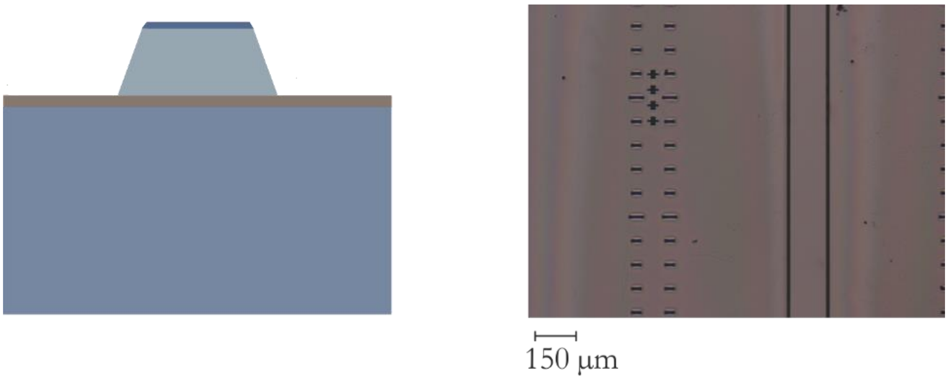

Figure 2.8: Schematic representation (left) and optical image (right) of the ridge after etching.

Wet etching is partially isotropic with slightly different etch rates in the horizontal and vertical directions resulting in slightly different etch height and width at the top and the bottom of the ridge, shown in Figure 2.8. The sample was then removed from the glass plate and the resist was cleaned by leaving the sample in acetone for 5 minutes. The sample was later cleaned in IPA and blow dried using dry N_2. Plasma ashing was also performed at similar power levels.

---

[1] The exposure time for usual lithography steps is 3 s and is used for all the photolithography steps from now on. However, a longer exposure time was used for edge removal step to ensure that thick resist at the corners was exposed properly.

2.3.3 Defining the bottom contact

The bottom contact layer, as mentioned earlier, is the n^+ layer buried underneath the active region. This layer is exposed by wet etching and to make an electrical contact, metallization and annealing was performed. The sample was spun with S1813 and baked at 115 ºC before photolithography. After exposure in the UV mask aligner, the sample was left in chlorobenzene to enable the lift-off process. In order to facilitate this, the sample after exposure was left in chlorobenzene for 2 minutes and blow dried. The sample was developed using MF 319 for 75 s and cleaned using DI water. Chlorobenzene changes the solubility of the resist in the exposed and unexposed regions thus creating an undercut profile [93, 94]. The sample was plasma ashed for 90 s at 25 W to clean the surface before loading on the thermal evaporator.

For bottom contact metallization, AuGeNi alloy was used. AuGeNi alloy is the most popularly used metal for Ohmic contacts on GaAs [95, 96]. The alloy was evaporated in Leybold thermal evaporator at vacuum pressure of $<1.9\times10^{-6}$ mBar and ~250 nm thickness was evaporated. After evaporation, the sample was left in acetone for 30 min for lift-off. The beaker with acetone and sample was placed in an ultrasonic bath for 2 minutes at 10% power to remove any unwanted metal flakes and resist residue left on the active region or on the edges. For a 150 μm ridge, the width of the bottom contacts was ~200 μm. The sample was cleaned using IPA and blow dried using N_2.

With the metal evaporated on the n^+ layer, the sample was annealed at 430 ºC for 1 min in Rapid Thermal Annealer (RTA) from AnnealSys. Annealing ensured that the Ge atoms are doped into the bottom n^+ layer thus reducing the contact resistivity [97, 98] (making it an Ohmic contact). Figure 2.9 shows the sample after (a) lithography, (b) metallization and (c) annealing. The change in the metal surface appearance is attributed to annealing effects.

The contact resistance between the two annealed metal contacts on both sides of the ridge was measured in a probe station using a multimeter and the resistance needs to be between 6–10 Ω. The resistance values of >15 Ω implies an over etch resulting in removal of the n^+ layer, in which case the sample is unusable.

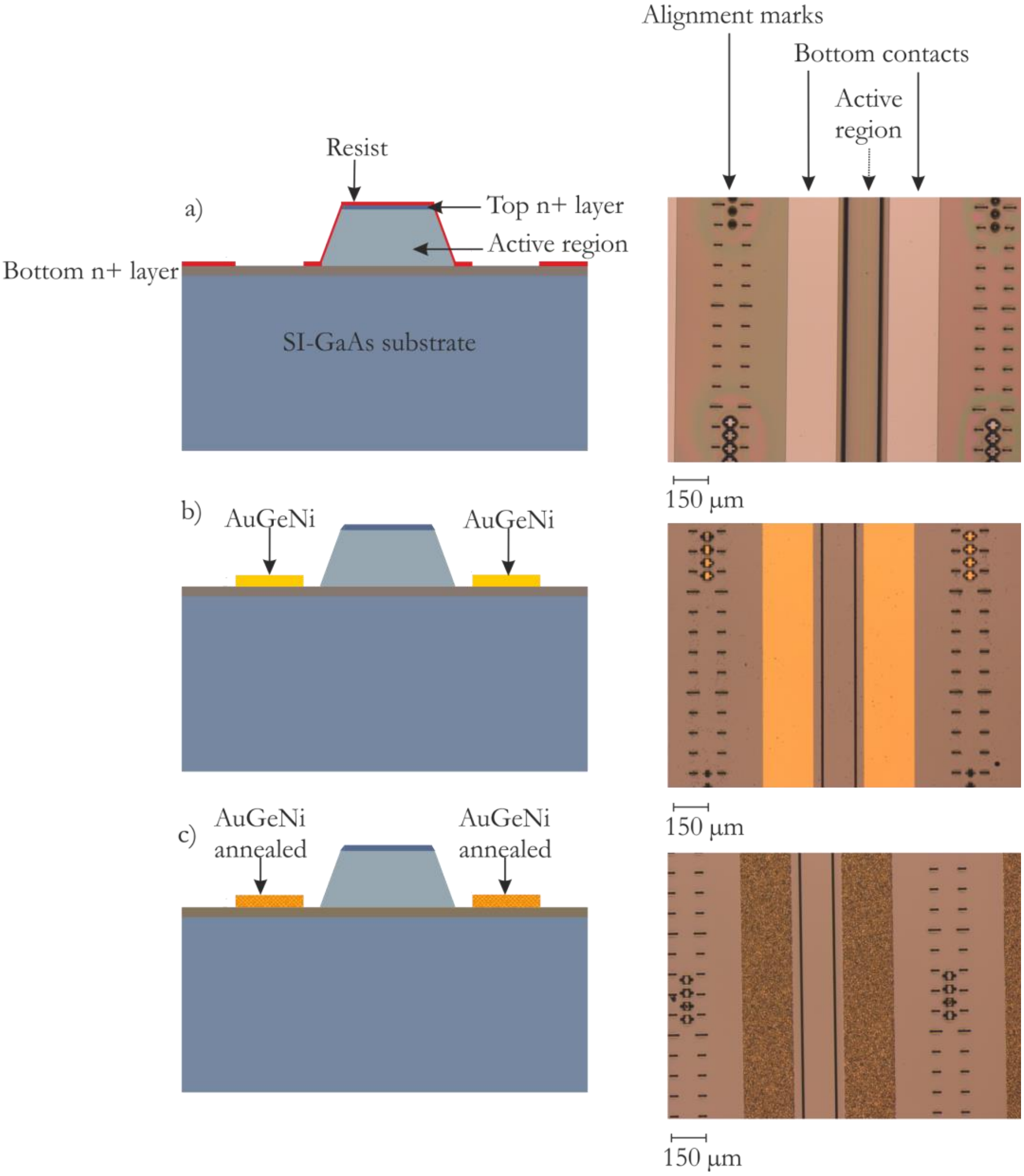

Figure 2.9: Schematic representation (left) and optical image (right) of the QCL defining bottom contact (a) after lithography (b) after metallization and (c) after annealing.

2.3.4 Defining top contact

To apply the electrical connection to a QCL, a top contact is also defined. As for the bottom contact, resist spinning, baking, lithography, chlorobenzene curing and development were conducted to create the top contact. The alignment marks made the process easier. Instead of completely covering the top surface of the ridge, two thin 20 μm wide strip lines were defined using photolithography to remedy waveguiding issues [99]. AuGeNi was used for metallization and the preferred thickness was 100 nm–120 nm.

Metallization was carried out in the Leybold thermal evaporator under similar vacuum levels as for the bottom contact and the sample was lifted off in acetone in an ultrasonic bath at 10% power for 2 min. The sample was later cleaned using acetone and IPA and blow dried using N_2. Figure 2.10 shows the top view of the surface after (a) lithography and (b) metallization. Unlike the bottom contact, the top contact was not annealed after metallization to prevent the diffusion of Ge atoms into the active region which can affect the waveguiding.

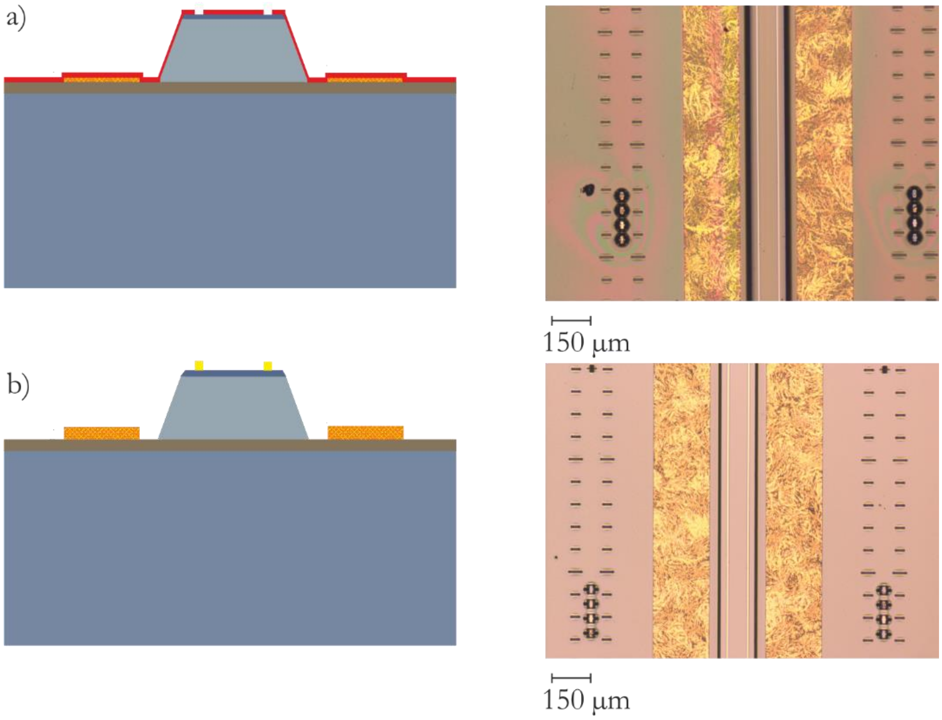

Figure 2.10: Schematic representation (left) and optical image (right) of the QCL defining top contact (a) after lithography (b) after metallization.

2.3.5 Over-layer deposition

Although the top and bottom contacts are defined, in order to ensure that the THz wave is confined within the laser cavity and also to make it easier for wire bonding, top and bottom contacts were covered with a Ti/Au over-layer. The Ti layer was used along with Au layer as an adhesive. The resist spinning, baking, photolithography, exposure, chlorobenzene curing and development process remained the same as the bottom contact definition discussed in Section 2.3.3.

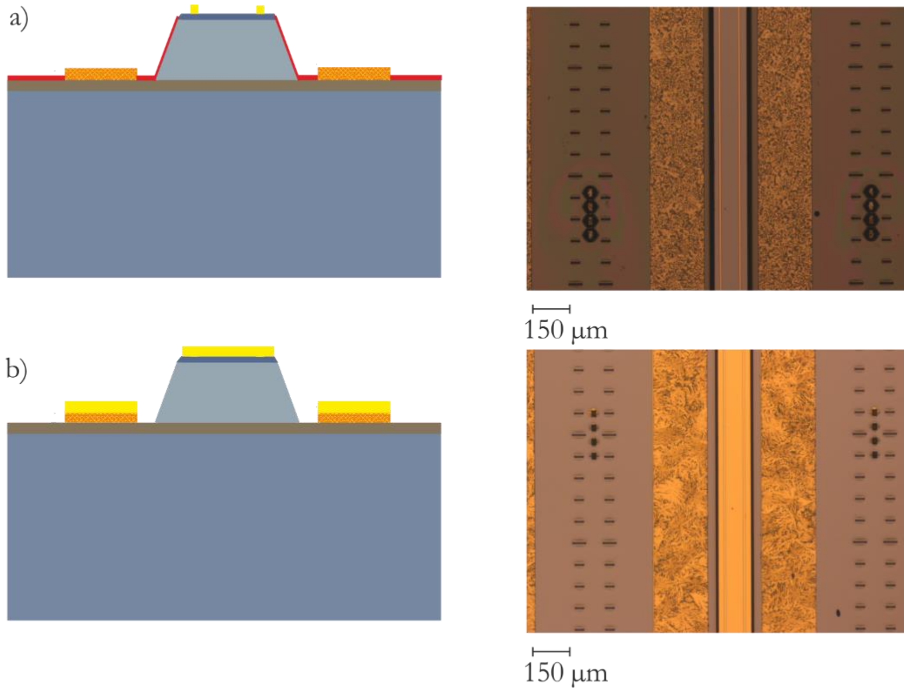

Figure 2.11: Schematic representation (left) and optical image (right) of the QCL defining overlayer (a) after lithography (b) after metallization.

The metallization was carried out in Leybold electron-beam evaporator 350. Ti/Au of 10 nm/150 nm thickness was deposited on the surface. After metallization, sample was left in acetone in an ultrasonic bath for 2 min at 10% power for lift-off. The sample was cleaned in acetone and IPA after lift-off and blow dried using N_2. Figure 2.11 shows the schematic and optical images of the sample soon after a) lithography and b) lift-off.

2.3.6 Substrate thinning

The whole fabrication process to this point was carried out on a ~500 µm thick SI-GaAs substrate. Since QCLs operate at cryogenic temperatures and the maximum operating temperature is 200 K [84] to date, the substrate thickness is reduced to ~150–200 µm to reduce thermal resistance.

Figure 2.12: Schematic of the QCL after substrate thinning and metallization. The thickness of the substrate is reduced from ~500 µm to ~200 µm.

The sample was stuck to a glass plate with the laser ridge facing down using wax. A small (5 mm×5 mm×3 mm) piece of wax was placed on one end of the glass plate which was left on a hot plate at 90 °C. When the wax melts the QCL was placed gently on top of it. It was ensured that the wax covered the top of the ridge and also sides, otherwise the sample can be damaged by etching the laser ridge.

The etching solution used for ridge definition, discussed in Section 2.3.2, was used with a different solvent concentration. The etch rate required for ridge definition needs to be lower or else it can result in over etching the substrate. To increase the etch rate, the solvent ratio was altered to be, H_2SO_4: H_2O_2: H_2O at 1:8:1 ratio. The sample stuck to the glass plate was immersed in the solvent and the etch depth was monitored using Testronic micrometer. Once the substrate thickness was reduced to ≤ 200 μm, the etching was stopped. The sample was removed from the wax on the glass plate by placing it on a hot plate at 90 °C and immersing the molten wax along with the sample in trichloroethylene (TCE). TCE ensured removal of any remaining wax on the laser ridges or bottom contact.

With the substrate thinned down, the sample was found to be extremely delicate to handle and special care was taken to avoid breakage. The back surface was then metallized in Leybold electron beam evaporator with Ti/Au of thickness 20 nm/200 nm to help it stick to the indium and then to the copper block, see Figure 2.12.

2.3.7 Top contact sintering

In Section 2.3.4, it was mentioned that the top contact was not annealed. However, the top contact was sintered at 270 °C for 4 minutes so that Ge atoms will not penetrate too deep into the active region. Annealing was carried out in an RTA for four minutes. Although this process could have been performed soon after top contact metallization, carrying out at this stage ensured that all deposited metal (including overlayer) is properly adhered to the substrate. The sample was further cleaned with acetone and IPA, and blow dried using dry N_2 to remove any waste deposited on the surface and was plasma ashed for 90 s at 25 W. With this, the sample is ready to be cleaved and mounted on a copper block for testing.

2.3.8 Cleaving, mounting and bonding

The sample had three ridges of 6 mm length and 150 μm width separated by ~1 mm. The cleaving process was started by separating the laser ridges. The JFP S-100 scriber was used for this purpose. A scribing mark was made on the sample using the scriber, as far as possible from the ridges, and was separated manually. The separated laser ridge was again scribed to specify the laser dimension of required length. The laser ridge was then checked under a microscope to ensure a mirror-like facet, or else this can contribute to losses in the cavity. Scribing using the machine ensured a length accuracy of ~hundreds of nm.

The laser ridge was mounted on a copper block in order to carry out the characterization at cryogenic temperatures. A 20 mm×7 mm×2 mm copper block was cleaved from a copper sheet. The top and bottom surface was polished in a lapping station with a mirror-like finish for the top surface. The bottom surface was also polished to get rid of any non-uniformities that might affect the thermal contact between the QCL and the cryostat. The copper block was then cleaned using acetone and IPA. The top surface was then deposited with Ti/Au of 10 nm/150 nm thickness in a thermal evaporator.

Two gold coated ceramic pads were glued using GE varnish at the two ends of the copper block for wire bonding the QCL. The copper block was kept at a heatsink temperature of 100 ºC on the hotplate on a Kulicke & Soffa 4524 ball bonder machine. A small piece of indium sheet was placed at the gap between the two ceramic pads. Initially, the hotplate heatsink temperature was increased to 145 ºC (slightly above the melting point of Indium, which is 142 ºC) and as the indium melted, it was spread into a uniform thin layer using a flat-end blade. With hotplate temperature reduced to 100 ºC, the QCL was placed on top of the indium. QCL was pressed slightly to the indium using two stationary metal needles. As the hotplate temperature was further increased to 145 ºC, the needles pressed the QCL gently into the molten indium and thus soldering the QCL to the copper block. The heatsink temperature was reduced to 100 ºC in which the bonding was performed.

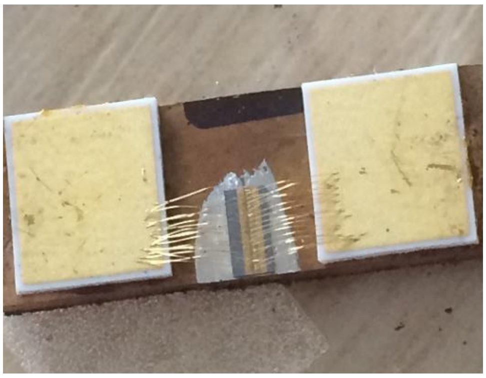

Figure 2.13: Photographic image of the QCL mounted on the copper block and wire bonded to contact pads.

Au bond wires were used to bond the top and bottom contacts to the two separate ceramic pads. The two ceramic pads used on the two sides of the copper block ensured that the THz radiation can be accessed simultaneously from both facets which is crucial for experiments, and will be discussed further in Chapter 6 of this thesis. Figure 2.13 shows the photographic image of the device mounted on a copper block.

2.4 Characterization of THz QCLs

A QCL mounted on the copper block was characterized soon after fabrication in a continuous flow liquid helium (Li:He) Janis ST-100 cryostat. The QCL was placed on the cryostat cold-finger (also made of copper) and two copper pins were used for providing electrical connections to the QCL. The cryostat was initially pumped down to a low pressure of ~4×10^{-6} mBar to isolate the He chamber from room temperature followed by cooling down using Li:He to 5 K. The QCL was characterized in both pulsed and CW mode, discussed in Sections 2.4.1 and 2.4.2 respectively.

2.4.1 Pulsed mode

The experimental setup used for acquiring light–current–voltage (LIV) characterization details of the QCL is shown in the Figure 2.14. An Agilent 8114A pulse generator (APG) capable of producing pulse trains of variable duty cycle from 0.1% to 99% was used. The APG was used to generate 10 kHz pulses at 2% duty cycle. The 10 kHz frequency pulses were electronically gated at 167 Hz by an Agilent arbitrary waveform generator (AWG). The voltage was measured using a digital Oscilloscope, Keysight 2002A. For the current measurement an inductive loop current probe was used. The temperature controller monitored the temperature of the heatsink. The cryostat was mounted on an XYZ linear translational stage enabling navigation of the THz beam position. Two *f/3* off-axis parabolic mirrors collected the THz radiation and focussed it onto a liquid helium (He) cooled bolometer. The bolometer response was measured using a lock-in amplifier referenced at 167 Hz, to match its frequency response (~6 ms response time). The cryostat and the parabolic mirrors were placed inside a purge box pumped with nitrogen to avoid any atmospheric absorption of terahertz radiation. The LIV of the QCL was acquired using a LabView program controlling the various instruments.

For the absolute power measurements, a Thomas Keating (TK) power meter was used. The bolometer was replaced with the power meter. Similar to the bolometer, the power meter had an optimised frequency of 30 Hz. Leaving the QCL running in a pulsed mode, the modulation frequency was changed from 167 Hz to 30 Hz for power measurement.

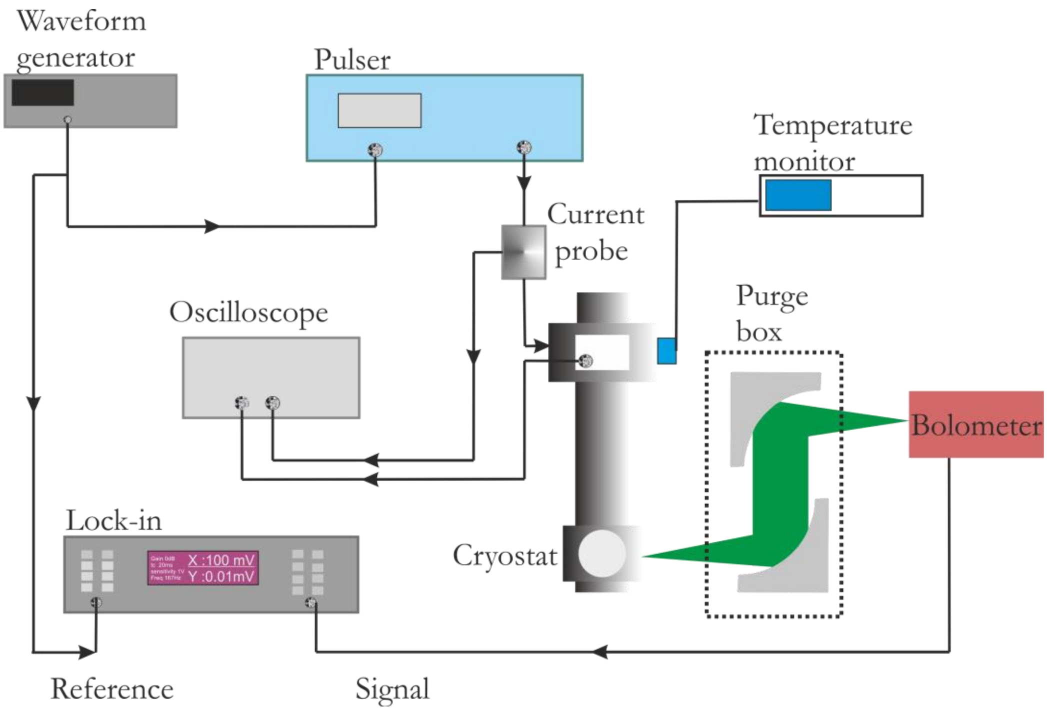

Figure 2.14: Experimental configuration used for characterizing QCL in pulsed mode with bolometric detection.

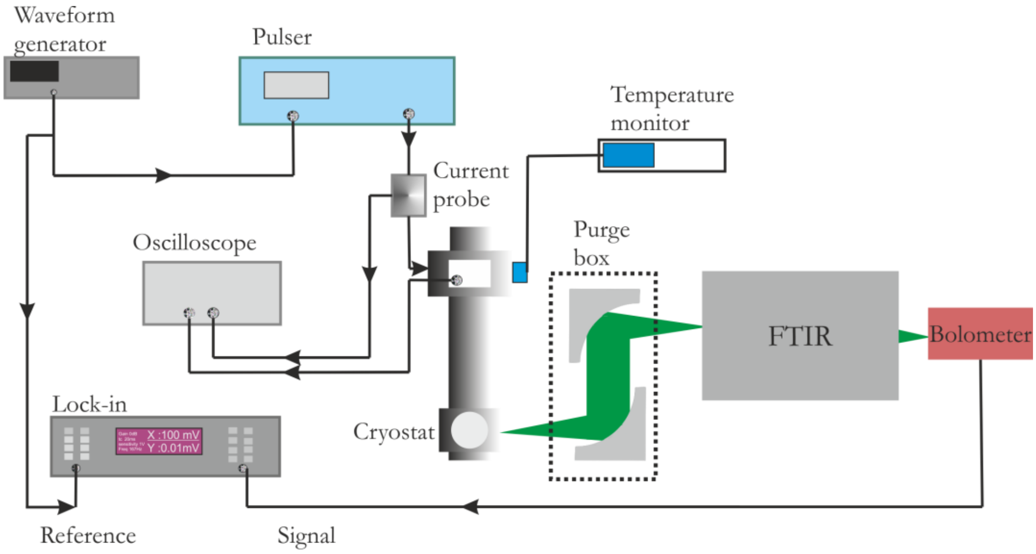

Figure 2.15: Experimental configuration used for measuring the spectra of the QCL in pulsed mode.

The spectra from the QCL was measured using a Fourier transform infrared (FTIR) spectrometer to confirm the exact frequency. The experimental setup used for FTIR measurement is shown in the Figure 2.15. The THz generated from the QCL was focussed into a Bruker Optics IFS66/V FTIR spectrometer with a resolution bandwidth of

7.5 GHz using two *f/3* parabolic mirrors. The FTIR spectrometer had a Michelson interferometer inside.

2.4.2 CW mode

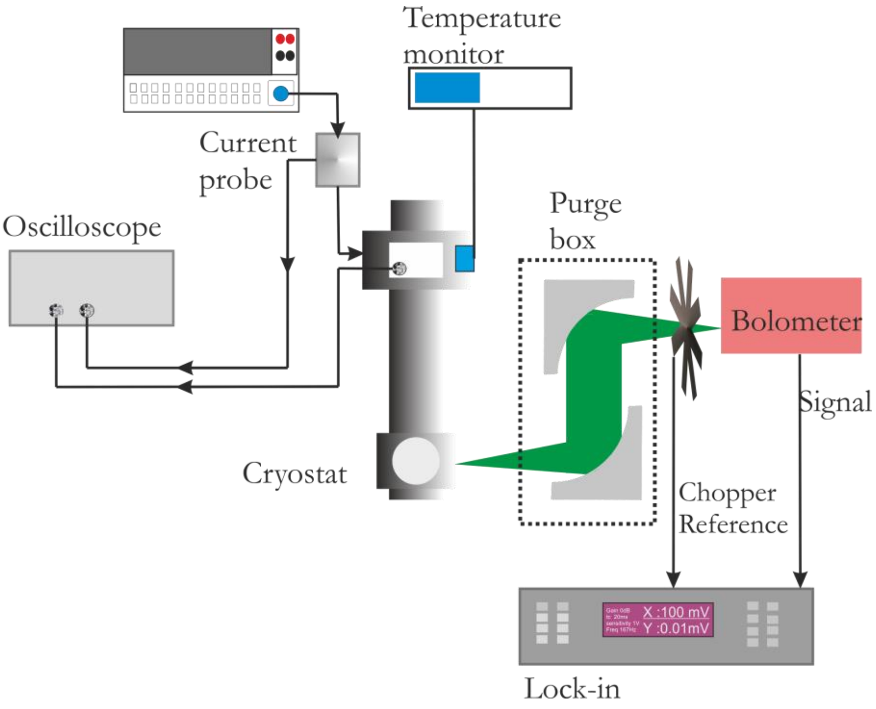

Figure 2.16: Experimental configuration used for characterizing QCL in CW mode with bolometric detection. An optical chopper is used for reference.

With the device confirmed to be lasing in pulsed mode, the duty cycle of the pulse was slowly increased from 2% to 95%, if the QCL still continued to lase, the pulse generator was replaced with a DC source. The experimental configuration for CW characterization is shown in the Figure 2.16. The pulse generator used for biasing the QCL was replaced by a DC source. A Keithley 2400 was used for applying DC bias. Since the bolometer has an optimum response frequency at 167 Hz, the THz beam was optically modulated using a mechanical chopper. The chopping frequency was adjusted to 167 Hz for LIV measurement and 30 Hz for the power measurement. The spectra was also measured using the same configuration as shown in Figure 2.15, except that the pulsed source was replaced with a DC source.

2.5 Results

Although a series of different active region QCLs were fabricated and characterized, characterization data of one particular QCL is mentioned in this section, L1071. This wafer has a BTC active region and was designed for emission at a low frequency ~1.95 THz [100]. For integration with QCLs involving photoconductive emitters, it is desirable to have frequencies lower than 2 THz, as will be discussed in detail in Chapter 6.

A 2.5 mm long, 200 μm wide device was cleaved from the laser ridge. The device was indium soldered and mounted onto a copper block as discussed in Section 2.3.8. The resistance between the top and bottom contact was measured to confirm that the device wasn't shorted or if there is an open circuit. Thermal grease was applied before placing the copper block on the cold finger to ensure better thermal contact between the two. With the thermal and electrical connections confirmed to be fine, the device was cooled down to 5 K and was characterized in pulsed and CW experimental configurations. The LIV, output power and spectral features are presented in the following subsections.

2.5.1 Pulsed mode

The LIV of L1071 THz QCL is acquired at different heat sink temperatures. The LIV characteristics was recorded for every 10 K step. In Figure 2.17 the LIV is plotted as a function of threshold current density. The QCL had a maximum operating temperature of 52 K and the QCL didn't lase beyond that. The peak output power measured at 10 K was ~4.0 mW. The threshold current density was low, ~135 Acm^{-2} at 10 K.

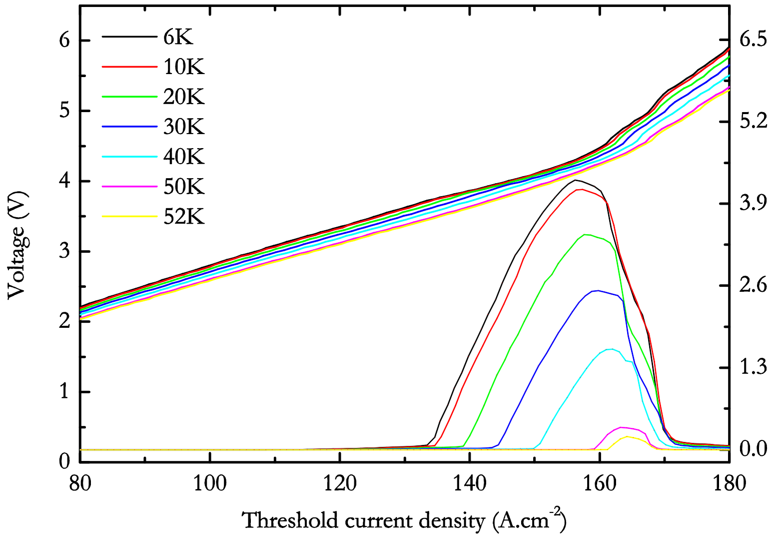

Figure 2.17: LIV from the L1071 2.5 mm long BTC QCL at different heat sink temperatures in pulsed mode. A maximum power of ~4 mW was measured at 10 K.

The spectral measurements were performed at 10 K, soon after the characterization to confirm the emission frequency of the device and is plotted in the Figure 2.18. The lasing frequency was predominantly single mode at 1.99 THz. The slight difference in the emission frequency compared to the paper 1.93 THz [100] is attributed to the growth difference, which was conducted at two different places.

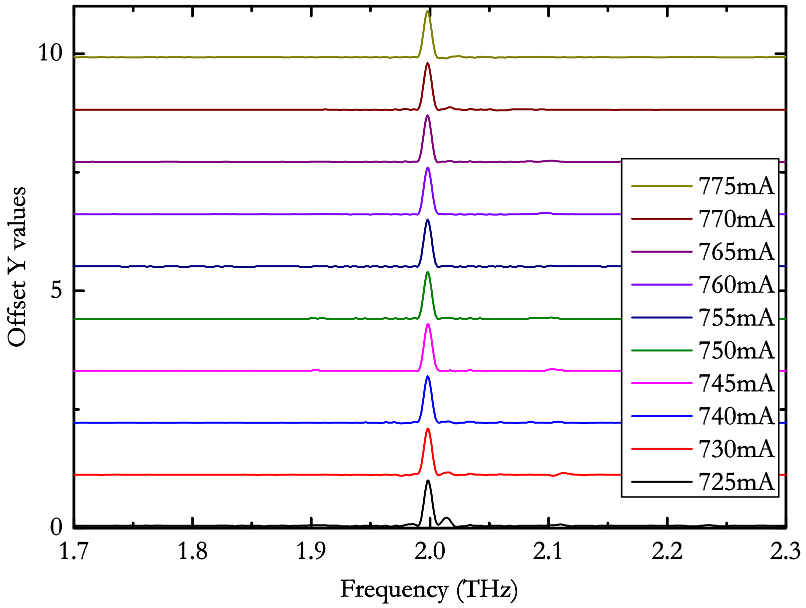

Figure 2.18: Spectra from the L1071 2.5 mm long device at different bias levels. Laser was predominantly single mode with a peak at 1.997 THz.

2.5.2 CW mode

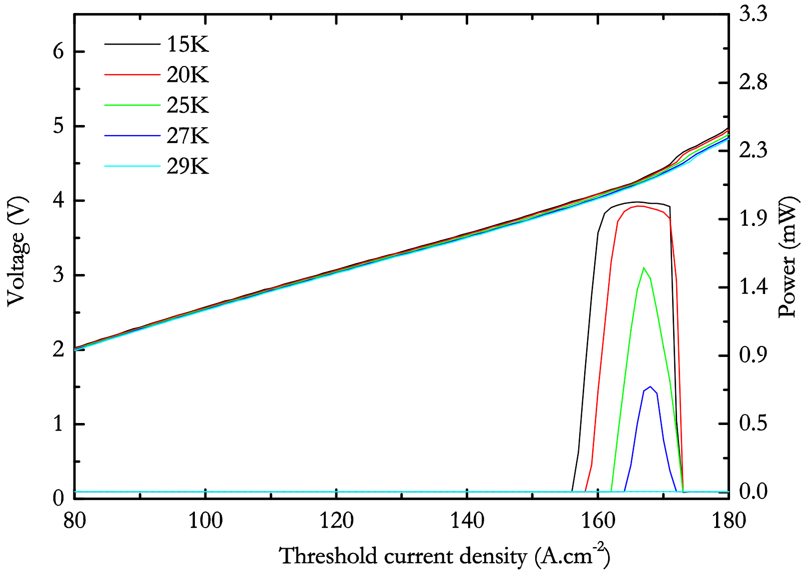

Figure 2.19: LIV from the L1071 2.5 mm long device at different heat sink temperatures in CW mode. A maximum power of ~2 mW measured at 10 K.

When the QCL was tested at 95% duty cycle, the device continued to lase. The device was tested in CW mode by replacing the pulse generator with a DC source. The applied bias to the QCL was slowly ramped up, recording the emitted signal for each bias step. The LIV plot is shown in the Figure 2.19. The flat top in the LIV plot is due to the bolometer saturation.

The power from the QCL was measured using TK power meter at 30 Hz by mechanically chopping the THz beam using an optical chopper. The measured spectra at different current levels is plotted in the Figure 2.20. The measured frequency was consistent with the pulsed measurements, having a peak emission at 1.997 THz. The QCL was predominantly single mode with a peak emission at 1.997 THz and Fabry-Perot mode appearing at 2.014 THz. The Fabry-Perot mode spacing was found to ~17 GHz which is consistent with the Fabry-Perot spacing equation,

$$\Delta\nu = \frac{c}{2nL} \tag{2.3}$$

where $\Delta\nu$ is the frequency difference between modes, c is the speed of light, n is the refractive index of the gain medium and L is the cavity length of the laser. For a 2.5 mm long laser cavity with refractive index of ~3.5 (GaAs), $\Delta\nu$ is found to be ~17 GHz.

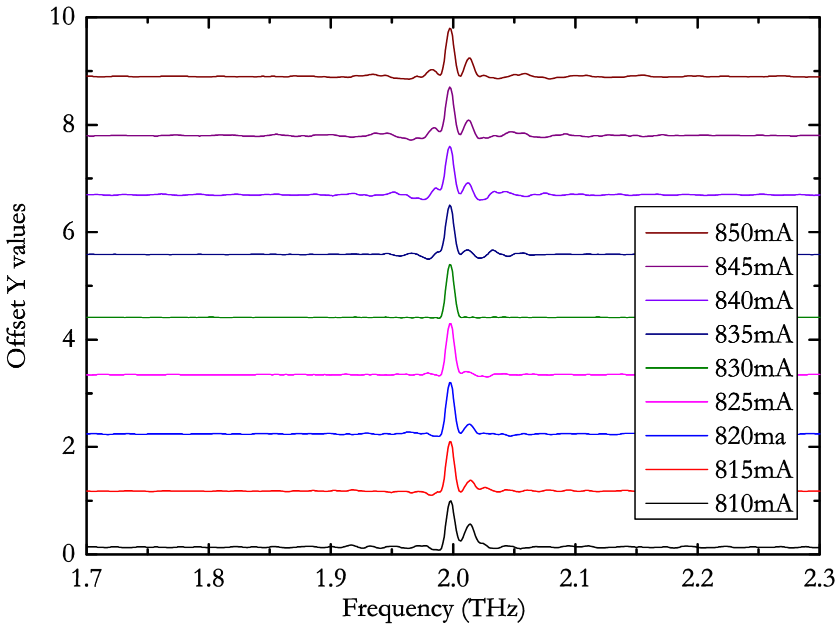

Figure 2.20: Spectra from the L1071 2.5 mm long device at different bias levels in CW mode. The laser was predominantly single mode with a peak at 1.997 THz and a second Fabry-Perot mode at 2.014 THz.

2.6 Conclusions

One of the most advanced THz sources, THz QCLs, their history and invention were discussed in the chapter. The fabrication procedures adopted for fabricating a SISP waveguide THz QCL was explained and the LIV and spectral features were discussed. The fabricated QCL had an emission frequency of 1.997 THz, which was almost consistent with the published result from this active region design [100]. The threshold current density of the device was low with ~135 Acm^{-2} at 10 K and it lased in both pulsed and CW mode. The main agenda behind the fabrication of this low THz QCL was to use it in injection-locking experiment which will be discussed in detail in Chapter 6.

Chapter 3 Photomixing theory

This chapter gives a theoretical background on photomixers, and how they can be used as coherent sources to injection lock QCLs. Photoconductive emission of electromagnetic radiation from semiconductors is discussed, followed by a brief comparison of pulsed and CW operation. An emphasis is then given to the theory of CW THz emission in photomixers and coherent detection of THz radiation using photomixing is explained. Characterization of the fibre coupled DBR lasers used for photomixing is then presented along with a commercial photomixer purchased from TOPTICA. The experimental setup that is used in the subsequent experimental chapters is next explained, including the importance of achieving zero optical delay. Finally, the bandwidth and THz power from TOPTICA emitter is measured.

3.1 Photoconductive emission

A range of sources adopted for the generation of THz radiation were presented in Chapter 1. Among the different techniques, photoconductive emission (PCE) is one of the most desirable due to its room temperature operation and good optical to electrical conversion efficiency. Unlike non-linear generation methods, PCE doesn't require relatively long interaction lengths and is not limited by the Manley-Rowe limit [101].

The first ever demonstration of photoconductive emission (PCE) was achieved when Auston developed the photoconductive switch in 1984 [53]. Ultrafast electromagnetic pulses were generated from silicon-on-sapphire (SoS) substrates, which had been irradiated with Ar^{+} ions. The 10 μm gap between the two contact electrodes was excited using 100 fs optical pulses from a ring dye laser, which gave 1.6 ps long electromagnetic pulses. Coherent detection, in which the generated electric field is probed using a second phase locked optical pulse with the appropriate time delay, was also demonstrated using an identical device. Since this time, several advances have been made in this field to improve the performance of the photoconductive emitters, naming a few, large aperture emitters [102, 103], antenna arrays [104], large area emitters (LAE) with microlens arrays [105, 106], plasmonic nanostructure emitters [107].

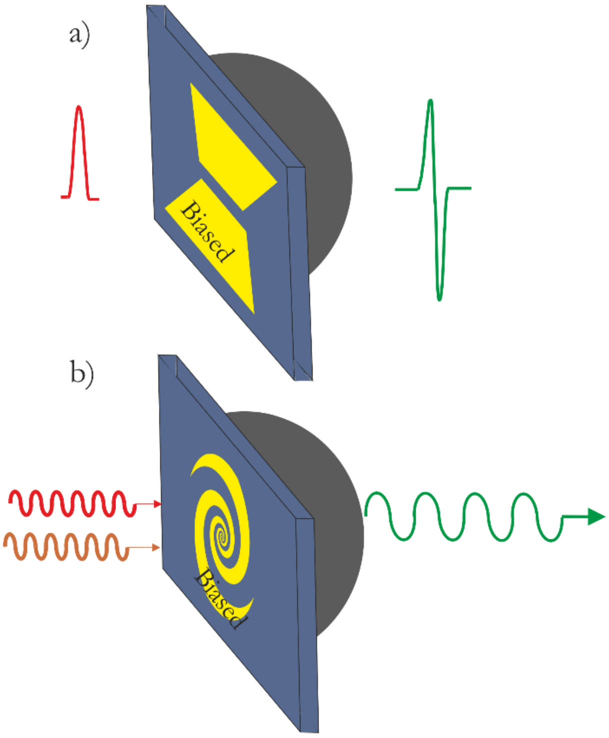

Figure 3.1: Schematic diagram of photoconductive emission from (a) a photoconductive switch and (b) a photomixer. One of the electrodes is biased (marked) and the other is grounded.

PCE from semiconductors can be classified into two modalities, pulsed, Figure 3.1 (a) and continuous wave (CW), Figure 3.1 (b). Pulsed operation is when a photoconductive switch is integrated with an antenna on the semiconductor surface and is excited by a single pulsed laser. CW operation is when a photoconductive semiconductor is excited using the beat frequency between two discrete CW lasers, resulting in the emission of CW THz radiation. The devices used in the CW modality are called photomixers. The two emission processes will be discussed in detail in the following subsections.

3.1.1 Pulsed THz emission

When laser pulses of photon energy, E_p, greater than or equal to the bandgap energy of a semiconductor, E_g, are incident on the semiconductor, the photons are absorbed and generate photocarriers. If the semiconductor surface has a biased antenna pattern, the generated electrons and holes will be accelerated towards opposite electrodes. If the laser pulse is ~10–150 fs long, and the carrier recombination rate is fast, THz transients (EM pulses <1 picosecond in duration) are emitted via the antenna. The rise time of the pulse is determined by the duration of laser pulse and fall time is determined by the recombination of photocarriers. The generated THz electric field in far-field, E_{THz} is proportional to the transient current density,

$$E_{THz} \propto \frac{dJ_{THz}}{dt} \tag{3.1}$$

where the current density, J_{THz}, is given by

$$J_{THz} = Ene(\mu_e + \mu_h) \tag{3.2}$$

Here E is the applied electric field, n is the carrier concentration, and μ_e and μ_h are the electron and hole mobilities respectively. Substituting Eq. (3.2) into Eq. (3.1), we get

$$E_{THz} \propto Ee\left[\mu_e \frac{dn}{dt} + n\frac{d\mu_e}{dt}\right] \tag{3.3}$$

where the hole terms have been ignored as $\mu_h \ll \mu_e$. The generated THz amplitude depends on mobility, carrier concentration and applied bias. In order to have a high THz electric field, it is ideal to have high dark resistance semiconductors, which can withstand high biases with a short carrier lifetime and high mobility [108]. Short lifetimes ensure fast recombination of the electrons and holes, reducing the fall time of the pulse.

Photoconductive switches are most commonly found in THz-time domain (THz-TD) systems. Usually, the system has a femtosecond laser beam, and a beam-splitter that divides the laser beam into two. The pump beam excites the biased emitter, and the generated THz transient is focussed into the detector and sampled using the probe beam, as shown in Figure 3.2. The detection technique used depends on the application. Incoherent detection of THz radiation is performed by collecting the signal on a receiver of e.g. a bolometer [109]. Coherent detection is mainly carried out in three different ways, photoconductive [110], non-linear optical detection and electro-optic detection [111]. A detailed comparison between the three detection process is discussed in detail in ref [112], and asserts that better SNR and bandwidths are obtained with electro-optic detection.

For electro-optic detection, the THz pulse and probe beam are made to coincide spatially and temporally inside the electro-optic crystal using a variable time delay. The electric field of the incident THz pulse causes a phase modulation of the probe pulse in a non-linear crystal (for e.g. ZnTe) which is converted into an intensity modulation. This is achieved using a quarter wave plate, a Wollaston prism and a pair of photodiodes [113]. The gated nature of the detection scheme ensures significant performance improvement compared to the incoherent bolometric detection as the THz pulse is measured only when the probe pulse is present. This reduces the system noise.

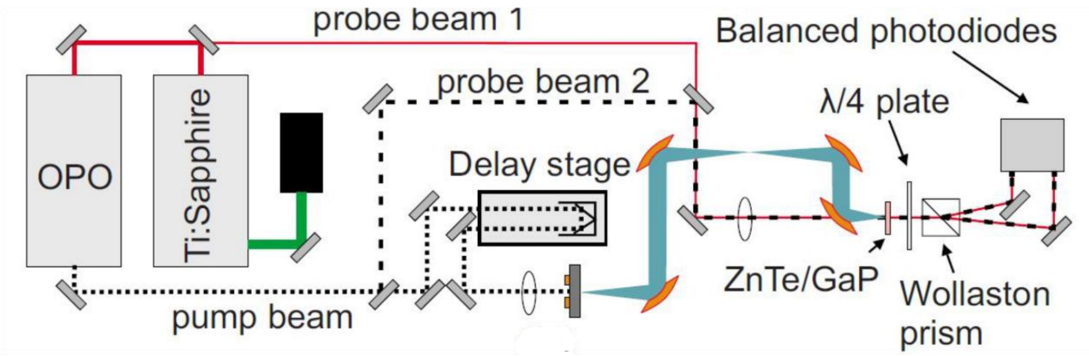

Figure 3.2: Schematic of a THz TD system with electro-optic detection system. An OPO is used in this set-up for switching the emission wavelength. Image reproduced from ref [109].

The term 'time domain' systems is used as the measurements are carried out in a time domain. The probe beam scans the THz electric field by delaying the beams with respect to each other. The generated THz has a pulse width of ~400–500 fs. A Fourier transform of the pulse retrieves the frequency response,

$$\Delta\nu \propto \frac{1}{\Delta T} \tag{3.4}$$

Since frequency, ν, and time, T, are inversely proportional, the frequency resolution of the data is inversely proportional to the time window of the recorded data. The pulse width is predominantly determined by the pulse width of the laser and the carrier lifetime. Although pulsed systems emit high THz power, the system cost and size restrict their applications.

3.1.2 CW THz emission - Photomixing

Although the demonstration of pulsed THz generation from semiconductors dates back to the early 1980's, the generation of CW THz radiation, also called optical heterodyne mixing or photomixing, was realised only a decade later due to the lack of materials with ultrafast lifetimes. With improvements in the intrinsic properties of semiconductors such as low-temperature gallium arsenide (LT-GaAs) [114, 115], grown at low temperature using MBE, the idea of photomixing for THz generation became practical. Photomixing for the generation of THz radiation was first demonstrated by Brown *et al.* in 1993 [54]. The photomixer was fabricated on an LT-GaAs substrate and had a reported bandwidth of 193 GHz. The device had ten 1.0 μm electrodes and nine 1.0 μm gaps fabricated in the gap of a 50 Ω coplanar waveguide connected to a 50 Ω transmission line and was illuminated at an excitation wavelength of 620 nm. A complete theoretical and experimental analysis of the photomixer was given for the generation mechanism and also the dependence on bias and optical powers. This initial device demonstrated approximately 200 μW power, but the same group went on to demonstrate upto 0.8 mW output power at 200 MHz using a slightly different photomixer design, where the photomixer had forty 0.2 μm electrodes with 0.3 μm gaps at the active region of an electrical coplanar waveguide structure [116]. The photomixer was excited using a single frequency Ti:Sapphire laser and the etalon was adjusted to produce two identical modes with equal optical powers separated by a frequency of 200 MHz. A quadratic dependence of THz power with bias was observed until 8 V, after which a super-quadratic behaviour was seen due to the space-charge effects. In the same work, they demonstrated that another design having twenty 0.4 μm electrodes separated by 0.6 μm gaps. When tested at 77 K, the performance was better than room temperature for biases above 10 V. The optical to electrical conversion efficiency was 1.5% at 77 K [116]. Using two Ti:Sapphire lasers and tuning one of the lasers to produce a beat frequency, the same group obtained constant output power up to 20 GHz before a 6 dB/octave roll-off in output power was observed, attributed to capacitive effects [117].

These initial demonstrations were, however, not strictly in the THz regime, producing wavelengths in the millimetre region of the electromagnetic spectrum. Furthermore, the lack of a proper antenna structure to couple out the THz radiation and the absence of a silicon lens to collimate the beam resulted in low output powers. In 1995, Jepsen *et al.* [118] studied the influence of silicon lenses on the THz radiation pattern from photoconductive switches and measured the beam shape of the emitted radiation. The beam shape was found to be Gaussian. Out of the total generated output beam only 21% was coupled out. Brown *et al.* [119] subsequently demonstrated photomixing up to 3.8 THz from an LT-GaAs photomixer in 1995. The photomixer had a three-turn self-complementary log-spiral antenna, as shown in Figure 3.1 (b) with a 20 μm square active region and a hyper-hemispherical silicon lens attached to the backside. The electrodes were 0.2 μm wide and gaps were 1.8 μm. When excited using two different Ti:Sapphire lasers of 50 mW optical power, an applied bias of 25 V, a constant output power (~100 μW) up to 300 GHz was observed using bolometric detection, followed by 12 dB/octave roll-off beyond 500 GHz.

Even though a bandwidth of ~3.8 THz was obtained, it involved the use of expensive, and bulky Ti:Sapphire lasers. Subsequently, using distributed Bragg reflector (DBR) lasers, using an active area design of 8 μm square on a log-spiral antenna with only 2 pairs of IDTs, ~5 THz bandwidth was reported in 1995 [119]. Matsuura *et al.* [120] later used single-frequency free-running diode lasers to excite dipole antennas fabricated on LT-GaAs. The lasers were tuned by changing the temperature. With bolometric detection, the bandwidth was greater than 3.5 THz. The use of resonant dipole antennas resulted in very high powers at the resonant frequency, which was set at 1 THz. Subsequently, they demonstrated photomixing using the two longitudinal modes of a laser diode at 0.9 THz. The longitudinal modes were defined by patterning the DBR on the laser diode and could be expanded to 4 THz [121].

Verghese *et al.* [122] addressed various issues associated with using photomixers as local oscillators including bias, optical power and temperature. The performance of the fibre coupled photomixers were studied at different bias levels and optical powers. Coherent emission and detection of microwave and THz waves was demonstrated using a coaxial transmission line to couple the radiation between 0.05 to 26.5 GHz between the emitter and detector. For higher frequencies a log-spiral antenna design with IDTs mounted on hyper-hemispherical silicon lens were used to measure frequencies up to 2 THz. The detector response was flat up to 600 GHz, followed by a signal-to-noise-ratio (SNR) of ~3 dB, roll-off at 2 THz [123].

3.2 Photoconductive emitters for imaging applications

Once photomixing was established as an efficient method of generating THz signals, practical applications of the technology were developed. Early work in THz imaging was pioneered with THz-TD systems. Imaging with THz radiation was reported by Hu *et al.* in 1995 [10]. They demonstrated imaging of samples using a THz-TD setup with the emitter and detector fabricated on SI-GaAs and radiation damaged SoS, respectively. The THz absorption was imaged. In this case, the THz beam was scanned over the sample and the transmitted amplitude was acquired. This demonstration of imaging using a THz-TD setup was a major breakthrough in the THz imaging field. Soon after the work by Hu *et al.*, THz-TD system was used to measure the absorption of various combustible products including –CH and NH_3 in a premixed propane-air flame in the 0.2 to 2.65 THz regime [124]. The amplitude spectrum confirmed the presence of various gases and the concentration was determined from the relative amplitudes. A real-time THz imaging system was then developed by Usami *et al.* [125]. With a resolution of 1.4 mm, images of static and moving objects were captured at frame rates of 30 and 10 frames per second, respectively. Numerous further applications, were also shown, including illicit drug detection [15] and biomedical imaging [21].

Most initial THz applications were demonstrated using a THz-TD system due to the high signal-to-noise-ratio (SNR), of the order of 10,000:1 [124], arising from the coherent detection techniques, although photomixing systems have better frequency resolution than THz-TD systems, the relatively poor SNR (100:1 from ref [126]) hampers their applicability. Continuous wave THz imaging using photomixers was, however demonstrated by Ostmann *et al.* [11]. An all optoelectronic CW THz imaging system was then developed by Siebert *et al.* [127]. A two colour Ti:Sapphire laser was used to excite an LT-GaAs photomixer and the generated THz was focused onto the sample using a hyperboloidal lens. Coherent detection was employed. Biological imaging was carried out at 1.1 THz and when compared with the pulsed system, CW imaging was found to be faster; a SNR of 100:1 was reported. Subsequently, they demonstrated *ex vivo* biomedical imaging [126]. CW imaging of a canine skin tumour (basal cell tumour) was also carried out at 1.1 THz in which the THz power transmitted through the sample was the parameter used for imaging.

Gregory *et al.* [128] demonstrated the first coherent CW imaging system using diode lasers. Two external cavity tunable diode lasers at an emission wavelength of 830 nm were used to excite the dipole antenna on an LT-GaAs substrate. The imaging of a razor blade enclosed in a cotton cloth was carried out at 0.4 THz and a SNR of 100:1 was reported. The frequency resolution provided from the CW system is one of the most attractive features, since many gas samples have absorption features of <1 MHz. Hindel *et al.* [129] demonstrated the use of photomixing for pollutant detection and quantification. Spectral features of the order of 1 MHz were resolved from H_2S and they were able to detect the particulate matter in cigarette smoke.

3.3 Comparison between pulsed and CW emission

Even though the use of both pulsed and CW THz radiation have been used for various applications, CW THz radiation still lags pulsed systems due to the poor SNR. The CW performance can be improved by using good quality semiconductors i.e., with short carrier lifetimes and high resistivity semiconductors, and this will be discussed in detail in Chapter 4 and by adopting improved photomixer designs by incorporating nano-electrodes, which will be discussed in Chapter 5.

Pulsed systems are inherently broadband since the emitted THz pulse incorporates information over a wide frequency range. The laser pulse width determines the bandwidth of the system, and the "extent of measurement" determines the resolution which is limited to a few GHz, for e.g., a 100 ps scan; the maximum resolution that can be attained is ~10 GHz, from Eq.(3.4). However, in CW systems, the linewidth of the exciting lasers determines the resolution. Diode lasers with a few MHz linewidths have long coherence lengths (several metres) resulting in narrow THz linewidths. Also the high spectral power density from the CW system implies high SNR at a particular wavelength. Another advantage with CW systems, is that components can be designed to be resonant at a particular frequency.

In the case of THz-TD systems, the THz pulse and probe pulse have to arrive simultaneously for sampling in order to retrieve the phase and amplitude information. In CW systems, this condition is relaxed. A difference of a few integer wavelengths will not alter the amplitude and phase information, but can affect the spectral bandwidth. However, CW systems suffer from low power levels, which is attributed due to an impedance mismatch between the active region and antenna.

Apart from log-spiral and dipole antennas, different antenna designs have been studied including slot antennas and dual dipole antennas to improve THz power. Since the emphasis of this work is to find a high power coherent CW source for locking a THz QCL, one of the most successful designs, an IDT active region is initially studied in Chapter 4, and a new design approach is investigated in Chapter 5.

3.4 Theory of photomixing

Photomixing is defined as the modulation in the conductance of a semiconductor due to the beating of two laser beams. The modulation in conductance arises due to modulation in the carrier generation, which is determined by the difference in laser frequencies. This difference frequency can be set to lie in the THz range. A biased planar antenna structure formed on a semiconductor surface can turn a modulated conductance into an emitted electromagnetic wave. Several factors can hinder the performance of a photomixer, including Joule heating due to the impedance mismatch between the antenna and active regions electrodes.

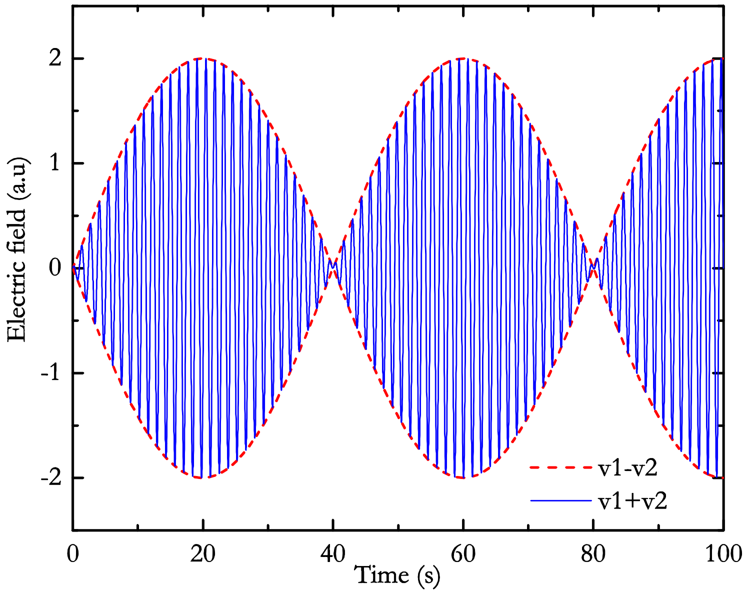

Figure 3.3: Schematic representation of the electric field profile from the superposition of two detuned continuous wave beam as a function of time. The sum frequency (blue curves) and difference frequency (red dotted lines) are marked.

In order to understand the physical phenomena behind photomixing, a theoretical background of the process is now given. Assuming two CW laser beams having perfectly sinusoidal beams with equal amplitude, E_0, and frequencies υ_1 and υ_2, on superposition these will yield,

$$E(t) = 2E_0 sin\left[\frac{2\pi(\upsilon_1 + \upsilon_2)t}{2}\right] cos\left[\frac{2\pi(\upsilon_1 - \upsilon_2)t}{2}\right] \tag{3.5}$$

Figure 3.3 shows the electric field profile from the superposition of two detuned continuous wave laser beams. The sum frequency (blue lines) is too fast for the semiconductor to respond and is ignored, it is the difference frequency (red dotted lines) that can interact with the semiconductor. The difference frequency, $\upsilon_{THz} = \upsilon_1 - \upsilon_2$, is set to lie in the THz frequency range. The difference frequency is focussed on the semiconductor surface to generate photocarriers. The instantaneous laser power incident on the material is the square of the electric field amplitude,

$$P(t) = 4E_0^2 cos^2\left[\frac{2\pi(\upsilon_1 - \upsilon_2)t}{2}\right] \tag{3.6}$$

If the two incident laser beams are of two different optical powers, then the laser power incident can be written as, which is in accordance with ref [54],

$$P(t) = P_1 + P_2 + 2\sqrt{mP_1P_2} cos[2\pi(\upsilon_1 - \upsilon_2)t] \tag{3.7}$$

where P_1 and P_2 are the power from the two laser beams and m is the parameter determining the overlap of the beam, having a maximum value of 1. The incident laser beam is absorbed by the semiconductor substrate and will generate photocarriers. The rate of change in photocarrier concentration, $n(t)$ due to an incident beam of power, $P(t)$, on an illuminated area of the photomixer, A, and depth of the active region, L_a in which the carriers are generated is given by;

$$\frac{dn}{dt} = \frac{\eta_e P(t)}{h\upsilon A L_a} - \frac{n}{\tau} \tag{3.8}$$

where η_e is the external quantum efficiency, $h\upsilon$ is the incident photon energy, τ is the decay lifetime of the photocarriers. The external quantum efficiency is defined here as the number of photocarriers generated per incident photon. The second term represents the decay of the generated carriers in time, τ. By substituting the incident power from Eq. (3.7) into Eq. (3.8) and integrating the equation, the instantaneous carrier density can be calculated. The time varying carrier density introduced into the semiconductor due to the THz periodic difference frequency [130] is,

$$n(t) = \frac{\eta_e(P_1 + P_2)\tau}{hvAL_a}\left[1 + \frac{2\sqrt{mP_1P_2}\omega\tau[sin(\omega t) + cos(\omega t)]}{P_1 + P_2\ (1 + (\omega\tau)^2)}\right] \tag{3.9}$$

where $\omega = 2\pi(v_1 - v_2)$. The photomixer illuminated area, or active region has interdigitated fingers (IDTs), thus $A = (N_f w_f + N_g w_g)L_f$, where N_f, w_f and N_g, w_g corresponds to the number and width of fingers and gaps respectively. L_f corresponds to the length of the fingers. The conductance of the semiconductor in the presence of the incident laser power can be thus written as [54],

$$G(t) = \frac{n(t)e\mu_e N_g L_f L_a}{w_g} \tag{3.10}$$

This conductance has a dependence on mobility, μ_e, and here the hole mobility is ignored as the hole mobility is very low compared to the electron mobility, and its contribution to the fast processes is negligible. The carrier density term from Eq. (3.9) is substituted in Eq. (3.10) to obtain the time dependent conductance, $G(t)$.

$$G(t) = \frac{e\mu_e N_g L_f}{w_g}\frac{\eta_e(P_1 + P_2)\tau}{hvA}\left[1 + \frac{2\sqrt{mP_1P_2}\omega\tau[sin(\omega t) + cos(\omega t)]}{P_1 + P_2\ (1 + (\omega\tau)^2)}\right] \tag{3.11}$$

This results in the ac component which is responsible for THz emission (inside the square brackets). The power radiated from the antenna was explained using an equivalent circuit model by Gregory *et al.* [130]. The impedance from the antenna and the active region incorporating IDTs are not purely resistive. The active region with the IDTs impose a capacitive impedance at THz frequencies. The power radiated from the antenna can be expressed as the power dissipated in the load, R_A, the radiation impedance (only the resistance component is considered here) of the antenna. The radiated power can be expressed as,

$$P_{THz} = i^2 R_A = \left(\frac{V_B}{Z(\omega, t)}\right)^2 R_A \tag{3.12}$$

In which, V_B is the applied bias and $Z(\omega, t)$ is the impedance of the circuit. The impedance of the circuit $Z(\omega, t) = R_A + Z_{PM}$. The impedance of the photomixer is given by $(G(t) + j\omega C)^{-1}$. Substituting the values of the conductance in the Eq. (3.12) and after simplification, the power radiated from the photomixer can be expressed as [54, 130],

$$P_{THz} = \left(\frac{\eta_e \mu e \tau}{rhv}\right)^2 \frac{2R_A V_B^2 m P_1 P_2}{A(1+(\omega\tau)^2)(1+(\omega R_A C)^2)} \tag{3.13}$$

So,

$$P_{THz} \propto \frac{1}{2}\frac{R_A V_B^2}{(1+(\omega\tau)^2)(1+(\omega R_A C)^2)} \tag{3.14}$$

The dependence of THz power from a photomixer can be understood from the above equation, where r is the spotsize of the laser beam. The THz power scales quadratically with the applies bias, thus requiring a semiconductor with a high resistivity so that high biases can be applied. The contribution from the denominator, carrier lifetime and capacitance terms is negligible at lower frequencies (<500 GHz).

For a typical self-complementary log-spiral antenna the radiation resistance is expected to be ~72 Ω on a substrate with a refractive index of ~3.6 (for GaAs [119]). The capacitance of the IDTs or MSM structure can be calculated using the following equation, from references [131, 132]:

$$\mathrm{C} \approx \frac{\varepsilon_0(1+\varepsilon_r)A\pi}{2(w_e+w_g)\log[2(1+\sqrt{\kappa})/(1-\sqrt{\kappa})} \tag{3.15}$$

where κ is given by,

$$\kappa = \left(1 - tan^4\left[\frac{\pi w_e}{4(w_e+w_g)}\right]\right)^{1/2} \tag{3.16}$$

This equation is valid for electrode gaps of the order of 1–2 μm and sub-micron wide electrodes, the capacitance of which are of the order of femtoFarads. The THz power does not have a frequency dependence at lower frequencies. At higher frequencies, when $\omega\tau$ >>1 the power rolls off at a rate of -6 dB/octave and when $\omega R_A C$>>1, there is a contribution of another -6 dB/octave. The THz power will thus roll-off at a rate of -12 dB/octave above the $\omega R_A C$>>1 limit and thus $P_{THz} \propto \omega^{-4}$ at higher frequencies. The emitted THz power also depends on the intrinsic properties of the semiconductor such as the carrier mobility, lifetime and resistivity, as discussed in the following subsections.

3.4.1 Carrier mobility

The mobility of the carriers needs to be high for efficient THz generation. In a CW system, the generated carriers need to be accelerated to the contact electrodes in order to contribute to the THz emission. If the mobility is too low due to scattering from the dopants or other impurities, the carriers cannot accelerate and thus do not contribute to THz emission.

3.4.2 Carrier lifetime

The lifetime of the semiconductor has to be short (hundreds of femtoseconds) to allow fast recombination of the carriers. If the recombination lifetime is long (few picoseconds), the generated carriers get accumulated at the contact electrodes which can screen the applied bias resulting in a cubic or even quartic bias dependency. This can result in the need to apply very high biases. If the recombination time is too short (less than 100 fs), the generated carriers get recombined before reaching the contact electrodes, thus not contributing to THz generation. The recombination lifetime of the carriers is an intrinsic property of the semiconductor, and can be reduced by introducing defects in the semiconductor for e.g. doping, low-temperature growth, annealing. The dependence of THz output power of a photomixer on carrier lifetime has been studied before [130]. The carrier lifetime of the semiconductor increased with bias due to the spatial separation of electrons and holes.

3.4.3 Wafer resistivity

The resistivity of the wafer affects the maximum limit of bias that can be applied before thermal damage occurs. An ideal semiconductor for photomixing will have high dark resistance and low photo resistance. LT-GaAs wafers are found to have very high electrical breakdown limit, 5×10^{2} kVcm^{-1}.

In summary, various factors affecting the THz power from a photomixer have been discussed and it is clear that a semiconductor with a short carrier lifetime, high mobility and resistivity will optimise the performance. However, the greatest challenge in operating in the THz frequency range is finding and engineering suitable semiconductor materials, as the vast majority of perfect semiconductors have unsuitable carrier lifetimes. The different materials adopted for the photomixing work in the THz range are discussed in Chapter 4.

3.5 Coherent detection

The output power from a photomixer is lower than other THz sources such as QCLs (the maximum reported power level is 1 W at 3.4 THz [36]), or UTC-PD (10.4 μW at 1.04 THz [133]. Incoherent detectors such as bolometers are often used to measure the output power, however, the disadvantage is that the phase information will be lost, which is an important parameter in many applications.

Photomixers can be used as coherent detectors and this has been demonstrated [123]. The combined laser beam is split and is focussed onto a photomixer emitter and receiver, just as in a THz-TD setup. In the detector, the generated photocarriers due to the laser beam absorption are driven by incident THz radiation inducing a current. The electric field of the incident THz field will thus generate a potential difference which is then measured as current induced due to the photomixer impedance. The phase between the incident THz radiation and the beat frequency in the detector is changed using a variable delay line, hence changing the optical path length. The detected amplitude of the current is proportional to the incident THz electric field. As there is no applied bias, there should not be any dc current flowing in the photomixer. This removes detrimental effects of Joule heating.

The detected current from a photomixer receiver can be written as [132],

$$|i(\omega)| = \left(\frac{R_A c \varepsilon A_{THz}}{2}\right)^{\frac{1}{2}} E_0 \left(\frac{\eta_e \mu e \tau}{w^2 h\upsilon}\right) \left[\frac{m P_1 P_2}{(1+(\omega\tau)^2)(1+(\omega R_A C)^2)}\right]^{\frac{1}{2}} \tag{3.17}$$

From Eq. (3.17), the roll-off for the detector has almost the same dependence as the emitter. However, there can be thermal noise in the system due to thermal agitation of the charge carriers, which can generate Johnson noise. As can be seen from Eq. (3.17), it is good to have a short carrier lifetime, high mobility, and the dark resistivity of the wafer needs to be very high. The crucial factor for THz devices is the carrier lifetime, which needs to be short enough (~ hundreds of femtoseconds) for the semiconductor to respond at higher frequencies. The advantage of a photomixer receiver is that precise phase information can be achieved. The amplitude of the THz current needs to be high for a better SNR. The generated THz current is amplified using a trans-impedance amplifier (V/A). But electrical noise in the system will be amplified as a result.

LT-GaAs has been a favourable choice for semiconductor photomixing, with a bandgap at ~800 nm and Ti:Sapphire lasers having an emission wavelength that matches this LT-GaAs bandgap. However, the need for chillers and associated components makes Ti:Sapphires quite expensive (in excess of £100,000). Diode lasers on the other hand are quite cheap (£1000–£10,000) and easier to operate. In the work of this thesis, photomixers were characterized using two diode lasers with an emission wavelength of ~1550 nm, see Section 3.6.

3.6 Characterization of 1550 nm diode lasers

A pair of commercially available, tunable fibre-coupled digital super mode distributed Bragg reflector lasers (Oclaro Lambda FLEX iTLA TL5000) with an emission wavelength around ~1534 nm (telecommunications 'C-band') were used. The fibres in this wavelength range have minimum dispersion and attenuation compared to other wavelengths [134], and also have the advantage of very well-developed optic components, such as amplifiers (erbium doped fibre amplifier [EDFA]) and couplers.

The distributed Bragg reflector (DBR) lasers have several added advantages over other lasers emitting at this wavelength, e.g. distributed feedback lasers and external cavity lasers. A DBR laser is a semiconductor laser with the active region split into a gain region and a grating region. There have been variations in the design methodologies of these lasers; e.g. having a single grating on one side or gratings on both ends of the active region. They are renowned for their single wavelength and narrow linewidth emission. The Bragg grating satisfies the Bragg reflection condition, $m\lambda = 2nd\ sin\theta$, where n is the refractive index of the gain medium, m is an integer, λ is the wavelength and θ is the angle of incidence. The grating acts as a reflector, reflecting the light back into the gain region with maximum reflection at the Bragg wavelength [135]. The lasers can be tuned by changing the applied bias or temperature. However, the tuning range is narrow, usually <10 nm [136].

In our work, we kept one laser (DBR1) at a fixed wavelength of 1534 nm, and the other laser (DBR2) was tunable, ranging between 1534 nm and 1560 nm providing a frequency difference of 0–2600 GHz. The lasers were packaged and programmed by Dr. Lalitha Ponnampalam from University College London, UK. The lasers had multiple sections of grating which were switched to give coarse frequency steps (>25 GHz). Fine tuning of the beat frequency (up to 20 GHz) was then possible by changing the applied current to lasers between 5.4 mA to 9.1 mA. Changing the current slightly changes the carrier concentration effectively changing the refractive index, resulting in a wavelength change.

Both lasers provided an output power of 15 mW, and the combined power was 30 mW. The output from DBR1 and DBR2 was combined and split using a 2×2 splitter. The two outputs, output1 and output2, had optical power of ~14.5 mW each. The insertion loss and coupling loss from the fibres caused the difference in the input and output powers, although the ends of the fibre had polished connectors (PoC). The optical power from the fibres were measured using a Thorlabs fibre power meter, by connecting output2. Output1 was connected to a 90:10 splitter. The 10% power arm was connected to a fibre coupled optical spectrum analyser (OSA), as shown in Figure 3.4.

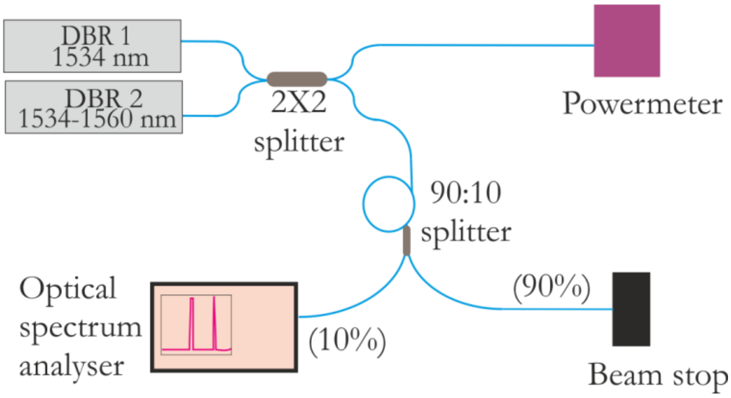

Figure 3.4: Experimental configuration showing the two DBR lasers combined and split using a 2×2 splitter. One arm is connected to the power meter for power measurement. The output from the 10% arm on the output1 is connected to the OSA.

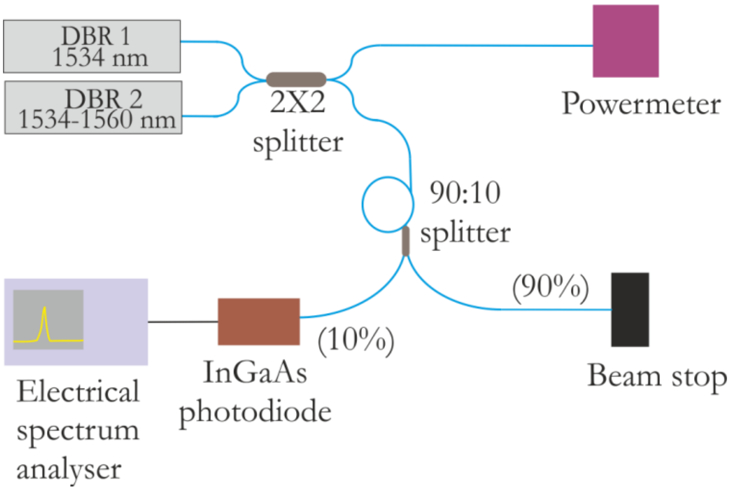

Figure 3.5: Experimental configuration used for laser jitter measurement. The 10% power arm of the splitter connected to an InGaAs photodiode, was fed to an electrical spectrum analyser.

The jitter of the lasers were measured by beating the two lasers on an InGaAs photodiode (Thorlabs 1550). The photodiode was fibre coupled and the output from the photodiode was connected to an Agilent electrical spectrum analyser (ESA). The 10% power arm of the 90:10 splitter was measured (with attenuators) since high optical powers saturated the photodiode. The frequency difference between the two lasers was set to be 0 GHz during measurement. The experimental setup in Figure 3.4 was modified for the measurement. The OSA was replaced by the photodiode, which was connected to the ESA, as shown in Figure 3.5.

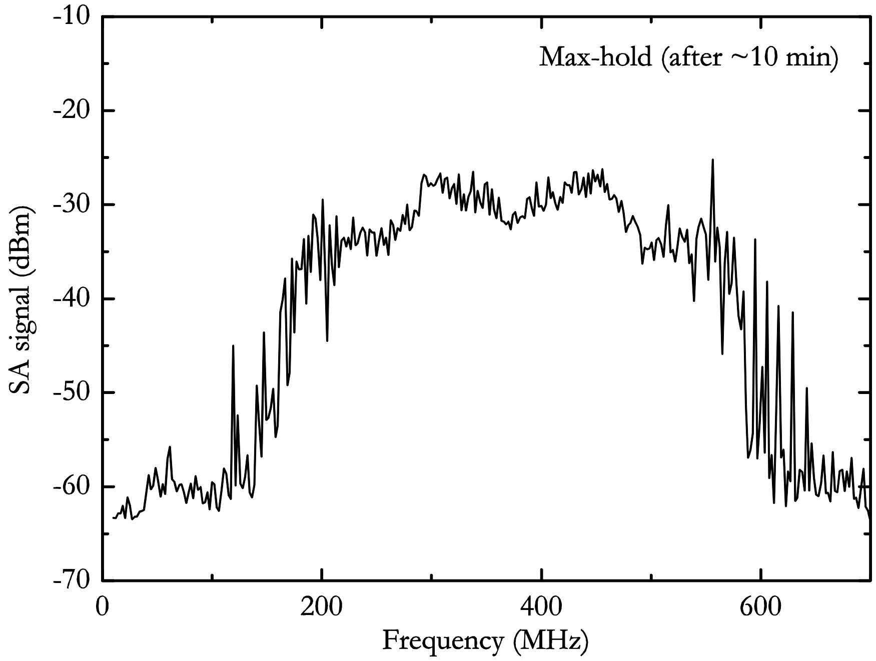

Figure 3.6: The spectrum analyser frequency measured as a function of the detected laser signal. Laser jitter measured from the two DBR lasers set at a beat frequency of 0 GHz.

Figure 3.6 shows laser jitter data over a 10 min measurement. Although the frequency difference was set to be 0 GHz, the ESA frequency showed a beat note between 200 MHz and 600 MHz. The laser jitter was measured to be slightly over 400 MHz over a 1 hour measurement, and can be quite disadvantageous for spectroscopy and imaging applications. However it won't impact photomixers bandwidth and power measurements, which is the scope of this and the following two chapters here.

Another important parameter is the optical power variation with laser frequency. There can be losses in the cavity since changing the laser frequency involves switching the gratings in the laser. Additionally, the dispersion and absorption losses in the fibre can contribute as they may vary slightly with wavelength. For the measurement, the combined laser power was measured between 100 GHz and 2000 GHz. Figure 3.7 shows the measured laser power as a function of beat frequency. It is apparent from the figure that the laser power didn't fluctuate with frequency and was constant, with <10% difference, between 100 GHz and 2000 GHz.

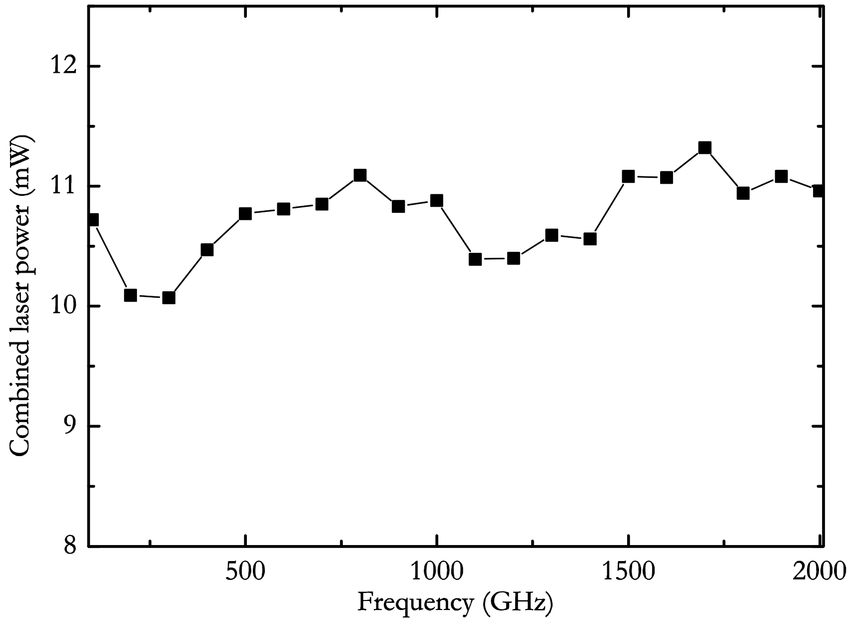

Figure 3.7: Laser power as a function of beat frequency between 100 GHz and 2000 GHz. The fluctuation in power is less than 10% in the measured range.

The coherence time of the lasers will be discussed in Section 3.7.1. With these measurements, including the laser jitter and laser power, an initial characterization of lasers was completed. These lasers were then used for the setup and characterisation of the photomixer system.

3.7 Characterization of a TOPTICA emitter and detector

A commercial fibre-coupled photomixer emitter and receiver was bought from TOPTICA Photonics, Germany to characterise the CW system. Although an in-house emitter can be used, the relatively low output powers from the emitter makes alignment difficult using an incoherent detector (bolometer). A photograph of the TOPTICA emitter is shown in the Figure 3.8. The TOPTICA emitter and receiver looked alike, and both emitter and receiver had a "coated" silicon lens attached to it, which blocked 1550 nm laser wavelengths. The fibres required for the system were bought from Thorlabs. They were polarization maintaining (PM), single-mode, low-loss panda fibres designed for 1550 nm.

Figure 3.8: Photographic image of the fibre coupled commercial photomixer-emitter, TOPTICA.

The initial experimental setup was a two parabolic mirror system. The emitter optical path involved a fibre length of 4.7 m, (1.7 m long (90:10 splitter) + one 2 m long fibre + 1 m long fibre attached to the TOPTICA emitter). For the detector optical path, the fibre length was 5 m (2 m long fibre + 2 m long fibre + 1 m long fibre attached to the TOPTICA detector). The reason for having a 2 m long fibre on both arms was to convert the connections. The fibres coupled out from the lasers were polished connection (PoC) fibres, whereas the TOPTICA emitter and receiver had angled polished connections (APC). Even though short converters (<0.5 m) are available, these were not used in the initial development of the THz photomixing system.

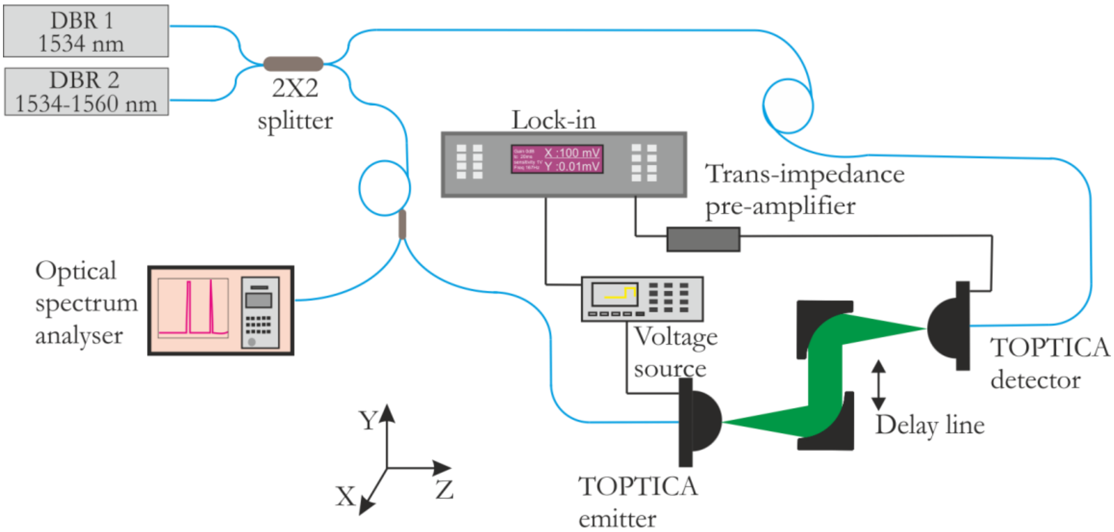

Figure 3.9: Experimental setup used for the characterization of the TOPTICA emitter and detector.

The system used for characterization of the emitter and detector is as shown in Figure 3.9. A 2×2 splitter was connected directly to the laser. For the emitter, the output1 of the splitter was connected to the 2 m long fibre cable using a PM mating sleeve (Thorlabs). The 2 m fibre had PoC on one end and APC on the other end. The PoC end had an anti-reflection coating on the facet to reduce the reflections back into the fibre. The APC end was connected to the APC end of TOPTICA emitter fibre using another PM mating sleeve. The loss from the fibres and connectors was negligible, with the laser power measured directly before the TOPTICA emitter to be around ~10–11 mW. In the detector arm, the output2 from the splitter was connected to two separate 2 m long fibres using mating sleeves. The second 2 m long fibre had APC at one end which was connected to the APC end of the TOPTICA receiver using mating sleeves.

The fibre facets were cleaned using fibre cleaning tissue, and were checked under a fibrescope. This step was repeated each time before making connections to ensure that the facets were free from any sort of dust or debris. An *f/2* parabolic mirror collected the THz radiation from the emitter and collimated the beam, which was focussed onto the detector using a second *f/2* mirror. The second parabolic mirror and the detector were placed on a mechanical delay line controlled by a motion controller (Newport Instruments). The delay line was ~0.15 m long, and thus can change the path length of the collimated THz radiation by moving the second parabolic mirror and the receiver together forward or backward. The delay was measured in ps, with a 10 ps = 3 mm conversion and, hence, the total scan length was ~500 ps.

The emitter was biased using an Agilent arbitrary waveform generator (AWG). The bias levels for the emitter were set to -2 V to 0.5 V square pulses at a frequency of 7.6 kHz, and a maximum laser power of ~12 mW was applied to the emitter and receiver, as recommended by the datasheet provided from TOPTICA. Although an EDFA could be used to amplify the laser power, it was not employed for emitter characterization as it tends to amplify the noise in the laser. A grounding strap was worn each time while making an electrical connection and disconnection to the emitter and detector to ensure there was no static discharge. Also, the laser was always on when making any electrical connections to avoid electrical discharge.

The generated THz radiation from the emitter was focused onto the receiver for coherent detection. Since the emitted THz waveform is a sine wave, accurate amplitude information is recovered when the delay is scanned. A number of factors can affect the measured THz amplitude, e.g. the step size of the delay; if sufficiently small steps are not used there is a high probability the peak amplitude can be missed. The second factor is the length of the scan; it is desirable to have as many sine waves in the scan length to minimize the amplitude errors and to retrieve the THz frequency. It was deemed appropriate to have at least 100 points per delay scan in order to optimise the scan quality, whilst keeping the total time for each measurement to a sensible limit. Also a time constant of 200 ms was used in the lock-in amplifier to reduce the electrical or mechanical noise. The noise level is not as significant at lower frequencies where the SNR is high, but at high frequencies the SNR is low and frequencies above 2.4 THz dropped below the noise floor. Earlier studies show significant reduction in noise levels above 10 ms [132].

The generated THz current was amplified using a FEMTO trans-impedance amplifier. The trans-impedance amplifier was left at a gain of 10^7 (V/A). At this gain, the bandwidth was 50 MHz. Increasing the gain further (10^8) resulted in less bandwidth (10 kHz). The trans-impedance amplifier output was connected to the lock-in amplifier referenced at 7.6 kHz frequency. The gain was left at 10^7 (V/A) for all the measurements with the TOPTICA receiver in this work (including Chapter 4, 5 and 6).

3.7.1 Zero path delay

For the system to be coherent, the part of the sine wave responsible for the generation of the THz radiation from the emitter has to be sampled by the same part of the sine wave in the detector. The free space propagation distance from the emitter to the detector is approximately 0.45 m. This time difference is compensated for using a fibre with an optical refractive index of $n = 1.5$ and, hence, a length of 0.3 m was added to achieve coherence.

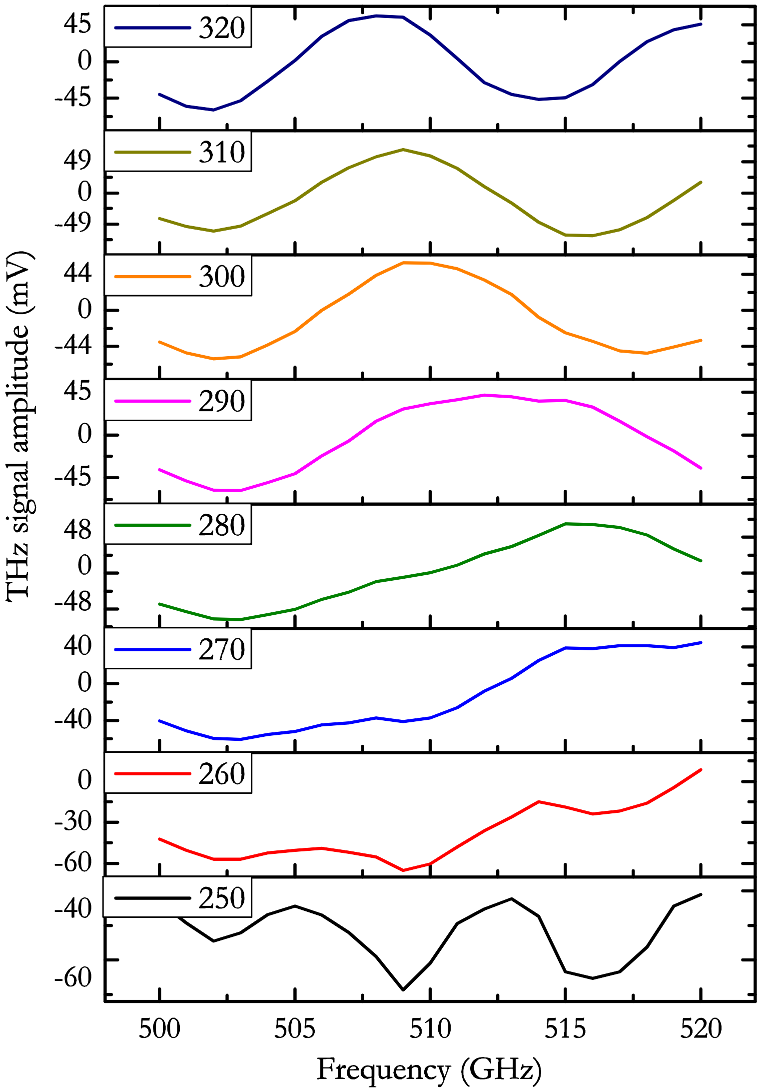

Figure 3.10: THz signal amplitude as a function of beat frequency between 500 GHz and 520 GHz at different delay positions. The optimum delay position was around 270–280 ps (blue and green lines) as the random change in phase was absent compared to the other positions.

However, in order to confirm that the receiver was at the exact zero delay position, multiple scans were performed in which the heterodyne/beat frequency was changed. While changing the beat frequency, the laser phase didn't change within a 20 GHz span. Hence, the detected THz phase shouldn't change with frequency if scanned at the peak amplitude zero delay position. Scans carried out at 'not optimum' delay positions resulted in the THz waveform taking random, non-sinusoidal shapes. To confirm this, the frequency was scanned from 500 GHz to 520 GHz with an increment of 1 GHz, for delay range between 10 ps and 450 ps with a 50 ps step.

With an initial delay scan set to have a 50 ps step size, the phase was fluctuating when the delay was between 0 ps to 250 ps and 330 ps to 500 ps. Thus the optimum delay was determined to be between 250 ps to 330 ps and a fine scan was carried out at 10 ps step size. In Figure 3.10, the THz amplitudes measured at the delay positions between 250–330 ps at 10 ps step size is shown. It is apparent that the optimum delay is 270–280 ps, as there was no phase change in THz amplitude and this is due to the sampling being carried out using the sine wave responsible for the emission (the measured delay position was saved as the zero position in the motion controller). This is due to the coherence time of the lasers. From ref [132], the detected THz electric field, $\Upsilon(t)$ can be represented in terms of the coherence time, t_c and frequency, ω as,

$$\Upsilon(\omega, t) = e^{-\frac{|t|}{t_c}} \cos(\omega t) \tag{3.18}$$

If the delay position is too far from the zero delay position, the amplitude will decrease and the period of oscillation decreases. The THz amplitude decreases exponentially with the coherence time of the lasers. From the laser jitter ($\Delta\nu$) measurement data in Figure 3.6, the coherence time can be calculated as,

$$t_c = \frac{1}{\Delta\nu} \tag{3.19}$$

$$t_c = \frac{1}{400 \times 10^6} = 2.5 \times 10^{-9} s$$

Aside from this calculation, when the fibre length was changed to have a path length difference of 1 m and 2 m, the change in THz signal amplitude at 500 GHz is shown in Figure 3.11.

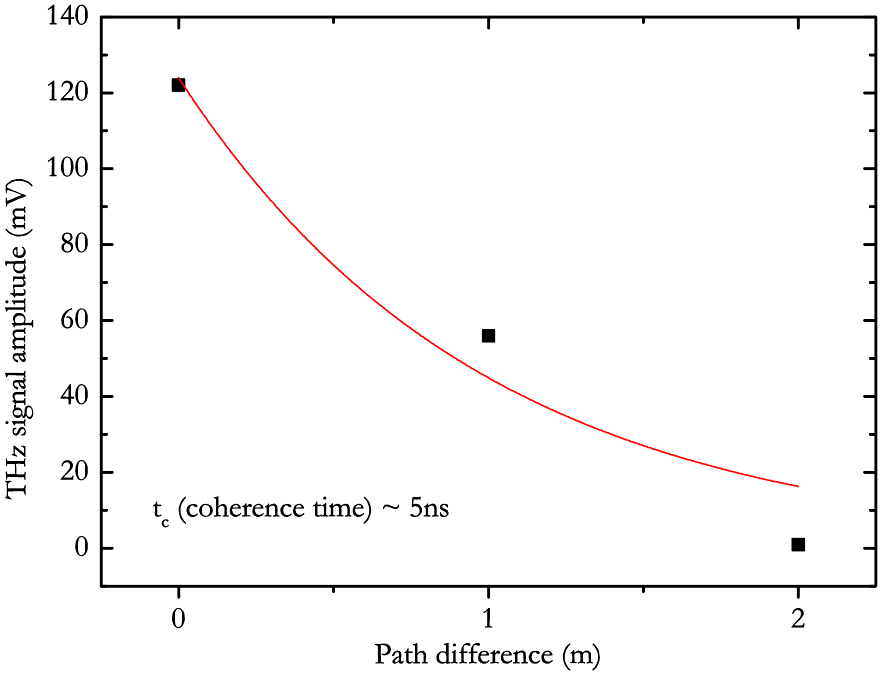

Figure 3.11: THz signal amplitude at 500 GHz as a function of path length difference. Black dots represent the data points and the red line is an exponential fit.

An exponential fit to the curve gives the coherence time of the lasers and was obtained to be ~5 ns. This method of calculating the coherence time is not accurate as there are only three data points limited by the fibre lengths available. However, the coherence time of the lasers calculated by both techniques confirm coherence time of the order of a few ns. This can explain the requirement for an optimum delay position. The free-space propagation path of the THz radiation was calculated to be around ~ 0.45 m. Thus, a 0.30 m optical path length difference in fibre was equivalent to ~0.45 m optical path length in air.

3.7.2 Bandwidth measurement

Once the optimum delay was measured, the emitter and receiver were aligned at the maximum signal. The alignment was carried out at different frequencies. Initially, the emitter was aligned for the maximum THz amplitude at 110 GHz followed by alignment at 500 GHz and 1.0 THz. Since the spotsize of the THz signal decreases with each increase in frequency, the emitter was aligned in the X and Y axis for maximum signal. As soon as the emitter was aligned for maximum signal at 1.0 THz, the detector was aligned in the X and Y axis. Carrying out the alignment using this method helped to reduce the misalignment, since alignment at lower frequencies can cause errors due to the larger spotsize.

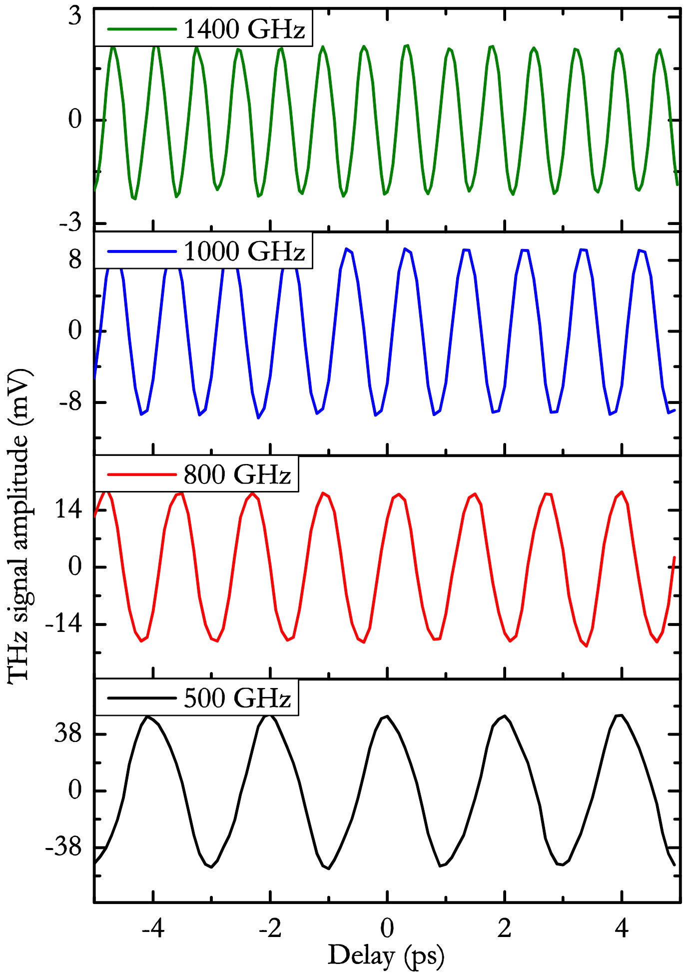

Figure 3.12: THz signal amplitude as a function of delay for 500 GHz, 800 GHz, 1.0 THz and 1.4 THz beat frequencies. The period of oscillations increases with frequency for a fixed delay scan between +5 ps to -5 ps with 500 GHz having the lowest value and 1.4 THz having the highest.

The datasheet provided by TOPTICA reported a bandwidth of greater than 2.5 THz. The bandwidth was measured in our experimental setup as well. With an incident laser power of ~11 mW on to the emitter which was biased using square pulses of -2 V to 0.5 V amplitude at a 7.6 kHz frequency, and ~13 mW laser power applied to the detector, the laser beat frequency was tuned between 100 GHz and 2600 GHz with a 10 GHz step size. For each frequency step, the delay was further scanned between -5 ps to +5 ps, with 0 ps being the optimum delay position. The gain of the trans-impedance amplifier was left unchanged (i.e. 10^7 (V/A)) which was connected to the lock-in amplifier referenced at 7.6 kHz frequency. The scans were taken using a Labview program written by Dr. Joshua R Freeman. Figure 3.12 shows the THz signal amplitude measured as a function of the fixed delay position between -5 ps to +5 ps. The period of oscillation increased as the frequency was increased from 500 GHz to 1400 GHz.

For each delay scan at different frequencies, a sine wave was fit using the programming language MATLAB. A first order sine wave was used for fitting and can be expressed as $f(x) = asin(bx) + c$, where a is the fitted amplitude, b = 2πν is the fitted frequency and c is the fitted phase. This allowed to compare the set frequency and fitted frequency from the measurement. Although, a fast Fourier transform (FFT) can be carried out to recover the amplitude and phase information, sine wave fitting was used for characterization of the TOPTICA emitter.

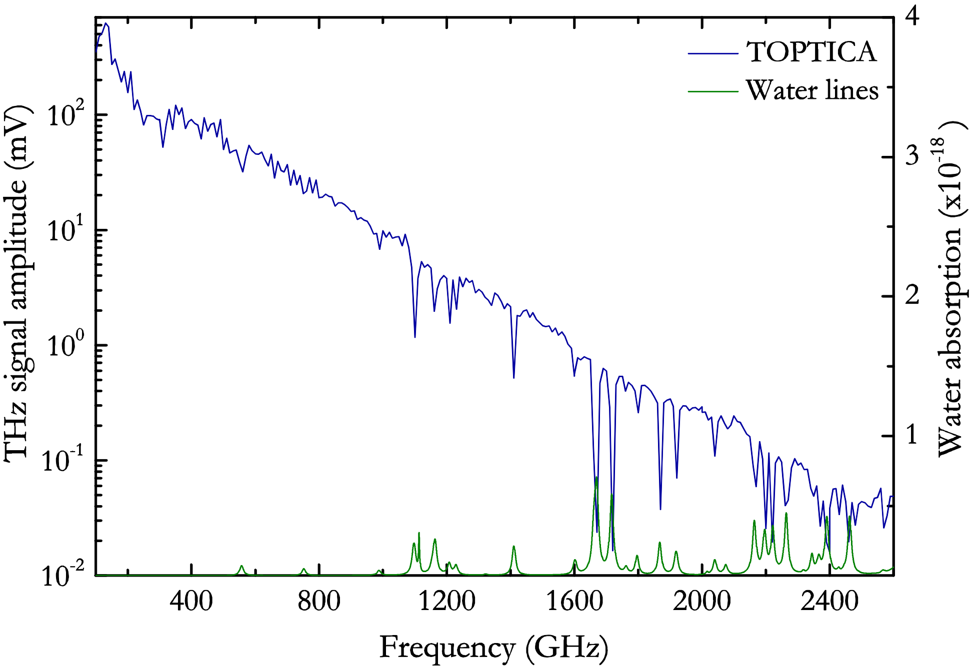

Figure 3.13: THz signal amplitude as a function of beat frequency between 100 GHz and 2600 GHz for the TOPTICA emitter. The water absorption lines are plotted (green curve).

Figure 3.13 shows the THz signal amplitude as a function of beat frequency for the TOPTICA emitter. The amplitude decreased with frequency and a maximum was measured at 100 GHz. The experiments were carried out in a non-purged environment causing the sharp dips around 1000 GHz, 1600 GHz, 2200 GHz due to the water absorption lines. At an incident laser power of 11 mW, and a bias of -2 V to 0.5 V applied to the emitter and 10^7 (V/A) gain, the bandwidth was >2.4 THz. The roll-off in the THz power was calculated by dividing the THz power at all frequencies with respect to

100 GHz which is the lowest measured THz power. The THz power spans more than 90 dB including both emitter and receiver roll-offs.

To remove the receiver roll-off in output power, the emitted THz power from the TOPTICA emitter was measured directly on a bolometer, (discussed in detail later) and then subtracted from the roll-off from the receiver, is shown in Figure 3.14. The roll-off was ~10 dB/octave in the 100–200 GHz range followed by a constant power regime in the 250–500 GHz regime. The reason for the sudden decrease in power within the 100–250 GHz frequency is currently unknown as it is too low for the carrier lifetime to trigger the roll-off and, hence, this may be attributed to the emitter design. The power was constant between the 250–500 GHz range. The emitter power spanned over 40 dB in the 100–2600 GHz range.

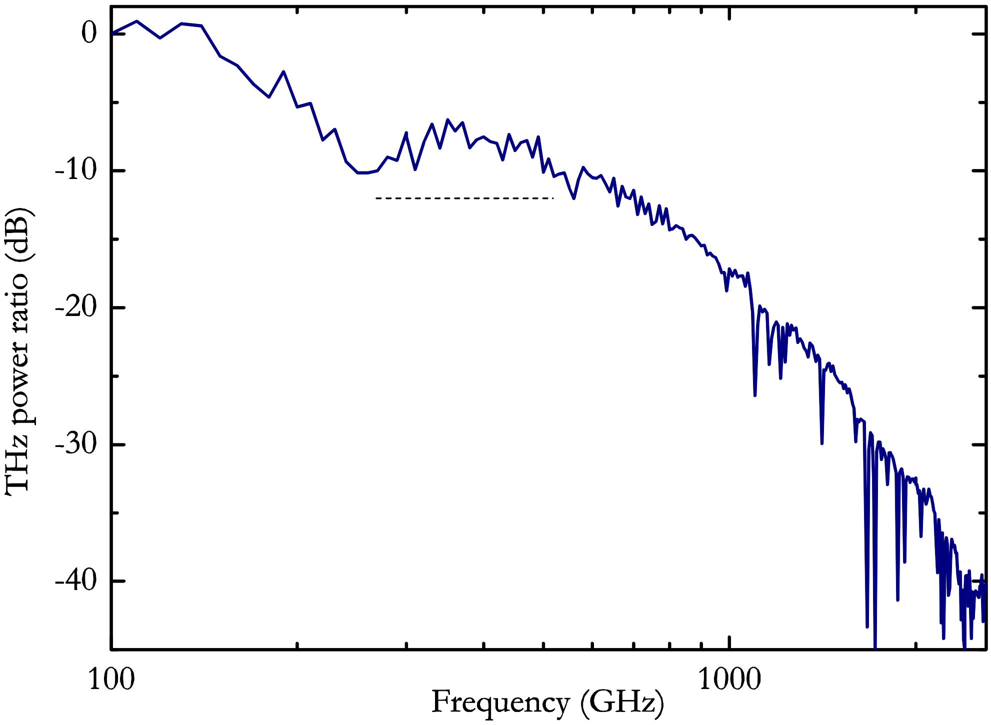

Figure 3.14: Roll-off in THz power plotted as a function of the beat frequency between the lasers. The roll-off was ~10 dB in the 100–200 GHz range followed by an almost constant power regime between the 250–500 GHz (marked using dotted lines).

The frequency of the THz radiation can be extracted from sine wave fitting. Although the scan length is an important parameter, the delay range that has been used in this work is sufficient to get an estimate of the frequency. The measured THz frequency values are plotted as a function of laser beat frequency in Figure 3.15. The frequency values between 100 GHz and 1000 GHz are plotted due to the better SNR of these frequencies. A linear fit to the experimental data gave a slope of ~ 1.00051. Furthermore, the poor SNR at higher frequencies can hamper the recovery of useful frequency information.

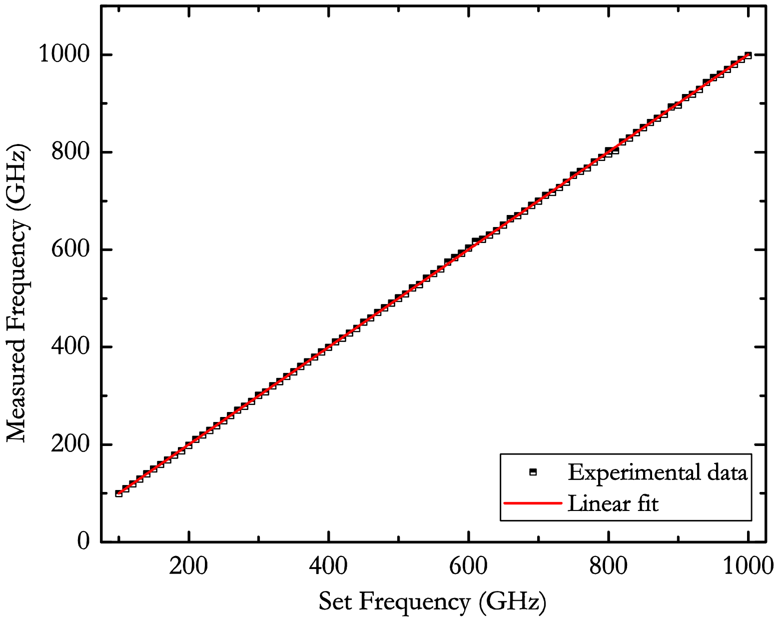

Figure 3.15: Measured frequency as a function of the set frequency between 100 GHz and 1000 GHz. A linear fit (red line) to the data (black dots) has a slope of 1.00051.

Unlike the TOPTICA detector which measures only the THz amplitude, a bolometer is an incoherent detector and it measures the power and the intensity of the THz radiation falling on the bolometer which is a direct measure of the THz power. A He cooled bolometer was used. The emitter was biased using square pulses of -2 V to 0.5 V amplitude at 167 Hz frequency and was placed directly in front of the bolometer. Since the bolometer is not fast enough to respond at 7.6 kHz, the emitter modulation frequency was altered to 167 Hz where the bolometer response is maximum. The bolometer was calibrated to THz power using a TK power meter and measuring the power from a THz QCL on both. The beat frequency was changed between 100 GHz and 1000 GHz. The measured powers were 5 μW and 30 nW at 500 GHz and 2 THz, respectively.

3.8 Conclusions

The advantages of using photoconductive emission for THz generation was discussed compared to other generation mechanisms. The theory behind photoconductive switch and photomixing operation was then reviewed with emphasis given to the CW emission. The physical underpinning the generation mechanism was outlined and expression for emitted THz power from a photomixer given. The incident laser power, applied bias, antenna design and semiconductor properties such as carrier mobility, lifetime and conductivity were considered. A brief overview on the theory of coherent detection using photomixers was then given.

Two DBR lasers with a 1550 nm emission wavelength were characterized. The combined laser jitter was of the order of ~400 MHz. A commercial emitter and receiver from TOPTICA were then characterized using the lasers. An optimum delay position was measured for the fibre coupled coherent detection system and the measurable bandwidth was ~2.4 THz. The output power from the emitter was calibrated using a bolometer. At 100 GHz, the measured power was 10 μW and 5 μW at 500 GHz.

With a stable DBR laser and commercial TOPTICA emitter and receiver, a high resolution photomixing system was built which had a bandwidth of greater than 2.4 THz. The SNR was extremely good at lower frequencies with ratios greater than 20 dB at 500 GHz.

Chapter 4 Materials for photomixing at 1550 nm

This chapter gives an overview of the materials adopted for photomixing at 1550 nm. Iron (Fe)–doped indium gallium arsenide (InGaAs) and indium gallium arsenide phosphide (InGaAsP) materials grown by MOCVD are used, and their performances as THz photomixers are illustrated. The first section gives a brief background about the recent advances in developing InGaAs and InGaAsP materials suitable for photomixing. The details of the growth process are discussed followed by the measurements of the material bandgaps. The procedures for fabrication of photomixers and the experimental setup for their characterisation are described. The performance of the Fe doped InGaAs and InGaAsP photomixers is then compared in terms of resistivity, photocurrent, bandwidth and THz power. The dependencies of the emitted power on the photomixer applied bias, incident laser power, and material doping level, were also studied. The chapter concludes with a comparison between the photoconductive switch and photomixer performance of the wafers.

4.1 Introduction

The theory of photomixing was discussed in detail in Chapter 3. Among the various factors affecting the generation of CW THz radiation from photomixers, the most significant is the semiconductor substrate. The THz power emitted from the photomixer depends on the intrinsic properties of the semiconductor i.e. carrier lifetime, resistivity and mobility, discussed in Section 3.4. One among the popular choices for photomixing materials for THz generation is low-temperature grown gallium arsenide (LT-GaAs) because of the sub-picosecond carrier lifetime and very high resistivity. The first demonstration of THz photomixing on semiconductors used LT-GaAs as the substrate [54, 116]. However, LT-GaAs has a bandgap corresponding to ~800 nm (~1.5 eV), which restricts the use of well-developed lasers, amplifiers, fibre optics and integrated components operating in the telecommunications C-band (1530–1565 nm) wavelength range. A bandwidth of <3.8 THz [119] and a power of greater than 1.8 mW at 250 GHz [137] has been reported before from a LT-GaAs based photomixer. Lasers in the ~800 nm wavelength range are quite expensive and bulky, for example dual wavelength Ti:Sapphire lasers. Although variants such as diode lasers, DBR lasers and distributed feedback (DFB) lasers are also available, they are still expensive compared to their 1550 nm counterparts. The operation of a GaAs photomixer in the 1550 nm wavelength range has been demonstrated [138] from an ErAs doped GaAs wafer. The extrinsic photoconductivity arising due to the incorporation of Er atoms in the GaAs resulted in absorption at 1550 nm. However, the bandwidth reported was < 1 THz.

A promising material to operate in the 1550 nm wavelength range is indium gallium arsenide (InGaAs). It is the most commonly used ternary semiconductor for optoelectronic applications. It is a III–V compound; indium and gallium are from group III and arsenic is from group V. The bandgap of $In_xGa_{1-x}As$ can be tuned by changing the alloy composition of indium and gallium. The most extensively studied InGaAs compound for various optoelectronic applications has a composition of $In_{0.53}Ga_{0.47}As$. This results in material lattice matched to indium phosphide (InP), with a bandgap, E_g of ~0.74 eV. This composition has been used extensively for the fabrication of fast photodiodes [139] and field effect transistors [140].

Undoped InGaAs has poor resistivity (~few Ωcm [141]) compared to the LT-GaAs substrates. Also, the carrier lifetimes are of the order of hundreds of picoseconds. Since the bandwidth and emitted THz power from a photomixer (Eq (3.14)) depends on the carrier lifetime, an ideal material should have a low carrier lifetime i.e. ~hundreds of femtoseconds [132]. Over recent years several schemes to improve the characteristics of InGaAs for THz emission have been reported, which will be discussed in detail in the next Section.

An alternative material that can be used for CW THz emission at telecommunications wavelengths is indium gallium arsenide phosphide (InGaAsP). InGaAsP is a quaternary semiconductor which has significant applications in the optoelectronics industry. It is a III–V compound like InGaAs. The bandgap of this quaternary material with different alloy compositions has been studied [142], and can be tuned between 0.75 eV and 1.35 eV when lattice matched to InP [143]. It has been widely used for the development of semiconductor lasers emitting in the wavelength range between 1300 nm and 1550 nm [144-146]. In this chapter, the various possibilities of using InGaAs and InGaAsP for photomixing at THz frequencies is discussed.

4.2 Historical overview

Research was carried out to improve the performance of InGaAs wafers in terms of resistivity, carrier lifetime and mobility [141, 147]. The different growth techniques used include molecular beam epitaxy (MBE), metal organic chemical vapor deposition (MOCVD), metal organic vapor phase epitaxy (MOVPE) and metal organic liquid phase epitaxy (MOLPE). To increase the resistivity of InGaAs, low-temperature (LT) growth, annealing, doping, ion implantation and ion irradiation have been carried out previously. Chen *et al.* [148] used Fe–doped $In_{0.53}Ga_{0.47}As$ material grown by liquid phase epitaxy (LPE) on Fe–doped InP substrates for the fabrication of low noise photoconductive detectors at MHz frequencies. The mobility of the doped wafer (5390 cm^2Vs^{-1}) was lower compared to the undoped wafer (8000 cm^2Vs^{-1}), and the dark resistance of the devices was found to decrease with Fe incorporation. Tell *et al.* [141] studied the resistivity of Fe doped $In_{0.53}Ga_{0.47}As$ wafers grown by metal organic vapor phase epitaxy (MOVPE) on InP substrates. A resistivity of 50–1000 Ωcm was measured from wafers with Fe doping concentrations between 10^{17} to 10^{18} cm^{-3}. The mobility changed from electron-like to hole-like when the Fe doping concentration was increased above 1×10^{17} cm^{-3}.

One of the earliest reported works to improve the resistivity of InGaAs was from Gupta *et al.* [149]. They found that LT-$In_{0.53}Ga_{0.47}As$ grown on InP substrates using MBE at a growth temperature of 180 ºC was found to exhibit resistivity values in the range, 0.01–1 Ωcm, and the carrier lifetimes were of the order of tens of picoseconds. Gulwadi *et al.* [150] implanted SI-InGaAs with Fe, Cr or group–V elements followed by a subsequent annealing at 850 ºC and 900 ºC, and found that the resistivity improved with Fe implantation. This is explained due to the introduction of Fe acceptor levels in the material. It was Carmody *et al.* [151] who first tried to implant the InGaAs wafer using Fe^+ for better resistivity and carrier lifetimes. They grew a 1.5 μm-thick $In_{0.53}Ga_{0.47}As$ layer on a SI-InP substrate using MOCVD followed by 2 MeV Fe^+ ion implantation at doses ranging between 1×10^{15} cm^{-2} and 1×10^{16} cm^{-2}. The wafers were annealed at temperatures between 500 ºC and 800 ºC. The Fe^+ dose of 1×10^{15} cm^{-2} annealed at 500 ºC had a sheet resistance of 4×10^5 Ω and a carrier lifetime of ~300 fs.

The first use of InGaAs for THz generation and detection was from a LT-$In_{0.3}Ga_{0.7}As$ wafer, excited using pulses of 1.06 μm wavelength by Baker *et al.* [152]. The LT-$In_{0.3}Ga_{0.7}As$ was grown on a SI-GaAs substrate using MBE at a growth temperature of 230 ºC. This work demonstrated a THz imaging system working at infrared wavelengths for the first time. The bandgap of the material was designed to absorb at 1.06 μm. Since this demonstration of a THz imaging system using LT-InGaAs, several attempts were made to make InGaAs more resistive and change the bandgap to 1550 nm. Suzuki *et al.* [153] used Fe–implanted $In_{0.53}Ga_{0.47}As$ grown on an InP substrate using the MOCVD technique for THz generation. Fe ions of 350 keV energy were implanted at a dose of 1×10^{15} cm^{-2}, and they reported a carrier mobility of 1500 $cm^2V^{-1}s^{-1}$ from the Fe implanted emitter. Chimot *et al.* [154] used heavy ion-irradiation of $In_{0.53}Ga_{0.47}As$ using Br^+ ions. The wafers were grown on a SI-InP:Fe substrate using MBE. A carrier lifetime of <0.2 ps, resistivity of 3 Ωcm and carrier mobility of ~490 $cm^2V^{-1}s^{-1}$ were reported for a Br^+ irradiation dose of $1\times10^{12}cm^{-2}$. They demonstrated coherent emission and detection of THz radiation using the same wafers excited at 1550 nm [155]. Takazato *et al.* [156] used Be-doped LT-$In_xGa_{1-x}As$ grown by MBE on a SI: InP substrate for the detection of THz radiation. Three different indium concentrations, x = 0.40, 0.47and 0.53 were grown with a Be^+ doping density of $7\times10^{17}cm^{-3}$, with the material later being annealed. With an indium concentration of x = 0.4, a dark resistivity of 700 Ωcm was reported. They demonstrated the detection of THz radiation using the materials with the different indium concentrations annealed at 650 ºC, and achieved bandwidths exceeding 3 THz when excited with 1.56 μm pulses. They were also able to demonstrate coherent THz emission and detection using LT-$In_{0.45}Ga_{0.55}As$ with the same Be doping density, which was annealed at 650 ºC. They found that LT-$In_{0.45}Ga_{0.55}As$ had a better emitter performance compared to LT-$In_{0.53}Ga_{0.47}As$, and the resistivities measured were 760 Ωcm and 170 Ωcm, respectively, from the two wafers [157].

Apart from these different methods adopted to increase the performance of bulk InGaAs layers on GaAs or InP substrates, various other complicated layer structures of InGaAs have been used. Driscoll *et al.* [158] reported the demonstration of ultrafast photo-response of InGaAs wafers embedded with ErAs nanoparticles. A superlattice of $In_{0.53}Ga_{0.47}As$ was grown by MBE on a SI-InP: Fe substrate. The superlattice included $In_{0.53}Ga_{0.47}As$ layers of varying thickness and $In_xGa_{1-x}As$ with different indium compositions. ErAs nanoparticles were incorporated on the active layer, which was later covered by another InGaAs layer. They observed carrier lifetimes of the order of 0.3 ps by doping the superlattice with Be and found that the carrier lifetime decreased with increasing ErAs concentration. Another work was reported by Guezo *et al.* [159] in which Fe–doped InGaAs/InP multiple quantum wells (MQW) provided an ultrafast electrical and optical response. MQWs were grown on InP substrates using gas source MBE and had 40 periods of InGaAs/InP layers in which Fe was doped uniformly on the various layers. A range of Fe doping concentrations was studied and obtained a photoresponse time of ~0.45 ps.

Other materials that have been studied to operate at 1550 nm include the narrow bandgap materials indium arsenide (InAs) and indium antimonide (InSb). Gu *et al.* [160] studied the THz emission from InAs and InSb wafers and found that the photo-Dember effect [161], i.e. THz emission due to difference in electron and hole mobility creating an oscillating dipole, is the dominating mechanism in both, due to the narrow gap. InAs and InSb wafers were excited at 800 nm and it was found that InAs is highly efficient compared to InSb, even though the latter had better electron mobility. On excitation at 1550 nm they obtained twice the THz signal than at 800 nm. Suzuki *et al.* [162] studied the wavelength dependence of InAs, InSb, lattice-matched $In_{0.53}Ga_{0.47}As$ and lattice-mismatched $In_{0.60}Ga_{0.40}As$ by exciting the emitters at 780 nm, 1050 nm and 1560 nm. The InGaAs layers were grown on a SI-InP substrate using MOCVD. With an excitation wavelength of 1560 nm, they reported the greatest emission from InSb but lower power when excited at 780 nm; they attributed this dependence in wavelength to be due to the change in carrier mobility.

All the previously mentioned reports about the studies to improve the material resistivity and carrier lifetimes on InGaAs wafers were performed using THz-TD systems. As discussed in Chapter 3, in order for a material to emit CW THz radiation, the carrier lifetime of the material is crucial. Unlike pulsed emission in which a simple bow-tie antenna can generate good THz power, photomixers require a well-designed antenna with active area incorporating interdigitated fingers for excellent performance.

The first use of an InGaAs material for photomixing was developed by Sukhotin *et al.* [163] in which the $In_{0.53}Ga_{0.47}As$ layers were embedded with monolayers of ErAs nanoparticles. The active layer was doped with Be during the MBE growth on a InP substrate. The wafer had a resistivity of ~100 Ωcm and picosecond carrier lifetime. They reported a breakdown field of 1×10^5 Vcm^{-1}. The emitters were excited at 1550 nm and 0.13 μW power was obtained at 100 GHz, although the bandwidth of the emitters were restricted to 650 GHz due to the capacitive loading. Baker *et al.* [164] demonstrated the use of a LT-$In_{0.30}Ga_{0.70}As$ emitter for CW THz generation. The wafers were grown on SI-GaAs substrates using MBE at 230 ºC, which was followed by post-growth annealing at 450 ºC. They reported a carrier lifetime of <500 fs and a resistivity of ~10^4 Ωcm. The emitters were excited at 830 nm and they obtained a bandwidth of >1 THz. Chimot *et al.* [165] demonstrated the use of ion-irradiated $In_{0.53}Ga_{0.47}As$ for photomixing. The undoped $In_{0.53}Ga_{0.47}As$ layer was grown on a SI-InP:Fe substrate using gas-source MBE which was irradiated with heavy Br^+ ions at 11 MeV energy and an irradiation dose of 4×10^{11} cm^{-2}. A carrier lifetime of 0.41 ps and mobility of 490 $cm^2V^{-1}s^{-1}$ were reported, and the wafer had a breakdown field of 0.17×10^5 Vcm^{-1}. When excited at 1550 nm, the bandwidth of the emitters were ~1 THz and power levels were lower compared to those obtained with LT-GaAs. Subsequently, the same group demonstrated THz emission up to 2 THz by changing the Br^+ irradiation dose to ~10^{12} cm^{-2} from the same $In_{0.53}Ga_{0.47}As$ wafer. The excitation wavelength was 1550 nm and a peak power of ~10 nW was obtained at 1 THz [166].

Although InGaAsP has found tremendous applications in the optoelectronics industry, its potential to act as a stable THz source has not been studied in detail yet. The first demonstration of InGaAsP as a THz emitter was by Fekecs *et al.* [167]. An InGaAsP layer grown by MOCVD on a SI-InP substrate was implanted with Fe ions at 83 K resulting in 1.1×10^{19} cm^{-3} Fe concentration. They obtained a resistivity of 2500 Ωcm and mobility 400 $cm^2V^{-1}s^{-1}$. The carrier lifetimes were between 300 fs and 3 ps. When excited at 1550 nm, the dipolar antennas gave a bandwidth of greater than 2 THz.

In this work, Fe doped InGaAs and Fe doped InGaAsP layers grown by MOCVD on InP substrates are used for the fabrication of CW photomixers. MOCVD ensures a better surface quality and more uniform doping compared to approaches such as ion-irradiation. Also, MOCVD is cheap compared to MBE growth or implantation methods.

The details of the growth technique are explained in detail in Section 4.3. The Fe:InGaAs and Fe:InGaAsP wafers used in this work for the fabrication of photomixers have previously been demonstrated for pulsed emission by our group. Pulsed emission and detection has been demonstrated before from Fe:InGaAs [109, 168] whereas only pulsed emission has been reported from Fe:InGaAsP [169] from a THz-TD system.

4.3 MOCVD grown Fe–doped InGaAs and Fe–doped InGaAsP

The wafers used in this study were grown by the MOCVD technique at the Centre for Integrated Photonics, United Kingdom under the supervision of Dr. Paul J. Cannard, Dr. Michael J. Robertson and Dr. David G. Moodie. The active layers used in the study, Fe:$In_{0.53}Ga_{0.47}As$ and Fe:$In_{0.70}Ga_{0.30}As_{0.87}P_{0.13}$, were grown on [100] InP substrates in a horizontal quartz reactor at a pressure of 810 Torr at 660 °C growth temperature. Baking and cleaning of the susceptor and reactor were carried out, to ensure the reproducibility for each growth. The precursors used were trimethylindium (TMI), trimethylgallium (TMG) and 100% Arsine (AsH_3) for the Indium, Gallium and Arsenic respectively. For the growth of InP and InGaAsP layer, 100% phosphine (PH_3) was used as the source. For the growth of Fe:InGaAs or Fe:InGaAsP active layer, Fe ions were sourced from Ferrocene ($Fe(C_5H_5)_2$) using a sublimation bubbler. The precursors and sources used for the growth were semiconductor grade. Epitaxy was performed under hydrogen (H_2) environment at a flow rate of ~115cm^3s^{-1}. H_2 was used for the dilution, pusher flows and bubbler pick-ups. The growth of the Fe:InGaAs and Fe:InGaAsP wafers were terminated with an n-InP layer in order to protect the surface from oxidation, since leaving an As terminated layer is detrimental (and to protect the active layers from *ex-situ* annealing). The growth rates of the active layer and n-InP layer were ~7.24 μm/hr and 3.00 μm/hr, respectively. The doping density of the different wafers was confirmed by secondary ion mass spectroscopy (SIMS) analysis. Figure 4.1 shows the layer structure of the Fe:InGaAs and Fe:InGaAsP soon after the growth. It was observed that the surface quality of the Fe:InGaAsP wafers was significantly better than that of the ternary Fe:InGaAs wafers, for which FeAs precipitates formed notable defects that were visible after fabrication (discussed in Section 4.5). This improved surface quality of the quaternary material is attributed to the better matching with the InP substrate [170].

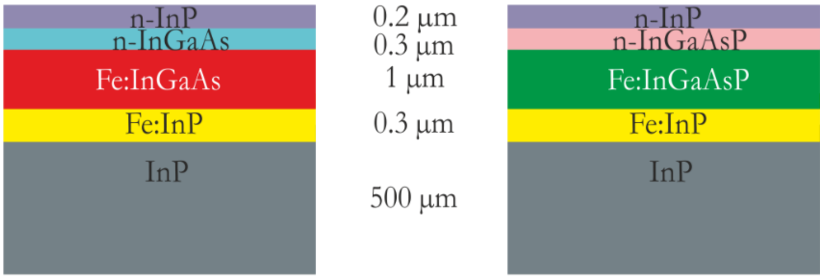

Figure 4.1: Layer structure and thicknesses of the Fe:InGaAs and Fe:InGaAsP wafers grown on InP substrate by MOCVD.

There are advantages of MOCVD over other growth techniques. Ion irradiation techniques damage the wafer surface due to bombardment with heavy ions. It can form defect clusters of the order of nanometres [155], which is not a major issue when fabricating large gap photoconductive emitters although it can be severely detrimental when fabricating electrodes or nanostructures [171] on the active region. Also, MOCVD is cheaper compared to other growth techniques such as MBE.

4.3.1 Bandgap measurement

The alloy composition used were Fe:$In_{0.53}Ga_{0.47}As$ and Fe:$In_{0.70}Ga_{0.30}As_{0.87}P_{0.13}$. The chosen alloy composition is quite unusual for InGaAsP wafer. This particular composition was chosen to enhance the absorption at 1550 nm. For an undoped quaternary $In_{1-x}Ga_xAs_yP_{1-y}$ wafer, the bandgap of the semiconductor is given by,

$$E_g = 1.35 - 0.72y + 0.12y^2$$

where E_g is the bandgap of the semiconductor. In order for the semiconductor to be lattice matched to InP, $y = 2.2x$ needs to be satisfied [143], and is not satisfied in the wafers chosen in this work. The advantage with this particular quaternary material is the freedom to change the bandgap of the material independently from the lattice constant through the choice of composition [144]. However, to confirm the absorption of the material at 1550 nm, photoluminescence and transmission spectroscopy measurements were carried out, which are discussed in the next two subsections.

4.3.2 Photoluminescence

Luminescence, in general, is defined as the emission of light from a material due to excitation. Depending on the excitation method luminescence can be of different types, for example photoluminescence, electroluminescence or bioluminescence. A schematic representation of PL in a semiconductor is shown in Figure 4.2. Photoluminescence (PL) is defined as the emission of photons with energy E_g from a semiconductor, when excited with photons of energy greater than E_g. This transition is usually observed in direct bandgap semiconductors where the conduction band (CB) minimum and valence band (VB) maximum has the same momentum value in the dispersion curve. When the semiconductor is excited with photons of energy, $E \geq E_g$, electrons from the VB are excited to the CB. Electrons from the VB are excited to the CB depending on the incident photon energy, creating excess electrons in the CB and holes in the VB. The electrons cannot stay at the high energy levels in the CB and tend to emit phonons (i.e. non-radiative recombination), and relax at the bottom of the CB. The non-radiative processes responsible for the transition of electrons from higher to lower energy levels follows the conservation of momentum and energy laws, and is faster (~10^{-15} s) compared to radiative processes (~10^{-9} s) [172]. The electrons from the CB each emit a photon and relax to the VB, and thus the photon energy equals the bandgap energy of the semiconductor. The photons emitted from the semiconductor are incoherent and non-directional. A schematic representation of PL in a semiconductor is shown in Figure 4.2.

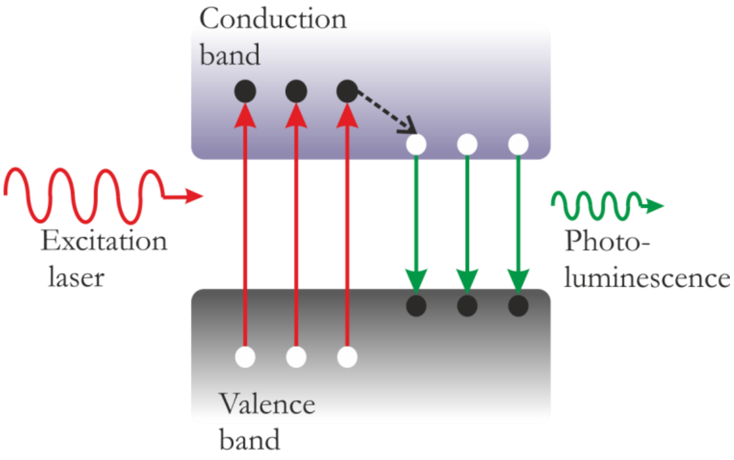

Figure 4.2: Schematic diagram showing the photoluminescence emission from a semiconductor.

In the present study, PL was used to measure the Fe:InGaAsP bandgap. The experimental setup for the PL measurement is shown in Figure 4.3. The experiments were carried out at room temperature. A continuous wave (CW) Helium-Neon (He–Ne) laser with an emission wavelength of 632.8 nm and an output power of 5 mW was focussed to the sample using a lens, at an incident angle of 45°. The sample was placed on a XYZ linear translational stage to facilitate alignment. The laser beam reflected from the wafer was blocked using a beam stop. Due to the incoherent and non-directional nature of PL photons, a lens with a large numerical aperture (NA) was used to collect a portion of the emitted photons. The collimated beam was then focussed onto the slit of a Princeton Instruments Acton Series 2150 spectrometer using another lens. A long-pass optical filter was placed in front of the spectrometer to block any diffuse He-Ne laser light. The grating spectrometer was scanned over the desired wavelength range and the photons were captured by a charge coupled device (CCD). The laser beam incident on the sample was mechanically modulated using an optical chopper at 185 Hz frequency, and the data acquisition output of the spectrometer was connected to the lock-in amplifier, which was referenced to the chopper frequency. The amplified signal was fed to the computer.

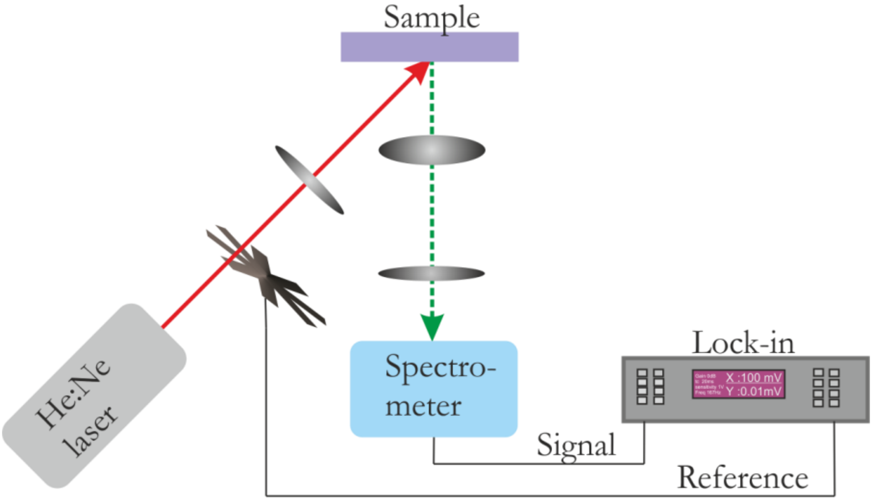

Figure 4.3: Experimental set-up for the photoluminescence measurement.

PL data was measured from the various Fe:InGaAs and Fe:InGaAsP wafers. During the measurement, the grating spectrometer was scanned over the wavelength range between 600 nm and 2000 nm with a 2 nm step size. Figure 4.4 shows the PL spectra obtained from the Fe:InGaAs and Fe:InGaAsP wafers. The Fe:InGaAs sample was found to emit photons in the wavelength range 1400 nm–1700 nm, corresponding to photon energies between 0.85 eV and 0.70 eV. The emitted photon energy indicates the series of energy levels occupied by the electron and hole, after transition from the higher energy level, which is the top of CB for electrons, and the bottom of the VB for holes. Figure 4.5 shows the PL data plotted in terms of energy. There is sharp rise in energy beyond ~0.734 eV i.e. the bandgap of the semiconductor. This is due to the contribution from excitons and the exponential decay observed beyond the bandgap due to the Boltzmann factor [172].

The peak emission wavelength was found to be from ~1640 nm (0.73 eV) implying the higher density of states in that particular energy level. Photon emission at wavelengths lower than the bandgap could be due to the presence of excitons. This particular bandgap is almost similar to that of lattice matched InGaAs (e.g. E_g ~0.74 eV for $In_{0.53}Ga_{0.47}As$) and we attribute this small change in bandgap to the growth conditions that have been used in the study ($Fe:In_{0.53}Ga_{0.47}As$). No dependence with Fe doping could be observed, suggesting that the Fe acceptors forming deep acceptor levels in the bandgap do not alter the bandgap.

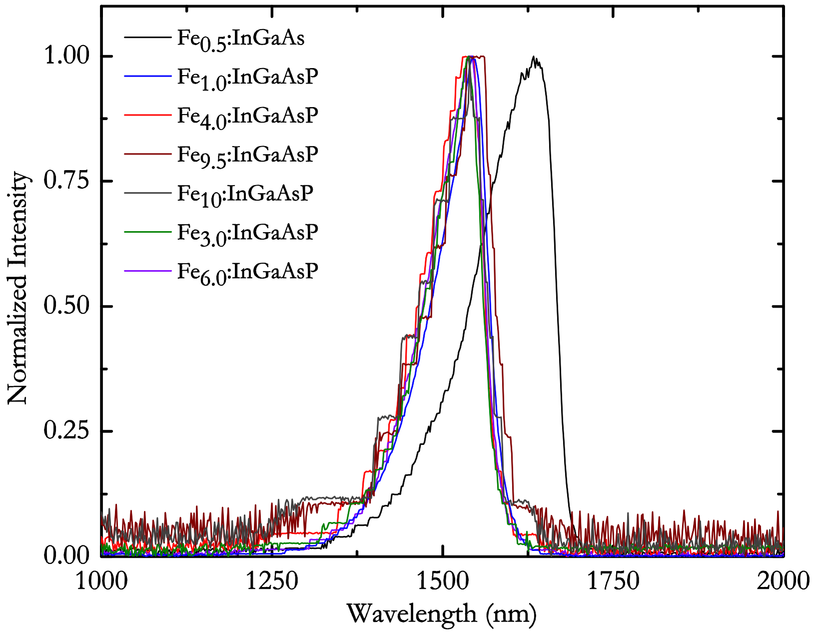

Figure 4.4: PL intensity measured from the Fe:InGaAs and Fe:InGaAsP wafers with different Fe concentrations plotted as a function of excitation wavelength.

The measurements were repeated with the Fe:InGaAsP wafers. Photons in the 1350 nm (0.89 eV)–1600 nm (0.75 eV) wavelength range were emitted with a peak emission at 1560 nm (0.78 eV). The bandgap of the material was observed to be ~1540 nm. As explained previously for the Fe:InGaAs wafer, the emitted photon range corresponds to the energy states occupied by the electrons in the CB and the emission lower than bandgap is due to exciton emission. An exponential decay was observed beyond, confirming the Boltzmann factor. The peak emission wavelength, ~1560 nm corresponds to higher density of states. This confirms that the bandgap of the Fe:InGaAsP wafer has shifted from 1300 nm, typically observed for $In_{0.70}Ga_{0.30}As_{0.66}P_{0.34}$ lattice matched to InP, to ~1550 nm. The quantised nature of the curves in Figure 4.4 and Figure 4.5 is due to the sensitivity range used in the lock-in amplifier; when the sensitivity range is set high (100's of mV, unintentionally set), small signals such as those measured here (a few μV) experience quantisation in the lock-in amplifier.

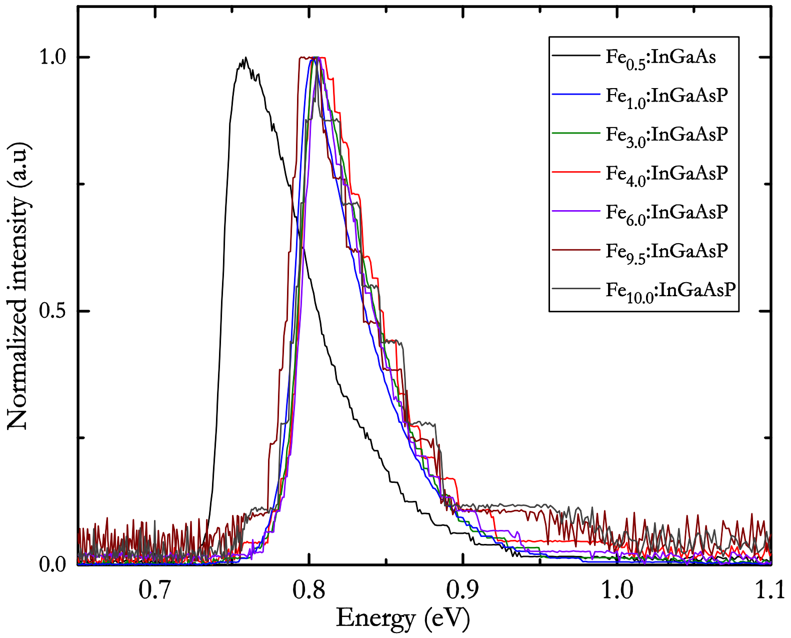

Figure 4.5: PL intensity measured from the Fe:InGaAs and Fe:InGaAsP wafers with different Fe concentrations plotted as a function of excitation energy.

4.3.3 Transmission spectroscopy

Another method adopted to confirm the bandgap of the samples was to measure the transmission through the wafers. Since photons with energies higher than the bandgap will be absorbed and the lower energies will be reflected back from the sample, transmission spectroscopy is an alternative method that can be employed to obtain the bandgap of materials.

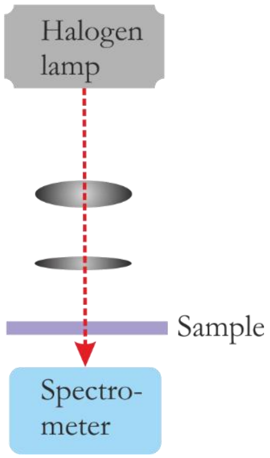

Figure 4.6: Experimental set-up for the transmission spectroscopy measurement.

The experimental setup is shown in the Figure 4.6. It involved a broadband light source (a tungsten-halogen lamp) which emitted photons in the wavelength range 400 nm to 1700 nm. The light was collimated and focussed to the wafer using a pair of lenses. The sample was placed in front of the spectrometer slit (same as the one used for the PL measurement), and the spectrometer was scanned over the required wavelength range. A reference scan was also taken before scanning each wafer.

Figure 4.7 shows the transmission data from the Fe:InGaAsP wafers. The wafers were scanned in the wavelength range between 1000 nm and 1800 nm. It was found that all the Fe:InGaAsP wafers were transparent above 1550 nm. No dependence with Fe doping could be found, again confirming that the bandgap of the material is not altered due to the presence of Fe acceptors. However it should be noted that this measurement does not give a complete picture of the band edge or presence of impurity states; measuring the transmission through the sample alone is not sufficient to confirm the bandgap precisely. The reflections from the wafers also have to be taken into account, since surface deformities can result in the reduction of transmitted light. A solution to the problem is to calculate the light absorbed by the sample, by subtracting the reflected and transmitted light. Furthermore, a peak appearing on the absorption spectrum cannot necessarily be assigned to the bandgap (i.e. same k values), but may be due to absorption from the VB to CB at a different k value.

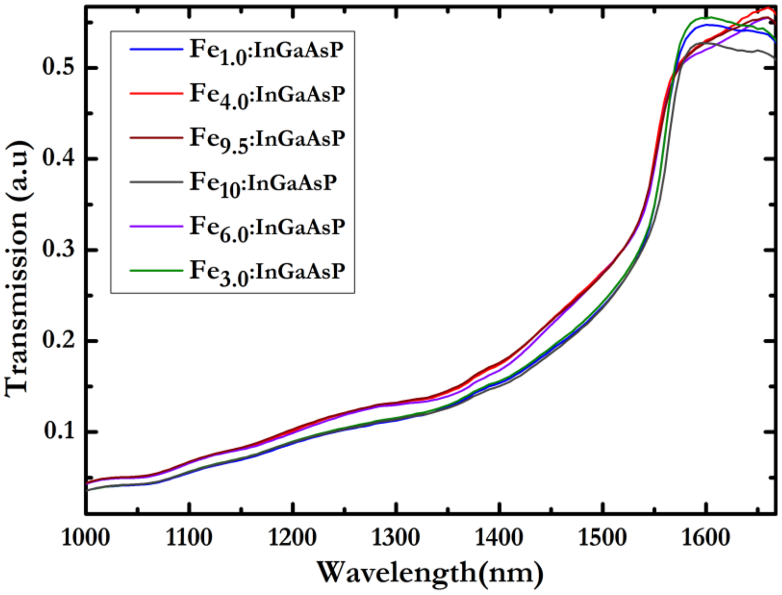

Figure 4.7: Transmission through the various Fe:InGaAsP wafers plotted as function of wavelength.

In summary, the shift in the Fe:InGaAsP bandgap due to the choice of composition has been measured using transmission spectroscopy and PL. Both techniques confirmed a bandgap of ~1550 nm for the Fe:InGaAsP wafers.

4.4 Antenna design

When the active region of the photomixer is excited with photon energy, $E \geq E_g$, photocarriers are generated. The photocarriers are then accelerated by the applied bias. The generated photocurrent has to be fed to a suitable antenna structure which can then couple the radiation to free space. The use of antennas for transmitting or receiving electromagnetic radiation dates back to early 19th century when Marconi invented the radio. The use of an antenna for coupling the radiation generated in a photoconductor was employed by Mourou *et al.* [173]. In the THz regime, planar antennas are typically used to couple the generated THz radiation from the photoconductor to free-space. The antennas usually employed for the microwave or millimetre regimes cannot be scaled down directly for THz due to the smaller wavelength compared to the thickness of the substrate [174]. The planar antennas can be classified into two types, resonant antennas and broadband antennas. Resonant antennas are strongly frequency dependent and are thus less efficient at frequencies away from the design frequency. On the other hand, broadband antennas are frequency-independent (in the frequency range we are interested here, 0 GHz–3 THz) i.e. a flat response over a wide bandwidth. The most commonly used broadband antennas are the bow-tie antenna, spiral antenna and log-periodic antenna. Among those, the logarithmic spiral antenna is preferred over the other log-periodic antenna designs due to its circular polarization emission, which is advantageous. For log-periodic antennas, linearly polarized radiation can only be detected if the polarization direction matches with that of the detector, thus creating constraints. Spiral antennas on the other hand do not have this issue. They emit a circularly polarized beam at lower frequencies, and this changes from elliptical to linear at high frequencies. For log-spiral antennas, the generated photocurrent travels along the spiral arms and will be emitted when the frequency resonance occurs. The log-spiral antennas can emit good radiation pattern with fewer than 2 turns [175].

In this work, a 3-turn self-complementary logarithmic spiral antenna with an active region of 11.3 μm×11.3 μm was used, as shown in Figure 4.8. The performance of this antenna has been optimized previously [176].

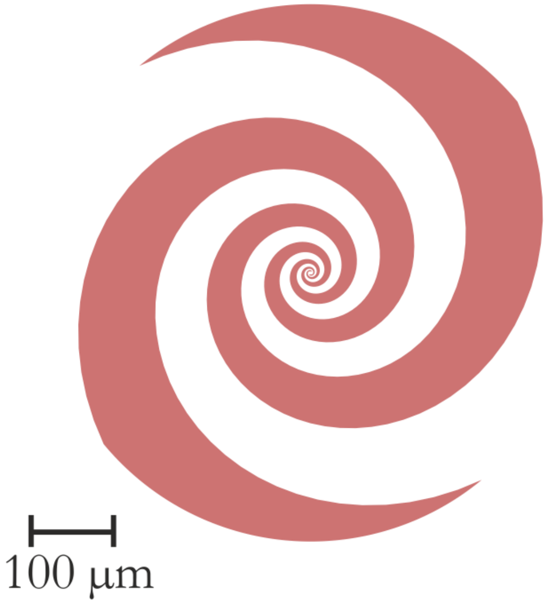

Figure 4.8: Schematic of the 3-turn self-complementary log-spiral antenna used with an active area of 11.3 μm×11.3 μm

4.4.1 Incorporation of IDTs

There has been successful demonstration of photomixing up to 3.5 THz from a bare gap active region [120], however, the power levels obtained were low. The photomixer performance is dependent on the capacitance of the active region, according to Eq. (3.14). Since the capacitance is inversely proportional to the active area, the obvious solution is to reduce the active area. This is inconvenient due to fabrication issues and also the difficulty of focussing the laser spot to a smaller active region. The practical solution for this issue is the incorporation of interdigitated fingers (IDTs) in the active region. The introduction of IDTs on the active region can ensure that, while the interaction area between the photocarriers and electrodes has been increased, the gap between the two arms of the antenna remains constant. The transit-time of the carriers is thus reduced, resulting in faster recombination and increasing the photocurrent. However, incorporating too many fingers can result in increasing the capacitance, thus reducing the output power. This capacitance results in a -12 dB/octave roll-off at high frequencies [119]. The influence of gap spacing on the performance has been reported previously [131]. Although a smaller active region with IDTs can enhance the power at higher frequencies, the higher photocurrent can result in joule heating, damaging the sample.

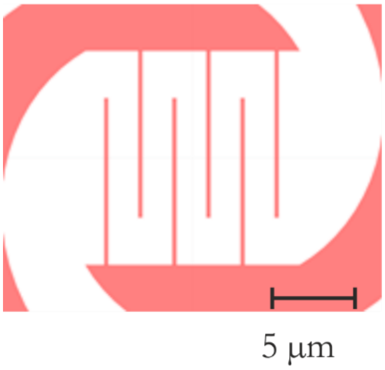

Figure 4.9: Schematic of the active region of the log-spiral antenna with 3 pair of IDTs, having a finger width of 0.2 μm and gap size of 1.6 μm.

In this work, 3 pair of IDTs with a finger width of 0.2 μm and a gap size of 1.6 μm was used. Optimization was carried out in ref [176] and a bandwidth of greater than 2.0 THz was obtained from the design on a LT-GaAs substrate photomixer excited at 780 nm.

4.5 Fabrication procedure

The layer structure of the Fe:InGaAs and Fe:InGaAsP wafers was shown in Figure 4.1. The fabrication procedure involved the removal of the cap layers n-InP and n-InGaAs/n-InGaAsP for both Fe:InGaAs and Fe:InGaAsP, respectively. The cap layers protect the Fe:InGaAs and Fe:InGaAsP active layers from oxidation, since the presence of Fe atoms on the surface makes the active layer susceptible to atmospheric oxidation. The fabrication procedure started with the cleaving of a 10 mm×10 mm piece from the 2-inch wafer. The scribing was performed using a JFP-S100 scriber. The cleaved sample was then cleaned using acetone in an ultrasonic bath at 10% power for 2 min to remove any debris or dust left on the surface. The sample was then blow-dried using dry nitrogen. The sample was later cleaned again using isopropyl alcohol (IPA) in ultrasonic bath at 10% power for 2 min to remove any organic waste deposited on the sample, followed by a blow dry in dry nitrogen.

Before the removal of the cap layers, the sample was stuck to a glass slide for ease of handling. For doing so, a drop of Shipleys® 1813 (S1813) resist was placed on the middle of the glass slide. The glass slide was then held vertically for 1 min to form a uniform thin layer of the resist. The sample was placed on top of the resist on the glass slide surface, which was baked using a hot plate at 115 °C for 1 min. The dried resist held the sample to the glass slide.

The cap layer n-InP was then removed using concentrated hydrochloric acid (HCl); InP is a III–V compound and is easily dissolvable in HCl. Depending on the thickness of the InP layer, the concentration of HCl can be varied [177]. HCl can be diluted using de-ionised water, which gives control over the etch rate. However, for the wafers used in this work, the 200 nm thick n-InP layer is followed by an n-InGaAs/n-InGaAsP layer. Since n-InGaAs/n-InGaAsP is not soluble in concentrated HCl, it can act as an etch stop layer. Thus, the sample stuck to the glass slide was immersed in concentrated HCl for 20 s. As soon as the sample was immersed in HCl, bubbles were found to be escaping from the sample surface confirming that the InP layer has been etched. This was followed by cleaning in DI water in 1 minute.

The n-InGaAs/n-InGaAsP layer was etched using a sulphuric acid wet etch solution. Concentrated sulphuric acid (H_2SO_4), hydrogen peroxide (H_2O_2) and water (H_2O) were used to prepare the solution. The ratio between the solvents H_2SO_4:H_2O_2:H_2O was 1:1:10. The solution cannot be used immediately after preparation since the etch rate was too high and didn't provide uniform etching. The prepared solution was therefore kept on a hotplate at 25 °C for 15 min for cooling to provide a uniform etch rate. After 15 min the solution was removed from the hotplate and the sample was immersed in the wet etch solution for 42 s. Since the bottom Fe:InGaAs/Fe:InGaAsP active layer is also dissolvable in the etch solution, caution was taken to ensure the solvent temperature and etching time to be precise. The 300 nm thick n-InGaAs/n-InGaAsP layer was completely removed during etching. The sample was then cleaned using DI water for 2 min, exposing the active layer. The surfaces of the Fe:InGaAs and Fe:InGaAsP layers soon after the processing are shown in the Figure 4.10.

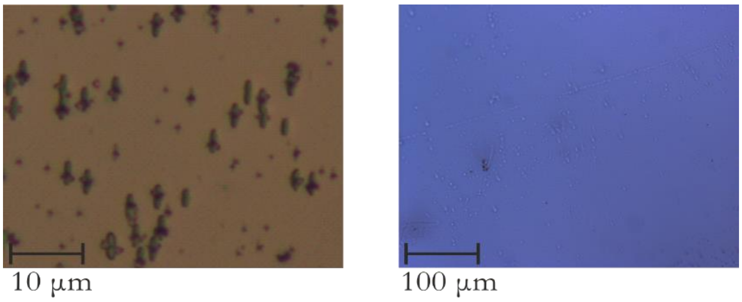

Figure 4.10: Wafer surface of the Fe:InGaAs (left) and Fe:InGaAsP (right). FeAs precipitates clearly visible on the Fe:InGaAs surface, whereas Fe:InGaAsP didn't have any visible surface deformities.

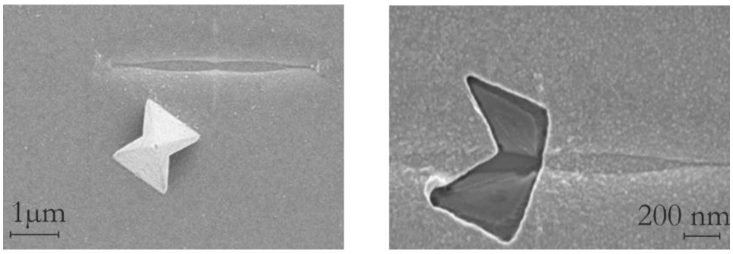

Figure 4.11: SEM images of the FeAs precipitate on the Fe:InGaAs surface.

The Fe:InGaAs surface had many visible deformities due to FeAs precipitates, where Fe:InGaAsP didn't have any deformities. In order to estimate the size and nature of the FeAs precipitates, images were captured using a scanning electron microscope (SEM). The size of the surface defects were of the order of a few microns. The defects were due to both precipitates deposited near the surface and deep intrusions into the active layers. Figure 4.11 shows SEM images of an Fe:InGaAs sample with the two major types of surface defects.

For large gap emitters (especially bow-tie antennas) the n-InGaAs/n-InGaAsP layer can be used for defining the contact electrodes. The gap between the contact electrodes is then later etched to expose the active layer [109]. However, in the present study, since the IDT design had dimensions of the order of 0.2 μm, etching after defining the lithography can be difficult.

The sample was separated from the glass slide by immersing in acetone for 2 min. It was then cleaned using acetone and IPA and blow-dried using dry nitrogen. The various stages involved in the preparation of the wafer structure are shown in Figure 4.12.

The sample was then coated with electron beam resist, ZEP 520A at 4000 rpm, resulting in a 420 nm thickness. The resist was baked at 180 ºC for 2 min. The electron beam lithography was carried out by Dr. Mark C. Rosamond using a JEOL e-beam lithography system. Electron beam lithography was used due to the better resolution and reproducibility. The exposed sample was developed using N-50 (n-amylacetate) for 90 s, followed by a rinse in IPA.

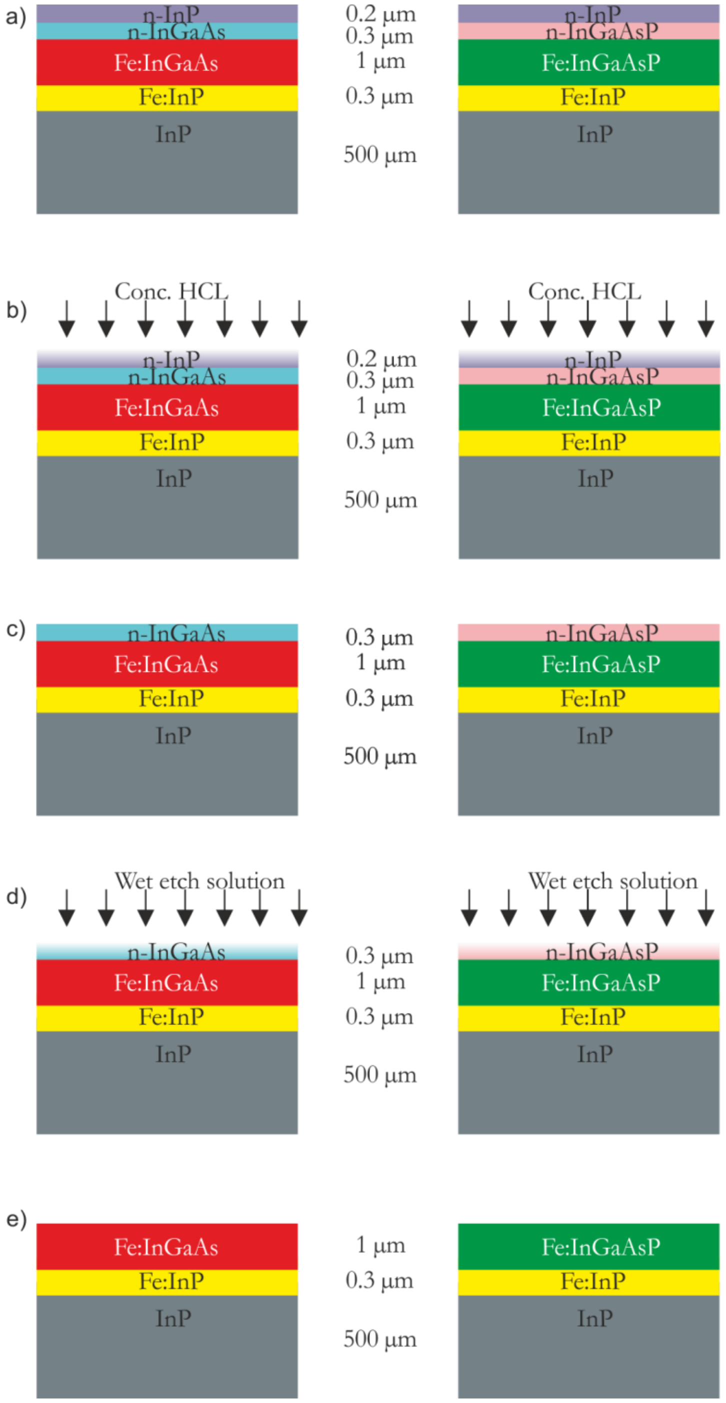

Figure 4.12: Various stages involved in the processing of the wafers (a) sample after growth, (b) and (c) concentrated HCl removing the n-InP cap layer, (d) wet etch solution dissolving n-InGaAs/n-InGaAsP layer, (e) final structure of the wafer before resist spinning and e-beam lithography.

The developed sample was then metallized in an electron-beam evaporator (Leybold e-beam 350). The e-beam evaporator was used instead of a thermal evaporator to avoid any cracks in the resist that may occur at the higher temperatures in a thermal evaporator.

Titanium/gold (Ti/Au) of thickness 10 nm/150 nm was used to ensure good contacts which can withstand milliamps of current. After evaporation, the sample was left in cyclopentanone at 60 °C for 10 to 20 min on a hotplate for lift-off, followed by a 10% power ultrasonic bath in cyclopentanone. The sample was then cleaned using IPA and dried using dry nitrogen.

A 10 mm×10 mm sample can usually have 6 antennas fabricated on it. The sample was then cleaved using a JFP S-100 scriber. The sample was coated using S1813 before scribing to prevent the wafer flakes from scribing getting deposited on the active region and damaging the IDTs.

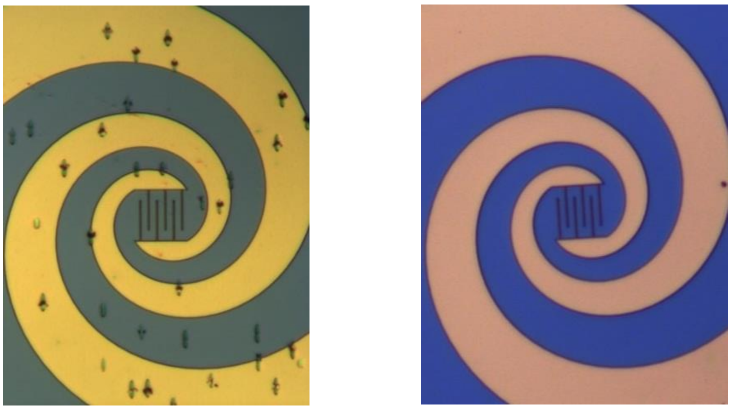

Figure 4.13: Fabricated log-spiral antennas on Fe:InGaAs and Fe:InGaAsP wafers.

Figure 4.13 shows the Fe:InGaAs and Fe:InGaAsP devices after fabrication. The separated devices were cleaned using acetone and IPA and dried using dry nitrogen. In order to define the contact pads a separate optical lithography was carried out. S1813 resist was spun on the devices using a spin coater at 4000 rpm for 30 s. This provided a coating thickness of around ~1 µm. The contact pads were then defined using an optical mask and exposed under UV light. The exposed device was cured using chlorobenzene for 2 minutes to define the undercuts and developed using MF 319 for 75 seconds followed by DI water cleaning. Ti/Au with a thickness of 20nm/100nm was used for metallization and the device was lifted-off using acetone, followed by an IPA wash and blow-dried using dry nitrogen.

The device was stuck to a specially designed printed circuit board (PCB), with copper defined contact lines, using RS® silver conductive paint. After applying silver paint, the device was left for 2 hours to dry before any measurements. An image of the fabricated device mounted on the PCB board can be seen in Figure 4.14

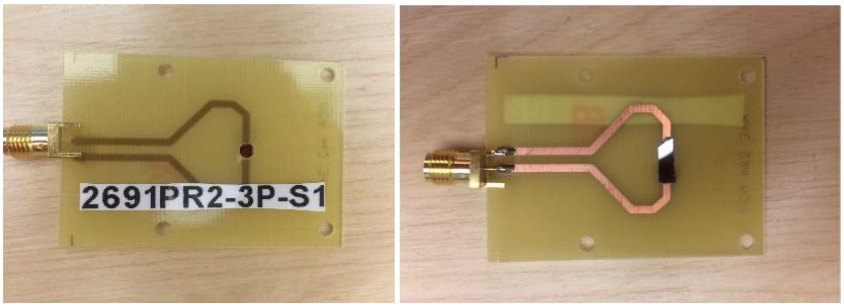

Figure 4.14: Samples mounted on PCB after fabrication

4.6 Emitter characterization

The experimental setup used for the characterization of emitters was identical to the setup used for characterization of the commercial TOPTICA emitters, as explained in Chapter 3. Except for the emitter, all other components and equipment remained the same, as shown in Figure 4.15. The TOPTICA emitter was fibre coupled, whereas the in-house emitters were not. The emitters thus had to be aligned to the excitation laser beam to generate THz radiation. The laser beam exiting out of the output arm 1 of the fibre splitter was collimated using a 1550 nm collimator (F220APC-1550), propagated through a half-wave plate (Thorlabs-1550nm) and focussed onto the emitter using an aspheric lens (C430TME-C).

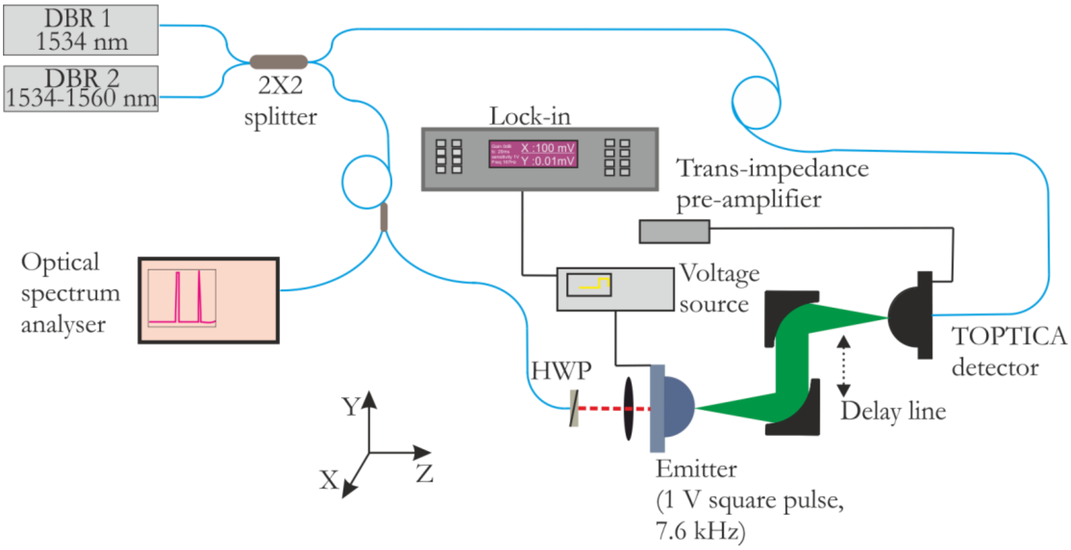

Figure 4.15: Experimental set-up used for the characterization of the in-house emitters

While mounting the sample on the PCB board, slight misalignment can occur due to the lack of alignment marks and manual errors, resulting in the sample not being exactly in-line with the contact lines on the PCB. In order to address this issue, a half-wave plate

(WPH05M-1550) was used. The half-wave plate (HWP) provides precise control over the linear polarization of the incident laser beam. The dependence of the polarization of the laser beam is discussed in detail in Section 4.7.5. An aspherical lens with anti-reflection coating and numerical aperture (NA) = 0.53 was used. The focal length of the lens was ~ 5 mm. Since the silver paint thickness can affect the position of the sample, the lens was mounted on an Z-controlled linear translational stage, enabling the beam to be correctly focused on the emitter.

The emitter was also placed on an XY- linear translational stage allowing precise control over the position of the focussed laser spot on the device. A hyper-hemispherical Si lens with 2.5 mm diameter was attached to the back of the device using a lens mount on a smaller XY- linear translational stage. Since the refractive index of Si is n = 3.44, close to the refractive index of the InP wafers studied in this work (n ~3.5-3.7), this reduced the reflections back into the substrate. The device was aligned initially at a low frequency (110 GHz due to the better SNR), followed by more precise alignment at 500 GHz, 1 THz and 1.5 THz. Once the sample was aligned, the Si lens position was adjusted to maximise the measured signal. As explained before in Section 4.4, the generated THz current propagates through the spiral arms and will be radiated when the resonance occurs. Therefore, the Si lens position was crucial to obtain the signal at higher frequencies (1.5 THz), for which the signal was emitted from the centre of the spiral. However, the signals at lower frequencies (100–600 GHz) were found to be less dependent on the exact alignment of the silicon lens.

The different components (collimator, aspherical lens and device) were all mounted in a 30 mm cage structure which was then mounted on an XYZ - linear translational stage. This arrangement of the optical components provided independent control of the incident laser beam on the device and the emitted THz radiation from the device. The THz radiation was collected by a *f/2* parabolic mirror which collimated the radiation. The collimated radiation was focussed to the TOPTICA detector by an another *f/2* parabolic mirror. The second parabolic mirror and the coherent detector were mounted on a mechanical delay to ensure the optimum delay between the emitter and detector. While aligning the position of the detector, special care was taken to perform the alignment at higher frequencies due to the small spotsize at lower wavelengths. The detected current was amplified using the FEMTO trans-impedance amplifier at a gain of 10^7 (V/A). This gain was the same as that used when characterizing the TOPTICA emitter, to ensure a fair comparison between the TOPTICA and in-house emitter.

Comparing the experimental setup discussed in Chapter 3, the introduction of the collimator, half-wave plate and aspherical lens onto the laser beam path caused a slight change in the optimum delay position. The difference induced by the new components on the beam path was less than 10 cm, which was adjusted by changing the delay position. A frequency scan at different delay positions was repeated to obtain the optimum delay position using a standardized in-house emitter that didn't require changing of fibres. The significance of the optimum delay position was discussed in Section 3.7.1.

4.7 Results from characterization

For the emitter comparison study, two Fe:InGaAs and four Fe:InGaAsP wafers with different Fe doping concentrations were chosen. The Fe doping concentration for the different wafers are given in Table 4.1. The Fe:InGaAs wafers were limited to only two doping concentrations due to wafer availability. All the Fe:InGaAs and Fe:InGaAsP devices were processed as explained before in Section 4.5 and mounted on the PCB for testing.

Wafer type	Fe doping concentration (cm^{-3})
Fe:InGaAs	0.5×10^{16}
Fe:InGaAs	5.5×10^{16}
Fe:InGaAsP	1.0×10^{16}
Fe:InGaAsP	4.0×10^{16}
Fe:InGaAsP	9.5×10^{16}
Fe:InGaAsP	10.0×10^{16}

Table 4.1: Various Fe:InGaAs and Fe:InGaAsP wafers with the respective Fe doping concentration.

4.7.1 IV characteristics

The devices were first tested for electrical connection using a Keithley 2400 source meter at an applied bias of 0.2 V without any incident optical beam. This approach was used for all devices since measuring the resistance directly using a multimeter can cause shorting of the interdigitated fingers due to the high current flow. Also a grounding strap was worn each time while mounting, changing samples, or making an electric connection to avoid any static discharge which may damage the IDTs.

The dark resistivity of the wafers was measured by colleagues using a 4-terminal Hall bar. The details of the experiments are discussed in detail [169]. Figure 4.16 (a) shows the four-terminal resistivities of the two Fe:InGaAs wafers and four Fe:InGaAsP wafers. In the case of Fe:InGaAs, the resistivity values were ~1.0 kΩcm and ~0.6 kΩcm for the $0.5\times10^{16}\,cm^{-3}$ and $5.5\times10^{16}\,cm^{-3}$ doped samples, respectively. For the four Fe:InGaAsP wafers, the resistivity was found to decrease from ~10.0 kΩcm to ~1.0 kΩcm as the doping increased from $1\times10^{16}\,cm^{-3}$ to $10\times10^{16}\,cm^{-3}$. As discussed previously, the aim of doping the InGaAs and InGaAsP material with Fe is to increase the resistivity of the intrinsic semiconductor. However, for the range of doping studied in this work, the resistivity was found to decrease with increased doping, suggesting that the material was over-compensated. In the case of Fe:InGaAs, the optimum doping level was found to be around $2.5\times10^{16}\,cm^{-3}$ [178], whereas no such optimum doping level was found for the Fe:InGaAsP. The earlier studies [141, 169, 179] also confirm that Fe-acceptors increase the resistivity from the measured intrinsic value of 1 kΩcm to a maximum at a doping of around $1\times10^{16}\,cm^{-3}$ for Fe doped InGaAs.

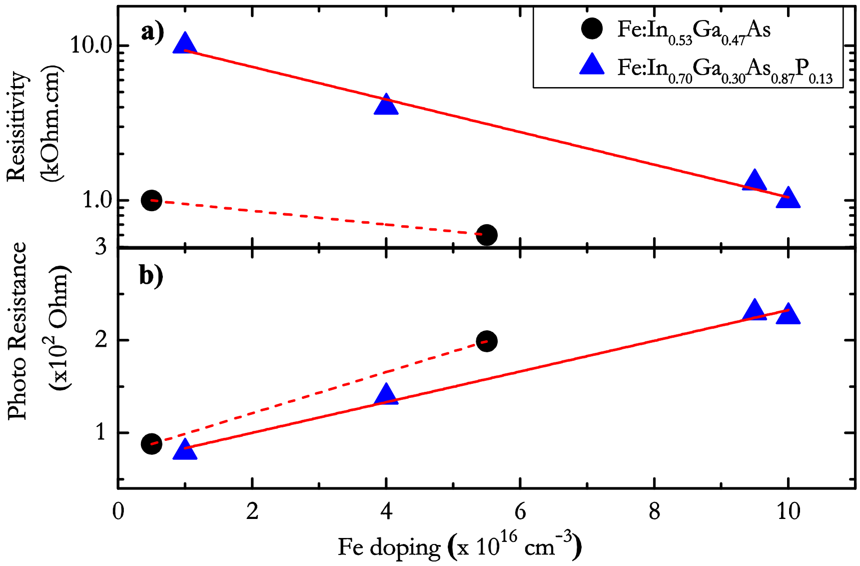

Figure 4.16: (a) Resistivity, measured under dark conditions, and (b) emitter photo-resistance at an incident optical power of 10 mW, as a function of Fe doping for InGaAs and InGaAsP material. Lines are guides for the eye.

The breakdown field of the devices used in this work was measured by biasing the emitter using a Keithley 2400 source meter and slowly increasing the applied bias until breakdown. The dielectric breakdown occurred at a field of ~12.5 $kVcm^{-1}$. The breakdown in the samples was initiated at the IDTs due to the concentrated electric field at the finger tips. All the devices were found to have a similar breakdown field.

Photocurrent is another crucial parameter determining the amount of emitted THz power. It gives a measure of the number of photo carriers generated for an incident photon. The devices were aligned for maximum photocurrent at an applied bias of 0.2 V by adjusting the device's X and Y-linear translational stages. The focusing lens was also adjusted to maximize the photocurrent. In this case, the larger spacing between the spiral arms compared to the smaller active region IDTs leads to a large difference in photocurrent (few µA between the spiral arms and a few mA at the IDT), making the alignment easier. An IR camera was also used to confirm the laser beam was hitting the active region of the photomixer.

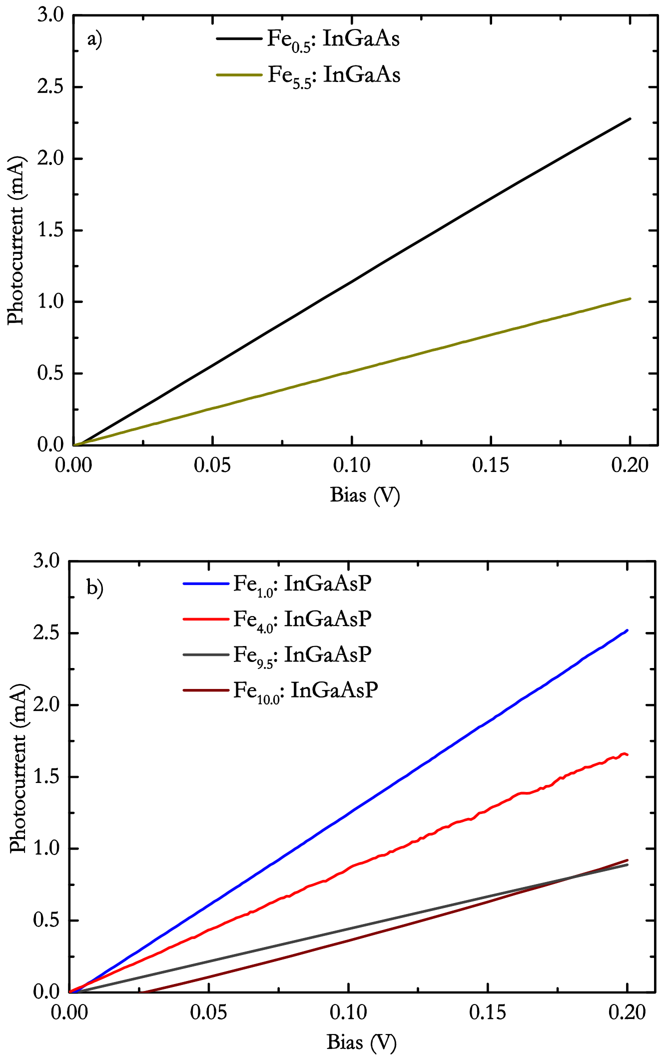

Figure 4.17: Photocurrent measured from the (a) Fe:InGaAs and (b) Fe:InGaAsP wafers as a function of bias at an incident laser power of 10 mW

Figure 4.16 (b) shows the photo-resistance of the devices when illuminated with 10 mW of optical power at 1534 nm. The resistance of each device was found to fall by almost three orders of magnitude under illumination. Photo-resistance of the devices were calculated using the measured photocurrent values at 0.2 V (using Ohm's law, V= IR). Unlike dark resistivity, the photo-resistance of the device increased with doping for Fe:InGaAs and Fe:InGaAsP. This is due to the increase in Fe trapping centres at high doping levels. In Figure 4.17, the photocurrents of the devices in the bias range 0 V to 0.2 V are plotted. In each case, the maximum photocurrent measured from the devices was of the order of milliamps, ~2.5 mA from the Fe:InGaAs and Fe:InGaAsP wafer with Fe doping concentration 0.5×10^{16} cm^{-3} and 1.0×10^{16} cm^{-3}, respectively. The lowly doped wafers were found to generate higher photocurrents compared to the highly doped wafers for both Fe:InGaAs and Fe:InGaAsP, as expected. For the higher doped wafers, maximum photocurrents were ~0.8 mA, in the case of both Fe:InGaAs and Fe:InGaAsP. This is attributed to increased trapping of photocarriers by Fe acceptors. For this measurement, the DC bias was limited to 0.2 V to avoid thermal breakdown in the devices across the 1.6 µm gap, and all devices showed ohmic behaviour in this range.

4.7.2 Bandwidth comparison between Fe:InGaAs and Fe:InGaAsP

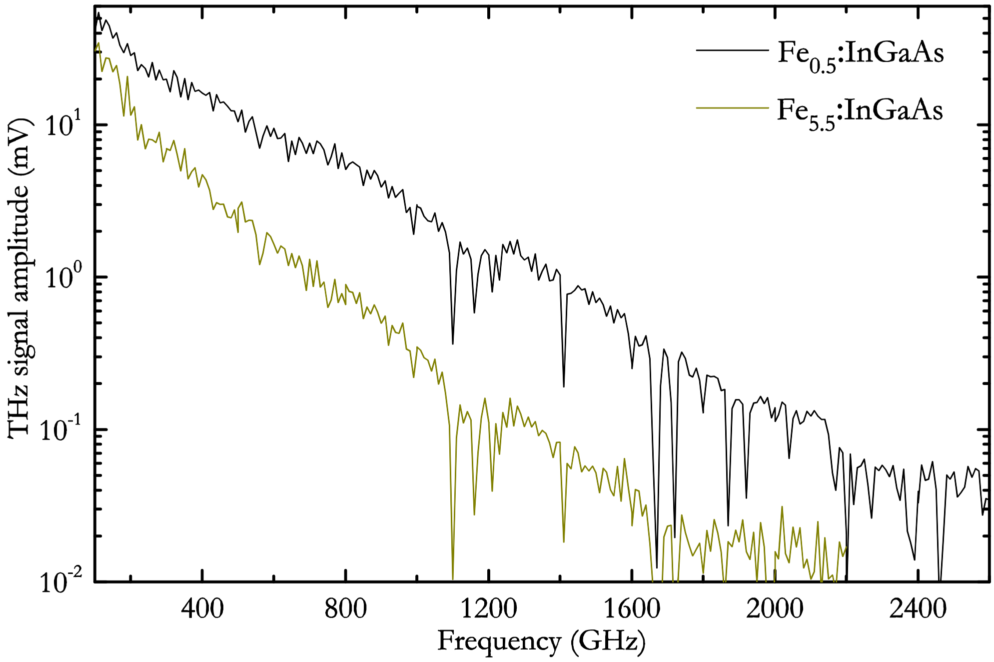

Figure 4.18: THz signal amplitude as a function of heterodyne frequency for Fe:InGaAs with different doping concentrations.

For THz emission measurements, all the emitters were biased using square pulses of 1 V amplitude at a frequency of 7.6 kHz. A constant laser power of ~10 mW was applied to each emitter, and the detector illumination was kept at a constant power of 13 mW. Similarly to the procedure used for characterisation of the TOPTICA emitters, the lasers were scanned between 100 GHz and 2600 GHz, with a 10 GHz step size, and the delay was scanned at each frequency step.

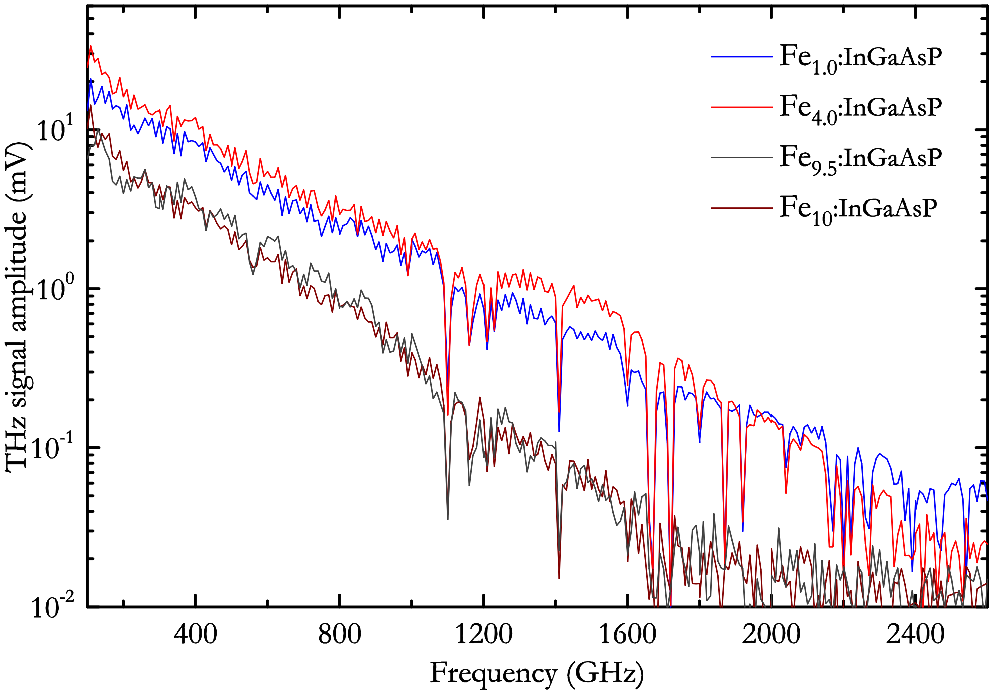

Figure 4.19: THz signal amplitude as a function of heterodyne frequency for Fe:InGaAsP with different doping concentrations.

The emission measured as a function of frequency is shown in Figure 4.18 for the two Fe:InGaAs wafers. In the case of Fe:InGaAs, the emission bandwidths of the emitters were found to decrease with increasing doping over the doping range studied here. The measured bandwidth was ~2.4 THz and ~2.0 THz for the two Fe:InGaAs wafers with 0.5×10^{16} cm^{-3} and 5.5×10^{16} cm^{-3} doping, respectively. This improved performance of the lower doped wafers can be attributed to the better carrier mobility compared to the higher doped wafers. Increasing the Fe doping is expected to cause higher carrier scattering, reducing the carrier mobility. This can result in increased trapping of charge carriers by the deep Fe acceptors, leading to the observed decrease in THz signal amplitude with increased Fe doping concentration. While there will be some benefit from having a reduced carrier lifetime, expected in the more highly doped samples, this appears not to be a dominant factor. Unfortunately, attempts to measure the mobility by Hall bar measurements were not successful, probably because of the presence of magnetic Fe ions in the sample. The carrier mobility of the InGaAs wafers reported in previous works were in the range ~400–1000 cm^{2}V^{-1}s^{-1} [108, 141].

The data obtained for the four Fe:InGaAsP wafers are plotted in Figure 4.19. The detectable signal bandwidth decreased from ~2.4 THz to ~2.0 THz for an increase in Fe doping from 1.0×10^{16} cm^{-3} to 10.0×10^{16} cm^{-3}. The THz signal amplitude was found to be highest for the 4.0×10^{16} cm^{-3} doping concentration, although the level was similar to that obtained for the lowest doping device (1.0×10^{16} cm^{-3}). The improved performance from the lower doped wafers could again be due to higher carrier mobility, as discussed above. It should also be noted that the polarization of the radiation emitted from the log-spiral antenna is circular for the lower emission frequencies and becomes linear for the higher frequencies [130]. Since the coherent receiver used, TOPTICA, detects linearly polarized THz radiation (according to the datasheet provided by the company), the detected signal at lower frequencies may by slightly lower compared to actual emitted signal strength. Since the measurement parameters are left unchanged, this difference will be the same for all devices and is thus ignored.

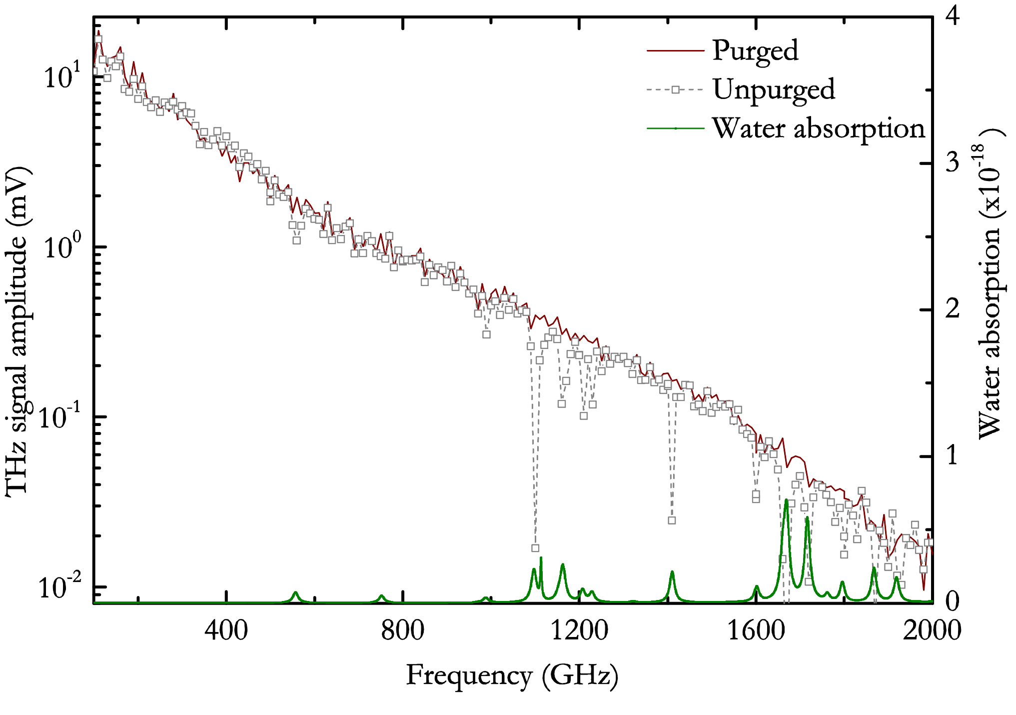

Figure 4.20: THz signal amplitude as a function of heterodyne frequency for Fe:InGaAsP with 10.0×10^{16} cm^{-3} doping with the system purged and non-purged.

The sharp absorption features observed in the emission spectra at 1.11 THz, 1.4 THz, 1.6 THz and 2.2 THz correspond to atmospheric water absorption, as a result of the experiments being carried out in a non-purged environment. The water absorption features from the HITRAN database fit well with the measured laser beat frequency. Also, when the emitter was measured under a nitrogen purged environment, with the humidity <10%, the sharp dips disappeared, confirming that the dips were indeed due to the water absorption. Figure 4.20 shows the THz signal amplitude measured from the Fe:InGaAsP wafer with 10.0×10^{16} cm^{-3} doping concentration in both purged and non-purged environments.

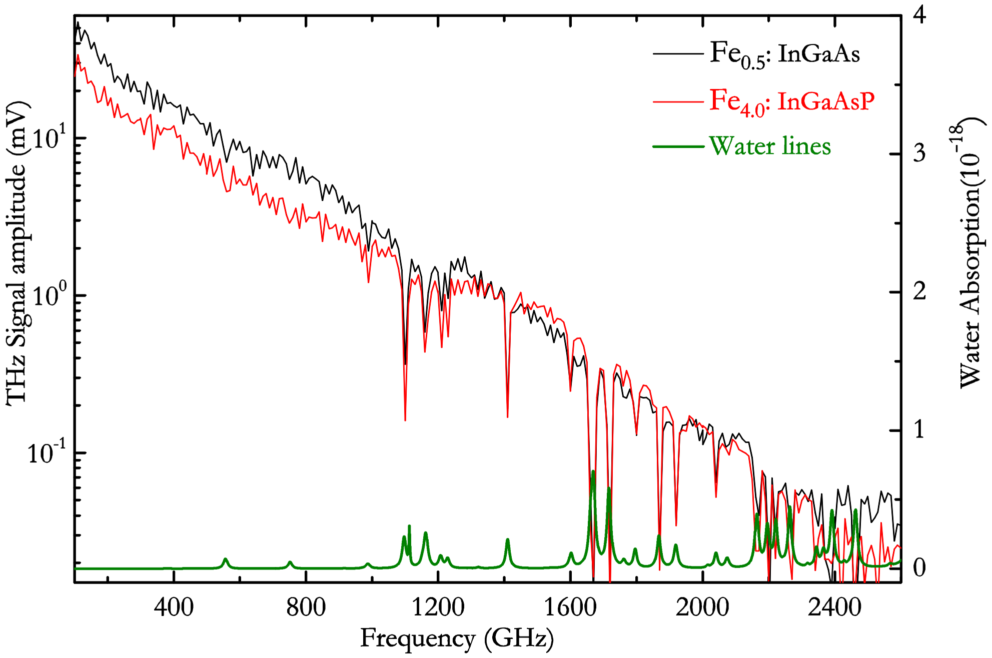

Figure 4.21: THz signal amplitude as a function of heterodyne frequency for the best performed Fe:InGaAs and Fe:InGaAsP wafer.

Figure 4.21 compares the THz signal amplitude measured as a function of frequency for the best performing Fe:InGaAs and Fe:InGaAsP wafers. As can be seen, the Fe:InGaAs wafers slightly outperformed the Fe:InGaAsP wafers in terms of emitted THz power at lower frequencies. This improvement is due to the bandgap difference. From the PL data, the Fe:InGaAsP wafer had an emission peak at 1540 nm, confirming the higher density of states. The wavelength of the excitation lasers used in the study was 1534 nm for the fixed laser and 1534 –1564 nm for the tunable laser. Since the wavelength of the tunable laser corresponds to the falling edge of the PL data, the absorption at this wavelength range will be smaller. On the other hand, Fe:InGaAs had the PL peak at ~1600 nm, with the absorption starting at ~1400 nm. The wavelength range in which the study is focussed is therefore more strongly absorbed, due to the higher density of states. This difference in the absorption at the excitation wavelength results in the observed difference in emitted THz power.

4.7.3 Carrier lifetime and output power roll-off

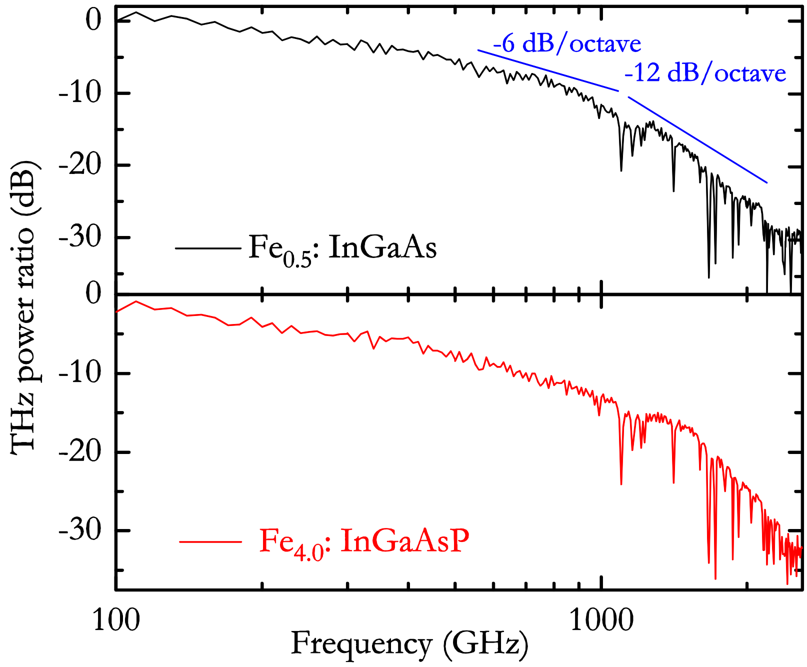

Figure 4.22: THz power as a function of heterodyne frequency for Fe:InGaAs and Fe:InGaAsP wafers with (top) 0.5×10^{16} cm^{-3} and (bottom) 4.0×10^{16} cm^{-3} Fe doping concentrations.

Figure 4.22 shows the roll-off in output power P_{THz} with frequency for the best performing Fe:InGaAs and Fe:InGaAsP devices. This roll-off is calculated by normalizing the THz signal amplitude at the lowest frequency (100 GHz) followed by the power conversion to the logarithmic scale. As can be seen, the THz power spanned over 30 dB in the 100 GHz to 2600 GHz range. This is higher compared to previously reported works on LT-GaAs wafers, due to the comparatively superior performance of our devices at high frequencies. The roll-off is dominated by the carrier lifetime τ_c and the capacitance of the active region, C_A, as described by Eq 4.1, and can be used to estimate the value of τ.

$$P_{THz}(\omega) = \frac{1}{2}\frac{V_b^2 G_o^2}{[1+(\omega\tau_c)^2]}\frac{R_A}{[1+(\omega R_A C_A)^2]} \tag{4.1}$$

The log-spiral antenna has radiation resistance of $R_A = 72\ \Omega$ [119], and the capacitance of the IDT fingers calculated from ref [131] is $C_A = 2.5$ fF. V_b is the applied bias to the emitter and G_0 is the dark conductance of the semiconductor. From Eq.(4.1), owing to the carrier lifetime and RC time constant of the antenna, the THz power is expected to exhibit a -12 dB/octave roll-off at high frequencies. Both Fe:InGaAs and Fe:InGaAsP emitters have a -6 dB/octave roll-off below 1100 GHz, caused predominantly by the carrier lifetime. Due to the extra contribution of the RC time constant of the antenna, roll-off increased to -12 dB/octave above 1100 GHz. From the RC constant, the calculated 3 dB roll-off frequency is 880 GHz, which is consistent with the experimentally observed roll-off [170].

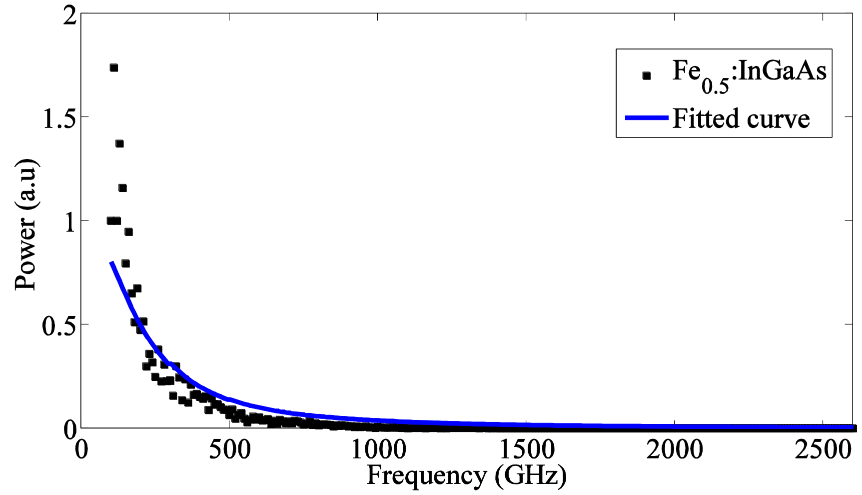

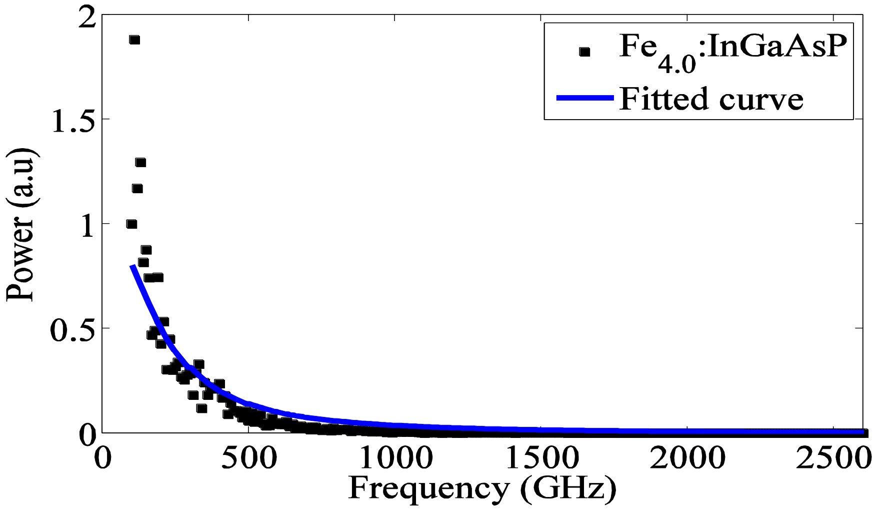

Figure 4.23: THz power as a function of beat frequency for the $Fe_{0.5}$:InGaAs (top) and $Fe_{4.0}$:InGaAsP (bottom) emitters. Black dots and blue curve represent experimental data and curve fit, respectively.

A least square curve fitting was performed in Matlab using the THz power (arbitrary units) and frequency to estimate the carrier lifetime. A curve was fitted to the measured power values using Eq.(4.1), leaving only the carrier lifetime, τ_c a variable term. The fit was performed on the best performed Fe:InGaAs and Fe:InGaAsP wafers. The carrier lifetime was estimated to be ~700–800 fs from fitting the experimental data, as shown in Figure 4.23, for both wafers. Although this method doesn't give the exact value of carrier lifetime, it can provide a good approximation with errors of the order of ±50 fs.

It is interesting to note that the short carrier lifetimes measured for these wafers are inconsistent with the large DC photocurrent measured, shown in section 4.7.1. In the present study, for the optical power (10 mW) used and the active area dimension of 11.3 μm×11.3 μm, one would expect a significantly lower photocurrent (few μA, according to Ohm's law). This could be due to an underestimate of the emitted THz power at lower frequencies (<500 GHz), due to poorer diffraction-limited coupling to the detector, resulting in an underestimation of the carrier lifetime. However, it is impossible to identify a single carrier lifetime that can explain both the photocurrent and the measured THz power at high frequencies, see Eq.(4.1). This apparent discrepancy can be resolved, however, by the presence of two different carrier lifetimes in the material, 'biexponential' lifetime. This sort of biexponential lifetime has been previously observed in pump-probe experiments on similar material, ErAs:InGaAs [180]. The existence of a finite number of trapping centres, which is significantly lower than the number of photocarriers, can result in a significant proportion of photocarriers with a longer lifetime (hundreds of ps). The longer lifetime carriers cannot contribute significantly to THz emission, however, can contribute to the photocurrent.

4.7.4 THz power

The THz power from the emitters was measured by calibrating the experimental arrangement with a helium-cooled germanium bolometer. In order to facilitate that, the power from the commercial emitter, TOPTICA is measured using the bolometer, as mentioned in Section 3.7. The commercial emitter TOPTICA is then characterized in the same two parabolic mirror experimental setup using TOPTICA receiver measuring the THz signal amplitude from 100 GHz to 2600 GHz. The emitted THz signal amplitude from the in-house, Fe:InGaAs and Fe:InGaAsP, emitters is compared to the TOPTICA THz signal amplitude and is then calibrated to calculate the THz power.

We estimate the power from the low doped (0.5×10^{16} cm^{-3}) Fe:InGaAs emitter to be 45 nW at 1 THz, and 6 nW at 2 THz. Similarly, for the Fe:InGaAsP emitter with doping 4.0×10^{16} cm^{-3}, the powers were 30 nW and 6 nW at 1 THz and 2 THz, respectively. Measuring the power from the emitters directly using the bolometer was not possible since the silicon lens was transparent to 1550 nm, due its higher bandgap. As a result, the 1550 nm detected by the bolometer resulted in added noise to the system. These powers are higher than the previously reported 10 nW at 1 THz obtained from an InGaAs emitter with interdigitated fingers [166].

4.7.5 Dependence on polarization

While characterizing the TOPTICA emitter, the polarization of the incident laser beam was left unchanged. As discussed in Section 4.6, the polarization of the incident laser beam has to be adjusted due to the slight misalignment arising while mounting the in-house devices. The dependence of polarization of the laser beam on the emitted THz radiation is pronounced if the distance from the metal electrodes is <10 μm and absent beyond this, was shown by Huggard *et al.* [181], in a THz-TD system. A horizontal beam with polarization direction perpendicular to the electric field direction between the two electrodes was found to provide the best performance [181]. As such, while aligning our emitters, the direction of the HWP was rotated to obtain the peak value in THz amplitude. The HWP was rotated at a 10° step size, causing a rotation of laser polarisation by 20°. The delay was scanned for each polarization step.

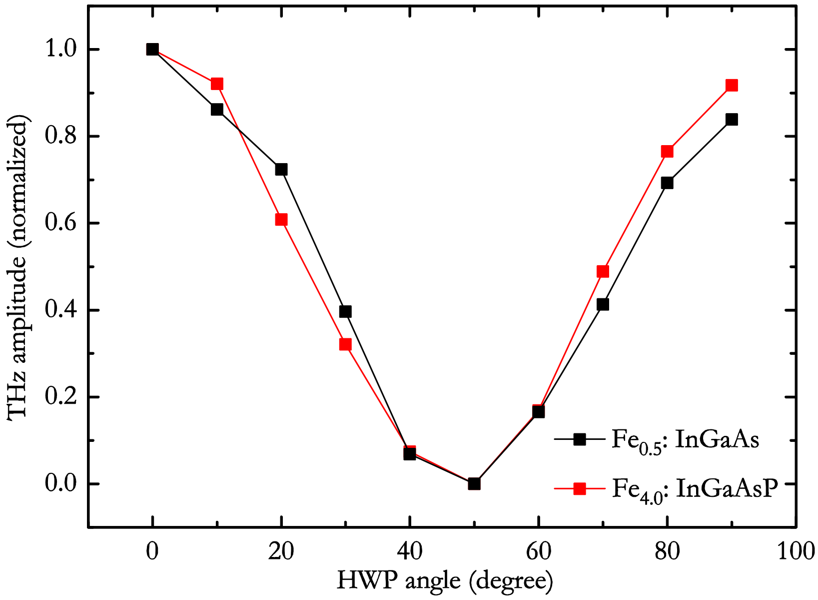

Figure 4.24: Normalized THz amplitude as a function of HWP rotation angle at 500 GHz for $Fe_{0.5}$:InGaAs and $Fe_{4.0}$:InGaAsP.

Figure 4.24 shows the THz signal amplitude as a function of the polarization of the incident laser beam at a laser beat frequency 500 GHz, measured for both the $Fe_{0.5}$:InGaAs and $Fe_{4.0}$:InGaAsP devices. In this Figure 4.24, the HWP rotation angle of 0° corresponds to the polarization of the laser beam perpendicular to the IDTs. A HWP rotation angle of 45° corresponds to a polarisation angle of 90° and thus parallel to the IDTs, as illustrated in Figure 4.25.

The THz signal amplitude decreased from the maximum to the minimum value when the HWP was rotated by 45°, changing the polarization by 90°. The THz signal amplitude changed more than 50% when the incident beam polarization was changed from horizontal to vertical direction (with respect to the IDTs). A similar trend was observed for all the wafers. The reason for this phenomenon could be due to the better absorption of the incident laser beam at perpendicular polarizations due to a resonance of the optical radiation in the substrate, as explained in ref [182]. This change in the absorption at a metal-semiconductor-metal interface at different polarizations has previously been studied on a SI-GaAs substrate [182].

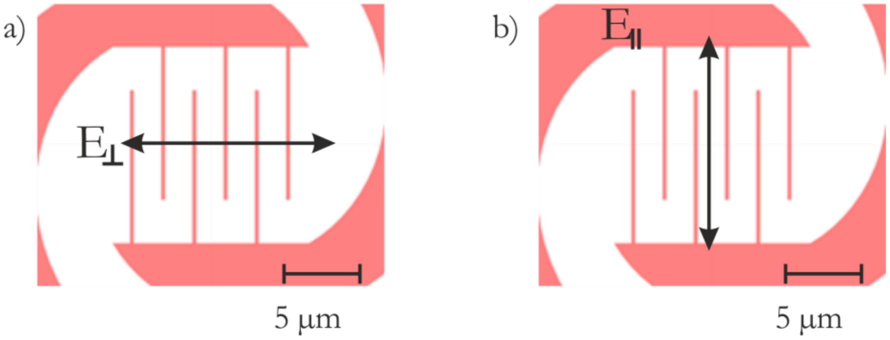

Figure 4.25: Schematic diagram of the polarization direction of the incident optical field, (a) corresponds to the perpendicular electric field (0° in the HWP), (b) corresponds to the parallel electric field (45° in the HWP)

4.7.6 Dependence on electrical bias

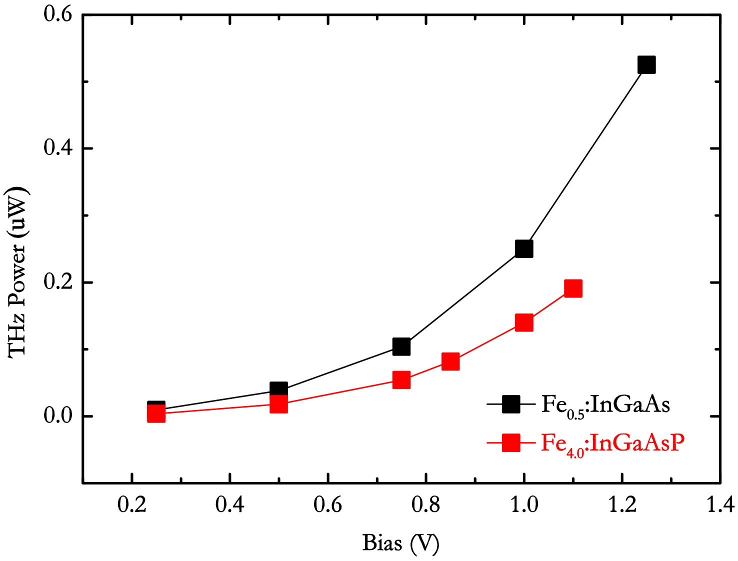

Figure 4.26: THz power as a function of bias at 500 GHz for $Fe_{0.5}$:InGaAs and $Fe_{4.0}$:InGaAsP

While discussing the photomixing theory in Chapter 3, it was mentioned that the emitted THz power has a dependence on the applied bias, Eq. (3.14). THz power increases quadratically with applied bias and is limited only by the potential device breakdown. In this section, a brief attempt is made to study the bias dependence of the Fe:InGaAs and Fe:InGaAsP photomixers.

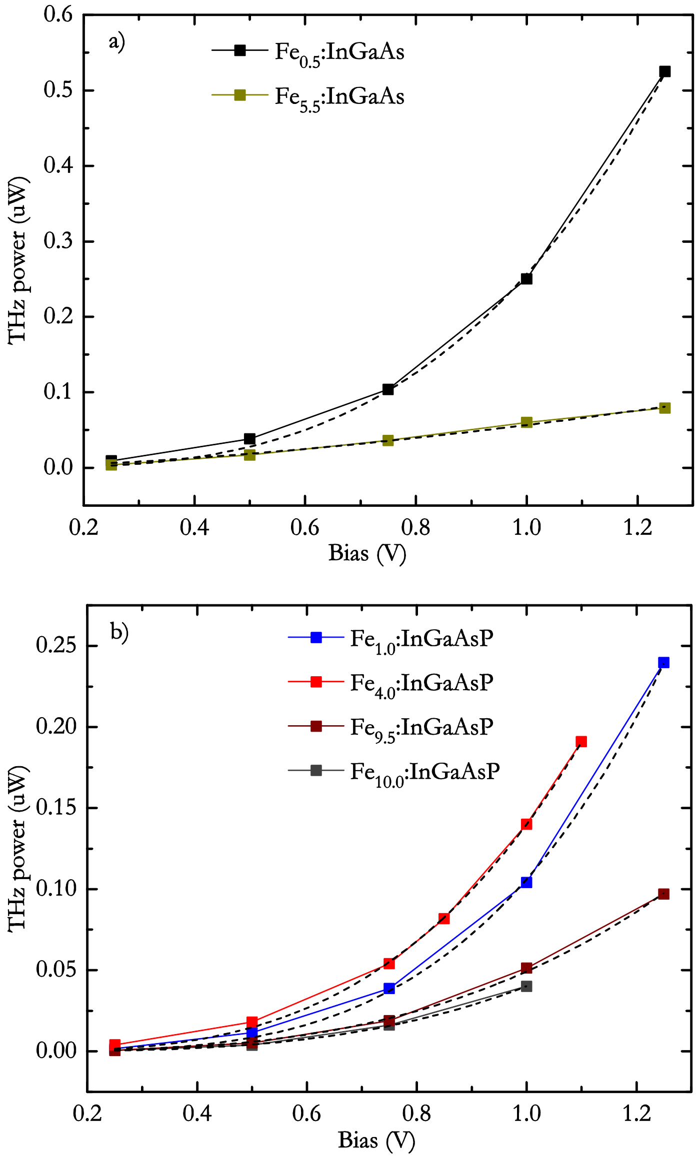

Figure 4.27: THz power as a function of bias at 500 GHz for the (a) Fe:InGaAs and (b) Fe:InGaAsP wafers with different Fe doping concentration. Lines are guides to the eye. Black dotted lines represents fitting to $P=aV^b$.

For the bias dependence studies, the best performing Fe:InGaAs and Fe:InGaAsP wafers with doping concentration of 0.5×10^{16} cm^{-3} and 4.0×10^{16} cm^{-3} respectively were chosen. A constant laser power of 10 mW and a 500 GHz beat frequency was used. Square pulses with amplitudes ranging from 0.25 V to 1.25 V at 7.6 kHz frequency were applied to both emitters. At each bias the measured THz amplitude was converted to THz power by comparing it with a calibrated device.

Figure 4.26 shows the emitted THz power as a function of bias for the best performing Fe:InGaAs and Fe:InGaAsP wafers. As can be seen from the graph, the emitted THz power increased as a function of V_{bias}^3 for both emitters. No saturation of the THz signal was observed, suggesting that the carrier lifetime does not change significantly in this bias range. A dependence of $P_{\text{THz}} \propto V_{\text{bias}}^2$ was reported by Brown *et al.* [116], however it is quite usual to have more than quadratic or superquartic dependence at high bias.

Figure 4.27 shows the THz power measured as a function of bias for all the different Fe:InGaAs and Fe:InGaAsP wafers. The dependence on bias is calculated by fitting a curve of the form $P = aV^b$ for all the wafers (black dotted line in the Figure 4.27). The values of the fitting co-efficient obtained are given in Table 4.2. The dependence was ~ V^3 for the low doped Fe:InGaAs wafer. In the case of the higher doped Fe:InGaAs wafer (Fe doping concentration of 5.5×10^{16} cm^{-3}), the dependence was different. In this case, the dependence with bias was slightly lower than quadratic (b=1.6) and this could be due to the carriers getting trapped by Fe acceptors before reaching the electrodes, thus not contributing to THz emission. THz power showed saturation behaviour, which was later found to be due to breakdown occurring at the tip of the electrodes. The device was damaged due to thermal breakdown from high currents (this device had the lowest device resistivity).

Wafer type	Fe doping concentration (cm^{-3})	Fit co-efficient, a	Fit co-efficient, b
Fe:InGaAs	0.5×10^{16}	0.256	3.19
Fe:InGaAs	5.5×10^{16}	0.056	1.60
Fe:InGaAsP	1.0×10^{16}	0.106	3.63
Fe:InGaAsP	4.0×10^{16}	0.139	3.24
Fe:InGaAsP	9.5×10^{16}	0.049	3.06
Fe:InGaAsP	10.0×10^{16}	0.040	3.25

Table 4.2: Fe:InGaAs and Fe:InGaAsP wafers with the respective Fe doping concentration and the fitting parameter values, a and b obtained from curve fitting the equation, $P=aV^b$.

For Fe:InGaAsP, the same trend was observed for the 1.0×10^{16} cm^{-3}, 4.0×10^{16} cm^{-3}, 9.5×10^{16} cm^{-3} and 10×10^{16} cm^{-3} Fe doping concentration, i.e. THz power varied as a function of V^3. The dependence with bias was b=3.63 for the lowest doped, 1.0×10^{16} cm^{-3}, however it reduced to ~3.06 for the 9.5×10^{16} cm^{-3}. The dependence was increased to ~3.25 for the highest doping, 10.0×10^{16} cm^{-3}. Similarly to Fe:InGaAs, this could be due to the trapping of charge carriers by deep Fe acceptors. No clear dependence with fitting parameter, b and Fe doping could be obtained.

The THz power increased as a function of V^3 for emitters as the 7.6 kHz square pulses were increased to a 1.25 V peak, except for the high doped Fe:InGaAs wafer. No saturation of the THz signal was observed (for the low doped Fe:InGaAs and all four Fe:InGaAsP wafers), suggesting that the carrier lifetime does not change in this bias range. When the bias was increased beyond 1.25 V, corresponding to an applied field in the gap of ~7.8 kVcm^{-1}, the interdigitated fingers of the devices were damaged along with the inner arm of the spiral, as shown in Figure 4.28. This damage is thought to be caused by thermal breakdown, since it is below the measured dielectric breakdown field of ~12.5 kVcm^{-1}. These breakdown fields are significantly lower than the field that can be applied to similar LT-GaAs devices, owing to the lower resistivities of InGaAs and InGaAsP. It is thus ideal to have substrates and active region designs which can withstand high currents.

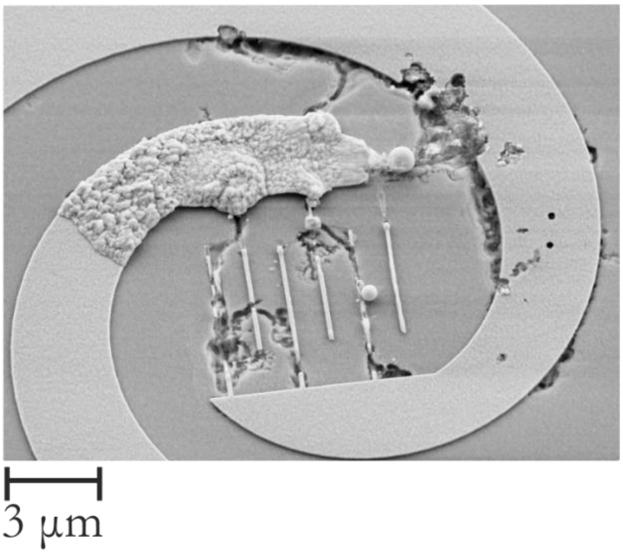

Figure 4.28: SEM image of the Fe:InGaAsP device with 1×10^{16} cm^{-3} Fe doping concentration. The sample was damaged due to excess bias. The bias level applied to this particular device was 2 V.

4.7.7 Dependence on optical power

Another contributing factor that can improve the emitted THz power from a photomixer is by increasing the incident optical power. According to Eq. (3.14), emitter power increases quadratically [166] with optical power. Similar to electrical breakdown occurring at higher biases, there can be device breakdown due to high optical powers causing heating effects. In this section, the THz power dependence on optical power is studied for both Fe:InGaAs and Fe:InGaAsP wafers.

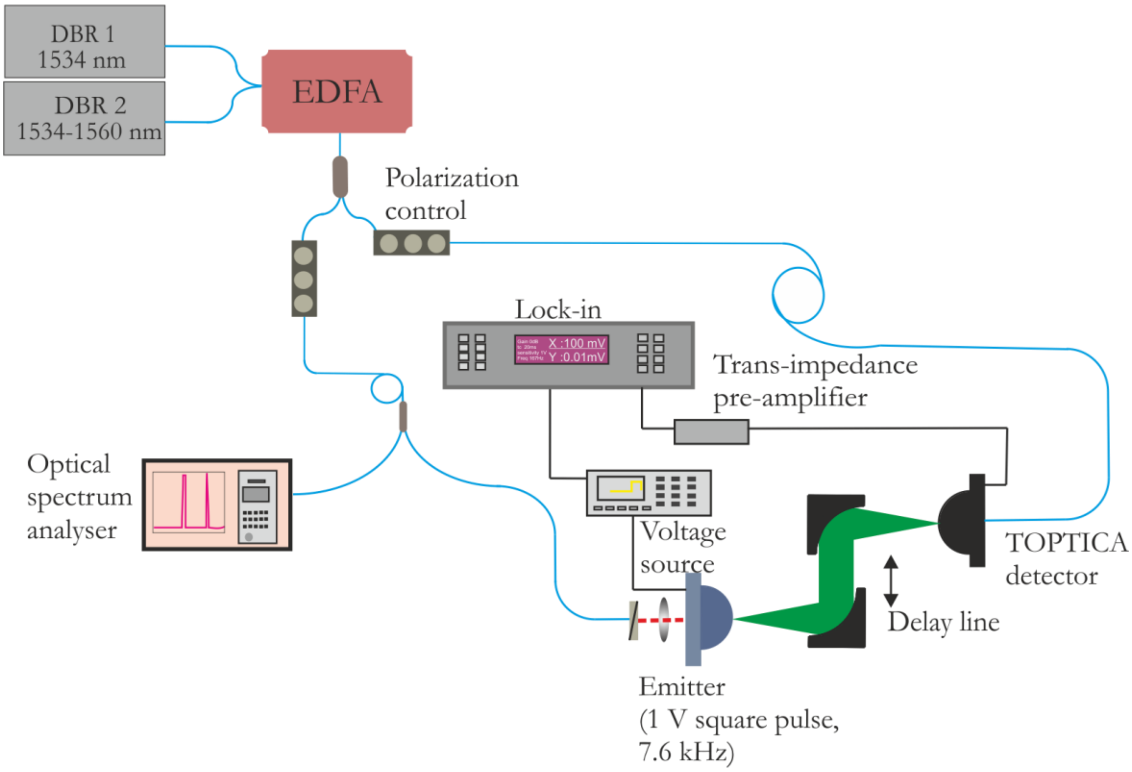

Figure 4.29: Experimental setup used for optical power dependence measurement

The dependence of the emitted THz power on the incident optical power is studied. The experimental setup used is as shown in Figure 4.29. To increase the optical power, an erbium doped fibre amplifier (EDFA) was used. The output from the EDFA was split using a 2×2 splitter, and fed to both the emitter and receiver. The fibres responsible for the gain amplification in the EDFA were found to be non-polarization maintaining and in order to compensate for that, two Thorlabs manual fibre polarization controllers (PC) were used. The paddles on the polarization controllers can be rotated giving independent polarization control on both arms. The three paddles on the PC consisted of a quarter wave plate, a HWP and a quarter wave plate in the order of arrangement; this gives a higher degree of freedom which isn't accessible using a single HWP. Increasing the gain of the EDFA can increase the power on the two output arms, which is not desired. To avoid this, the output power from the EDFA was kept at a constant value (P_{out}=20.90 dBm) yielding an optical power of ~40 mW on each arm (measured using a Thorlabs fibre power meter after the splitter). The difference in the set power of the EDFA and the measured power is due to the various losses, including insertion loss, coupling loss and splitter loss (since fibre splitters can be wavelength dependent).

An optical attenuator with fixed attenuation (~5 dB) was also used on the detector arm, giving a constant output power of ~13 mW. The power to the emitter was then controlled by using a free-space adjustable attenuator. The THz amplitude was measured at different optical powers supplied to the emitter, ranging from 5 mW to 20 mW at a laser beat frequency of 500 GHz. The two best performing Fe:InGaAs and Fe:InGaAsP devices, with doping concentrations 0.5×10^{16} cm^{-3} and 4.0×10^{16} cm^{-3}, respectively, were chosen for the study. The emitters were biased using square pulses of 1 V amplitude at 7.6 kHz frequency, and the measured THz amplitude was converted to THz power by comparing it with a calibrated device.

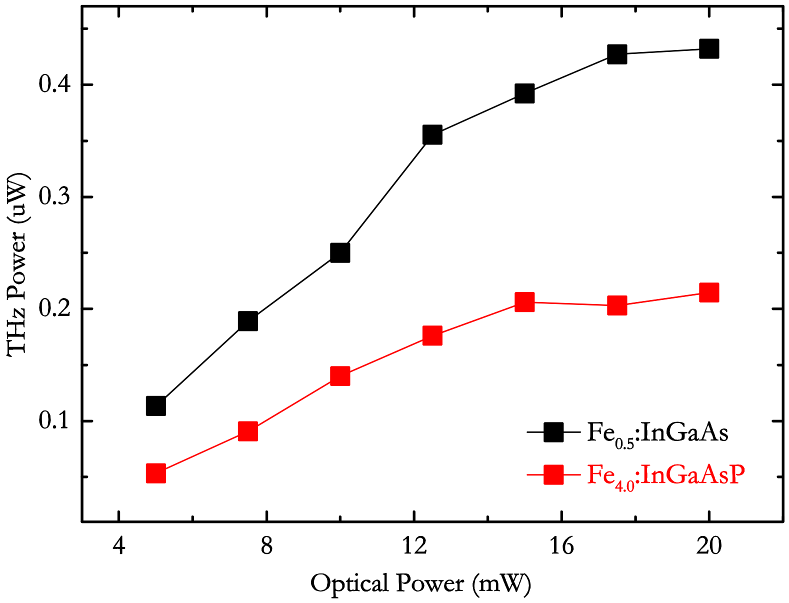

Figure 4.30: THz power as a function of optical power at 500 GHz for $Fe_{0.5}$:InGaAs and $Fe_{4.0}$:InGaAsP.

The THz power measured as function of optical power for both the Fe:InGaAs and Fe:InGaAsP device is plotted in Figure 4.30. As can be seen, THz power varies approximately linearly with optical power in the 5 mW to 12 mW range for both wafers. This linear relationship is due to the increase in the number of photo-generated carriers with increase in optical power. As the optical power is increased above 15 mW, a saturation effect is evident for both wafers. This saturation effect can be attributed to screening of the applied bias by the photo-generated carriers. Due to the high density of photocarriers at high optical powers, accumulation of charge carriers can occur near the contact electrodes, which can generate a space charge region, thus creating an electric field that screens the applied bias. As a result, the high density of photocarriers generated cannot all contribute to the emitted THz power. In addition, a quadratic dependence with the optical power was not observed at lower optical powers (5 mW), unlike the previous reported photomixer studies on InGaAs [166]. We attribute this effect due to the wafer not operating in the small signal limit even at smaller optical power levels. Another probable reason could be the low mobility of the carriers, since the scattering of the carriers can result in reduction of the carrier mobility [165].

4.8 Comparison with the THz-TDS data

The same wafers studied in this chapter were initially tested as photoconductive switches using a (pulsed) THz-TD system [109, 168, 178]. Photoconductive emitters with 300 μm gaps were fabricated on Fe:InGaAs wafers with Fe doping concentrations in the range between 4×10^{16} cm^{-3} and 5×10^{18} cm^{-3}. A range of wavelengths were used to excite the emitter, between 830 nm and 1550 nm, and most powerful emission was obtained when excited at 1550 nm. The bandwidth obtained was > 2.5 THz.

In the pulsed system, the low-doped wafers performed better compared to high-doped wafers - consistent with the CW measurements. As explained above, this is due to the lesser compensation in these wafers. However, no differences in bandwidth were observed between differently doped wafers in the pulsed measurements. This is because the pulsed bandwidth is dictated by the pulse duration, which is not the case for CW measurements, the bandwidth of the low-doped wafer (0.5×10^{16} cm^{-3}) was 2.4 THz compared to the 2.0 THz for the high-doped wafer (5.5×10^{16} cm^{-3}).

A combination of several factors is responsible for the difference in the pulsed and CW operation:

a) detector responsivity; the detector used in the CW measurement has its own characteristic roll-off limiting the detected signal

b) signal-to-noise ratio (SNR); the signal emitted could be below the noise level in the CW system since there is noise associated with laser jitter, unlike pulsed systems, where the signal is measured only when a probe pulse is present reducing the background noise.

No saturation of the emitted THz power was observed at an incident optical power of 100 mW in the pulsed system, whereas the emitter saturated when the laser power was increased beyond 15 mW in CW. This can be explained by the fact that a CW laser power of 15 mW incident on a 1.6 μm gap can produce an irradiance 30 times higher than 100 mW laser power on a 300 μm gap. This huge difference in the irradiance due to the different antenna design resulted in saturation.

Fe:InGaAsP wafers with different Fe doping concentrations ranging between 1×10^{16} cm^{-3} and 1.5×10^{17} cm^{-3} were also studied. The emitters were excited at a range of wavelengths from 1150 nm to 1550 nm, and peak THz power was obtained at 1250 nm. When excited at 1550 nm, Fe:InGaAsP with 7.0×10^{16} cm^{-3} Fe doping concentration performed better, in terms of emitted power. The measurable bandwidth was 2.5 THz at 1550 nm excitation and 3.5 THz at 800 nm excitation, and no dependence with doping was observed. Similar to Fe:InGaAs, a quadratic dependence with applied bias and incident optical power was reported and there was no saturation observed for the Fe:InGaAsP wafers, up to an incident optical power of 100 mW.

The emission characteristics of the Fe:InGaAsP wafers observed in the pulsed system is in agreement with the CW emission in terms of emitted power, with low-doped wafers performing better compared to high-doped wafers. However, there is slight disparity in the power levels obtained from the different Fe doping. In CW measurements, 1.0×10^{16} cm^{-3} and 4.0×10^{16} cm^{-3} performed much better than the higher doped 9.5×10^{16} cm^{-3} and 10.0×10^{16} cm^{-3}, whereas in pulsed 9.5×10^{16} cm^{-3} was found to have better THz power levels. This discrepancy is associated with the difference in the generation mechanisms for pulsed and CW excitation. When the photoconductive switch is excited with the laser pulse, the transient current generated due to the sudden acceleration and deceleration of the charge carriers is related to the conductivity of the substrate. Whereas, in the CW system, the modulation in the generation of carriers is transformed into conductance modulation which is coupled out as THz radiation.

Similar to the Fe:InGaAs wafers, the change in bandwidth associated with the CW measurement is due to the carrier lifetime, detector responsivity and poor SNR. Also the saturation obtained with high incident optical power in the CW measurements is associated with the difference in the design and irradiance levels.

When excited using 1550 nm femtosecond pulses, Fe:InGaAsP performed better than Fe:InGaAs. However, Fe:InGaAs outperformed Fe:InGaAsP with 1550 nm CW laser excitation.

4.9 Discussions and conclusions

In this chapter, two different materials, Fe:InGaAs and Fe:InGaAsP have been studied for CW THz generation by photomixing at 1550 nm. Two materials were grown by MOCVD on InP substrates. The Fe atoms create deep acceptors in the bandgap thus acting as a midgap level which can trap the carriers before reaching the contact electrodes, thereby increasing the resistivity. The alloy compositions were chosen to give a bandgap of ~1550 nm for both InGaAs and InGaAsP. The bandgap of the wafers was characterised using a PL setup. For Fe:InGaAs, it was found that the bandgap was ~1600 nm and for Fe:InGaAsP, it was around ~1540 nm. A 3-turn self-complementary logarithmic spiral with 11.3 μm×11.3 μm active region was chosen for the antenna design. The active region consisted of 3 pairs of 0.2 μm-wide fingers with a 1.6 μm gap and 8.3 μm length. The cap layers were first removed and the devices were fabricated on the active Fe doped layer using e-beam lithography, and mounted on a PCB board for testing. For characterization, two tunable 'C-band' lasers emitting at 1534 nm were used. One of the lasers was kept at fixed wavelength and other laser was tuned between 1534–1565 nm to give a frequency difference of 0–2600 GHz. The emitted THz radiation was detected using a coherent TOPTICA InGaAs receiver.

Two Fe:InGaAs and four Fe:InGaAsP wafers with different Fe doping concentration were studied. For Fe:InGaAs and Fe:InGaAsP, the lowest-doped wafer had the highest resistivity but lowest photo-resistance. Dark resistivity decreased with doping, whereas photo-resistance increased with doping, and is attributed to overcompensation of the wafers at higher doping levels. The bandwidth from Fe:InGaAs wafers with Fe doping concentration 0.5×10^{16} cm^{-3} and 5.5×10^{16} cm^{-3} was found to be ~2.4 THz and 2.0 THz, respectively. The lowest-doped wafer also outperformed the high-doped wafers in terms of THz power, ~45 nW at 1 THz from the low doped wafer, which is almost 10 times higher than the high doped wafer, for Fe:InGaAs. In the case of Fe:InGaAsP, the 4.0×10^{16} cm^{-3} wafer was found to outperform the higher-doped wafers. The low-doped wafers also had higher dark resistivity than the higher-doped wafers. The maximum bandwidth attained was ~2.4 THz from the two lowest-doped wafers and ~2.0 THz and ~1.9 THz from the 9.5×10^{16} cm^{-3} and 10.0×10^{16} cm^{-3} Fe doping respectively.

Due to the absorption differences at the excitation wavelength, the emitted THz power from the Fe:InGaAs wafers was better compared to the Fe:InGaAsP wafers. The THz power output from the emitters was found to exhibit a -12 dB/octave roll-off at higher frequencies, arising due to the RC time constant of the antenna and the carrier lifetime. The measured photocurrents from the wafers suggested the possibility of more than one carrier lifetime, possibly a biexponential lifetime.

Lower doped wafers out-performed higher doped wafers in both Fe:InGaAs and Fe:InGaAsP, when excited at 1550 nm due to increased mobility. The THz power dependence of the Fe:InGaAs and Fe:InGaAsP emitters was also characterised at different electrical biases and various optical powers. It was found that THz power had a V^3 dependence with bias and there was no saturation confirming that the lifetime didn't change. The THz power saturated when the applied optical power was increased beyond 15 mW. This saturation is explained by screening of the applied bias by the photo-generated carriers, which affects the mobility of the carriers.

The performances of the photomixers were also compared to photoconductive switches fabricated on the same wafers. The performance of the Fe:InGaAs wafers was found to be consistent with the THz-TD measurements, with low-doped wafers outperforming the high-doped wafers.

Chapter 5 Nanostructure emitters

This chapter is an analytical study of emitters with nanostructured electrodes for THz generation. The first section describes the advantages, fabrication and characterization of resonant dipole antennas. In the second section, a brief historical context of nanostructure emitters is described including the recent advances made in the field. The reasoning behind the adoption of two different nanostructure designs, single-sided nanostructure (SSN) and double-sided nanostructure (DSN) is discussed in the following section. The fabrication procedure is discussed followed by the characterization of the SSN and DSN emitters. The performance of SSN and DSN emitters is compared in terms of spectral bandwidth and power. The generated power of the emitters as a function of excitation position was mapped at different frequencies, polarizations, and bias directions in both photomixing and THz-TD systems. This chapter concludes with a discussion on the performance of the SSN and DSN emitters.

5.1 Introduction

Although IDT emitters are one of the most favoured designs in photomixing measurements [165, 166], the low obtainable power levels (~10 nW at 1 THz [166], ~45 nW from Fe:InGaAs emitter discussed in Chapter 4) limit their applications. The output power from the emitters can be increased by three methods: by increasing the power at a particular frequency using resonant antennas; overall enhancement at all frequencies by employing improved semiconductor substrates; or improved active region designs. The concept behind the first approach of using resonant antennas, is that it reduces the severe impedance mismatch between the photomixer-active region and antenna. In the second approach, a broad frequency enhancement in power is achieved using quality semiconductors with carrier lifetimes of the order of femtoseconds and broadband antennas. The third method also attain broad frequency enhancement using improvised active area designs. The second approach was already used and was discussed in detail in Chapter 4. In this work, since the goal is to achieve a high power CW THz source at 2 THz, the first and third methods are attempted and will be discussed in detail.

5.2 Resonant antenna

As mentioned in Chapter 3, the impedance of a photomixer has resistive and capacitive components arising from the photomixer active region. These include the IDTs and the antenna used. The radiation resistance of the broadband spiral antenna is ~72 Ω and the impedance of the active region (with IDTs) can be between 10–100 kΩ [183, 184]. With larger differences between the photomixer active region and antenna impedance, the output power scales with the radiation resistance of the antenna. One type of resonant antennas are dipole designs; these can be engineered to have high impedances at the target frequency, increasing the overall output power. These antennas have been widely used for applications including radio wave communications and television bands. The high directivity from these antennas is a contributing factor to this [54].

There has been several reports of using dipole antennas for CW THz radiation, Matsuura *et al.* [120] providing the reported instance. In this work centre feed dipole antennas of three different dipole lengths, 20 μm, 30 μm and 50 μm were fabricated on a LT-GaAs substrate. They obtained an order of magnitude increase in signal at 1 THz using the 50 μm dipole, when compared to a bow-tie antenna. The maximum attainable bandwidth was greater than 3 THz. However, the resonance peak was broad and there was a shift in the designed and measured resonance frequency. Gregory *et al.* [184] designed lower frequency dipole antennas for CW THz radiation (~400 GHz). By simulating end feed and centre feed dipole antennas, they observed good performance from the centre feed dipole at the fundamental and harmonic frequencies. Chokes were used on the biasing lines to prevent leakage of the THz current. The simulations were in agreement with the experimental results. An increase of 6.5 dB in power was obtained, compared to the spiral antenna.

Duffy *et al.* [183] performed electromagnetic simulations to maximize the power coupling between the IDTs and the antenna. By simulating single and dual dipole antennas with choke elements, they observed that the dual dipoles are superior, due to better beam shapes and higher radiation resistance. For this design, coplanar strip lines (CPS) connected the photomixer active region (IDTs) and the dual dipoles, thus tuning the electrode capacitance. Four different designs with resonance at 850 GHz, 1050 GHz, 1600 GHz and 2700 GHz were simulated and when fabricated on a LT-GaAs substrate, the experimental results were in agreement with simulations.

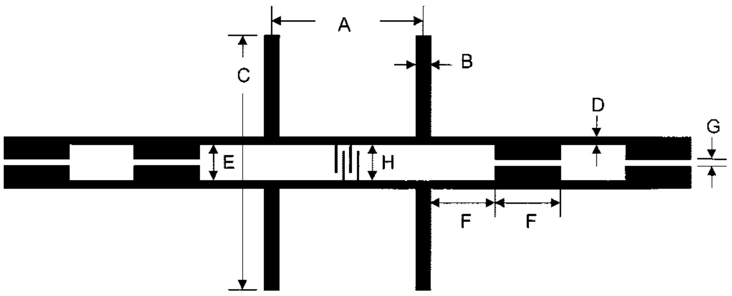

Name	A	B	C	D	E	F	G	H	N_f	w_f	w_g
D1	55.4	2.5	68.4	1.0	5.0	33.7	1.0	5.0	8	0.2	0.8
D2	46.7	2.5	54.6	1.0	5.0	27.7	1.0	5.0	8	0.2	0.8
D3	28.8	1.5	34.3	1.0	5.0	17.9	1.0	5.0	8	0.2	0.8
D4	20.0	1.0	20.7	1.0	4.0	10.6	1.0	4.0	6	0.2	0.8
S1									8	0.2	0.8

Figure 5.1: Schematic of the dual-dipole dual-slot antenna with the parameters marked. The dimension of the parameters for the 850 GHz (D1), 1050 GHz (D2), 1600 GHz (D3) and 2700 GHz (D4) designs are given in the table. Image reproduced from ref [183].

These promising results for a dipole emitter meant they could be utilized for various applications and an attempt was made to experimentally replicate the performance. In order to achieve this, the dual-dipole dual-slot antenna with IDT active region designs, discussed in Duffy *et al.* [183] were fabricated. Of the four different designs presented in the work, the 1050 GHz design was used in the 1550 nm CW photomixing system. Although the desired frequency to have enhanced output power is 2 THz (for integration with QCLs), initial trials at lower frequencies (1050 GHz) were performed due to the larger expected signals, according to Eq. (3.17) in Chapter 3. Figure 5.1 shows the schematic of the design fabricated in the work.

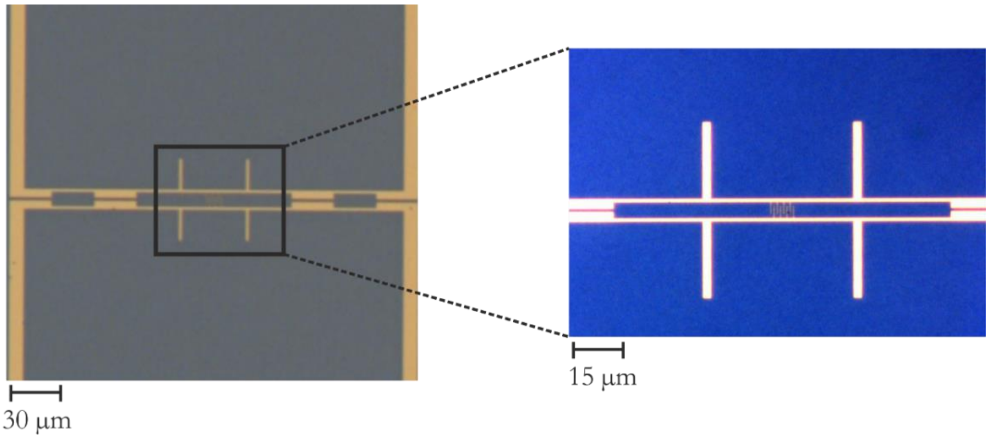

Figure 5.2: Optical images of the 1050 GHz dual-dipole resonant antenna fabricated on the Fe:InGaAsP wafer. A zoomed version of the active region with four pairs of IDT is shown on the right.

For this device, one of the best performing samples of Fe:InGaAsP with Fe doping concentration of 1.0×10^{16} cm^{-3} was chosen, due to the improved surface quality compared to Fe:InGaAs wafer. The fabrication steps, discussed in detail in Chapter 4, involved the removal of the cap layers, lithography, metallization and lift-off, while the dipole design was fabricated on an active Fe doped layer by e-beam lithography using the JEOL system. The emitters were mounted on a PCB. Figure 5.2 shows the 1050 GHz dipole design soon after fabrication on Fe:InGaAsP wafer. The dual-dipole dual-slot antenna had 4 pairs of IDTs in the middle. In order to apply bias to the emitter, contact lines were fabricated on the four corners of the dipole.

These devices were tested with the experimental setup discussed in Chapter 4. The beat frequency between the lasers was tuned between 100 GHz to 1200 GHz. The emitters were biased using square pulses of 0 to 1 V amplitude at a frequency of 7.6 kHz. A silicon lens was attached behind the substrate to collimate the THz radiation. Figure 5.3 shows the measured THz amplitude as a function of laser beat frequency. No visible resonance could be observed at the designed frequency. Also, no signal could be seen at the lower or higher harmonics. With the detector and gain of the trans-impedance amplifier fixed to the same value, the signal levels measured were low, compared to the 3-turn log-spiral antenna with 3 pairs of IDT emitters discussed in Chapter 4. The radiation emitted by the dipole antenna is linearly polarized. The TOPTICA receiver detects only linearly polarized radiation and in order to confirm whether the orientation was correct, the measurements were repeated for two orthogonal rotations of the receiver. For the two rotational positions, 0° and 90° no resonance could be observed. The poor performance could be due to the presence of contact lines as, along with the contact pads, this creates an additional impedance resulting in poor resonance from the design as shown in Figure 5.4.

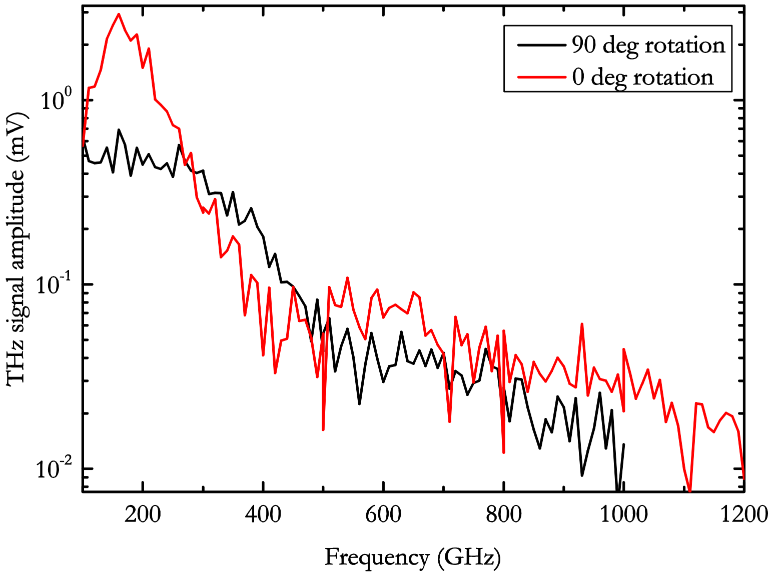

Figure 5.3: THz signal amplitude measured as a function of beat frequency between the lasers from the 1050 GHz dual-dipole antenna. Red and black line corresponds to the two different orientations of the receiver.

The poor performance of the dipole antennas, irrespective of the resonant frequency, made them a poor choice for this work. In order to solve this issue, a new emitter design was fabricated. This design had nanostructured electrodes on the active region of the photomixer and will be discussed in detail in the following section.

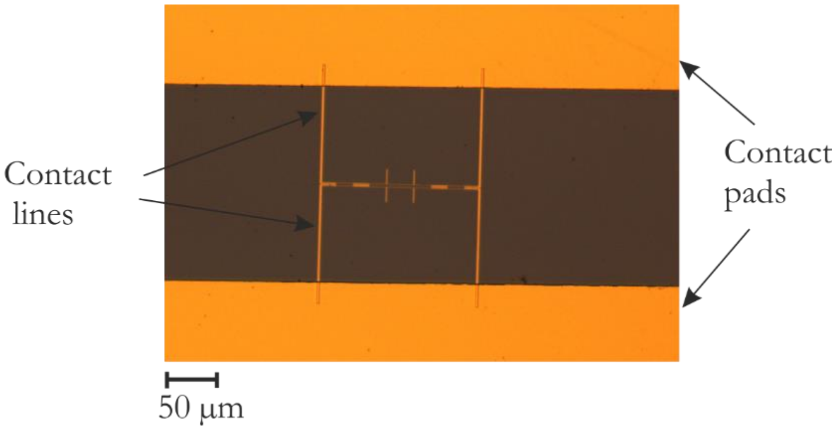

Figure 5.4: Optical images of the 1050 GHz dual-dipole resonant antenna fabricated on the Fe:InGaAsP wafer. The contacts lines and contact pads used for biasing the emitter are pointed out.

5.3 Nanostructure emitters

The term ‘nanostructure’ has been used to describe various aspects of emitter design. From previous works, it can be either that the active region has nanostructured (NS) electrodes separated with a wide gap [107, 185], or NS electrodes with nanometre gaps between them [171]. Both methods have been reported to emit high CW THz power from broadband antennas and CW powers of the order of milliwatts have been reported from the former group. Although improvements in terms of CW THz power have been reported, a complete understanding of the influence of the geometric layout over the emission characteristics has not been realised. The various aspects behind the emission and reasoning for high output power will be studied in this chapter with the goal of achieving high emitted power.

5.3.1 Historical overview

There have been several reports of an enhancement in measured THz power from photoconductive emitters by adopting new antenna designs. The initial reports were on THz-TD systems. Among the various reports, the first was ‘near anode enhancement’ reported by Krokel *et al.* [186]. A rise in the measured THz amplitude was reported when focusing the excitation beam near the anode and is attributed to the higher electric field strength [187]. Although this effect was mainly observed in large gap emitters (tens of μm), a dependence from small-gap emitter with gap ~5 μm was reported by Keil *et al.* [188]. This emission enhancement was further improved when sharp or pointed anode structures were implemented. This was due to a ‘singular electric field’ present at the anode tips [189]. There were no reported enhancement in the THz amplitude from CW photomixers with this mechanism, which could be due to the small gaps (<5 μm) in the IDT designs.

As discussed in Chapter 3 the carrier lifetime, τ of the material is a crucial factor in determining the photomixer’s performance. Ideally the carriers possess a short lifetime, (<500 fs in annealed LT-GaAs substrate [147]) the reason for which in this instance is that the generated carriers recombine faster, allowing them to contribute to THz generation, while avoiding heating effects. The requirement for a short carrier lifetime in a semiconductor implies stricter growth conditions, LT growth [114] or molecular beam epitaxy (MBE) [149], which can be costly. A solution to this problem is to reduce the spacing between the contact electrodes. This geometry reduces the number of photo-generated carriers by blocking the majority of the semiconductor surface.

It was Tanoto *et al.* who demonstrated an enhancement in CW emission, for the first time, by using a nano-electrode photomixer. The design was a nano-electrode (100 nm electrodes with 300 nm spacing) with a nano-gap active region design fabricated on a LT-GaAs substrate. A modified meander antenna was used, which is a dipole antenna with better impedance matching. The active region was approximately 5 μm×8 μm. They reported ~100 μW power at 300 GHz from nano-electrodes with nano-gap spacing emitter. An IDT emitter, when used with a similar inter-digitated spacing emitted 1000 times lower power. They attributed this enhancement in the power level from nano-gap emitters to the enhanced electric field occurring at the tip of the electrodes. By varying the nano-gap between the nano-electrodes in the range of 50 nm to 1000 nm, they obtained an enhancement of approximately 400 and 100 times respectively, compared to an IDT structure. The 'evanescent wave tunnelling in the sub-wavelength gap' between the electrodes, was given as the reason for enhanced output [171].

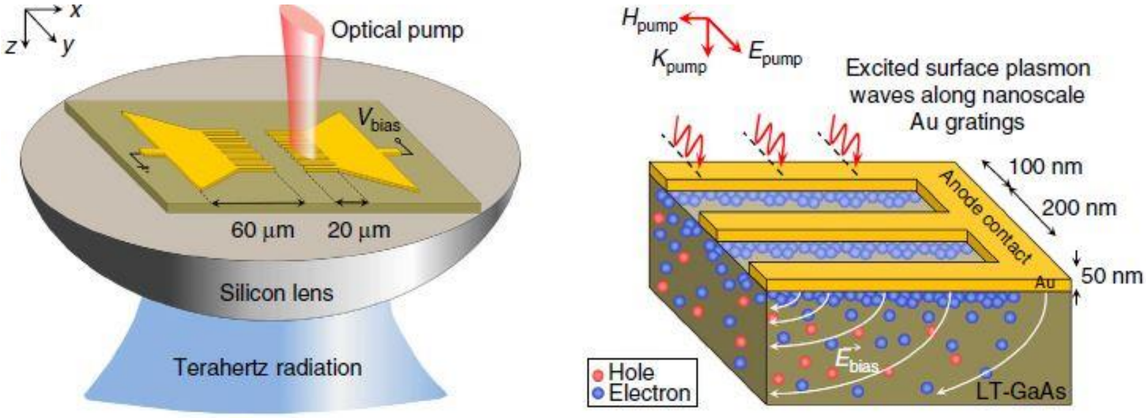

Figure 5.5: Schematic diagram showing the antenna on a silicon lens with laser exciting the NSG (left) and the photocarrier transport underneath the NSG electrodes (right). The p-polarized light coupled into the substrate generates surface plasmons underneath the NSG resulting in faster carrier recombination due to the reduced transport length. Image reproduced from ref [107].

However, a superior design than the nano-gap nano-electrode design was reported by Berry *et al.* [185]. Their approach for designing a high power emitter involved the concept of surface plasmons. They refer to their electrodes as nanostructure gratings (NSG). The NSG consisted of 100 nm electrodes, with a 200 nm period. It incorporates an anode and cathode, separated by a few micrometre gap and they reported enhanced pulsed and CW emission from the structures. The excitation of surface plasmons underneath the NSG causes a high concentration of generated photo carriers, refer Figure 5.5. These carriers thus had reduced transport path lengths, recombining quicker with the contact electrodes.

The research in the field of plasmonic NSG (dimensions remaining the same) performed by the same group in the field of THz-TD emitters and photomixing is discussed below.

The earliest example of using a plasmonic (NSG) was reported by the same group in 2012 [190] in THz-TD systems. They choose plasmonic NSG on both the anode and cathode electrodes, using a dipole antenna design. This was fabricated on $In_{0.53}Ga_{0.47}As$, grown on a layer of InAlAs and lattice matched to InP substrate. A central ground line was fabricated in the middle of the gap to collect the excess electrons which did not contribute to THz emission. The carriers generated within 100 nm of the substrate surface contributed to emission. The emitters were excited using 150 fs pulses at 925 nm wavelength. They reported 50 times more power compared to an emitter with a single photoconductive gap. Subsequently, they demonstrated photoconductive detection from plasmonic NSG based device and reported 30 times higher detection sensitivity [107]. They observed that the peak emission power was when the laser beam was focused on to the anode, as this generated a higher density of electrons with greater drift velocity (0.5×10^7 cms^{-1} from ref. [190]). The substrate used was LT-GaAs and was excited using 200 fs pulses of 800 nm wavelength. Using a 3×3 log-spiral antenna array with plasmonic NSG electrodes, they reported power levels as high as 1.9 mW in the 0.1–2 THz range from a LT-GaAs emitter [37]. Subsequently, the same group demonstrated power levels of 3.8 mW in the 0.1–5 THz range, from a large area emitter design on a LT-GaAs substrate [191].

All the above reported performance enhancement were on time domain systems and the first enhancement in CW emission reported using the NSG was on an InGaAs substrate [185]. The designs were fabricated on an ErAs:InGaAs substrate. The NSG gratings on each arm of the spiral were of the dimension 15 μm×15 μm, with a gap of 20 μm. They reported power levels of the order of 0.8 mW at 1 THz. This is one of the highest ever reported CW THz power from a photoconductive emitter on a semiconductor.

When the log-spiral antenna design with plasmonic NSG was fabricated on a LT-GaAs substrate, they obtained 17 μW at 1 THz. The plasmonic NSG had the same dimension as the ErAs:InGaAs emitter i.e. 15 μm×15 μm, but the gap between them was ~5 μm. When the dimension of the plasmonic NSG was changed from 10 μm×10 μm to 20 μm×20 μm while keeping the gapsize constant, they observed the latter giving higher power at lower frequencies, while the 10 μm×10 μm emitted higher power at higher frequencies. This difference was due to the difference in the RC roll-off at higher frequencies and active area dimension at lower frequencies [192].

In order to have a better understanding behind the surface plasmon effect, a theoretical explanation of the process is studied. This is followed by an analytical confirmation and includes the mapping of the sample.

5.3.2 Theory

Surface plasmons are defined as the collective oscillation of electrons at a metal-dielectric interface. The electromagnetic waves propagate at the metal-dielectric interface until they are absorbed or scattered. Since surface plasmons cannot be excited with normal incidence due to momentum mismatch [193], gratings or prisms can be used to satisfy the dispersion relation.

$$\mathrm{k}_{sp} \propto \frac{\omega}{c}\sqrt{\frac{\varepsilon_1\varepsilon_2}{\varepsilon_1+\varepsilon_2}} \tag{5.1}$$

where k_{sp} is the momentum vector of the surface plasmon, ε_1 and ε_2 are dielectric permittivity of the metal and semiconductor, ω is the plasma frequency and c is the speed of light. When excited using a grating, the higher order diffraction modes can cause a momentum match resulting in the excitation of surface plasmons. For surface plasmons (SP) to exist, the thickness of the medium (metal) must be comparable to the skin depth, or else the plasmon will decay [172].

The plasmonic effect arising from the NSG is the key point of interest. By exciting the NSG, the optical beam incident on the emitter surface is coupled more efficiently into the substrate. Diffraction of the laser beam at the NSG imparts the additional momentum required, resulting in the excitation of the SP at the interface. With a 44 nm thick Au layer [194] on the semiconductor surface, surface plasmons can exist underneath. The enhanced transmission of the optical pump into the semiconductor with a large absorption co-efficient (at $E>E_g$), results in the increased generation of photocarriers. The electron transport path length is significantly reduced, due to the immediate absorption of the carriers present underneath the anode electrode, as shown in Figure 5.5. This means that carriers have a very short distance to travel to the anode.

Since the active area remains constant, there is no extra capacitive loading of the antenna. This method also considers that the carriers are generated approximately ~1 μm beneath the semiconductor surface. Within the earlier demonstration of high power photomixers using LT-GaAs and ErAs:InGaAs, these have normally been fabricated with NSGs for higher powers.

5.4 Single-sided and double-sided nanostructure design

The mechanisms contributing to THz emission in plasmonic nanostructure were discussed in the subsection 5.3.2. With promising reports of high powers from these designs, it was an obvious choice to adopt this technique to improve the CW THz power from photomixers. The objective behind using this design is to help fully understand the process behind its emission characteristics, as well as to develop a high power THz emitter for use with QCLs. There are two new NSG-based designs that have been developed, both positioned within the active region of a two-turn log-spiral antenna. One of these possesses a single-sided nanostructure (SSN) and the other a double-sided nanostructure (DSN). These are shown in Figure 5.6. The SSN had a NSG on one contact electrode, while on the other side was plane metal electrode (no NSG). For the DSN, there was a NSG on both electrodes. The NSG chosen for this work consisted of 100 nm-long electrodes separated by 100 nm (or 200 nm pitch) as shown in Figure 5.7. The dimensions of this NSG are identical to earlier work by Berry *et al.* [185], which showed milliwatts of output power level from the ErAs:InGaAs emitter.

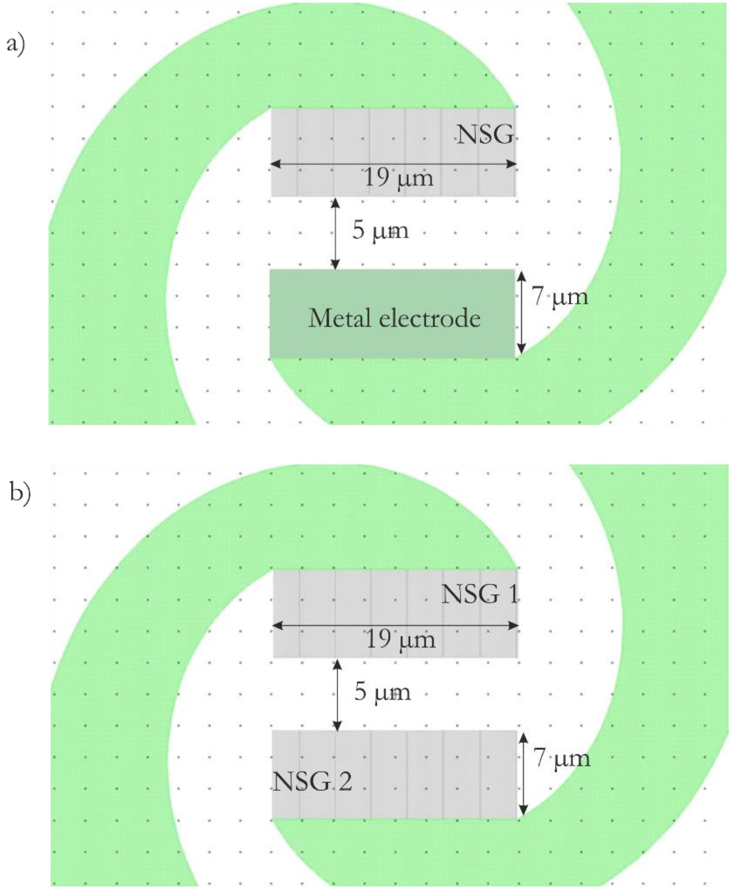

Figure 5.6: Schematic layout of the (a) SSN and (b) DSN emitter showing the NSG electrodes. SSN has plane metal electrode on one side unlike DSN which has NSG on both sides. The dimensions of the NSG (19 µm), plane metal (7 µm) and the gap between the electrodes is shown.

In order for the generated THz radiation to be effectively coupled out of the emitter, a broadband spiral antenna was chosen. The 2-turn self-complementary log-spiral antenna was designed using ANSYS® HFSS (high frequency simulation software) package. A simulation of the antenna design could not be carried out due to the lack of computational memory (RAM). The maximum available RAM that could be used was 32 GB, which wasn't sufficient for simulating. However, self-complementary log-spiral antennas with more than one and a half turns have been reported to exhibit good performance in terms of bandwidth and power [175] with respect to the spiral antennas.

The 2-turn self-complementary log-spiral antenna design had an active area of 19 µm×19 µm. This large gap was chosen to incorporate the NSG on both anode and cathode (for DSN design). The NSGs on the DSN and SSN had a dimension of 19 µm×7 µm. The plane metal electrode had the same dimension as the NSG, i.e.

19 μm×7 μm. The gap between the NSG and metal electrode in SSN and between the two NSGs in the DSN design was 5 μm.

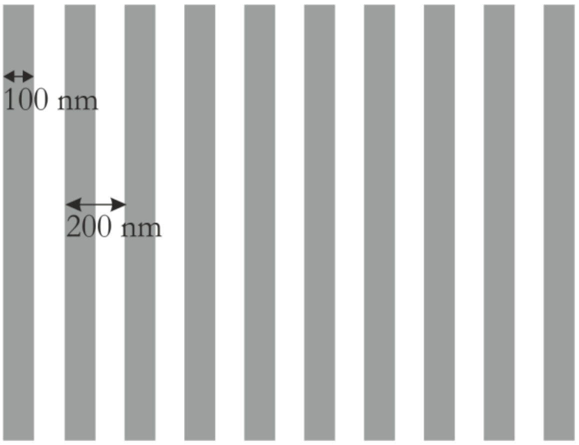

Figure 5.7: Schematic diagram of the NSG showing the 100 nm metal width and 200 nm pitch.

For the fabrication of nanostructure emitters, the best performing Fe:InGaAsP wafer was used, with an Fe doping concentration of 4.0×10^{16} cm^{-3}. Although the Fe:InGaAs performance was superior to the Fe:InGaAsP wafers, surface defects visible in the Fe:InGaAs meant that the latter was chosen.

5.5 Fabrication of nanostructured emitters

A Fe:InGaAsP wafer with an Fe doping concentration of 4.0×10^{16} cm^{-3} was used for the study. A 15 mm×15 mm piece of this wafer was used for processing, and (as explained in Chapter 4) the cap layers, n-InP and n-InGaAsP were removed to expose the Fe–doped active layer.

Fabrication of the SSN and DSN emitters were carried out in two different steps by Dr. Mark C. Rosamond using the JEOL e-beam lithography system. The first step involved defining the nanostructured active region, along with the first turn of the spiral arm. The second step comprised of defining the spiral arm and contact pads. The reason for carrying out the lithography and metallization in two separate steps was due to the different feature sizes in the active region and spiral arms. The 100 nm wide electrodes and 200 nm period make the active region two orders of magnitude smaller than that of the biggest feature in the spiral arm. With this in mind, the patterning resolution could be adjusted for the different sized features, speeding up the lithography process. Another factor is the difference in metal thickness required for the electrodes and spiral arms. The optimum Au thickness for surface plasmon enhancement is ~44 nm [194], whereas the spiral arms require a thickness of greater than 150 nm.

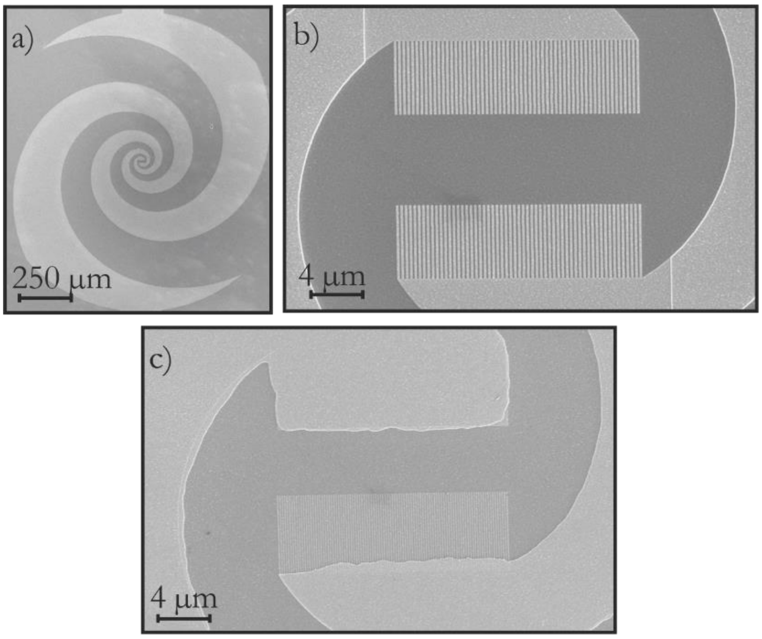

Figure 5.8: SEM images of the fabricated (a) log-spiral antenna fabricated on the Fe:InGaAsP wafer. The active region of the (b) DSN and (c) SSN emitter is shown.

The e-beam resist, ZEP 520A was spun on the wafer at 4000 rpm giving a thickness of 140 nm. This was followed by a bake at 180 °C for 2 min. The nanostructure and first turn of the spiral was defined in the e-beam system. The sample was developed in N-50 (n-amylacetate) for 40 s and later metallized in an e-beam evaporator (Leybold e-beam 350). Ti/Au of thickness 5 nm/45 nm was deposited on the wafer surface at a slow and steady rate to ensure a uniform thickness. Later the sample was developed in cyclopentanone at 60 °C for 30 min. Leaving the sample in cycolpentanone, the sample was given a quick (10–15 s) ultrasonic bath to remove any metal flakes left between the nanostructured electrodes, followed by acetone and IPA rinse for 2 min.

Once cleaned, the sample was coated with poly-methylmethacrylate (PMMA A5) e-beam resist at a rate of 2500 rpm using a spin coater and then baked at 180 °C for 2 min. The use of PMMA A5 instead of ZEP 520A was due to the better adhesion to the Au surface. After the definition of the antenna pattern, sample was developed in H_2O: IPA (7:3 ratio) for 90 s. The antenna patterns were metallized using Ti/Au of 10 nm/150 nm thickness followed by an acetone lift-off. The overlap of the two lithography steps was checked using a SEM (shown in Figure 5.8) and alignment errors were <20 nm (at the spiral arms).

Although alignment marks were used, the sample was examined each time to confirm the overlay. The SSN shown had slight overlay issues. However, this was not an issue with the tested device, which is shown in the Figure 5.20.

The devices were separated using a JFP S-100 scriber and sample was stuck to PCB using silver conductive paint as shown in Figure 4.14 in Chapter 4. The SSN and DSN devices were less susceptible to damage caused by electrostatic discharge (ESD), compared to the IDT devices. This is due to larger gap between the electrodes. However, a grounding strap was worn each time while mounting/un-mounting and making an electrical connection.

5.6 Results from SSN and DSN emitter

The devices were tested in the experimental set-up discussed in Chapter 4. All the optical components remained the same and the emitter was changed. The emitter was DC biased at 0.1 V using the Keithley 2400 and the incident optical power was 10 mW. The sample was aligned for maximum photocurrent by changing the X and Y linear translational stages (holding the emitter) followed by adjusting the aspherical lens.

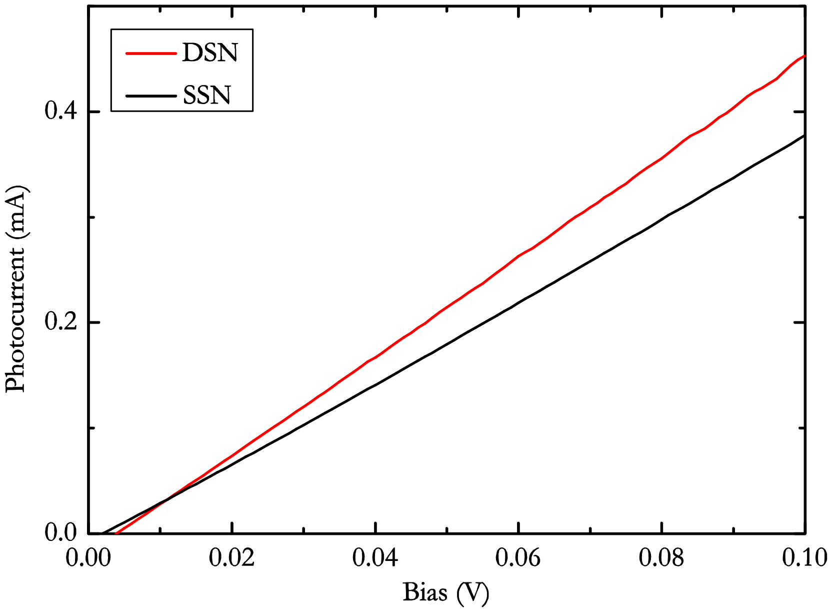

Figure 5.9: Photocurrent measured as function of the applied DC bias for the SSN (black line) and DSN (red line) emitter. The photocurrents were measured at an incident laser power of ~10 mW.

Figure 5.9 shows the I−V data obtained from the SSN and DSN emitter. The NSG arm of both the SSN and DSN was biased during measurement, thus electrons are attracted to the NSG for both SSN and DSN emitter. Holes are attracted to plane metal for SSN emitter and NSG2 for the DSN emitter. However, both emitters gave a photocurrent of ~0.4 mA at 0.1 V bias. They showed ohmic behaviour in the bias range measured, from 0 to 0.1 V. Although the two emitters have geometrical differences, the similar photocurrent measured from the emitters implies a higher contribution from electrons due to the higher mobility (since SSN had a plane metal electrode unlike DSN which had two NSG). The presence of sharp electrode tips at the ends of the NSG on both emitters, can cause a thermal breakdown at this point, thus limiting the applied DC bias to 0.1 V.

5.6.1 Bandwidth

The emitters were biased using 1 V amplitude, 25% duty cycle pulses at 7.6 kHz frequency from an AWG. With emitter having an incident laser power of 10 mW and the coherent receiver TOPTICA at 13 mW, the beat frequency between the lasers were scanned between the 100 GHz−2000 GHz range with a 10 GHz step size scanning the delay at each frequency.

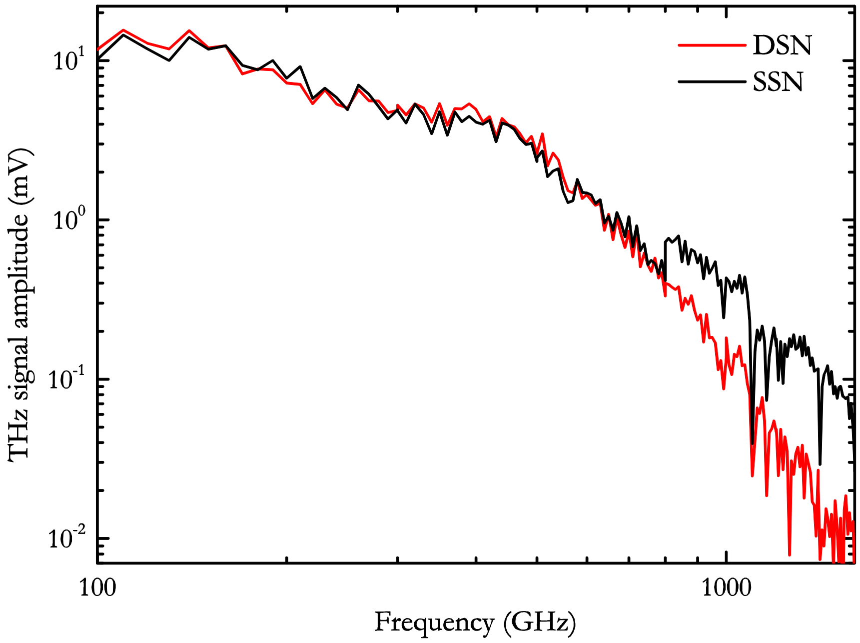

Figure 5.10: THz signal amplitude measured as a function of laser beat frequency for the SSN (black) and DSN (red) emitter. The NSG electrode of the SSN and DSN emitter was biased at 1 V amplitude 25% duty cycle pulses at 7.6 kHz frequency.

Figure 5.10 shows the THz signal amplitude measured from the SSN and DSN emitter. The THz signal amplitudes measured from the SSN and DSN emitter were similar until ~800 GHz. However there was a slight difference in THz amplitude after 800 GHz, with SSN emitter outperforming the DSN emitter. This difference was observed only in this particular device and wasn't reproducible. However the measurable bandwidth from these emitters was ~2 THz and ~1.8 THz, for the SSN and DSN, respectively. The measured power level at 500 GHz was ~3 times lower than the 3 pair IDT design fabricated on the same wafer, the devices discussed in Chapter 4. This observed drop in the measured bandwidth and THz output power has raised concerns as to whether the surface plasmons are actually contributing to the overall signal, or if they even present at all.

5.6.2 Bias – Forward and Reverse

Despite the difference between the two designs, the SSN and DSN, the THz signal amplitudes and bandwidths appeared to be similar. In order to determine the contribution of the NSG in THz emission, the SSN and DSN emitter were tested in the reverse bias condition, i.e. the plane metal electrodes at 1 V bias and NSG at 0 V for the SSN emitter and NSG2 at 1 V bias and NSG1 at 0 V bias for the DSN emitter.

Figure 5.11 shows the measured THz signal amplitude over a range of frequencies from the SSN and DSN emitter, in forward and reverse bias conditions. The THz signal amplitude from the SSN dropped significantly when tested in the reverse bias, with similar amplitudes at 100 GHz, to less than half the signal at 510 GHz. The amplitude decreases significantly at higher frequencies (>800 GHz) compared to the forward bias. The bandwidth of the emitter reduced from ~2 THz to ~1.2 THz when the bias was switched. However, for the DSN emitter, there was no change in terms of emitted power or bandwidth, since it didn't involve any geometrical change.

In the forward bias condition, the emitted power level was low (<1 nW at 1 THz for both SSN and DSN emitter obtained by calibration) compared to the previous reported work (0.8 mW power at 1 THz at 10 V bias, 2% duty cycle and 150 mW incident optical power from ref [185]). This difference in the measured power level from the in-house emitters cannot be explained unless the geometrical dependence of the THz generation is understood. This can be done in two ways. The first technique involves monitoring the position of the incident laser beam on the emitter using a CCD camera (sensitive to 1550 nm) and comparing the peak signal with varying incident laser spot position. Alternatively, this can be achieved by systematically moving the emitter and maintaining the position of the laser spot. This allows us to map out the measured emitted signal from the photomixer, as a function of distance by altering the position of laser beam on the active region. In this work, the second approach was adopted due to the reliability of the method and resolution of the incident beam. This will be discussed in detail in the Section 5.7.

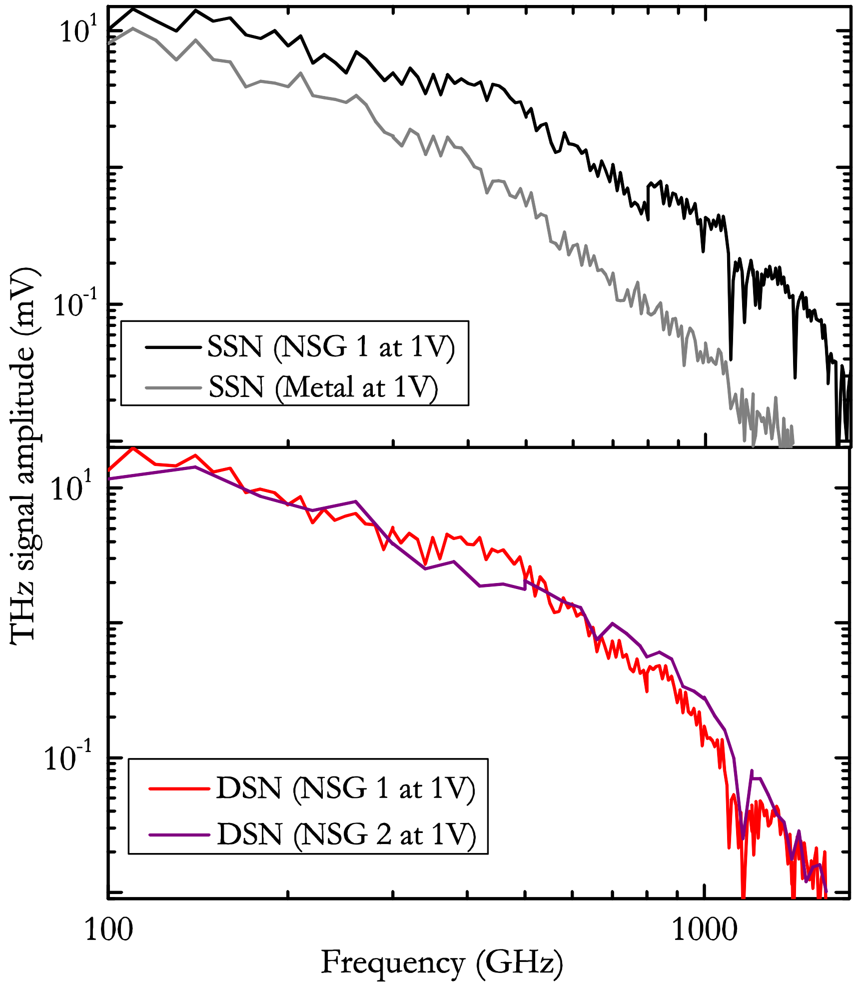

Figure 5.11: THz signal amplitude measured as a function of laser beat frequency for the SSN (top) and DSN (bottom) emitter biasing the two different electrodes. The NSG (black line) and plane metal electrode (grey line) of the SSN emitter was biased at 1 V amplitude 25% duty cycle pulses at 7.6 kHz frequency. Similarly the NSG1 (red line) and NSG2 (purple line) of the DSN emitter biased at 1 V amplitude 25% duty cycle pulses at 7.6 kHz frequency.

5.7 Mapping the excitation position of nanostructured emitters

The spectral bandwidth of the two-turn antennas, with SSN and DSN designs fabricated on Fe:InGaAsP (4.0×10^{16} cm^{-3}) was found to be <2.0 THz. A 3 pair IDT device fabricated on the same wafers had an emission bandwidth of <2.4 THz (refer Figure 4.21). In order to understand the reason for the decrease in power level obtained from the SSN and DSN emitters, each emitter has undergone a mapping procedure. Mapping the structure can give an insight into the geometrical process or structural dependence on the THz emission. In this context, the term mapping implies that the output power from the emitter is measured at different laser excitation positions. Mapping can be carried out using two different methods: changing the position of the incident laser beam on the sample by either moving the sample position or moving the laser beam. In this work, the first approach is adopted to minimize errors in handling the incident laser beam.

The experimental setup used for the mapping of SSN and DSN emitter is shown in the Figure 4.15 in Chapter 4. For mapping, an Olympus ×20 microscope objective was used instead of the Thorlabs 1550 aspheric lens. This ensures a smaller spotsize and thus a higher resolution. The spotsize of the lens was measured using knife-edge measurement. A knife-edge measurement, similar to that demonstrated below has been reported by Suzaki *et al.* [195].

5.7.1 Knife edge measurement

For this knife edge measurement, a sharp pointed object (scalpel blade) was used. The laser beam was assumed to have a perfect Gaussian distribution with a beam waist W. It is also assumed to propagate in the Z-direction. The collimated beam was focussed using the Olympus ×20 lens. The scalpel blade was placed in the beam path and the transmitted power is measured using an InGaAs photodiode DET08CFC, as shown in the Figure 5.12. The beam waist is minimum at the focal point of the lens.

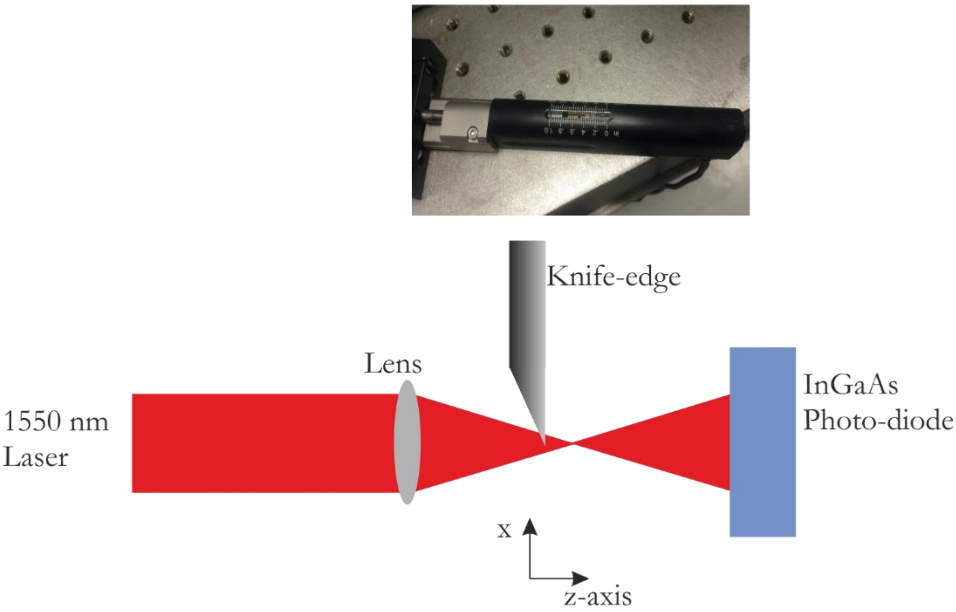

Figure 5.12: Schematic of the knife edge measurement setup. Knife edge is introduced in the beam path by a motorised actuator. The transmitted beam is collected by the photodiode. The motorised actuator is shown in the inset.

The scalpel blade was initially positioned arbitrarily at a point on the Z-axis (not too far away from the lens focus). The X position of the scalpel was varied using a motorised actuator (Newport Instruments). The minimum step size available from the actuator is ~300 nm. The photocurrent generated in the photodiode was measured using Keithley 2400. The current was at its maximum value when the blade was completely removed from the beam path and at its minimum when entirely blocked. The measured power at different X positions can be written as [196, 197],

$$\mathrm{P(x)} = P_b + \frac{P_0}{2}\left[1 - erf\left(\frac{\sqrt{2}(x - x_0)}{w_x}\right)\right] \tag{5.2}$$

where P_b is the background power, P_0 is the maximum power, x_0 is the centre co-ordinate of the beam, erf is the Gaussian error function and w_x is the $1/\mathrm{e}^2$ half-width of the beam. The background power term acts as an offset and contributes to the power when the laser beam was completely blocked. This is minimal as the photodiode has a dark current of ~20 nA. However, the presence of an error function makes the interpretation of the data difficult.

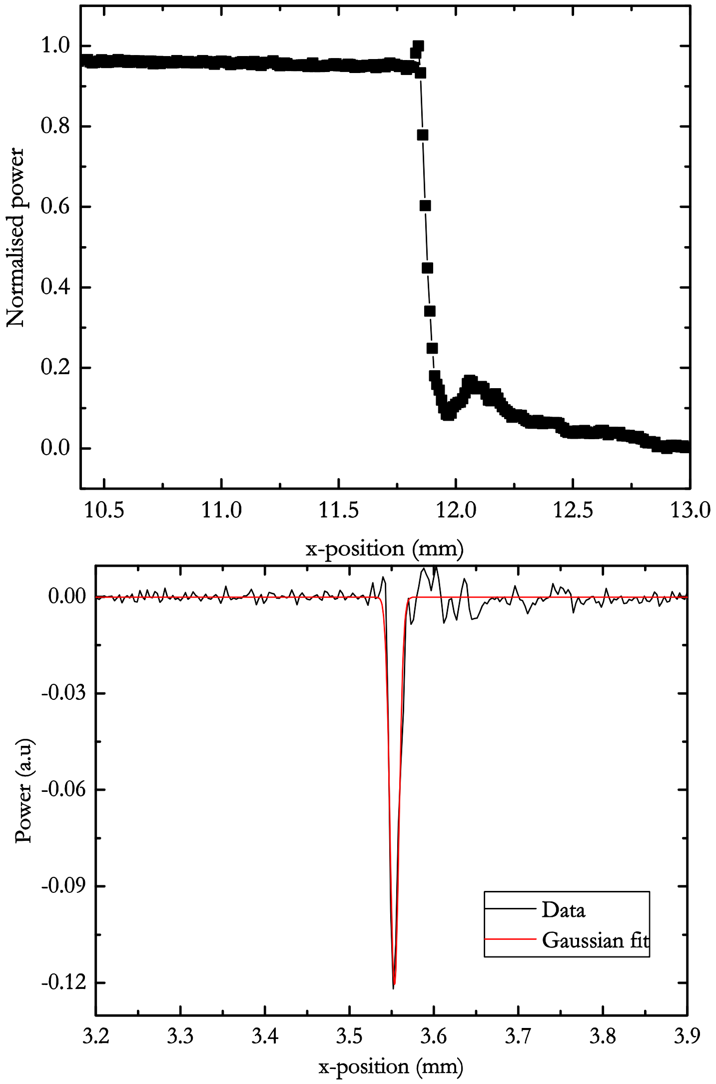

Figure 5.13: Normalized power plotted as a function of actuator movement in the X-direction (top). The differentiated data (black) is fitted with a Gaussian curve (red) and the FWHM corresponds to the laser spotsize (bottom).

Under the assumption that the laser beam is a perfectly Gaussian curve, the power values measured at different X positions for a particular Z value can be analysed by differentiating the power values and then fitting a Gaussian curve with radius, r to the data. Figure 5.13 shows the data plot at a particular Z position with the corresponding Gaussian fit.

The experiment was repeated at different Z positions and the laser spotsize was obtained as ~6±0.25 μm. Although the beam shape was assumed to be Gaussian with a perfectly circular spot, the experiment was repeated for confirmation and the measured spotsize was 6±0.84 μm. A small spotsize is necessary to obtain a high resolution image of the nanostructures within the design (~100 nm). However, this is restricted by the diffraction limited spotsize [198]. This is governed by $d = \frac{1.22\lambda}{NA}$, where d, λ, NA correspond to the diffraction limited spotsize, the wavelength of the laser (1550 nm) and the numerical aperture of the lens (0.4), respectively. From this equation, the maximum resolution that can be achieved is ~3.6 μm, which is in good agreement with our measured spotsize.

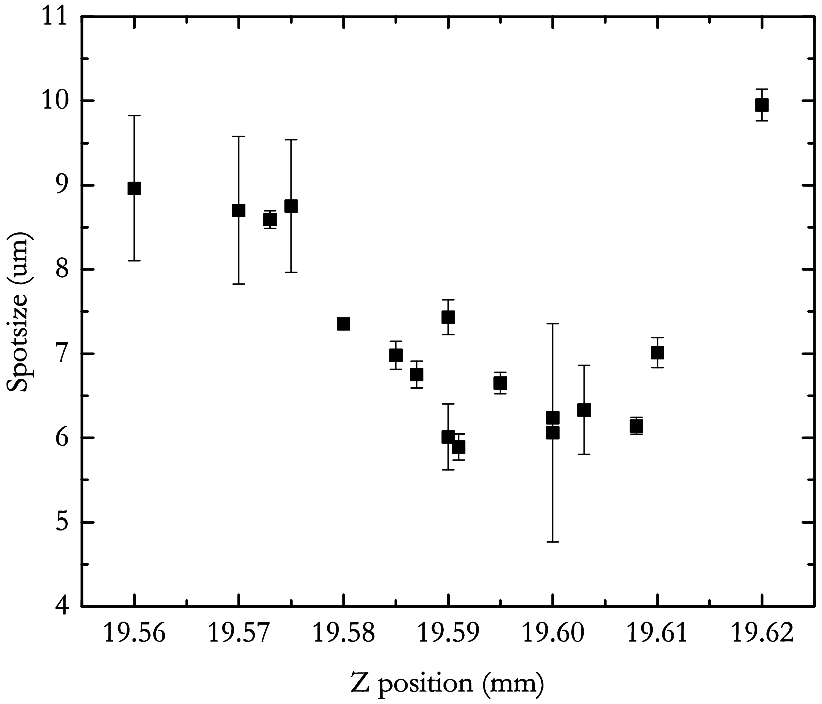

Figure 5.14: The measured FWHM values (spotsize) plotted as a function of focussing position in the Z-direction. The error in calculating the FWHM is represented by the error bars.

5.7.2 Experimental setup

The experimental setup used for the characterization of the emitters, discussed in the previous chapter, was also used for mapping, with the free-space optical path of the laser beam to the emitter modified. An Olympus ×20 microscope objective (with a spotsize of 6±0.25 μm) was used for mapping and has a smaller spotsize than the aspherical lens (used for emitter characterization). The collimator, HWP and lens were mounted on a XYZ - linear translation stage. The sample was mounted on a three dimensional linear translation stage. The silicon lens, used to increase output power, was mounted on a separate XY mount to have independent control. This arrangement of the lens, sample and silicon lens on separate translational stages allowed for independent control of the laser beam and the THz radiation. The first step in alignment for mapping was to maximize the photocurrent of the sample at a bias of 0.1 V. The difference in the spotsizes of the two lenses (aspherical lens and Olympus lens) resulted in a discrepancy in the measured photocurrent, with lower values (0.2 mA at 0.1 V bias) for the smaller spotsize.

In order to generate THz radiation, the emitter was biased using 1 V amplitude, 25% duty cycle pulses at 7.6 kHz frequency. The sample was aligned for the THz signal at 210 GHz, 510 GHz and 810 GHz. During alignment, precautions were taken to ensure that the position of the laser beam does not change, making only small changes to the sample and silicon lens. As the emitter was aligned for maximum THz signal, the detector was also aligned to maximise the signal.

The linear translational stage controlling the X-direction of the sample was replaced by a motorised actuator, the same actuator used for spotsize measurement (Newport Instruments). Although the actuator had a minimum step size of ~300 nm, the step size used for measurement was ~900 nm taking into account the laser spotsize. While the X-direction was controlled using the automatic actuator, movement in the Y-direction was manually stepped. A minimum step size of ~1±0.5 μm can be achieved in the Y-direction.

The emitter was aligned for maximum amplitude of the signal at the desired frequency. The optical delay was then scanned in order to find the peak amplitude position. The mechanical delay line was controlled by LabView programming, so that the receiver moves to the peak amplitude position, as shown in the Figure 5.15 (a). For mapping, it was confirmed that the THz radiation from different parts of the active region were in phase, as the thickness of the substrate and silicon lens do not vary within the mapped region, thus the optical path length remains unaffected. The collection efficiency was not affected since the silicon lens had twice the diameter (d=2.56 mm) of the log-spiral antenna (~1.1 mm).

With the sample aligned for peak THz amplitude, the motorized actuator was then scanned between 2.7 mm and 3.6 mm with a step size of ~0.9 μm corresponding to a scanning range of ~0.9 mm. This equates to a pixel size of 0.9 μm×1.0 μm. The measured signal amplitude in the scanned direction (X-axis) for a particular Y value is shown in Figure 5.15 (b). This scan was taken at 510 GHz, using the SSN active region design. The experiment was repeated for a range of Y-values, to cover the first two turns of the spiral antenna. By plotting the THz signal amplitude as a function of both the X and Y transitions, a 2D (or 3D plot) can be formed.

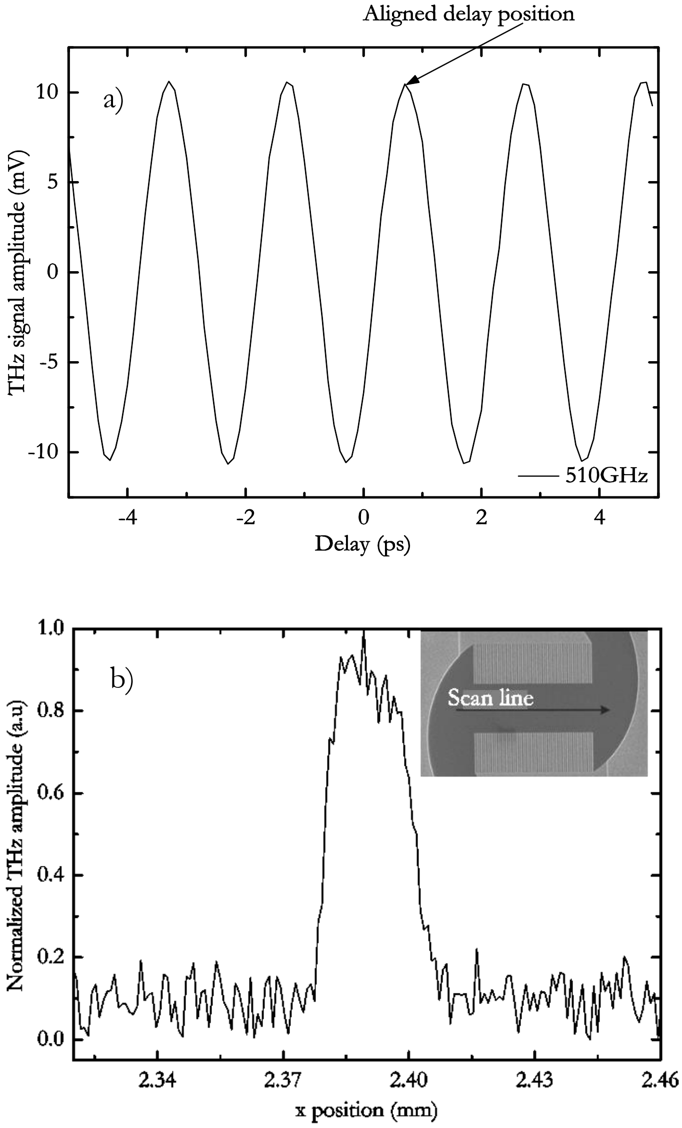

Figure 5.15: (a) THz signal amplitude as a function of delay at 510 GHz from the SSN emitter with the aligned delay position for the peak signal marked. (b) Normalized signal amplitude plotted as a function of the actuator position in the X-direction for the DSN emitter. The scan line is marked on the inset figure.

5.8 Mapping the photomixers results

5.8.1 510 GHz

Mapping was carried out on the SSN and DSN emitters. The beat frequency between the lasers was set at 510 GHz with a horizontal polarization (rotating the HWP). The NSG arm of the SSN and DSN was biased at 1 V. Figure 5.16 shows the map obtained from both emitters, with the spiral overlay. An overlay of the spiral pattern was added to the image to help visualise the design. The THz amplitudes were normalized to the maximum value obtained from the designs, which is approximately the same for both emitters, ~2.5 mV.

For the SSN emitter, in Figure 5.16 (a), the measured THz amplitude is at its maximum when excited at the gap between the NSG and the plane metal electrode. The highest amplitude of THz signal was recorded when the laser spot was focused at the centre of the gap. With a gap of 5 μm the laser spot excited both the electrodes simultaneously (spotsize of laser was ~6±0.25 μm) generating the peak emission. This could be due to the high optical electric field present in the tips. Although an emission peak was observed from the centre of the gap, it is difficult to determine whether this was from the centre between the electrodes or due to the larger laser spot exciting both electrodes simultaneously.

The generated signal when the spot is focused on the biased NSG was found to be <40% of the maximum amplitude output. Since the NSG length (7 μm) was larger compared with the laser spotsize (~6±0.25 μm), any enhancement in output signal originated from the NSG should be visible with this mapping process. This implies that either there were no surface plasmons generated or if present, their contribution to the emission process was minimal.

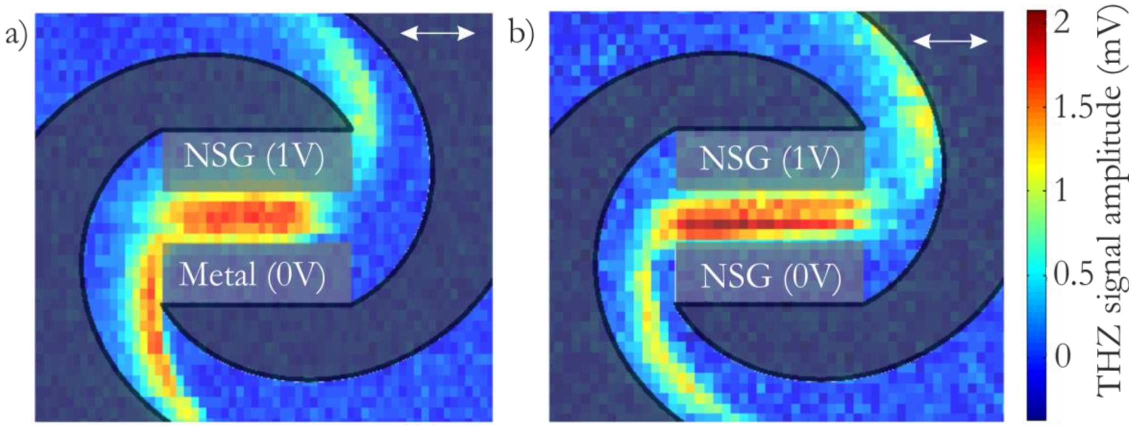

Figure 5.16: Raster scanned image showing THz amplitude as a function of the laser exciting position for the SSN and DSN design with NSG and plane metal electrode. The 2-turn log-spiral antenna design is used as an overlay on top of the data for understanding. The electrode biased at 1V, 25% duty cycle at 7.6 kHz frequency is shown. (a) SSN design with NSG biased and (b) DSN with NSG1 biased respectively. The polarization direction of the laser is shown on the top right corner on both image.

There was emission (~50% of maximum) from the gap between the spiral arms. This gap is slightly larger than the gap between electrodes. Predictably, no THz radiation was detected when the laser beam excited the plane metal electrodes as the beam is shielded.

For the DSN emitter, shown in Figure 5.16 (b), the emission was found to be highest when excited at the gap between the electrodes, similar to the SSN emitter. This enhancement could be due to greater electrical field strengths at the tips of the metal electrodes. As explained above, no clear enhancement was obtained when the NSG grating electrodes were excited.

5.8.2 510 GHz – Opposite bias

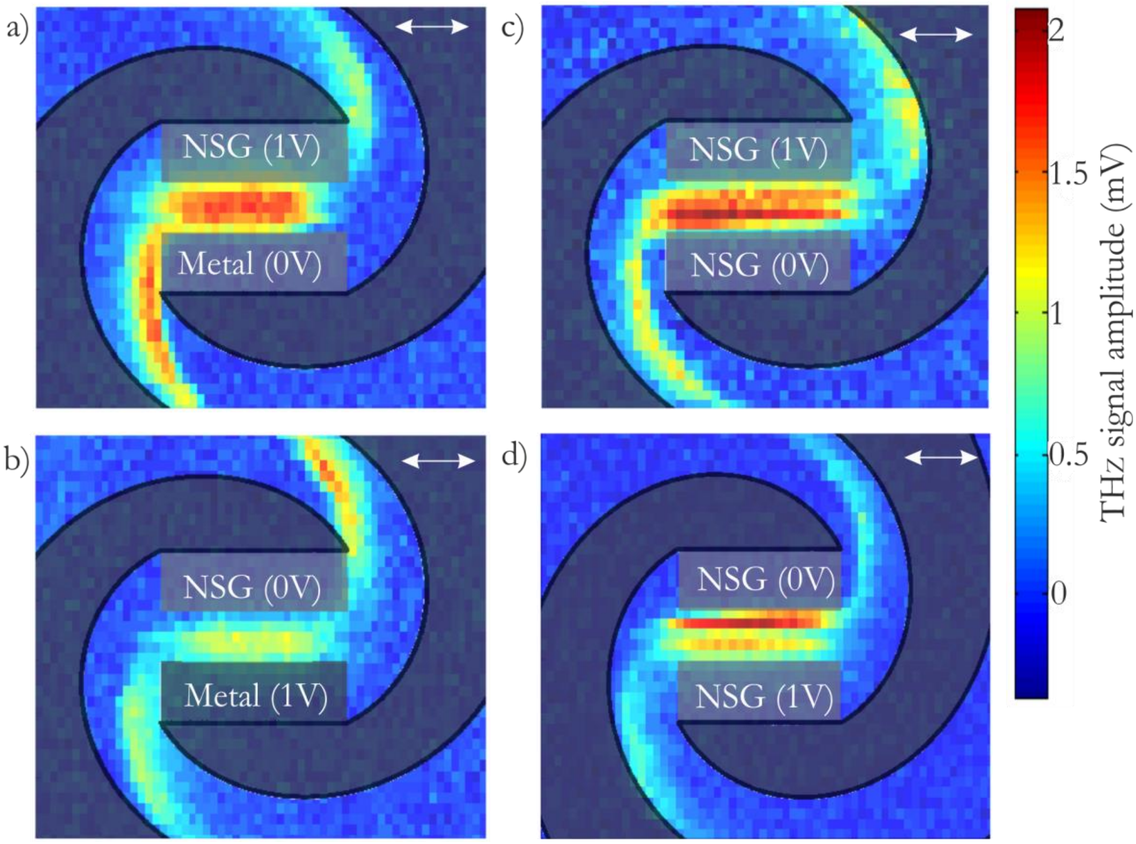

Figure 5.17: Raster scanned image to show the THz amplitude as a function of the laser exciting position for the SSN and DSN emitter design. The 2-turn log-spiral antenna design is used as an overlay on top of the data for understanding. The electrode biased at 1V, 25% duty cycle at 7.6 kHz frequency is shown. SSN design with (a) NSG biased and (b) plane metal electrode biased and DSN design with (c) first NSG biased and (d) second NSG biased respectively. The polarization direction of the laser is shown on the top right corner on both image.

With the mapping procedure performed at 510 GHz, biasing the NSG for both SSN and DSN, the majority of THz emission was found to be from the gap between the electrodes.

For the DSN device, it was observed that switching the electrodes did not alter the THz bandwidth or amplitude , while a significant decrease in both parameters was observed for the SSN. In order to understand this behaviour, the mapping process was repeated with the bias reversed. Figure 5.17 shows a raster scanned image of the SSN and DSN emitters.

For the SSN emitter, it can be seen that there is a significant decrease in the THz signal amplitude with the bias direction switched. However, the excitation position for peak emission remained the same. The signal level obtained in this bias direction was <40%, compared to when biasing the NSG electrode. This decrease in signal could be explained by the lack of sharp edges, resulting in a reduced electric field enhancement. The NSG has 99 electrodes of 100 nm width separated by 100 nm gap - thus 198 sharp corners whereas the plane metal electrode has only two sharp corners at both ends of the electrode. This may cause the significant reduction in signal amplitude that was measured. This is also responsible for the decrease in bandwidth observed in these devices discussed in Section 5.6.2. Another interesting point is that the observable contribution from the holes for THz generation is low, when compared to the electrons. The reason for this could be the low mobility of holes, which is ~10 times less than electrons.

For the DSN, switching the bias had no noticeable effect on the spectral bandwidth or emitted power. This was expected as there was no major geometrical change for the accelerated electrons and holes. The excitation position that gave the maximum THz amplitude shifted approximately 1 μm towards NSG2 (compared to the maximum amplitude position when NSG1 was biased at 1 V), which was at 1 V bias. Although the polarization of the incident laser beam was perpendicular to the NSG electrodes, when the excitation beam was focused on NSG2, no enhancement in signal was observed. This is contradictory to previous reported works [185].

5.8.3 510 GHz – Polarization

For surface plasmon excitation at a metal-dielectric interface, for maximum coupling efficiency the polarization of the incident beam needs to be parallel to the plane of incidence (p-polarized light). For all previous measurements discussed, mapping was performed using a horizontally polarized (perpendicular to the NSG) beam. With no higher powers detected at this polarization when exciting the NSG, it was decided to check the performance at vertical polarization (parallel to the NSG).

The HWP was rotated 45° which resulted in 90° rotation of the laser electric field. The mapping of SSN and DSN emitters was repeated with this change in polarization. Figure 5.18 shows the THz amplitude as a function of laser excitation position for both SSN and DSN emitter designs. For the two orthogonal polarizations. For this measurement, the NSG1 electrode of both devices was biased at 1 V.

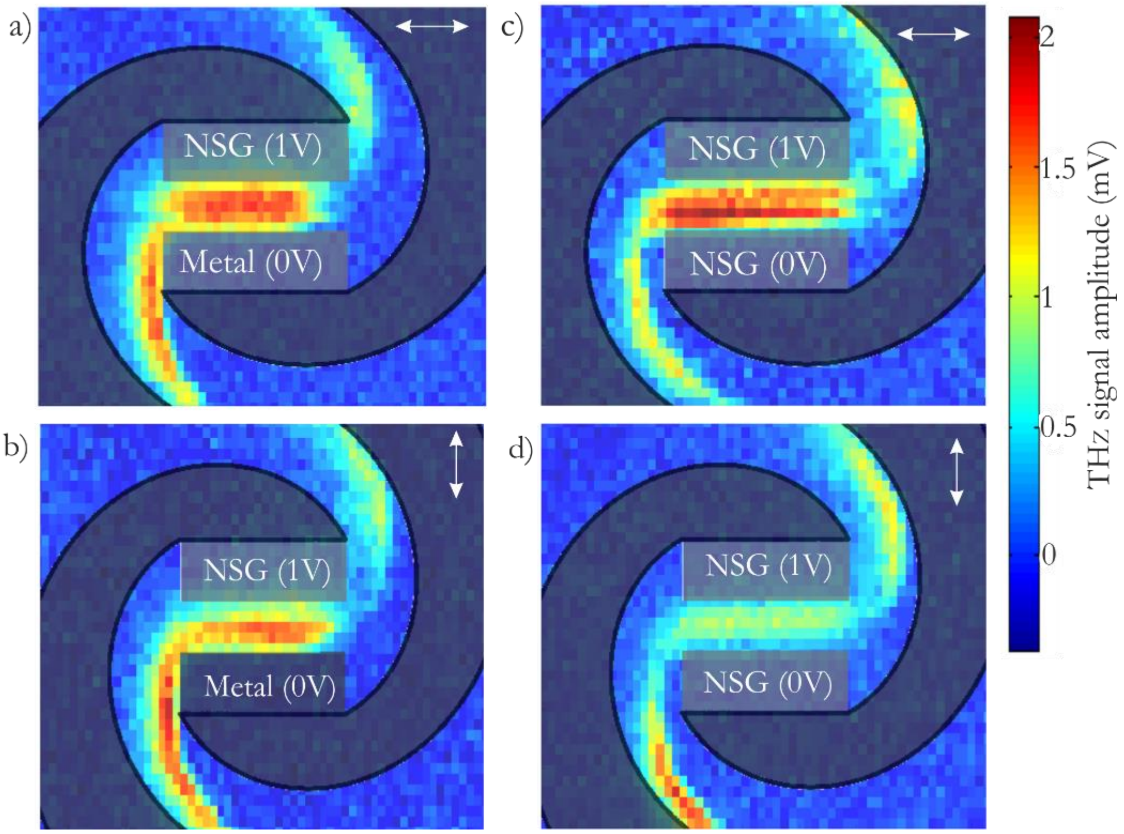

Figure 5.18: Raster scanned image to show the THz amplitude as a function of the laser exciting position for the SSN and DSN emitter design, for two orthogonal polarizations. The 2-turn log-spiral antenna design is used as an overlay on top of the data for understanding. The electrode biased at 1V, 25% duty cycle at 7.6 kHz frequency is shown. SSN design with (a) horizontal and (b) vertical polarizations and DSN design with (c) horizontal and (d) vertical polarizations respectively.

For the SSN emitter, when the polarization of the laser was changed from horizontal to vertical polarization (parallel with the NSG), a decrease in the peak emitted power of ~30% was observed. The excitation spot for the maximum THz signal remained the same. For the DSN design there was a significant drop of ~70% in peak signal when compared with the horizontal polarization beam input. The peak THz signal was observed when the excitation spot was between the spiral arms. THz signal remained almost similar in amplitude for horizontal and vertical polarization between the spiral arms. This difference in the measured signal level at the vertical polarization for the SSN and DSN emitter could be explained in terms of the wire-grid polarization filter [199, 200]. The metal electrodes of the dimension λ/5 or λ/10 can act as a wire-grid polarizers, thus reducing the coupling efficiency of light between free-space and the semiconductor. The dimension of the NSG electrodes were 100 nm, although greater than λ/10, it is expected to be a contributing factor. The measured amplitude from SSN emitters was ~70% of horizontal polarization due to the presence of a single NSG, whereas the presence of two NSGs; NSG1 and NSG2 for the DSN resulted in twice the reduction in the signal amplitude resulting only ~30% of the amplitude.

5.8.4 Emission mechanism

Mapping the emitters at different bias and polarization as a function of excitation spot confirmed that the THz generation was not on the NSG and was found to be at the gap between them, by exciting both anode and cathode tips simultaneously. The decrease in THz signal amplitude with the reverse bias for the SSN emitter, discussed in Section 5.8.2 confirms that the NSGs are contributing to emission. The laser spotsize dimension of ~6±0.25 μm, focussed at the gap (5 μm) excites both anode and cathode tips, causing an enhanced optical electric field, shown as red circles in Figure 5.19. It is these intense optical electric fields that are responsible for emission. This generation technique is similar to mechanism reported in ref [171].

The assumption was valid when the emitter was tested for orthogonal polarizations. When the incident beam polarization was changed from horizontal to vertical, it resulted in a reduced coupling to the semiconductor substrate, causing a reduction in THz amplitude. The difference in SSN emitter, as shown in Figure 5.18 (b), is prevalent near the NSG due to the significant absorption of the vertically polarized beam by the NSG electrodes and not near the plane metal electrode. On the other hand, in the case of DSN emitter there is significant decrease near both NSGs Figure 5.18 (d), due to absorption at both NSGs.

Both bias and polarization measurements confirm the emission mechanism to be due to enhanced optical absorption near the NSG tips for a horizontally polarized beam thus resulting in an enhanced optical electric field. If the generation was due to the photo-generated carriers between the NSG (at the 5 μm gap), there would not have been any decrease in the emitted power levels. However, the decrease in signal observed implies that, for horizontal polarization, coupling of the laser light through the NSG results in carriers recombining at the sharp tips.

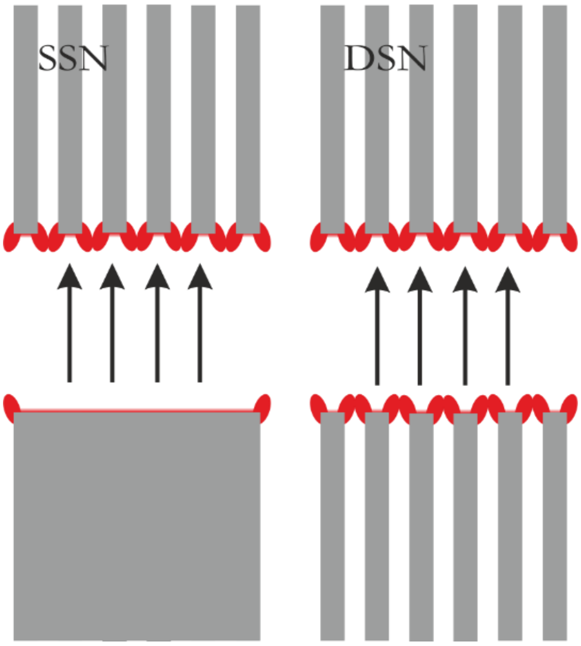

Figure 5.19: Schematic representing the generation mechanism in NSG contact electrode SSN and DSN photomixers under the presence of an incident laser filed and applied bias. Most of the THz generation takes place at the electrode tips due to the intense optical electric field (marked as red). Black lines represent the electric field lines.

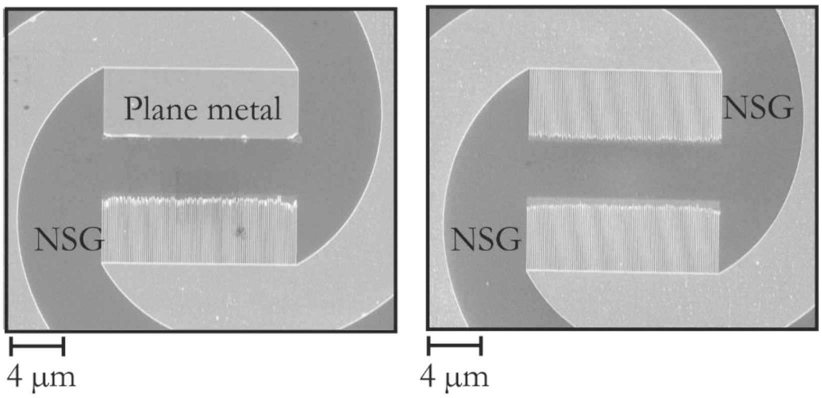

Figure 5.20: SEM images of the SSN (left) and DSN (right) emitter after prolonged measurements showing the damage to the electrode tips.

The high concentration of photocarriers at the tips of the electrodes combined with performing the measurements for a prolonged time, resulted in the burning of the electrode tips. The SEM image of the SSN and DSN emitter after the measurement is shown in the Figure 5.20 and with a zoomed in version of the electrode tips provided in Figure 5.21. The SEM images of the sample show that the metal tips were lifted off from the semiconductor substrate. However, the burnt tips don’t seem to significantly affect the performance of the device, with only <10% difference in the output amplitude.

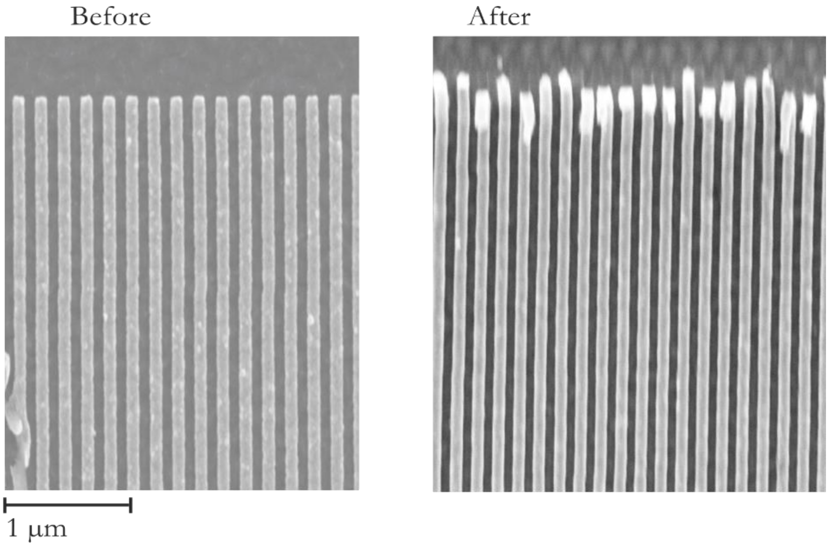

Figure 5.21: SEM image of the electrode tips of the DSN emitter before measurement and after measurements for a prolonged time. The metal tips were slightly lifted-off from the semiconductor surface.

A probable reason for the non-ideal performance of the SSN and DSN could be related to the dimension of the NSG. The metal electrodes used in the present study had a width of 100 nm. The incident optical radiation transmitted through the slit should interfere constructively with the optical beam transmitted from the consecutive slit. However, if the dimensions of the slits are not correct, destructive interference can happen. These designs were optimized before for performance at 800 nm and 1550 nm [190], although unlikely, the metal widths can be a contributing factor.

5.9 Other frequencies and photocurrent

5.9.1 210 GHz and 810 GHz

In both designs (SSN and DSN), it has been shown that the gap between the electrodes is responsible for the majority of the THz generation at 510 GHz. The mapping was also performed at 210 GHz and 810 GHz to confirm the geometrical effects. Although the peak emission amplitude was again concentrated within the gap between electrodes, there was THz signal detected when the laser beam excited the gap between the first turn of the spiral arms. This emission is due to the carriers recombining at their respective anode and cathodes. In order to determine the signal levels originating between the spiral arms and to confirm whether it is present at all frequencies, the mapping was performed at 210 GHz and 810 GHz as well.

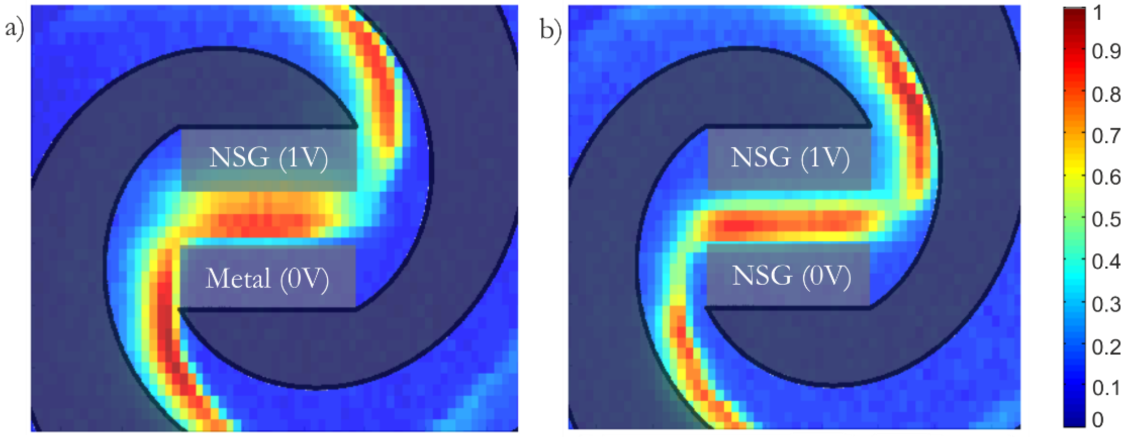

Figure 5.22: Raster scanned image to show the THz amplitude (normalized) as a function of the laser exciting position at 210 GHz for the (a) SSN and (b) DSN emitter design respectively.

The beat frequency between the lasers were set at 210 GHz and 810 GHz and with the horizontal polarization incident on the emitters. The emitters were mapped once again, with the NSG electrode of the SSN and NSG1 of the DSN emitters biased with 1 V Pk-Pk 25% duty-cycle pulses. Figure 5.22 and Figure 5.23 show the mapped data from the SSN and DSN emitter, at 210 GHz and 810 GHz respectively.

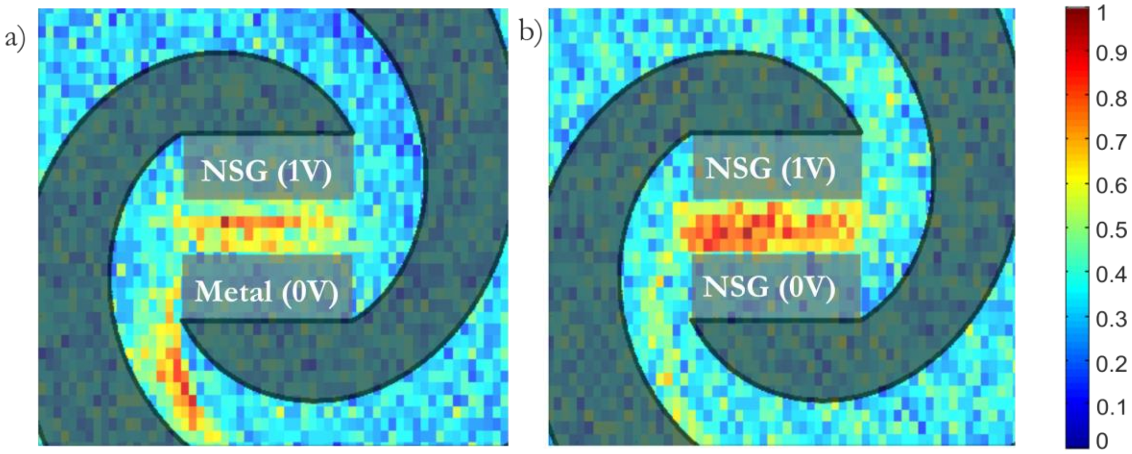

Figure 5.23: Raster scanned image to show the THz amplitude (normalized) as a function of the laser exciting position at 810 GHz for the (a) SSN and (b) DSN emitter design respectively.

The region of maximum THz emission is consistent with the mapping at 510 GHz, in which it is concentrated mainly between the electrodes. The geometrical effect behind the emission mechanism was observed to be confined to the gap between the electrodes with almost the same signal level between the spiral arms at 210 GHz and less or negligible emission between the spiral arms at 810 GHz. For both SSN and DSN emitters, the THz signal amplitude reduced by 40% when the excitation position was shifted from the gap between the electrodes to the NSG at 210 GHz. However, no emission was observed from underneath the NSG for both SSN and DSN emitters at 810 GHz. The peak amplitude position remained the same, at the centre of the gap between the electrodes.

The emission distribution on the active region was found to concentrate within the gap between the electrodes as the excitation frequency increases. The signal level emitted between the spiral arms reduced from 70% of the maximum output at 210 GHz to ~50% at 510 GHz and to <30% at 810 GHz owing to the high electric field between the gap.

5.9.2 Photocurrent

The THz signal amplitude plotted as a function of laser spot position revealed that the geometrical position of the maximum emission remained the same for the SSN and DSN emitter. This has been shown to be within the gap, irrespective of the fact that the SSN has a plane metal electrode on one side. Photocurrent was mapped as a function of excitation position for the SSN and DSN emitter, with NSG biased at 0.1 V. Figure 5.24 shows the measured photocurrent as function of the laser excitation spot position.

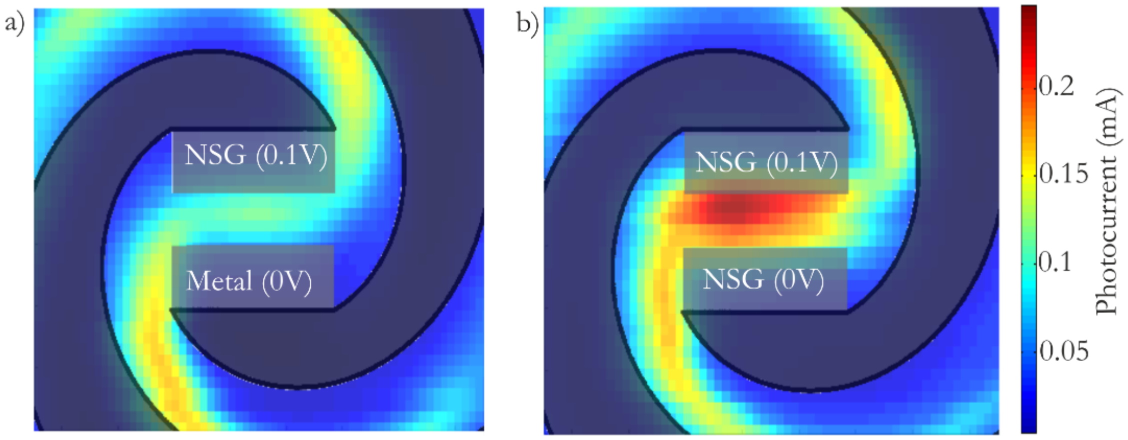

Figure 5.24: Raster scanned image to show the measured photocurrent as a function of the laser exciting position at 0.1 V for the (a) SSN and (b) DSN emitter design respectively.

For the SSN emitter, the area of the maximum photocurrent was between the spiral arms, with lower photocurrents generated from the gap between NSG and plane metal electrode. This is the opposite to when detecting the THz signal amplitude as a function of spot position. The explanation for this photocurrent difference is unknown. For the DSN emitter, the geometrical position of the maximum photocurrent is consistent with the position of the maximum THz amplitude, which is the gap between the two NSGs.

Although the NSG is expected to enhance the optical transmission in the substrate, resulting in higher photocurrent, it was not found to be the case. The high value of photocurrent generated in the gap suggests that faster recombination occurs at the electrode tips of the NSG due to the higher optical electric field. Since mapping in CW suggested that surface plasmons were not contributing to emission, it was decided to map using pulsed excitation as well.

5.10 Mapping in pulsed system

5.10.1 Experimental setup

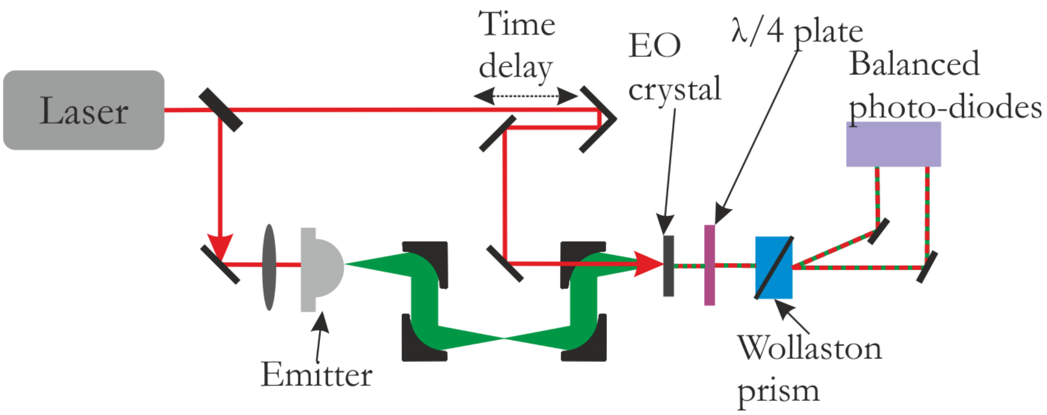

Figure 5.25: Schematic of the THz-TD experimental set-up used for mapping the emitters.

Mapping in the CW system involved the excitation of the semiconductor gap with two beating laser beams. The CW THz signal mapping of the SSN and DSN emitter, at three different frequencies, suggested the majority of THz emission originates from the gap between the NSG and plane metal of the SSN and the two NSGs for the DSN emitter. However, the measured power levels from these emitters was low and no surface plasmon enhancement was observed. The earlier works [107] on these NSG device suggested enhanced performance from the devices, when the anode is excited in a pulsed system. In order to have a better understanding of the emission process, the sample was mapped in a THz-TD system.

The laser source used is a TOPTICA fibre Pro dual wavelength laser which emits at wavelengths of 1560 and 780 nm and a pulse width of 95 fs. The laser uses a coiled fibre inside which has a reported emission wavelength of 1560 nm. A non-linear crystal, periodically poled lithium niobate (PPLN) could be manually inserted or removed from the beam path using a mechanical lever which allows us to switch the wavelengths between 1560 nm and 780 nm by second harmonic generation. Only one wavelength can be generated at a time. The fibre, non-linear crystal and the accompanying optics were placed inside a box. There were two separate beam exits for the 1560 nm and 780 nm wavelength, which helped with system alignment.

A standard THz-TD system was used with electro-optic (EO) detection method, encompassing an EO crystal and a pair of balanced photodiodes, as explained in Chapter 3. Figure 5.25 shows the experimental setup. Although the laser can emit 1560 nm and 780 nm, the mapping was carried out at 780 nm, due to the unavailability of a phase-matched crystal at 1560 nm. The wafers used for the SSN and DSN emitter fabrication, Fe:InGaAsP (with Fe doping concentration of 4×10^{16} cm^{-3}) has a bandgap of ~1540 nm (Section 4.3.2), thus this can absorb photons with energy greater than the bandgap. These wafers have demonstrated pulsed THz emission in the wavelength range 800 nm–1550 nm and have reported a bandwidth of >2.5 THz [178].

An average optical power of 200 mW from the laser (with a repetition rate of 80 MHz) was split into two using a beam splitter; arm 1 (pump) was focused onto the sample, while arm 2 (probe) was focussed on to the 1 mm thick ZnTe crystal [201, 202] through the 4th parabolic mirror. The pump beam, incident on the emitter, generates THz pulses which are then collimated and focused using parabolic mirrors onto the same point on the ZnTe crystal as the probe beam is focused. A birefringence is induced in the ZnTe (EO crystal) and is proportional to the incident THz field. It changes the polarization of the probe laser beam, which is monitored using $\lambda/4$ plate and Wollaston prism. A $\lambda/4$ plate and the Nirvana balanced photodiodes, designed for 780nm, were used to detect any variation in the orthogonal polarised components of the probe pulse. Due to the small active region dimensions (19 μm×19 μm), the laser power was reduced using an attenuator to prevent thermal breakdown. An incident laser power of ~20 mW was focussed onto the sample using Olympus ×20 objective lens (the same lens used for CW mapping). The THz power expected from these devices was lower than a standard bow-tie emitter due to the small active region. This limits the maximum bias and maximum laser power that can be applied. The silicon lens applied in the CW mapping setup was used in this system to increase THz coupling efficiently from the substrate.

The sample was initially aligned for the maximum photocurrent at a bias voltage of 0.1V. A Keithley 2400 was used to bias the emitter. Once the sample was aligned for photocurrent, it was tested for THz signal. For this signal measurement, the sample was biased using Agilent waveform generator applying 0 to 1 V bias, at 25% duty cycle at 7.6 kHz frequency. The delay between the arrival of the pump and probe pulses is stepped to obtain a time-resolved THz pulse. The silicon lens was aligned to optimise the signal.

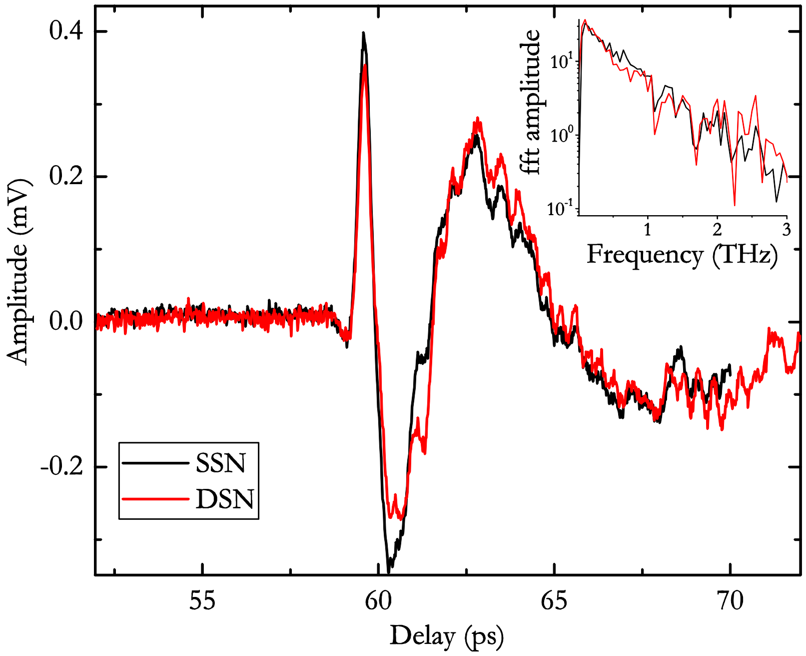

Figure 5.26: Measured THz time domain waveforms from the SSN and DSN emitter. The Fourier transform of the THz pulse is shown in the inset with a bandwidth exceeding 2 THz.

Figure 5.26 shows the THz time domain pulses obtained from the SSN and DSN emitter. A Fourier transform of the THz pulse was performed to retrieve information in the frequency domain. The deformity in the pulse shape is due to the dispersion and chirped output from the log-spiral antenna [122]. Both devices provided a bandwidth greater than 2 THz. The low amplitude of the pulses was due to the smaller active region, limiting the bias.

5.10.2 Mapping SSN and DSN emitter

The THz peak amplitude measured as a function of the laser spot position, for the SSN and DSN emitters, is shown the Figure 5.27. The NSG electrode of the SSN and NSG1 of the DSN emitter were biased during measurement. We observed that the magnitude of the THz signal waveform remained similar for both emitter types. As we can see from Figure 5.27, the laser excitation position, which generated the majority of the output signal was between the electrodes for both (a) SSN and (b) DSN emitters. This suggests the laser beam excited both electrodes simultaneously, enhancing emission due to the presence of higher optical electric field. The signal strength when the laser beam excited only the anode (biased at 1 V) was again lower, when compared with both electrodes excited at once. This is contrary to what has been previously reported, for a NSG emitter in pulsed setup [107]. They reported 50 times more power when the anode NSG is excited due to the presence of surface plasmons. However, in the present work no such surface plasmons could be observed, when only the anode was excited.

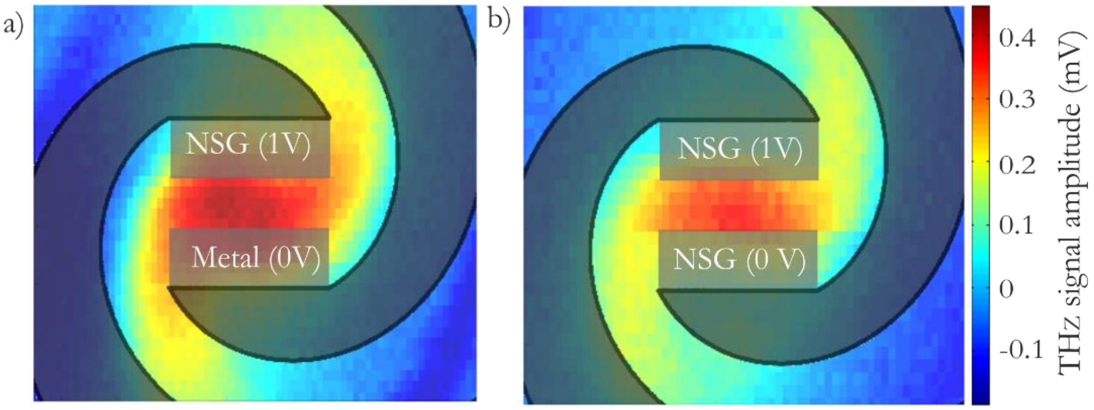

Figure 5.27: Raster scanned image to show the peak THz amplitude as a function of the excitation position at 11 V for the (a) SSN and (b) DSN emitter design respectively. The electrode biased at 1V, 25% duty cycle at 7.6 kHz frequency is shown. The spotsize is larger compared to the CW mapping due to the chromatic aberration of the lens.

Since the laser excitation spot was raster scanned across the emitter with the motorised actuators, there was a possibility that the peak THz amplitude would be shifted forwards or backwards in time, with respect to its aligned position. In order to confirm whether this phenomenon occurred, the pump-probe delay was scanned for each pixel position (1 μm×0.9 μm). Figure 5.28 shows the measured THz pulse as a function of delay for the different excitation positions, without changing the silicon lens position. THz pulse had a maximum when the excitation position was between the delay position 17.7 mm (59 ps) and 18 mm (60 ps). We can infer from this that the position of the THz pulse does not move with a change in excitation positions, although the amplitude was different for different positions. This confirms that measured THz peak amplitude as a function of laser excitation position shown in the Figure 5.27 is the actually THz pulse peak amplitude.

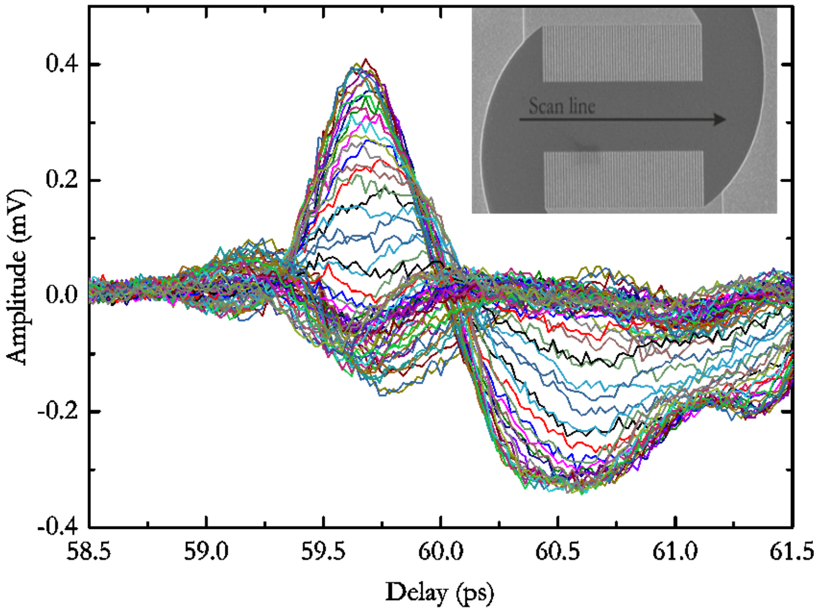

Figure 5.28: Measured THz time domain waveforms for different laser excitation positions. Inset shows the scan line which corresponds to the laser excitation positions.

5.11 Three-turn designs

The same design approaches were repeated on the three-turn log-spiral antenna, in order to characterize the Fe:InGaAs and Fe:InGaAsP wafers in Chapter 4. These possessed an active area of 11.3 μm×11.3 μm. The difference in the active area size, compared to the 2-turn log-spiral, was accounted for while designing the SSN and DSN structure, with the gap size scaled with the length of the NSG. The NSG on the DSN design had a length of 3.5 μm, resulting in a gap size of 4.3 μm, whereas for the SSN design the NSG was approximately 7 μm long, thus having a gap of 4.3 μm. The active region design for the SSN was varied, to remove the metal electrode that was present in the 2-turn antenna design.

The designs were fabricated on Fe:InGaAsP wafer with an Fe doping concentration of 6×10^{16} cm^{-3}. A similar doping level was chosen to those used in previous experiments, as this was proved to provide acceptable power levels. The wafer was processed to remove the cap layers and the antenna design was defined using the e-beam lithography technique previously referred to. The same procedures discussed in Section 5.5 were repeated and the devices were mounted on the PCB system and were tested on the CW THz photomixing system. SEM images of the fabricated emitters are shown in Figure 5.29.

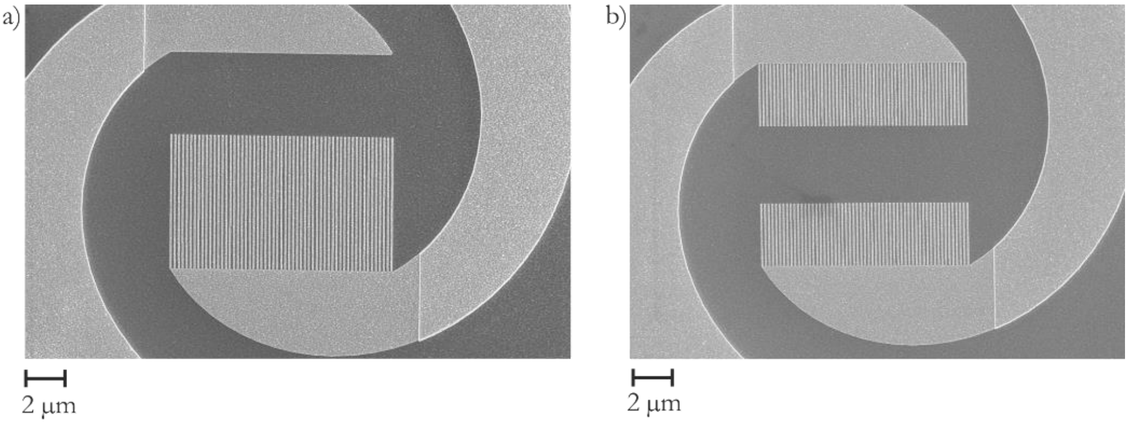

Figure 5.29: SEM images of the 3-turn log-spiral (a) SSN and (b) DSN emitter fabricated on Fe:InGaAsP wafer. The SSN had 7 μm long NSG on one side and DSN had 3.5 μm long NSG on both arms of the spiral.

The samples were aligned to maximise photocurrent, using an average optical power and bias of 10 mW and 0.1 V, respectively. The reason for choosing this low bias at this point, was to avoid burning the electrode tips. To provide the bias, a Keithley 2400 was once again utilised. The inset in Figure 5.30 displays an IV sweep for both emitters. The devices showed similar photocurrents and had an ohmic response within the measured bias range, ~0.45 mA at 0.1 V bias. For THz signal measurements, the NSG electrode of the SSN and DSN emitter were biased at 1 V amplitude, with a 25% duty cycle and at a frequency of 7.6 kHz.

Figure 5.30 shows the bandwidth obtained from the SSN and DSN emitter. The THz amplitudes were the same at all frequencies with a minor difference at frequencies greater than 1 THz. Both emitters gave a bandwidth of ~2 THz. The performance from these devices is consistent with the 2-turn designs with similar amplitudes and bandwidth for the SSN and DSN. Also no enhancement in the output power was observed.

When comparing the 2-turn and 3-turn SSN and DSN emitters, in all cases the devices with a 3-turn spiral antenna gave superior THz output signal, for the same input conditions, than that of the 2-turn emitters. We attribute this difference to the laser spotsize. While measuring bandwidth, an aspherical lens with a spotsize of ~12 μm was used, thus covering the whole active region for a 3-turn emitter generating more photo carriers. Irrespective of this, the obtained power levels from these emitters was still lower compared to the 3 pairs IDT design on the same Fe: InGaAsP wafer, with power levels of <1 nW at 1 THz from the SSN and DSN emitter.

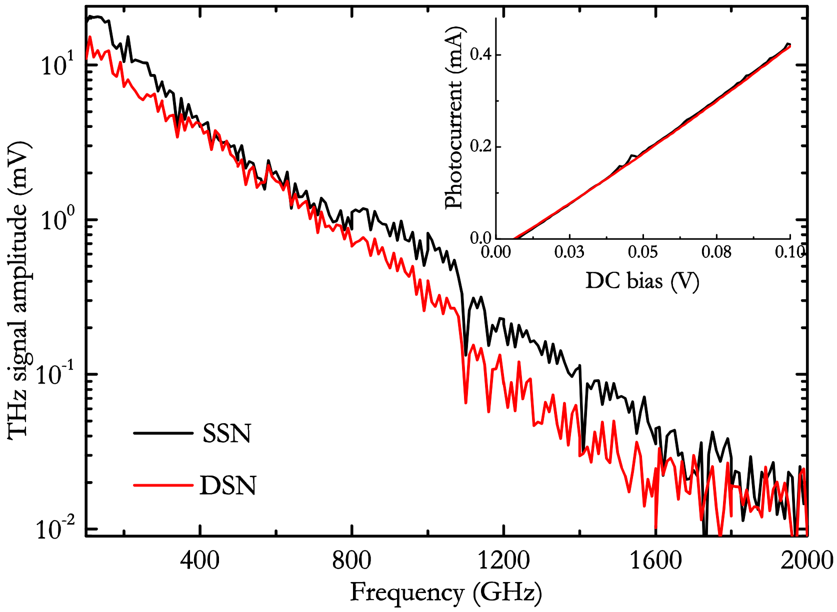

Figure 5.30: Measured THz signal amplitude as a function of laser beat frequency from the 3-turn log-spiral antenna SSN (black lines) and DSN (red lines) emitter. Inset shows the photocurrent measured from the devices. Colour coding is the same.

5.12 Discussions and conclusions

Two different emitter types were tested for CW THz power. Firstly, the resonant dual-dipole dual-slot antennas designed for enhanced performance at 1050 GHz were tested on the 1550 nm CW photomixing system. These emitters, engineered for enhanced emission characteristics were first designed by Duffy *et al.* [183], incorporating enhanced impedance matching for resonant emission. However, when the designs were fabricated on the Fe:InGaAsP wafer and tested on the 1550 nm CW photomixing setup, resonant emission was not observed. We attribute this discrepancy to the contact lines that provide additional impedance.

Secondly, a broadband spiral antenna with NSG electrodes was attempted. The NSG design has reported high power CW THz radiation. The NSG electrode design by Berry *et al.* [185], on a photomixer with ~10 μm gap between the anode and cathode reported ~0.8 mW THz power at 1 THz. Another NSG (of different dimension) with nanometre spacing between anode and cathode reported high output powers [171]. With these earlier reports about exemplar THz power levels, in this work, two different design variations of NSG electrodes was attempted. This could be used for integration with QCLs.

Furthermore, it can help to understand the contribution of carriers in CW THz emission and to confirm the existence of surface plasmons underneath the NSG. The two designs were SSN and DSN, with SSN having only one NSG and the DSN possessing two.

The designs were fabricated on a Fe:InGaAsP wafer which exhibited the best performance with 3 pairs of IDT as mentioned in Chapter 4. The designs were tested with the NSG electrode positively biased for both the SSN and DSN emitters. The measured bandwidth of the two emitters was < 2 THz and the output power levels was approximately half of that from the 3-pair IDT design fabricated on the same wafer. When the bias was reversed the performance of the SSN emitter was adversely affected, with reported bandwidth less than ~1 THz. However, the DSN emitter did not exhibit any difference in the signal strength or bandwidth when the bias was reversed. This variation in the performance of the emitters confirms that there is some contribution from the NSG for THz generation but it still raises an obvious question as to whether surface plasmons exist underneath the NSG and if that is the case, why superior emission characteristics are not observed in this instance. In order to determine this, the emitters were mapped using motorized stages.

The SSN and DSN emitters were mapped in the CW photomixing setup. This was achieved by varying the position of the laser spot on the emitter and observing the response. A smaller spotsize was used for mapping the emitters. When the emitter was mapped at 510 GHz with a horizontally polarized laser beam, it was observed that the emission from the SSN and DSN emitters was concentrated on the gap between the two electrodes. For the SSN design this was between the NSG and plane metal, while for the DSN it was in between the two NSGs. No significant enhancement in signal was obtained when only the NSG was excited. The improved signal strength from the gap is believed to be due to the laser beam exciting both anode and cathode simultaneously, creating an enhanced optical electric field at the NSG tips and resulting in a shorter recombination time of the photo carriers.

The emitters were also mapped with the bias reversed, i.e. the metal electrode at 1 V and NSG at 0 V for the SSN and NSG1 at 1 V and NSG2 at 0 V for the DSN emitter. This brought about a significant drop in the THz signal amplitude for the SSN emitter, as the optical electric field strength present at the plane metal electrode was less than when biasing the NSG, collecting fewer carriers. Although holes are attracted to the NSG tips, their lower mobility causes a reduction in the signal amplitude. Nevertheless, the maximum signal amplitude was observed when the gap between the electrodes was fully illuminated and this is due to the laser beam overlapping both the electrodes simultaneously. In the case of DSN emitter, there was no difference in the measured amplitude when the electrodes were reversed, since it does not involve any geometrical difference, electrons still attracted to NSG2 and holes to NSG1.

An interesting effect was observed when the polarization of the laser beam was changed from horizontal to vertical. The signal amplitude reduced by ~70% for the SSN emitter whereas for the DSN emitter the reduction was ~30%. An explanation for this behaviour is the wire grid polarizer effect preventing the beam from coupling into the semiconductor through the NSG. There is less absorption of the incident optical beam by the semiconductor at the tips even though the spot is in the centre, due to the absorption by the NSG electrodes. The presence of two NSGs on the DSN design, resulted in the effect being twice that experienced by the SSN, with just the one NSG. This effect also confirms the previous assumption that the laser beam hitting the gap overlapping both tips on the anode and cathode, results in maximum THz generation. The difference in signal amplitude with the two orthogonal polarizations also confirms the major role played by the optical electric field at the electrode tips.

Although the major contribution of THz signal amplitude was found when exciting the gap between the electrodes, there was signal produced (~50% at 510 GHz) when the laser excitation spot was within the first turn of the spiral. The signal amplitude produced from the spiral antenna was ~80% of the maximum signal at 210 GHz and was reduced to ~30% at 810 GHz. This confirmed that the exact region for the maximum generation of THz radiation is when the laser excitation spot was between the gap exciting both the electrodes and not when only the NSG is excited. This questions whether surface plasmons are actually contributing to the THz generation, or at least in the present scenario, in which the NSG electrodes were separated by 5 μm gap and smaller than the laser spotsize.

Furthermore, emitters were tested in a THz-TD setup to help further determine the existence of surface plasmons. Although the focusing lens allowed for a lower spatial resolution, compared to the CW THz photomixing setup, the laser excitation spot for the peak amplitude of the THz pulse was once again located in the gap between the NSG, rather than on the NSG electrodes. This confirms that the high concentration of optical electric field at the tips results in the faster recombination of the photocarriers resulting in THz generation. Measurements were repeated on a 3-turn log-spiral antenna with smaller active area, 11.3 μm×11.3 μm. Both SSN and DSN emitters, had similar THz amplitude and spectral bandwidth performance, which is in consistent with the 2-turn antenna results.

Chapter 6 Injection locking of THz QCL

This chapter gives an overview about the experimental procedures carried out to injection lock QCLs to a telecommunications wavelength (1.55 μm) laser source. A brief account of the various historical advances in the field of THz QCL phase locking, and the theory behind injection locking is briefly explained. The THz power and bandwidth of different photomixers, discussed in the previous chapters, are compared in the subsequent section. The experimental configuration used for locking is described, followed by the characterisation of the system performance in terms of telecoms laser linewidth and QCL voltage modulation due to self-mixing in the following sections. The injection locking of a THz QCL to a 1550 nm source using photomixers is then described. The locking range is measured at different EDFA gains and QCL biases. This chapter concludes with a discussion about the interpretation of the measured data and the physical explanation of the locking phenomenon.

6.1 Introduction

A laser utilises a gain medium in an optical resonator cavity, formed by two mirrors, which is pumped by an external source. Being a coherent source, the frequency and phase of the emitted photons is constant. However, due to mechanical vibrations, electrical noise and thermal fluctuations, instabilities in the emission wavelength/frequency can occur. This effect can be detrimental and various techniques to lock the emission wavelength of laser have been developed. A stable, inexpensive and low power source can be used to lock an unstable, expensive and high power source, thus rendering the locked source characteristics extremely desirable.

Locking of signals was observed by Huygens in 1865, who observed that the pendulums of two clocks synchronized when placed in close proximity. The explanation for this locking was that the mechanical vibrations were transmitted through the wall. A theoretical analysis for locking in electrical oscillators was given by Adler in 1946 [203]. Injection locking of lasers usually employs a master and a slave laser and locking is unidirectional by incorporating an isolator on the beam path. The injection locking of lasers using optical injection dates back to 1966, when Stover and Steier demonstrated locking of a He–Ne laser using a second He–Ne laser [204]. They predicted a theoretical locking range of 3.75 MHz and their experimental results were in agreement with the theory.

Locking of lasers can be broadly classified into two types, frequency locking [205] and phase locking [206]. In the case of frequency locking, the emission frequency from the laser is locked, thus reducing jitter, however, there will be no control over the emitted phase. The intrinsic linewidth of the laser remains the same. On the other hand, phase-locking reduces the jitter in terms of emitted frequency/wavelength and locks the phase to an internal/external source depending on the locking mechanism. In this case the laser linewidth reflects the line profile of the reference laser ensuring a narrow linewidth as low as 1 Hz [207].

Similarly to the other solid-state or gaseous lasers, THz QCLs are also prone to mechanical and electrical vibrations. Additionally, operation at cryogenic temperatures can contribute to frequency jitter as temperature fluctuations can change the refractive index of the gain medium. The jitter observed is highly undesirable and several methods have been adopted to reduce the linewidth, including gain medium engineering [208], locking using a phase locked loop [207], external cavity lasers [209] and DFB lasers [210].

The non-invasive and non-ionizing nature of THz radiation combined with the narrow linewidths produced by QCLs, make a suitable tool for sensing applications. Gas sensing applications typically require the QCL to have a linewidth lower than ~8 MHz [211], and other applications, for example molecular gas spectroscopy [212] and astronomical applications [1], require, both a narrow linewidth (few kHz) and a stable wavelength emission. Since the QCL requires a cryogenic operation temperature, thermal fluctuations can contribute to instabilities in the emission wavelength. Several methods adopted to lock the THz QCL are discussed in the Section 6.2.

6.2 Historical overview

Ever since Köhler *et al.* [213] demonstrated the first THz QCL, there have been efforts to measure the laser linewidth and to phase-lock QCLs. Barkan *et al.* [214] measured the linewidth of a THz QCL by heterodyne mixing a free-running THz QCL with two far-IR gas lasers in a GaAs monolithic membrane diode mixer, and they measured an instantaneous linewidth of <30 kHz. Barbieri *et al.* [215] also measured ~20 kHz linewidth by heterodyning two THz QCLs using a point-contact Schottky diode. Although a few kHz linewidth was reported, the linewidth was also observed to broaden to greater than 21 MHz when measured over longer timescales, [214] and they attributed this effect to thermal fluctuations causing a refractive index change in the gain medium. Soon after, several techniques were implemented to lock THz QCLs to reduce frequency jitter, phase noise, and linewidth enhancement, and to retrieve phase information. In this section, the key methods adopted for locking (both frequency and phase) reported over the past few years are given.

The first demonstration of locking a THz QCL was reported by Betz *et al.* in 2005 [216]. They locked a 3.0 THz QCL with resonant phonon (RP) active region with double-metal waveguide to a far IR laser (from methanol line, 3.1059368 THz) in a GaAs-Schottky-diode mixer at room temperature. An intermediate frequency (IF) from an oscillator was also mixed in the diode mixer, generating sum and difference frequency components. By comparing the second harmonic terms, an error signal was generated in a conventional phase-lock loop which controlled the QCL current. By controlling the QCL current, the emission frequency is changed dynamically, thus reducing the frequency difference. They measured the linewidth of the locked QCL to be ~65 kHz at -3 dB level which was limited by the reference oscillator linewidth.

Baryshev *et al.* demonstrated phase-locking of a THz QCL by mixing the two lateral modes in the QCL [217]. The lasing modes at 2.742 THz and 2.749 THz from the RP design with double-metal waveguide were mixed in a NbN hot electron bolometer (HEB) mixer. The beat frequency output was amplified by a MMIC amplifier and finally fed to a locking counter. The generated error signal was fed to the QCL bias current through a phase-lock loop (PLL). They reported a Lorentzian curve with a linewidth of 12.6 kHz from the two lasing modes implying a narrow linewidth of ~6.3 kHz from each mode. Rabanus *et al.* [218] also reported phase locking of a QCL using a HEB mixer. They mixed a 1.5 THz double metal QCL and a local oscillator signal in a HEB, which generated the IF frequency and was down converted in another mixer. The error signal produced was fed back into the QCL to alter the current via a PLL. Not only was the QCL phase-locked, the frequency stability was ~100 MHz and limited only by the resolution bandwidth (RBW) of the spectrum analyser. Also, by slightly modifying the arrangement, the THz QCL acted as a local oscillator for the HEB. Khosropanah *et al.* [207] used a NbN HEB for mixing a 2.7 THz QCL and a microwave signal (using a chain of multipliers) and feeding the error signal to control the QCL bias using a PLL. They measured a narrow beat linewidth of 1 Hz limited by the RBW.

A slightly different approach was taken by Danylov *et al.* [219]. They used a Schottky barrier diode (SBD), instead of cryogen cooled HEB, and a THz frequency gas laser. The 2.408 THz frequency SISP waveguide QCL and the CO_2 optically pumped laser (OPL) at an emission wavelength of 2.409293 THz was mixed in the SBD. The IF signal produced was then used to generate an error signal which controlled the QCL current through a PLL. They observed a THz frequency linewidth of ~3–4 kHz which is a tenth of the reference CO_2 OPL linewidth. Subsequently, they demonstrated the frequency locking of a 2.32 THz BTC QCL with SISP waveguide and the harmonic of a microwave source (110 GHz) using 21 multiplier chains in a GaAs Schottky diode mixer [220]. They reported better SNR due to the coupling and AM noise reduction from using the GaAs Schottky membrane diodes. Hayton *et al.* demonstrated the phase-locking of a third order DFB THz QCL using a GaAs/AlAs superlattice device at room temperature, which acted simultaneously as a frequency mixer and multiplier [221]. A conventional PLL controlled the QCL bias and the linewidth of the locked QCL was 48 kHz.

All the methods discussed above used either a microwave source (with multiplier chains) or a gas laser as the local oscillator. Both these techniques are inconvenient due to the low power at higher frequencies from the former and the bulkier nature of the latter. In order to compensate for this, a new method for frequency locking THz QCL was demonstrated by Richter *et al.* [222]. They used the absorption features in methanol vapour as a locking reference. The 2.5 THz QCL was focussed onto a liquid He cooled Ge:Ga photoconductor through the methanol vapour-filled gas cell. This in turn produced an error signal which controlled the QCL bias through a conventional PLL. They observed that frequency jitter reduced from 15 MHz to 300 kHz by using this technique. Ren *et al.*

also exploited the molecular absorption of methanol vapour to frequency lock a QCL [223]. They used a third order DFB QCL at an emission wavelength of 3.5 THz and a NbN HEB for detection. They reported a locked linewidth of 18 kHz compared to the free running linewidth of 1 MHz. The use of cryogen cooled detectors was to ensure a fast and sensitive response with reduced noise. Subsequently they demonstrated the locked THz QCL performance as a LO [223].

Locking to a molecular transition line has been shown to greatly improve the linewidth of THz QCLs, however, it has a limitation of locking to only specific THz frequencies which have strong gas vapour absorptions. In order to avoid complexities in terms of source power and cryogenic detectors another approach to lock the phase is to lock to the frequency comb of a mode-locked femtosecond laser. Barbieri *et al.* [224] demonstrated that a THz QCL can be phase locked to the comb of a mode-locked femtosecond erbium doped fibre laser. The 2.7 THz QCL was phase-locked to the n^{th} harmonic of the 90 MHz repetition rate of a 775 nm laser using a ZnTe crystal. The frequency-doubled 150 fs laser pulse, on coinciding with the QCL radiation in a ZnTe crystal, modulates the amplitude of the laser beam. By measuring the signal (filtered) from the photodiodes and comparing with the RF synthesiser, the error signal was fed to the QCL through a conventional PLL. They measured a locked linewidth of 1 Hz limited by the RBW of the spectrum analyser, compared to a free-running linewidth of 1 MHz. Subsequently they demonstrated the mode-locking of a THz QCL using a similar setup [225]. Ravaro *et al.* [226] implemented a slightly different approach to phase-locking to a femtosecond source using photomixers. Instead of using an electro-optic crystal for detection, a GaAs photomixer was used to generate the photocarrier THz comb. The beat notes were produced as a result of the interaction of the QCL frequency and THz comb. The IF photocurrent was compared using a RF mixer and the error signal was fed to the QCL and they reported a RBW limited linewidth of 1 Hz.

Injection-seeding, in which an external THz pulse is injected into the QCL cavity, can be used for selecting the longitudinal modes of the laser, [227] and is different from injection-locking. For injection-seeding, the THz pulse is injected into the QCL as the laser power is building up from the noise floor, and will determine the QCL output [228]. Phase-seeding on the other hand employs a weaker THz pulse and the phase of the injected pulse determines the phase of the QCL output [229]. In the case of injection seeding, the spontaneous emission (small signal) and the injected THz pulse (large signal) gets amplified in the laser cavity and the phase of the laser emission is determined by the large signal (usually injected THz pulse, unless there is no injection). In the case of injection locking, the laser is running in CW and the spontaneous emission determines the laser emission frequency and phase during switching on and will change slightly afterwards. By injecting the signal close to the emission frequency, the frequency and phase is controlled.

Due to the expensive and bulky size of the femtosecond lasers and the requirement of complex optical and electrical components, phase-locking using ultrafast lasers is inconvenient. An ideal source for locking is expected to have sub Hertz linewidth, broadband tunability and high power at THz frequencies. In the experiments described later in this chapter, the injection locking technique is used to lock a 2.0 THz QCL to a 1550 nm telecoms lasers using photomixers. Photomixers are continuously tunable devices with the emission linewidths dictated by the excitation laser linewidths. All QCL frequencies lying within the spectral bandwidth of the photomixer can be injection locked.

6.3 Theory of injection-locking

A theoretical explanation for the locking phenomena in oscillators was first given by Adler [203] in 1946. A simple schematic representation of injection locking is shown in Figure 6.1. It involves two lasers or oscillators: master (ω_1), and slave (ω_0). The master laser is the reference and the slave laser in the source being controlled. The master signal is fed into the slave laser thus controlling the slave output. The master output, ω_1 is usually isolated from the slave by using an isolator to avoid feedback.

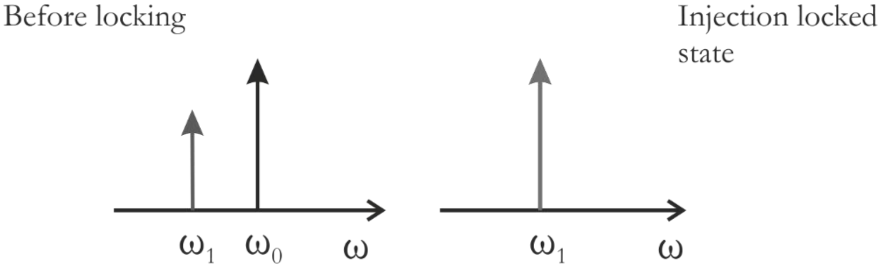

Figure 6.1: Schematic diagram explaining the injection locking of two laser. A master laser (ω_1) is tuned closed enough to the free-running slave laser (ω_0). When ω_1 is the same as ω_0, the slave laser is injection locked and emitting only ω_1.

Initially, the slave laser is free running with an intensity I_0 at a frequency of ω_0. A weak external signal is injected into the slave laser cavity from the master source with an intensity I_1 at a frequency of ω_1. If ω_1 is too far from ω_0, then the slave laser is not properly locked and ω_1 may not get amplified. As ω_1 approaches ω_0, the injected signal results in stimulated emission and gets amplified in the slave laser cavity. This amplification of the external signal in the laser cavity was termed ‘regenerative amplification’ by Siegman [228]. If the injection frequency is tuned close enough to ω_0, there can be interference or beating and the system can exhibit complex behaviour, as shown in Figure 6.2. When ω_1 is close enough to ω_0, the slave laser is forced to lase at the master frequency ω_1 and the slave laser intensity, I_0. No matter how close the master frequency is tuned closer to the slave frequency, the intensity remains constant at I_0 within a certain range defined as the ‘locking range’.

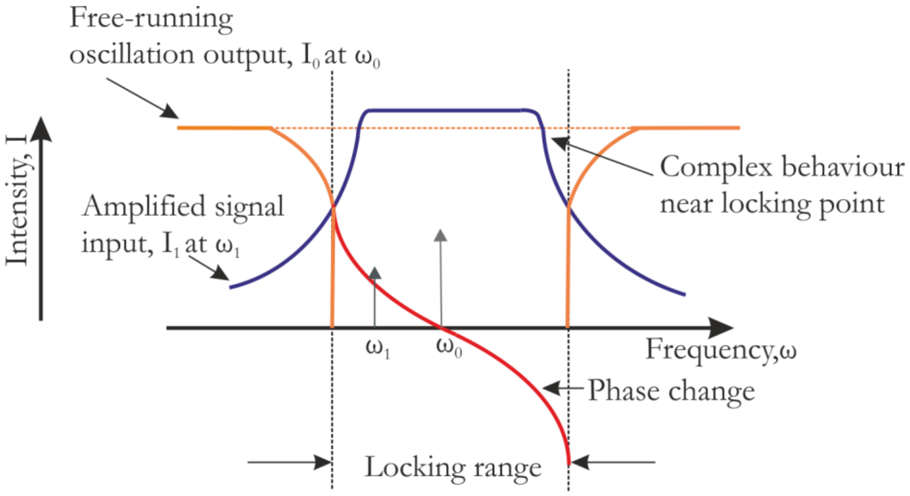

Figure 6.2: Intensity and phase response of the slave laser frequency inside or outside the injection locked range. The locking range, free-running oscillation intensity and the phase change (red curve) is marked. Image reproduced from ref [228].

If ω_1 is tuned close enough to ω_0 and is within the locking range of the slave laser, the slave behaviour resembles that of the master. The amplified intensity of the master output, I_1 will be equivalent to the free-running slave laser intensity, I_0. Another important parameter affected by injection locking is the phase of the slave output with respect to the master input. The phase change in injection-locked oscillators was described by Adler [203]. The phase change in the locking range is π radians or (180º), as shown by the red curve in the Figure 6.2. The difference in the phase for a stable locked slave output is π radians within the locking range.

In this work, in order to lock the QCL, a second laser or a coherent source was required to interact with the QCL active region. As mentioned in Chapter 2, the active region of the QCL is a GaAs/AlGaAs heterostructure with a bandgap of ~1.5 eV, which is equivalent to ~820 nm. Since the lasers used in the present work have telecoms wavelengths, it is practically impossible to lock the QCL without using an intermediatory source which can convert the 1550 nm to THz wavelengths, or a non-linear crystal to convert the 1550 nm to 780 nm by frequency doubling. The latter option is not preferential due to the low efficiency and system complexity [230]. Photomixers, however, can generate tunable CW THz radiation in the 100 GHz to 2.4 THz range (see Chapter 3 and Chapter 4), they do not require high power lasers (unlike non-linear generation) nor cryogenic temperatures and are comparably easier to operate. In the following section the different photomixers studied in Chapters 3 and 4 are compared to find the most suitable source.

With photomixers being identified as an appropriate source, the following experimental work utilises the photomixer signal as the "master" and the QCL as the "slave". The QCL emission frequency is dictated by photomixer frequency i.e., the pump laser heterodyne frequency. When the heterodyne signal is tuned closer to the QCL emission frequency, there can be stimulated emission in the laser cavity, thus the QCL starts lasing at the heterodyne frequency. In fact, the phase of the THz signal from the photomixer (outside the locking range) passing through the QCL at a particular heterodyne frequency is dependent on the path length difference between the emitter, QCL facet and receiver. However, if the heterodyne frequency is changed, there can be a slight difference in the emitted THz phase due to the difference in optical path length for different heterodyne frequencies. The locking range for small signal coupling is given as [228],

$$\Delta\omega_{lock} \propto \sqrt{\frac{\mathrm{P}_i}{\mathrm{P}_s}} \tag{6.1}$$

where $\Delta\omega_{lock}$ is the locking range, P_i and P_s is the injected (photomixer) and slave (QCL) power respectively. The locking range will increase with injected signal strength. For a stable locked state, the phase angle, $\phi = \phi(\omega_1)$ of the output signal I_0 with respect to I_1 is defined as [203, 228],

$$sin[\phi(\omega_1)] = \left(\frac{\omega_0 - \omega_1}{\omega_m}\right) \tag{6.2}$$

and thus

$$\phi(\omega_1) = sin^{-1}\left(\frac{\omega_0 - \omega_1}{\omega_m}\right) \tag{6.3}$$

where ω_m is defined as the half locking range. From Eq. (6.2), the term on the right-hand side can only have values ranging from -1 to +1, corresponding to a $\phi(\omega_1)$ value between -π/2 radians (-90°) to +π/2 radians (+90°), thus a total phase change of π radians (180°). As the photomixer frequency is tuned closer to the QCL frequency, the emitted intensity will not change largely due to the 'flat top' intensity profile shown in Figure 6.2 in the locking range and the phase inside this range will change by π radians. The first step in injection-locking the QCL is to find a suitable photomixer. The performance comparison of the potential photomixers is discussed in the Section 6.4.

6.4 Comparison between commercial and in-house emitters

A weak monochromatic signal with frequency ω_1 close to the THz QCL frequency ω_0 (~2.0 THz) is required for locking. The 1550 nm photomixers discussed in Chapters 3 and 4 are ideal sources due to their high spectral bandwidth of ~2.4 THz and narrow linewidth (limited by the excitation laser jitter ~400 MHz). However, the reported power levels from these emitters is low compared to the commercial TOPTICA emitter.

Figure 6.3 shows the THz signal amplitude as a function of laser beat frequency for the Fe:InGaAs, Fe:InGaAsP and TOPTICA emitter. The measurement was performed on a two parabolic mirror set-up, described in Figure 4.15, with an incident laser power of 10 mW. The best performing Fe:InGaAs and Fe:InGaAsP emitters with 3-turn log-spiral antennas and 3 pairs of IDT designs are compared here. The Fe doping concentration for the Fe:InGaAs and Fe:InGaAsP wafers was 0.5×10^{16} cm^{-3} and 4.0×10^{16} cm^{-3}, respectively. The applied bias was modulated with a 7.6 kHz square wave between 0 V and 1 V for use with the in-house emitters (Fe:InGaAs and Fe:InGaAsP) and between -2 V and 0.5 V for use with the commercial TOPTICA emitter. Although the difference in the THz signals could be attributed to the bias values, the contributing factor for this disparity is the substrate. Unlike the in-house emitters which have a single semiconductor layer responsible for the emission process, the TOPTICA emitter has a heterostructure comprising multiple periods contributing to emission. By calibrating the experimental arrangement with a helium-cooled germanium bolometer, the average power, after accounting for the 50% duty cycle, from the best performing Fe:InGaAs and Fe:InGaAsP emitter at 2.0 THz was estimated to be ~6.0 nW. This power level is 5 times lower compared to the value of ~30 nW for the TOPTICA emitter.

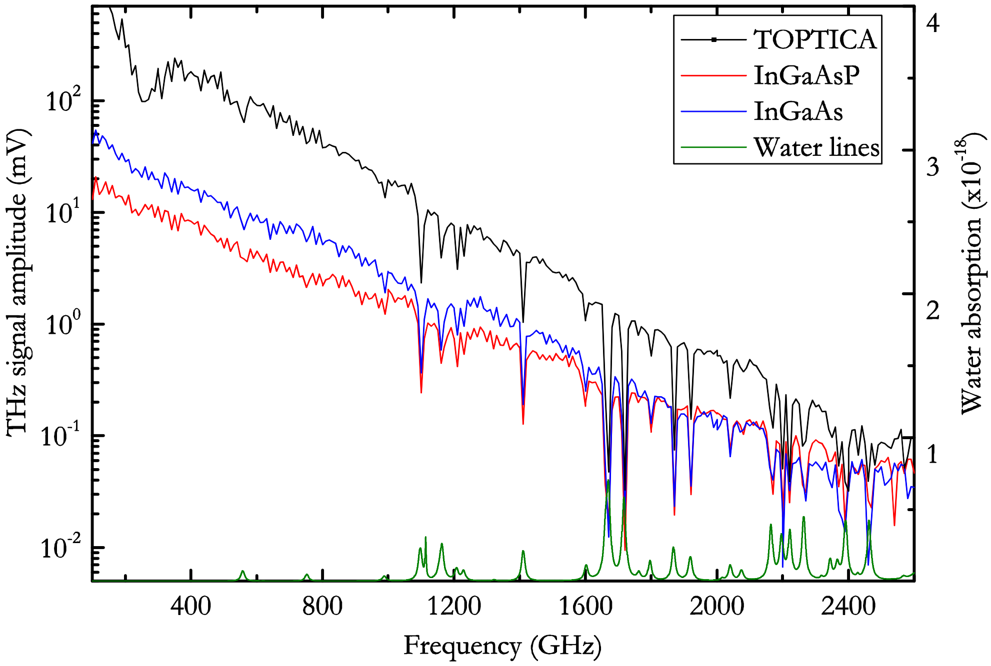

Figure 6.3: THz signal amplitude as a function of heterodyne frequency plotted for the TOPTICA emitter, Fe:InGaAs and Fe:InGaAsP wafers having a 3-turn log-spiral antenna with 3 pairs of IDT design and Fe doping concentration of 0.5×10^{16} cm^{-3} and 4.0×10^{16} cm^{-3}, respectively. The bias levels for TOPTICA (black line) was -2 V to 0.5 V and for Fe:InGaAs (blue line) and Fe:InGaAsP (red line) were 0 V to 1 V amplitude, square pulses at 7.6 kHz frequency.

Since the in-house emitters have a low breakdown field (12.5×10^3 Vcm^{-1}) and saturated at higher laser powers (~15 mW), increasing the THz power from the emitters by increasing the applied bias or incident optical power is not practical, thus the commercial TOPTICA emitter was chosen for subsequent measurements. The maximum laser power applied to the TOPTICA emitter was ~35 mW for a square wave bias from -2 V to 0.5 V. With exemplar power levels from the TOPTICA emitter, its ability to lock the QCL was then investigated.

6.5 Experimental setup

The experimental configuration discussed in Section 3.7 of Chapter 3 used two 90 degree off-axis parabolic mirrors to guide the THz radiation from the emitter to the detector. This system therefore had to be converted to use four *f/2* parabolic mirrors in order to focus the photomixer THz radiation into the QCL and collect the QCL output, as shown in Figure 6.4. Although the DBR lasers, characterized in Chapter 3, had a frequency jitter of ~400 MHz, these were used initially to align the system.

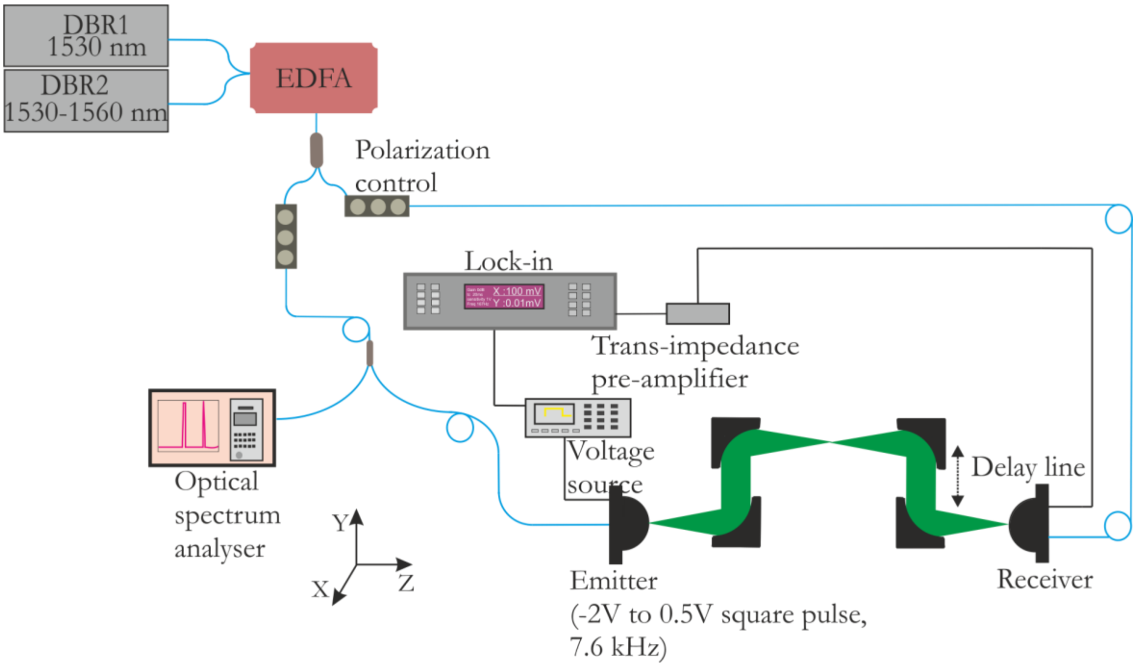

Figure 6.4: : Schematic diagram of the QCL injection-locking alignment. DBR lasers were used.

The output 1 from the fibre coupled DBR lasers was fed into the EDFA. The output from the EDFA was split into two using a 2×2 splitter, which were fed into the emitter and detector through manual polarization controllers (PC). The emitter position was changed to incorporate the two additional *f/2* parabolic mirrors on the beam path. Since incorporating two mirrors on the beam path changes the optical path length, appropriate fibre lengths were also chosen to compensate for this. The fibre path length to the emitter was 4 m (1 m + 2 m + 1 m) and the fibre path to the detector was 4.7 m (1.7 m + 2 m + 1 m). The fibre length difference of 0.7 m was used to compensate the 1.05 m THz signal path length in free space, thus ensuring the system is at zero path difference. The 1st and 2nd parabolic mirrors were aligned followed by the 3rd and 4th parabolic mirrors for better beam focusing between the 2nd and 3rd mirrors. The 4th parabolic mirror and the TOPTICA receiver were placed on the delay stage for controlling the optical path length.

The emitter was biased using an Agilent AWG with a square wave of -2 V to 0.5 V at 7.6 kHz frequency. The gain of the FEMTO trans-impedance amplifier was set to 10^7 (V/A). The procedures followed to obtain optimum delay, discussed in Chapter 3 were repeated here. The PC controllers were adjusted each time the frequency was changed to obtain the maximum THz signal.

6.5.1 2.0 THz QCL

The QCL based on a BTC active region emitting at 2.0 THz, characterized in Section 2.5.2 Chapter 2, with a ridge length of 2.5 mm and ridge width of 200 μm, was used for this work. The measured LIV and spectra are plotted in Figure 6.5 (a). The threshold current was ~720 mA and the lasing maximum occurred at 760 mA at 15 K.

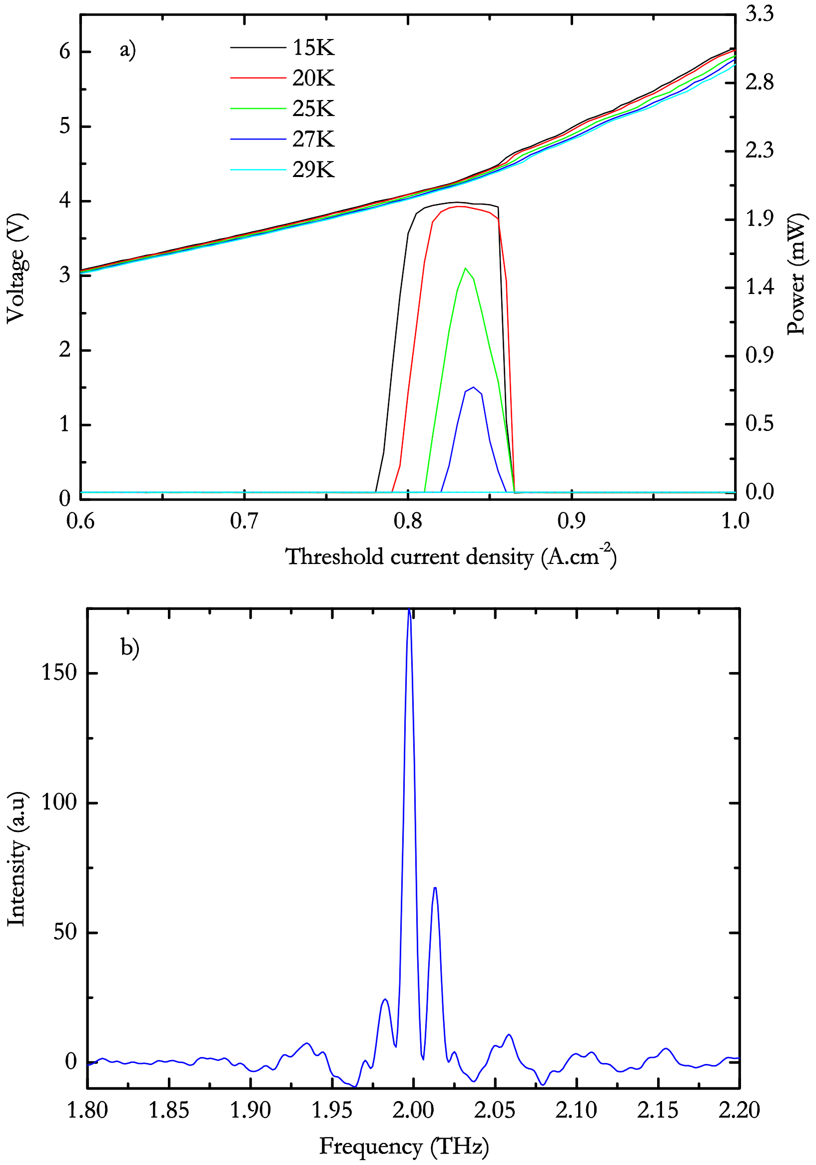

Figure 6.5: (a) LIV from the L1071 2.5 mm long device at different heat sink temperatures in CW mode. (b) Spectra of the QCL at a DC current of 750 mA and 15 K heatsink temperature.

For the locking measurement, the QCL was cooled to 10 K and a constant current of 750 mA using the DC source (Keithley 2400). The CW spectra measured from the QCL showed two strong modes at 1.997 THz and 2.012 THz at 750 mA, as shown in Figure

6.5 (b). It was also observed that the QCL lased at two different modes, 1.997 THz and 2.012 THz.

6.6 System characterization

6.6.1 Fibre laser jitter measurement

The DBR lasers used for the characterization of emitters in Chapters 3, 4 and 5 had a frequency jitter of ~400 MHz over a measurement span of 30 minutes. This jitter is highly undesirable and results in unstable locking of the QCL. Also, as the locking range of the QCL can be well below this value, it was clear that a narrower linewidth (~few kHz) laser source was required.

The Agilent 8164B Lightwave Measurement system consists of a DFB laser with a wavelength tunability between 1450 nm and 1580 nm at an output power of ~15 mW. A single wavelength Rio ORION laser module was used in conjunction with the Agilent source to produce the beat frequency. This had an emission wavelength of 1554.97 nm and an output power of ~10 mW. The laser had a narrow linewidth of <15 kHz and a very low frequency jitter. Being a single frequency laser, the Rio laser was run continuously at a set wavelength whilst the Agilent laser was controlled using a LabView program. The lasers were coupled and split into two using a 2×2 combiner-splitter and the combined laser frequency jitter was measured using an InGaAs photodiode connected to a spectrum analyser, similar to the setup shown in Figure 3.5.

Figure 6.6 shows the laser jitter data for a measurement span of 20 minutes. The jitter was ~20 MHz and compared to an instantaneous jitter of ~4 MHz (not shown in the figure). Although the laser jitter was still in the MHz range, it was 20 times lower compared to the DBR lasers, hence, all the locking measurements were carried out with the Agilent and Rio lasers.

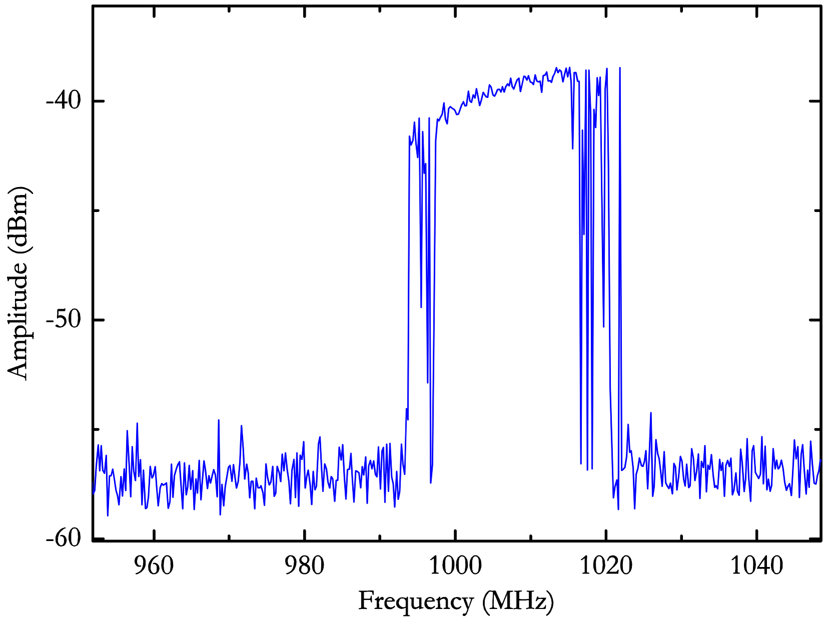

Figure 6.6: Combined laser jitter of the Agilent and Rio sources over a 20 minute interval. The difference frequency was set to be 0 GHz and the laser jitter was approximately 20 MHz.

6.6.2 QCL voltage modulation

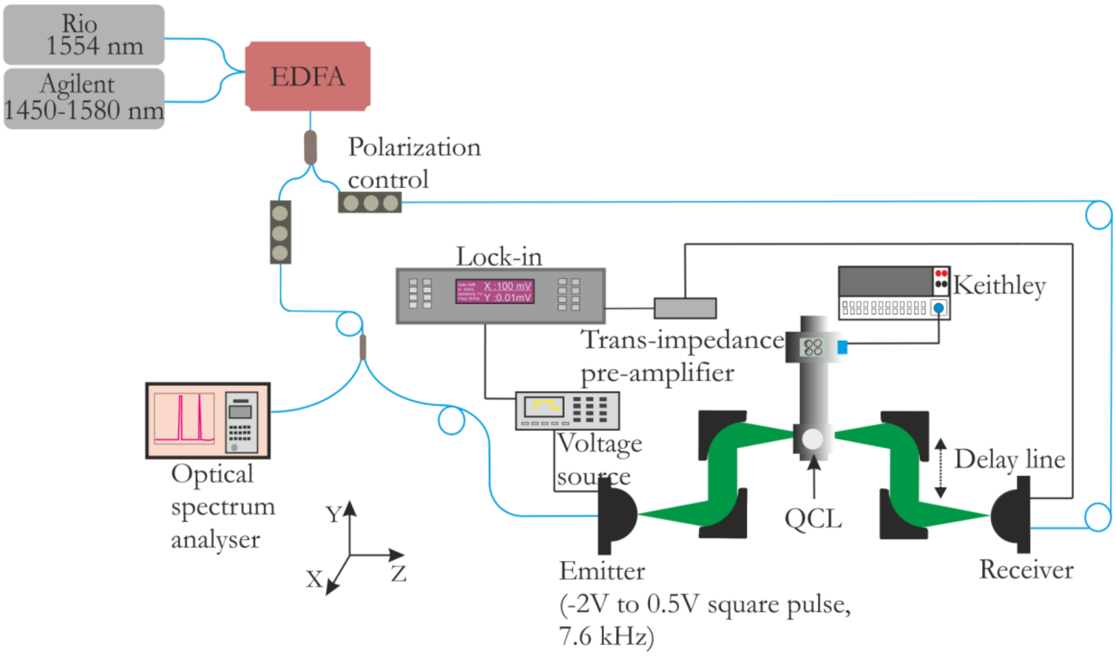

Figure 6.7: Schematic diagram of the QCL injection-locking experiment. TOPTICA emitters and receivers were used and QCL was cooled down to 10 K using a continuous flow liquid Helium cryostat.

The focused THz spotsize from the photomixer was measured using knife edge measurement, similar setup used in Section 5.7.1, at the focal point between the 2nd and 3rd parabolic mirrors, and was found to be ~250 μm at 1 THz [176]. This size is comparable to the depth of penetration of the waveguide mode into the substrate of the QCL. Although the ridge height of the QCL was ~14.5 μm, the mode penetration depth of the QCL due to the SISP waveguide ensured efficient coupling into the QCL active region.

When the photomixers, parabolic mirrors, and detector were all aligned, the QCL was then introduced into the THz beam path, between the 2nd and 3rd parabolic mirrors as shown in the Figure 6.7. The QCL position was optimised to ensure that the THz beam passed through the facet. The alignment procedure involved maintaining the QCL and cryostat at room temperature and manually controlling the position using an XYZ linear translation stage. A 1 mm aperture mounted to the front of the QCL facet, as shown in Figure 6.8, was used to verify the THz beam passed through the QCL active region. The QCL was then cooled to 10 K and was biased using a DC source (750 mA), whilst maintaining alignment with the XYZ stage.

Interestingly, a strong modulation of the QCL drive voltage due to self-mixing was observed when monitored using a lock-in amplifier referenced to the emitter modulation frequency of 7.6 kHz. The QCL drive voltage was modulated heavily when the QCL was in the THz beam path and, therefore, this phenomenon was also used to monitor alignment of the system. This was particularly useful as the system alignment was very sensitive to even subtle changes of the optical bench. The drive voltage modulation was due to the self-mixing effect [231, 232]. This is where the THz radiation emitted by the QCL is reflected from the emitter surface and fed back into the laser cavity resulting in a change of the QCL threshold gain, power and drive voltage [232]. The QCL voltage was thus modulated at 7.6 kHz since the surface reflectivity of the emitter changed with the applied bias. The modulation voltage vanished when the emitter was turned off suggesting a thermal effect, resulting a shift in temperature. Furthermore, the modulation voltage didn't had any dependence with the heterodyne frequency, however it was found to depend on the emitter modulation frequency. The QCL was aligned to maximize the modulation voltage as it depends on the position of the QCL as well the phase of the THz´[1] beam. The Z position of the QCL thus had to be aligned carefully to optimise the modulation signal.

---

[1] THz´ refers to the THz radiation emitted by the QCL

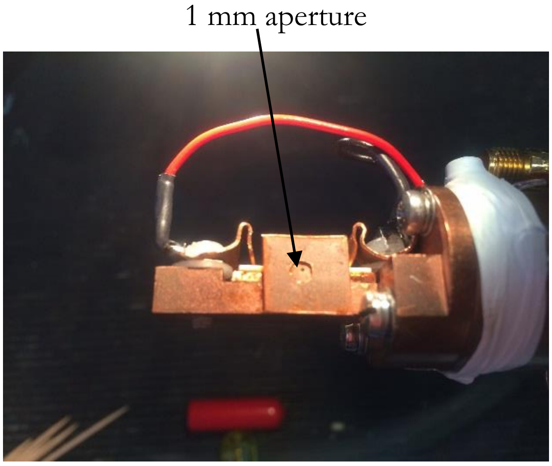

Figure 6.8: Photographic image showing the 1 mm hole on a copper sheet attached to the cryostat infront of the QCL for alignment purpose.

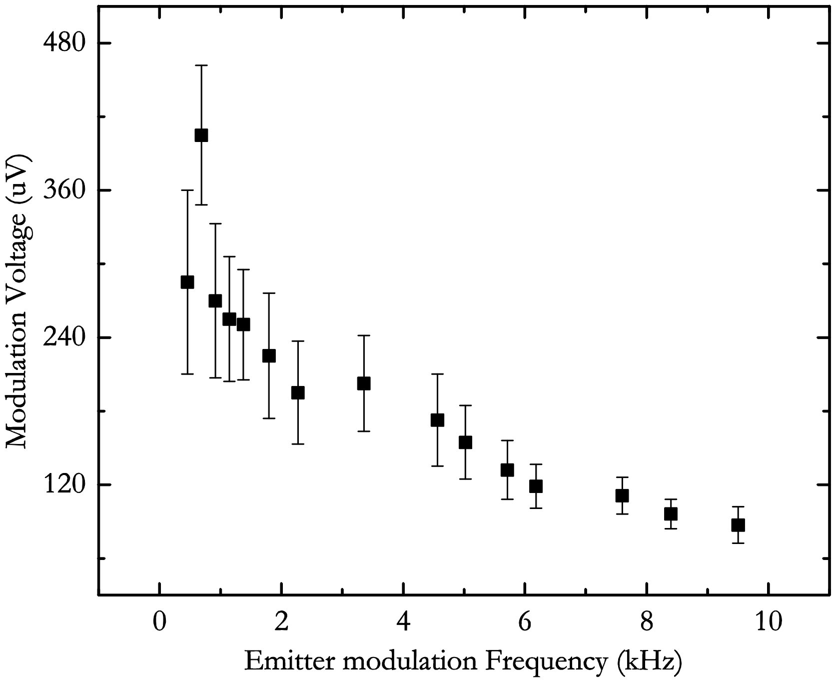

Figure 6.9: QCL modulation voltage plotted as a function of emitter modulation frequency. The error bars correspond to the fluctuations in the voltage signal and decrease with frequency.

Figure 6.9 shows the QCL modulation voltage as a function of emitter modulation frequency. The QCL modulation voltage amplitude decreased monotonically with increase in emitter modulation frequency, where a peak was observed at 1.3 kHz. However, the instabilities (or error bars) were quite high at this frequency range. Although, a higher amplitude was measured below 7.6 kHz, the signal became noisy and made it difficult to align as the fluctuations were as high as ~±20 % at lower frequencies. This increase in noise is attributed to the longer time for which the signal perturbed the laser cavity and is due to the thermal effects in the emitter. As such the 7.6 kHz frequency was thus chosen to carry out further measurements. Also it was observed that the modulation voltage slowly drifted from the peak value to a lower value (~10%) when left for 10 minutes, which could be due to the misalignment arising from the thermal effects in the QCL. With the QCL in the path of the beam and aligned for peak modulation signal, it can be verified experimentally if the QCL was indeed injection locked.

6.7 Coherent detection of locked signal

The THz signal amplitude in the locked state was measured at the receiver, referenced to the emitter modulation frequency. The amplitude and phase of the measured THz radiation was observed to change with the presence of the injected signal, as will be discussed in the following subsections.

6.7.1 Signal on the receiver

The QCL was electrically connected at a DC current of 750 mA and the emitter biased using square waves from -2 V to 0.5 V at 7.6 kHz, with an EDFA power of 18.60 dBm. The heterodyne frequency was then scanned in the range ±1 GHz from the QCL emission frequency (i.e. 1998 GHz) whilst measuring the receiver signal via the lock-in amplifier. The receiver signal increased twenty times when the heterodyne frequency was tuned to 1997.14 GHz. This signal was optimized by incrementally moving the XYZ linear translational stages. It was observed that the signal vanished when the QCL position was misaligned. The delay line was moved to the peak THz amplitude position and the heterodyne frequency scanned. Special care was taken to ensure that the QCL temperature didn't fluctuate by more than ± 500 mK during these measurements.

Figure 6.10 shows the THz signal amplitude measured as a function of heterodyne frequency between 1960 GHz and 2050 GHz using a 20 MHz step size. The measured amplitude had three major peaks and a few minor peaks spaced 16 GHz apart, corresponding to the Fabry-Perot modes of the QCL cavity. The peak amplitude was at 1997.12 GHz, which is the emission frequency of the QCL. The THz signal amplitude was measured to be greater than 145 mV, which suggested that the QCL was fully locked by comparing the power measurements. The QCL and emitter measured directly onto the helium cooled bolometer was ~9 V and ~1.6 mV respectively. For the measurement, a DC current of 750 mA was applied to the QCL and emitter was at 2 THz (heterodyne frequency). The ratio of powers is ~5625 and thus the electric field ratio is ~75. The emitter field measured on the receiver at 2 THz was ~2 mV and hence the expected electric field amplitude at the receiver from QCL is 75×2=150. This value is in consistent with our measurements as in Figure 6.10.

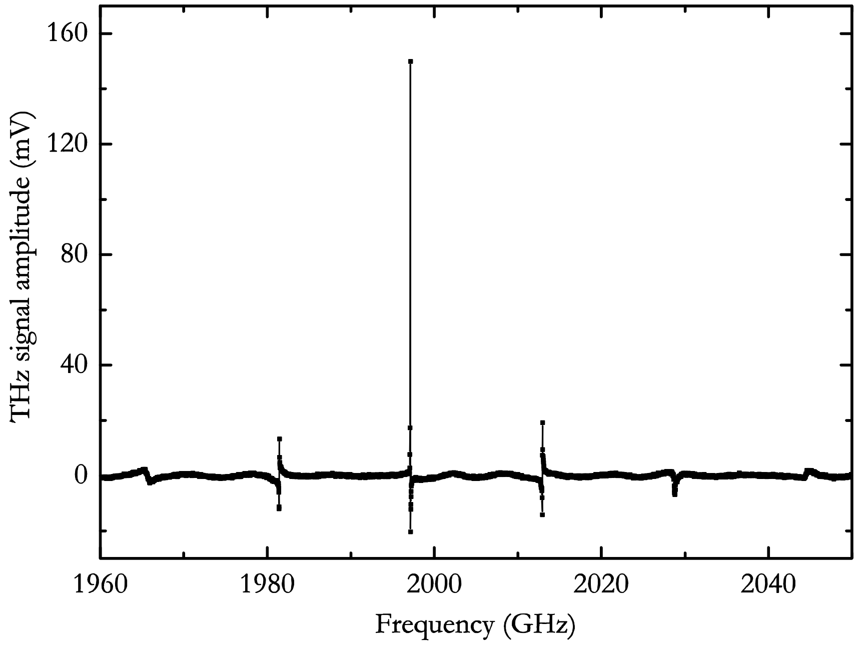

Figure 6.10: THz signal amplitude measured from the receiver (referenced to emitter frequency) as a function of heterodyne frequency between lasers. QCL was on the THz beam path and was electrically connected at a DC current of 750 mA.

Figure 6.11 shows the change in QCL voltage modulation measured for different heterodyne frequencies. When the QCL was locked at 1997.12 GHz, there was a sudden drop in the modulation voltage amplitude as the emitter radiation interacted with the laser dynamics. The heterodyne frequency had a strong dependence in the modulation voltage. The experiment was repeated multiple times, which confirmed that there was a change at the locked frequency, 1997.12 GHz. However, over the course of the measurements it drifted to 1997.11 GHz, which was attributed to laser jitter (~10–20 MHz).

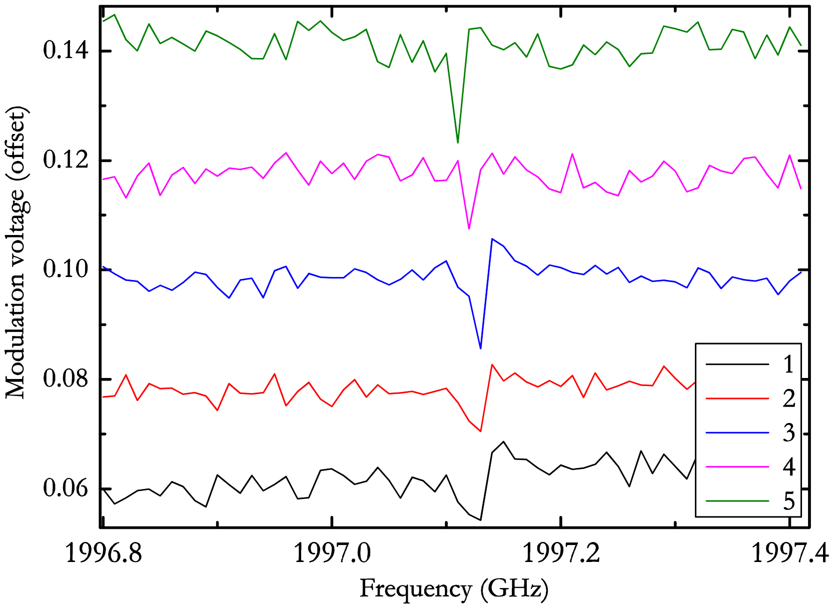

Figure 6.11: QCL modulation voltage plotted as a function of heterodyne frequency (referenced to the emitter modulation frequency). The QCL was injection locked at 1997.12 GHz and the different colour lines represent the same scan taken at time intervals of approximately 10 minutes.

6.7.2 Phase change

The signal detected at the receiver showed a change in phase at both the injection locked frequency (1997.12 GHz) and the different QCL Fabry-Perot modes. By changing the heterodyne frequency and aligning the QCL XYZ position for these frequencies, the THz signal amplitude and the corresponding phase change was measured, as shown in the Figure 6.12. For this measurement, the heterodyne frequency was incremented by 10 MHz steps and the delay was scanned at each frequency step. When the QCL is locked, the phase of the lasing cavity is expected to change in π radians according to Adler [203], as illustrated in Figure 6.2. The expected phase change is represented in Eq.(6.3) and the measured results are in good agreement.

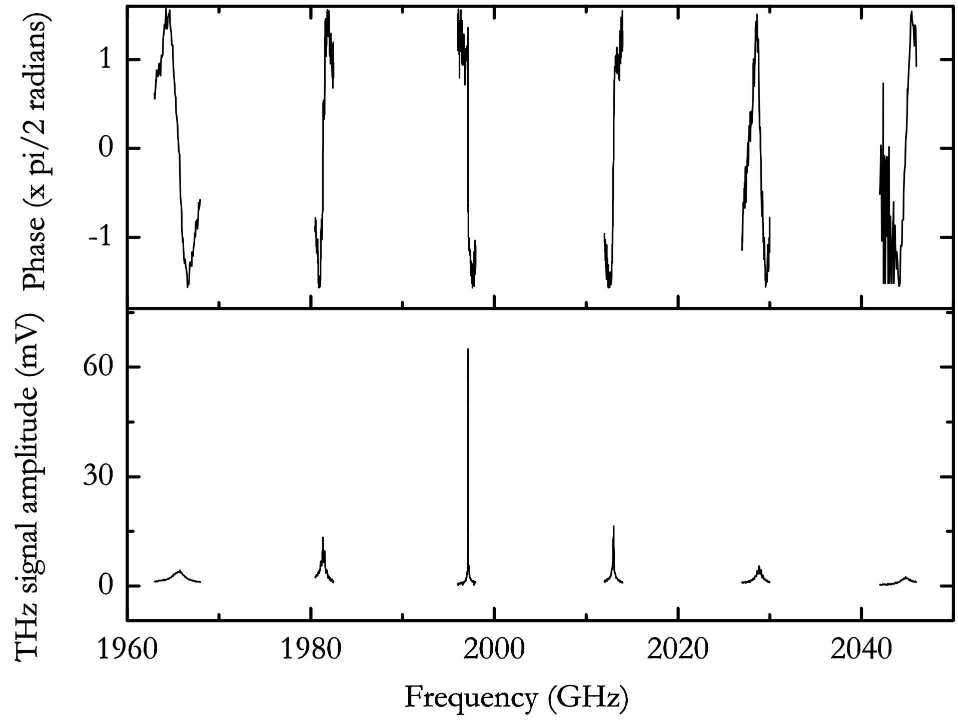

Figure 6.12: THz signal amplitude and the corresponding phase change plotted as a function of heterodyne frequency for the different QCL Fabry Perot modes with the QCL was DC biased at 750 mA.

The phase change at the locked frequency of 1997.12 GHz exhibited a sharp change from -90° (-π/2) to +90° (+π/2) in the measured frequency range, as shown Figure 6.13, which can be explained as follows. When radiation is injected into the QCL cavity that lies within the locking range, the QCL frequency starts lasing at the injected frequency. If the heterodyne frequency is the same as that of QCL emission frequency, there is no additional phase shift to the cavity. However, if the heterodyne frequency is approaching the locking range or just inside the locking range, the QCL frequency starts lasing at the heterodyne frequency. This sudden jump in the frequency is compensated as a phase shift due to the cavity effects such as changes in the gain and loss. This phase shift is accumulated in the cavity to match the frequency shift and thus results in a total of π radians phase shift. This shift will always be π radians within the locking range, and is dictated by Eq.(6.3).

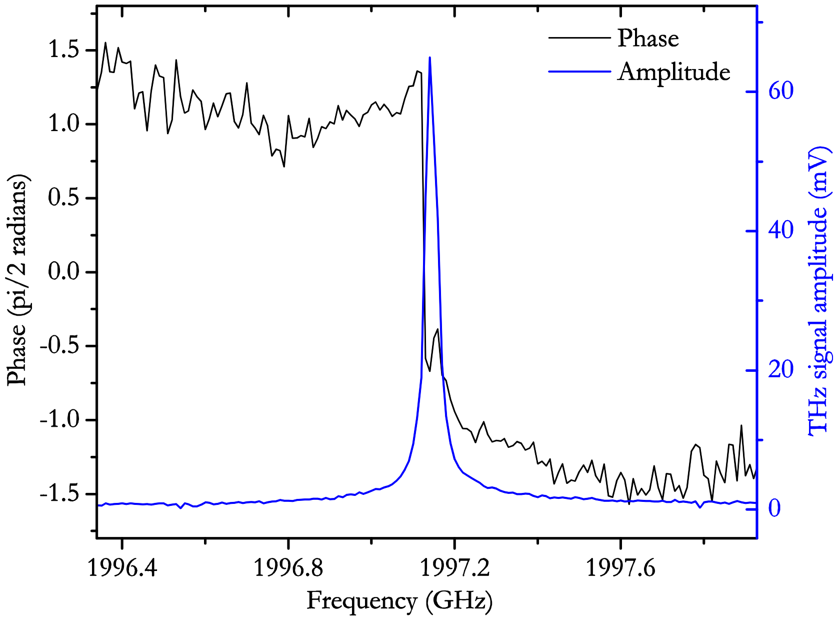

Figure 6.13: THz signal amplitude and the phase change plotted as a function of heterodyne frequency for the QCL aligned at the injection locked frequency (1997.12 GHz). In the locked state, the phase of the emitted THz radiation has a sudden π shift (within ~20 MHz). QCL was electrically connected at a DC current of 750 mA.

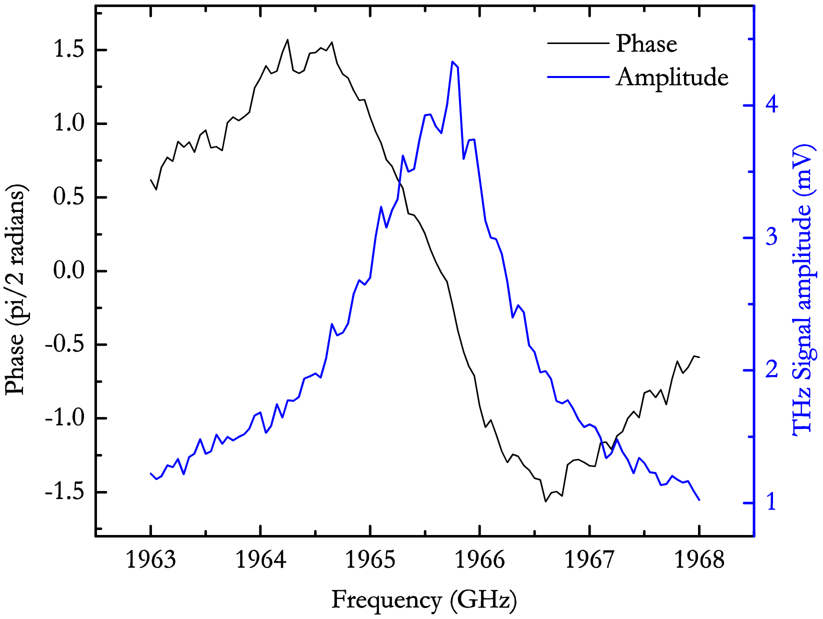

Figure 6.14: THz signal amplitude and the phase change plotted as a function of heterodyne frequency for a Fabry-Perot mode at 1965 GHz, for the QCL aligned for the injection locked state (1997.12 GHz). In the locked state, the phase of the emitted THz radiation has a broad π shift (within ~4–5 GHz). QCL was connected at a DC current of 750 mA.

However, for the other Fabry-Perot modes, 1965.4, 1981.42, 2012.96, 2028.82 and 2045 GHz although the phase change is π, the frequency range over which it occurs is much broader, with 1965.4 GHz, shown in Figure 6.14, and 2028.82 GHz being the broadest. When the laser is initially operating below threshold for the other modes, the observed phase shift depends on the difference between the cavity loss and growth rate. The higher cavity losses result in a broader shift and smaller cavity losses above the threshold result in a sharp change in phase [228].

6.8 Locking range

For the following measurements discussed in the subsections 6.8.1 and 6.8.2, the Rio laser was fine-tuned by changing the applied bias, keeping the Agilent laser at constant wavelength. For the Rio laser, a change in applied bias between -1 V to +1 V can result in a total tuning range of ~200 MHz. The bias to this laser was tuned using a LabView code which changed the bias in 0.01 V steps, corresponding to ~2 MHz frequency steps. This is much lower than the combined frequency jitter of 20 MHz. Changing only the Rio laser can thus reduce the jitter values. For each frequency step, the delay was scanned to measure the peak THz amplitude.

6.8.1 EDFA power dependence

According to Seigman [228], a weak monochromatic signal is sufficient for injection locking, and the locking range dependence on injection power is explained in Eq. (6.1). The injection power ratio has a direct dependence on the locking range, implying a large locking range for high input powers. In the present study, the emitters had an emission power of ~30 nW at 2 THz without any EDFA. In order to increase the injection signal and locking range, the injected power was increased using an EDFA. The output power of the EDFA was increased and the signal in the receiver was measured as a function of heterodyne frequency at each gain value.

Figure 6.15 shows the THz signal amplitude measured as a function of the heterodyne frequency (set frequency values by calculation). For EDFA power lower than 17.60 dBm, the QCL was not locked properly, although there was amplification of the signal at 1997.12 GHz, since the amplitude of the measured signal was <50 mV and the shape of the waveforms were just cleaner sine waves and didn’t exhibit any random shapes, which is expected to be present once the QCL starts getting locked, as shown in Figure 6.16. At the

EDFA power of 17.80 dBm, the QCL was locked at 1997.10 GHz and at 18.00 dBm the locked frequency shifted slightly to 1997.14 GHz. When the power was increased further to 18.60 dBm, the QCL was locked again at 1997.12 GHz. We attribute this behaviour to frequency jitter of the heterodyne lasers and therefore it is not clear if there is a red shift or blue shift of the QCL frequency with locking.

When the laser is locked, the gain is clamped and the emitted intensity remains at the peak value of the slave laser and it exhibits a ‘flat top’ for the measured intensity. The locking range at 18.60 dBm was measured to be ~20 MHz and at 18.00 dBm and 17.80 dBm was ~10 MHz. For lower EDFA powers (14.80 dBm to 17.00 dBm), a proper locking range could not be measured, since the injected power is reduced and the locking range is proportional to injected signal strength, consistent with Eq. (6.1). At 17.00 dBm, the power level at 2.0 THz from the emitter was ~30 nW compared to ~5 nW power at 14.80 dBm. Also, since the laser frequency jitter beyond the locking range is expected to be the contributing factor for the QCL failing to lock, a more stable source would be required to measure these lower powers.

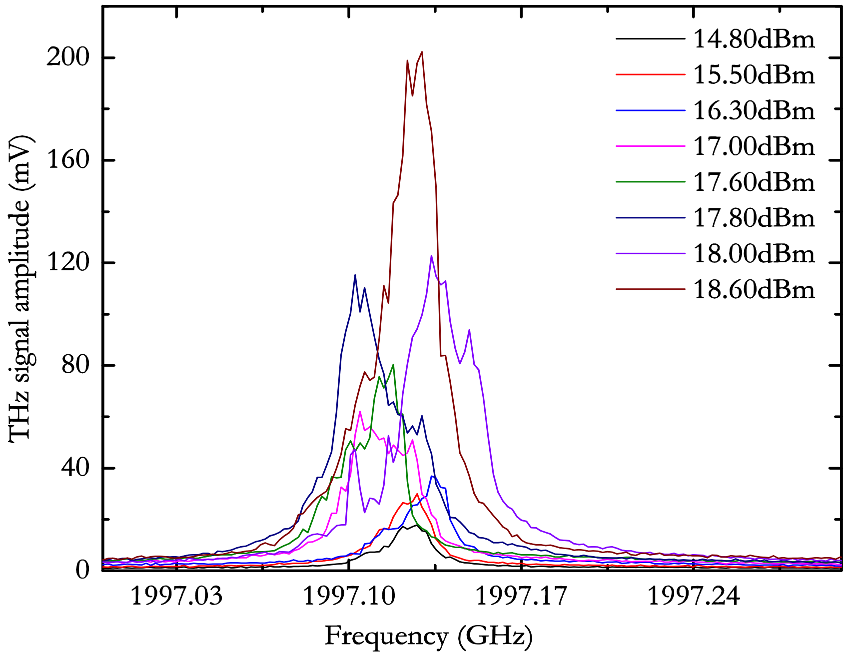

Figure 6.15: THz signal amplitude plotted as a function of heterodyne frequency at different EDFA powers. QCL was electrically connected at a DC current of 750 mA and was aligned for injection locked signal at 1997.12 GHz.

Within the locking range, the phase of the slave laser is expected to change over π radians (180°) to incorporate the frequency shift. For measuring the locking range, the THz signal amplitude and phase change were measured as a function of frequency at 18.60 dBm EDFA power , as shown in the Figure 6.13. The measured THz signal amplitude is found to be flat between 1997.11 and 1997.14 GHz with a small increase at 1997.13 GHz. However, the measured phase is not exactly an arcsine function with a small kink in the phase at 1997.12 GHz. This effect is attributed partly to the feedback from the detector.

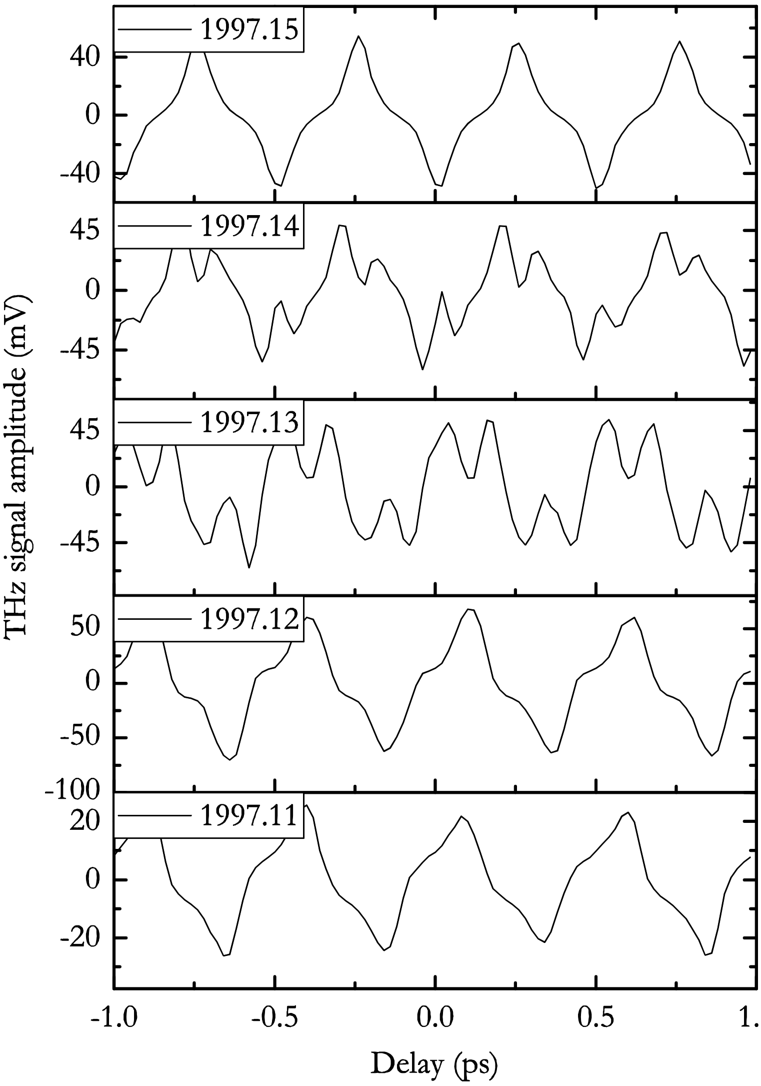

Figure 6.16: THz signal amplitude measured as a function of delay position for different injection frequencies, i.e. below (1997.11 GHz), at (1997.12 GHz), and beyond (1997.13, 1997.14 GHz) the QCL locking range. The output waveform from the emitter changes from a perfect sine wave at the locking frequency (1997.12 GHz) to a random shape (1997.14 GHz) due to the feedback.

The amplitude of the THz signal waveform measured at 1997.12 GHz (locked frequency) and four other neighbouring frequencies are plotted as a function of delay in Figure 6.16.

The non-sinusoidal response of the waves measured at 1997.13 and 1997.14 GHz are included, which corresponds to the heterodyne frequency being close to the centre of locking range of the QCL. The waveform shape suggests the presence of more than one frequency component (i.e. 1.9 THz and probably ~3.9 THz). This is attributed to the feedback from the receiver (THz´ radiation traversing the path twice instead of once and thus resulting in measuring approximately double the frequency).

6.8.2 QCL bias

The locking range experiments were also repeated at different QCL biases. At a DC bias of 750 mA, the QCL was lasing above threshold bias but below the maximum output power. In principle, increasing the applied bias will increase the temperature thus changing the refractive index of the active region, and also causing a red shift in the spectra.

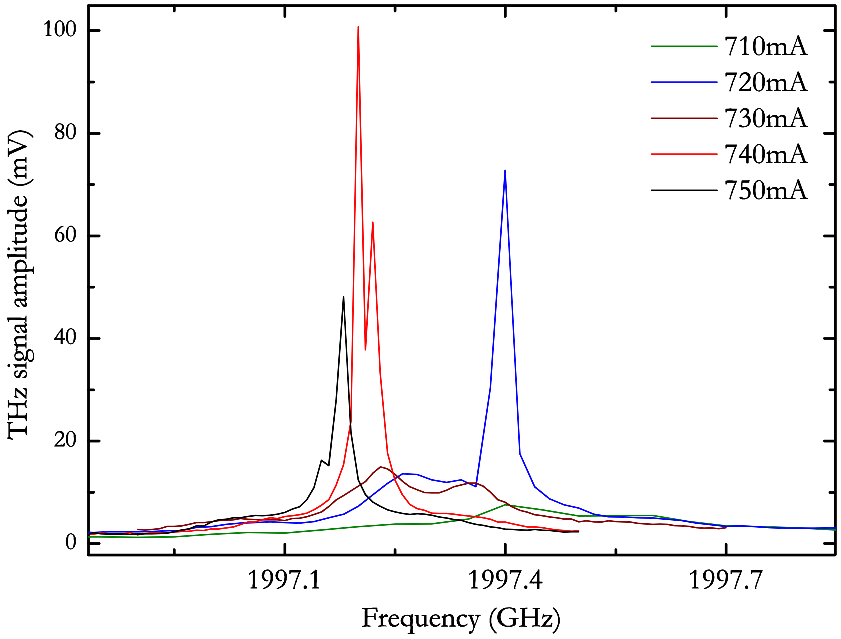

Figure 6.17: THz signal amplitude plotted as a function of heterodyne frequency at different QCL biases. EDFA was left at a power of 18.60 dBm and was aligned for injection locked signal at 1997.12 GHz.

The measurements were repeated at 18.60 dBm EDFA power for different QCL biases to observe frequency ‘pulling’ [233] or other locking effects. Figure 6.17 shows the THz signal amplitude measured at the receiver as a function of the heterodyne frequency at different QCL biases (without altering the QCL position). It was observed that with the increase in QCL bias there was a red shift in the locked frequency and heating of the QCL was assumed be the main reason for this. The QCL was locked at 720 mA (1997.4 GHz), 740 mA (1997.14 GHz) and 750 mA (1997.12 GHz) current levels. Due to the frequency jitter of the heterodyne laser, the measured signal amplitude is not high at these bias levels, since the QCL didn’t get locked fully.

The QCL was not locked at 730 mA, although it was lasing, and this is likely due to the alignment difference. When the QCL was separately aligned at 730 mA, it locked properly to the injected signal. The measured THz amplitude at 740 mA was higher than at 750 mA. This implied a better locking at that particular QCL current due to the heterodyne frequency matching with the exact QCL frequency.

The change in locking range for various QCL biases could not be measured accurately, as changing the bias required realignment to lock. The locking range is presumed to be different for different QCL biases. Indeed, changing the QCL bias will result in a change in QCL output power and can thus affect the injection locking range, according to Eq. (6.1).

6.9 Spectra of the locked QCL

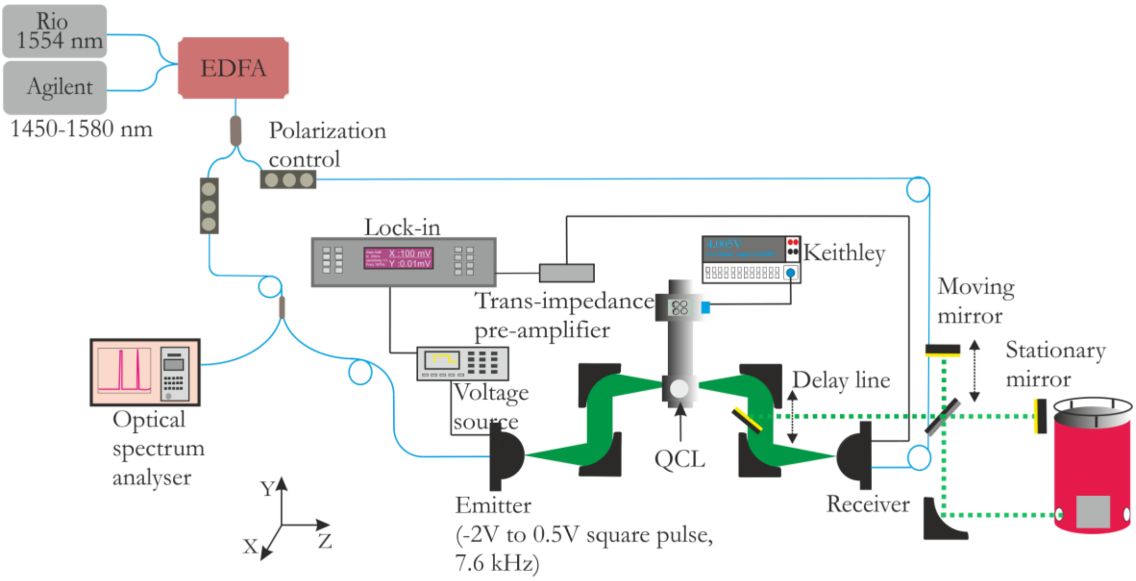

Figure 6.18: Schematic of the experimental configuration used for injection locking the QCL and measuring the spectra simultaneously. The mirror on the THz beam path reflected part of the beam which went onto a Michelson interferometer setup with the output being measured at the bolometer.

The spectra of the QCL was measured whilst in a locked state to study the emission of the laser and to analyse the locking range. The experimental setup was altered to incorporate an FTIR system so that both spectra and the signal amplitude at the receiver could be measured simultaneously. The modified experimental configuration used a Michelson interferometer and was setup as shown in Figure 6.18. A small stationary mirror (silver coated) was introduced between the 3rd and 4th parabolic mirror which reflected 10% of the THz´ radiation. The THz´ radiation was split using a beam splitter and subsequently reflected off both, a stationary mirror and moving mirror (on a delay stage) forming the Michelson interferometer. In this arrangement the reflected THz´ beam from the stationary and moving mirror is combined at the beam splitter and focussed to the bolometer using a parabolic mirror. By controlling the position of the moving mirror, both the beams are made to interfere for a range of relative path length differences, resulting in an interferogram, which is measured using the bolometer. A lock-in amplifier was used to interpret the bolometer signal. The experimental setup thus incorporates an injection locking setup and a FTIR setup with a 400 ps scan range (hence a spectral resolution of ~3 GHz).

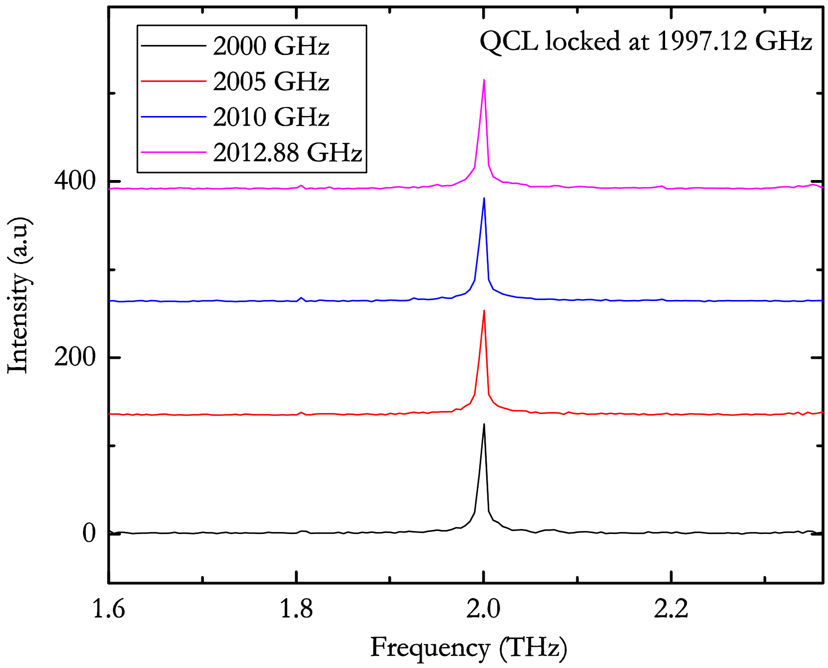

Figure 6.19: Spectra of the injection locked QCL measured from the FTIR setup. With the QCL injection locked to the heterodyne frequency at 1997.12 GHz, changing the heterodyne frequency didn't affect the QCL emission frequency (measured peak at 1999 GHz due to the low resolution).

It was observed that the QCL locked to photomixer emission frequencies of 1997.12 GHz and 2012.88 GHz. However, it could not be locked properly to the other modes. Before doing any measurement with the FTIR, the QCL was aligned for locking at 1997.12 GHz using the signal measured on the receiver (~200 mV). With the locked signal on the receiver, the interferogram was measured. The QCL was found to lase at exactly the same frequency as the heterodyne frequency i.e., 1997.1 GHz, within the resolution of the FTIR measurement. However, when the heterodyne frequency was changed to 1996.12 GHz, there was no change in the QCL frequency. The QCL was found to preferentially lock to whatever it was originally aligned to. This was seen when the QCL was lasing at 1997.12 GHz and the photomixer was set to 2000 GHz, 2005 GHz, 2010 GHz, and 2012.88 GHz frequencies. For each photomixer frequency, the QCL remained lasing at 1997.12 GHz, as shown in Figure 6.19.

This was also observed when the laser was aligned to an emission signal of 2012.96 GHz and the photomixer was set to 1997.12 GHz, 2005 GHz, 2010 GHz and 2012 GHz frequencies, as shown in Figure 6.20. Since the QCL was lasing only in these two modes, aligning for locking to the other modes was not attempted.

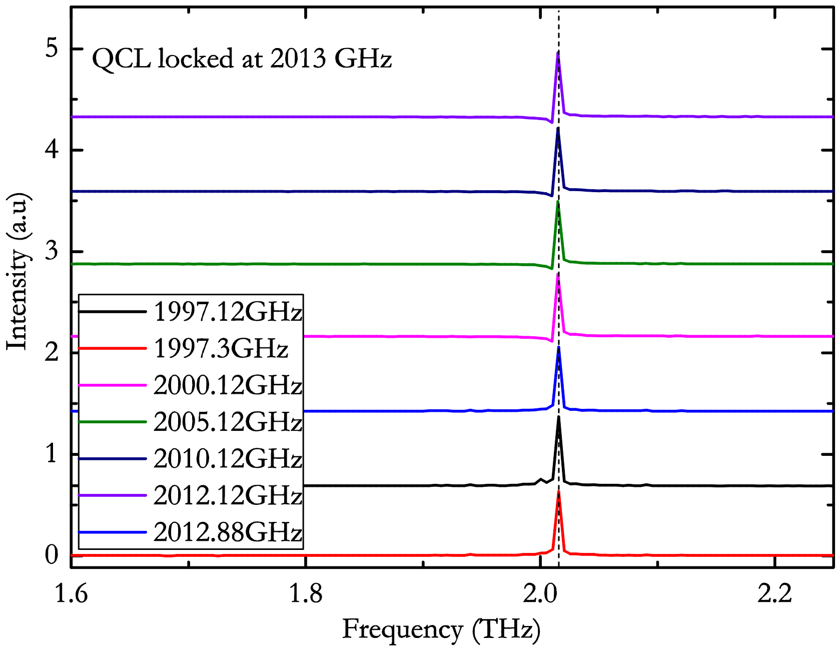

Figure 6.20: Spectra of the injection locked QCL measured from the FTIR setup. With the QCL injected locked to the heterodyne frequency at 2012.88 GHz, changing the heterodyne frequency didn't affect the QCL emission frequency. The black dotted line corresponds to 2012 GHz.

With no injected signal i.e. when the emitter was off, the emitted QCL frequency was free-running and was lasing at the QCL design frequency of ~1997.1 GHz. However, once the QCL was locked, the QCL frequency didn't change with heterodyne frequency. This measurement was repeated a few times with the emitter in the on and off state and the result was found to be consistent. Thus we can conclude that the QCL emission frequency had a dependence on the locked heterodyne frequency and was sensitive to the QCL position implying a self-mixing effect inside the QCL arising from the emitter and detector path. Since the system is limited by the resolution of the heterodyne frequency linewidth (≤20 MHz which is equal to the locking range) and resolution of the FTIR system (~2 GHz), it was difficult to interpret any frequency pulling effects in the measured range.

It is difficult at this instance to comment if the self-mixing effects in the locked state have an effect on the emission frequency of the QCL. The self-mixing in a QCL is expected to shift the emission frequency due to feedback [232]. However, the poor resolution of the FTIR system (~1 GHz) limits the frequency information and it is difficult to assert whether a shift is present or not.

6.10 Discussions and conclusions

In order to injection-lock a THz QCL, a stable, continuous-wave monochromatic source is required. Since the QCL cannot be injection-locked directly to the 1550 nm 'telecoms' laser, photomixers were used in this work to generate THz radiation at a controllable frequency. For the first time, a 2.0 THz BTC active region THz QCL was injection locked to a 1550 nm telecoms laser using photomixers. A weak THz frequency signal was focussed to the active region of the DC biased QCL. Due to the reflected THz´ radiation from the emitter, the drive voltage of the QCL was modulated at the emitter frequency. The QCL modulation voltage was sensitive to alignment due to self-mixing effects inside the laser cavity. With the QCL aligned for the highest modulation voltage, scanning the heterodyne frequency closer to the emission frequency confirmed the amplification of the fundamental and neighbouring Fabry-Perot modes. The amplitude of the measured THz radiation at the receiver confirmed the amplified signal. The phase of the THz radiation exhibited a π radians shift in the amplified modes. The shift in the phase, however, took place over a broader frequency range at higher order Fabry-Perot modes when compared to the fundamental mode, which exhibited a sharp phase change. This observation is consistent with the locking theory explained by Adler [203] and Siegman [228]. When the heterodyne frequency was moved closer to the fundamental frequency of the QCL, the THz QCL was injection-locked, i.e., when the heterodyne frequency was tuned slightly, no change in the THz signal amplitude was observed confirming the 'flat top' gain in the locking range. In order to confirm the locking range, the experiment was repeated at different EDFA gains and QCL biases.

The locking range of the device was measured to be ~20 MHz at an EDFA power of 18.60 dBm, corresponding to an injection power of 300 nW at 2.0 THz. The locking range at 18.00 dBm and 17.80 dBm was less than 10 MHz, and for lower EDFA gains the QCL failed to lock. Also, in agreement with Eq. (6.1), the locking range increased with injected signal strength. Another reason for failing to measure the locking range at lower injection power was due to the range being lower than the laser frequency jitter (20 MHz).

The observed phase change in the locking range was not a perfect arcsine shape as predicted by Adler, and this is attributed to the presence of self-mixing effects. The THz´ radiation reflected from the detector was responsible for this. This suggests the requirement for an isolator in the beam path between the QCL and the receiver to prevent such feedback.

Repeating the measurements at different QCL biases resulted in a redshift in the locking frequency for increased bias, which was attributed to the thermal effects in the QCL. Although the QCL was aligned to be injection locked at 1997.12 GHz, it was observed that the QCL didn't lock at 730 mA, where the sensitivity to the position of the QCL was assumed to be the predominant factor.

The QCL emission spectra was also measured in the locked state using an FTIR system. The emission frequency depends on the heterodyne frequency or more specifically the mode of the QCL it is locked to. With the QCL emission determined by the heterodyne frequency, it was observed that the QCL continued to lase at that frequency, until the alignment was changed. With the QCL position aligned for locking at 1997.12 GHz, the spectrum of the QCL didn't change with heterodyne frequency. When the QCL was locked to 2012.88 GHz frequency, changing the heterodyne frequency didn't have an effect on the lasing frequency. Overall, we can conclude that the QCL emission frequency had a dependence on the locked heterodyne frequency but was also highly sensitive to the QCL alignment in the system. A mode hopping or pulling effect was expected, however no such effects could not be observed.

Chapter 7 Conclusions and future work

7.1 Conclusions

In this thesis, it was shown that Fe doped InGaAs and Fe doped InGaAsP materials can be used for photomixing at 1550 nm. Although the emitter had a bandwidth of ~2.4 THz, the measured power level at 2 THz was low. In order to improve the power, various nanostructured grating electrode designs were designed and fabricated, integrated within multiple antenna structures. The work presented a better understanding of the geometrical dependence of the emission mechanism. In this work, it was proved that a THz QCL can be injection locked to a telecoms wavelength laser using a photomixer. This chapter concludes by giving future work in the field of injection-locked QCLs and their applications.

7.1.1 Materials for photomixing at 1550 nm

Two new different materials, $Fe:In_{0.53}Ga_{0.47}As$ and $Fe:In_{0.70}Ga_{0.30}As_{0.87}P_{0.13}$, grown by MOCVD, was tested for photomixing. The purpose of Fe doping the wafers was to increase the resistivity of the material. The alloy composition of the wafers was chosen such that the bandgap of the material was shifted to 1600 nm and 1540 nm for Fe:InGaAs and Fe:InGaAsP, respectively. The bandgap change was confirmed by photoluminescence and transmission spectroscopy measurements. A detailed description of the fabrication procedure to process the wafers were given in Chapter 4. In order to facilitate enhanced CW performance in terms of bandwidth and output power, a 3-turn logarithmic spiral antenna with an active region dimension of 11.3 μm×11.3 μm, and an IDT design of 0.2 μm finger width and gap size of 1.6 μm was fabricated on both, Fe:InGaAs and Fe:InGaAsP wafers.

Two InGaAs and four InGaAsP wafers with different Fe doping concentration were used. Fe doping concentration used were 0.5×10^{16} cm^{-3} and 5.5×10^{16} cm^{-3} for the two InGaAs and 1.0×10^{16} cm^{-3}, 4.0×10^{16} cm^{-3}, 9.5×10^{16} cm^{-3} and 10.0×10^{16} cm^{-3} for the four InGaAsP wafers. From Hall bar measurements, it was observed that the dark resistivity of the wafers decreased with increase in doping, in both Fe:InGaAs and Fe:InGaAsP. The breakdown field was measured to be ~12.5 kVcm^{-1} for both materials.

The dark current measured from these wafers were extremely low, of the order of ~5-10 μA. There was almost three order difference in the magnitude when excited optically at 0.2 V DC bias, resulting in ~2–3 mA photocurrent. The excitation lasers used to achieve this were a pair of fibre-coupled, DBR lasers with tunable emission wavelength between 1534 –1560 nm, corresponding to a heterodyne frequency between 0–2600 GHz. When tested for spectral bandwidth in a coherent detection setup, the low doped Fe:InGaAs and Fe:InGaAsP emitters gave a bandwidth of greater than 2.4 THz. The measured bandwidth decreased with doping, with the higher doped Fe:InGaAs (5.5×10^{16} cm^{-3}) and Fe:InGaAsP (10.0×10^{16} cm^{-3}) emitters providing a bandwidth of ~ 2.0 THz only. Also, the measured THz signal amplitude showed a similar trend i.e., a decrease in measured signal amplitude with doping. Fe:InGaAs slightly outperformed Fe:InGaAsP in terms of measured signal and this difference is attributed to the difference in bandgap.

The Fe:InGaAs and Fe:InGaAsP emitters with the best performance had a doping concentration of 0.5×10^{16} cm^{-3} and 10.0×10^{16} cm^{-3}, respectively. The low bandwidth obtained from the highly doped wafers is attributed to the low carrier mobility associated with increased carrier scattering due to the presence of Fe ions. The measured power at 1 THz was ~45 nW and 30 nW from the best performed Fe:InGaAs and Fe:InGaAsP emitter, respectively, which is the highest compared to any standard IDT emitter on InGaAs substrate till date.

The measured THz power spanned more than 30 dB and the roll-off in power was found to be -6 dB/octave at frequencies less than 1.1 THz due to carrier lifetime and the roll-off rate increased to -12 dB/octave above due to added contribution from the RC constant and carrier lifetime effects. From the least square fitting, the carrier lifetime of the best performing Fe:InGaAs and Fe:InGaAsP emitters was estimated to be approximately ~700–800 fs. This lifetime is inconsistent with the measured photocurrent values and this discrepancy is associated with a biexponential lifetime in the material, implies carriers have more than one particular lifetime. However, the contribution from these long lifetime carriers towards THz emission is negligible.

The measured THz power had V^3 dependence with bias for both Fe:InGaAs and Fe:InGaAsP within the 0–1.25 V range. The dependence with optical power changed from linear, between 5 mW and 12 mW, to saturated levels after 12 mW.

7.1.2 Nanostructure emitters

THz power from IDT emitters at 2 THz was ~6 nW from both Fe:InGaAs and Fe:InGaAsP emitters. In order to improve the power at 2 THz, two new antenna designs were attempted and were discussed in Chapter 5. Firstly, a dual-dipole dual-slot antenna with an IDT active region design adopted from Duffy *et al.* [183] was fabricated on a Fe:InGaAsP wafer. Although the resonant frequency of the design was 1050 GHz, no resonance was detected at the designed frequency or any of its harmonics. The additional impedance introduced by the contact lines was found to be responsible. Secondly, a nanostructured electrode design was implemented on a broadband antenna. The NSG dimensions were adopted from Berry *et al.* [185] and the designs were reported to have ~mW's of output power at high frequencies.

Since the primary goal of the project is to improve the power at 2 THz, the NSG design was attempted on a 2-turn logarithmic spiral antenna with a 19 μm×19 μm active area. The NSG had 100 nm wide electrodes separated by 100 nm gap. Two different approaches to the NSG design were developed, SSN and DSN. The SSN had NSG on one contact electrode and the other was plane metal. The electrodes of the DSN consisted of 2 NSGs. Performing a bandwidth scan, it was observed that both SSN and DSN had similar spectral bandwidth (~2 THz), irrespective of the structural differences. Switching the bias to opposite electrodes, a significant drop in the measured THz signal amplitude and output power confirmed the contribution of electrons in THz generation mechanism.

The SSN and DSN structures were mapped as a function of excitation laser spot to identify the geometrical dependence of THz emission. THz signal amplitude as a function of laser excitation position was studied by switching the biasing electrodes and orthogonal polarizations at 510 GHz. The emission was concentrated on the gap between the NSG and metal electrode for the SSN design and between the two NSGs for the DSN design, respectively. Instead of having an emission underneath the NSG due to surface plasmons, mapping confirmed that emission was concentrated at the metal electrode tips from an enhanced optical electric field. The laser spot exciting both NSG tips resulted in an improvement in THz emission. Emitted THz signal amplitude decreased massively when the metal electrode in the SSN was biased whereas no change in the DSN could be observed, confirming the optical electric field contribution since the plane metal electrode didn't have sharp tips. The change in signal amplitude with polarization was due to a wire grid polarizer effect, resulting in reduced absorption of the incident laser beam. Mapping was performed at 210 GHz and 810 GHz as well to validate the results at 510 GHz and these measurements showed very good agreement. The emitters were tested in a THz-TD system and no surface plasmonic effects could be observed. Emission was concentrated between the gap, rather than on the NSGs.

When the experiment was repeated on a 3-turn log-spiral antenna with a smaller active region, the results were consistent; no enhancement could be observed with the SSN and the DSN when a bandwidth scan was performed.

7.1.3 Injection locking of a THz QCL

In this thesis, it was demonstrated that a THz QCL can be injection locked to an external laser with an emission wavelength of 1550 nm using photomixers. The different photomixers discussed on Chapter 4 and Chapter 5 was compared with the commercial emitter, TOPTICA. At 2 THz, the power from the commercial emitter was 10 times higher than the in-house emitters and the injection-locking experiment was performed with the commercial emitter.

The 2.0 THz BTC SISP waveguide QCL, discussed in Chapter 2, was used for the locking experiment. By tuning the heterodyne frequency of the stable laser source, with an injected signal of ~300 nW at 2 THz, the QCL was injection locked to 1997.12 GHz and was locked to five other longitudinal modes. The signal was coherently detected using the commercial receiver. The locking range of the QCL was measured to be ~20 MHz at an injection signal of ~300 nW. The injected signal strength was controlled using an EDFA.

The locking range of the QCL increased with injection signal strength, from not locked at ~30 nW (14.80 dBm) to fully locked at ~300 nW (18.60 dBm).

The spectral characteristics of the locked QCL were studied by measuring the spectrum in an FTIR setup. Simultaneous coherent detection of the locked signal and QCL emission spectrum could be assessed. The emission frequency of the QCL was largely dependent on the locking frequency. However, due to the reflection of the THz signal back into the QCL by the receiver resulted in a self-mixing effect in the QCL resulting in a shift in the phase but unfortunately no final conclusions regarding the phase could be made.

7.2 Future work

The SSN and DSN emitters with only a 7 μm gap between the anode and cathode were tested. Although the emitted power levels were low, it was found that the NSG has some contributions to THz emission. Mapping the emitters for different excitation positions suggested the absence of surface plasmons, but could not explicitly point out the exact geometrical position due to the laser spotsize. In order to obtain a better insight about the generation, a smaller spotsize lens, preferably ~200–300 nm would be ideal.

Additional work needs to be carried out by varying the gap between the NSG electrodes in the DSN emitters. It was shown that the polarization affected the signal strength. It will be interesting to estimate the THz power difference as a function of gap at different polarizations since the light coupling to the semiconductor will be affected.

Although the injection locking of a THz QCL to a telecoms wavelength heterodyne source was reported, the locking range measured was only in the tens of MHz. Improving the locking range is the progressive step to undertake in this work. This could be achieved by employing high power THz emitters. Increasing the injected signal strength will increase the locking range, according to the theory of injection locking. Furthermore, using a highly stable laser source, with narrow linewidth (few kHz) and laser jitter of a few Hz can result in stable QCL locking for a prolonged time. The laser jitter of the laser source (~20 MHz) was approximately the same as the locking range.

Another major setback was the feedback from the coherent receiver affecting the phase of the locked QCL. The reflected THz beam from the receiver on the delay line resulted in a self-mixing effect in the QCL. This feedback can be avoided by introducing a polarizer on the beam path, thus ensuring a proper phase-locking of the QCL. Apart from introducing a polarizer, a promising approach is by introducing the delay line on the laser beam path, rather than on the THz beam path. This can be achieved by free-space coupling of the laser beam between two optical fibres, one stationary and the second one on the delay line. The fibre placed on the delay line can be controlled to achieve the optimum delay. Precise control over the emitted phase of the THz radiation is a mandatory requirement for imaging applications and this is the immediate step to take to improve locking.

References

[1] M. Tonouchi, "Cutting-edge terahertz technology," *Nat Photon,* vol. 1, pp. 97-105, 2007.

[2] D. Giles and L. Edmund, "Bridging the terahertz gap," *Physics World,* vol. 17, p. 37, 2004.

[3] P. W. Gwyn, "Filling the THz gap—high power sources and applications," *Reports on Progress in Physics,* vol. 69, p. 301, 2006.

[4] P. H. Siegel, "Terahertz technology," *Microwave Theory and Techniques, IEEE Transactions on,* vol. 50, pp. 910-928, 2002.

[5] M. C. Gaidis, H. M. Pickett, C. D. Smith, S. C. Martin, R. P. Smith, and P. H. Siegel, "A 2.5-THz receiver front end for spaceborne applications," *IEEE Transactions on Microwave Theory and Techniques,* vol. 48, pp. 733-739, 2000.

[6] R. W. M. Hoogeveen, P. A. Yagoubov, A. Maurellis, V. P. Koshelets, S. V. Shitov, U. Mair, M. Krocka, G. Wagner, M. Birk, H.-W. Huebers, H. Richter, A. Semenov, G. N. Gol'tsman, B. M. Voronov, B. N. Ellison, B. J. Kerridge, D. N. Matheson, B. Alderman, M. Harman, R. Siddans, and J. Reburn, "New cryogenic heterodyne techniques applied in TELIS: the balloon-borne THz and submillimeter limb sounder for atmospheric research," 2003, pp. 347-355.

[7] H. M. Pickett, "THz spectroscopy of the atmosphere," in *Optoelectronics' 99-Integrated Optoelectronic Devices*, 1999, pp. 2-6.

[8] T. G. Phillips and J. Keene, "Submillimeter astronomy [heterodyne spectroscopy]," *Proceedings of the IEEE,* vol. 80, pp. 1662-1678, 1992.

[9] J. M. Gary, R. S. John, L. N. A. Matthew, A. B. Edwin, C. Gordon, R. E. Neal, F. G. Paul, H. Martin, E. H. John, C. K. Steven, G. K. David, A. N. David, M. P. Brian, P. René, S. Rudolf, L. S. Ronald, T. Volker, W. Zhong, W. Gisbert, and Z. Yun Fei, "The Submillimeter Wave Astronomy Satellite: Science Objectives and Instrument Description," *The Astrophysical Journal Letters,* vol. 539, p. L77, 2000.

[10] B. B. Hu and M. C. Nuss, "Imaging with terahertz waves," *Opt. Lett.,* vol. 20, pp. 1716-1718, 1995.

[11] T. Kleine-Ostmann, P. Knobloch, M. Koch, S. Hoffmann, M. Breede, M. Hofmann, G. Hein, K. Pierz, M. Sperling, and K. Donhuijsen. (2001, Continuous-

wave THz imaging. *Electronics Letters 37(24),* 1461-1463. Available: http://digital-library.theiet.org/content/journals/10.1049/el_20011003

[12] F. F. John, S. Brian, H. Feng, G. Dale, B. Robert, O. Filipe, and Z. David, "THz imaging and sensing for security applications—explosives, weapons and drugs," *Semiconductor Science and Technology,* vol. 20, p. S266, 2005.

[13] Q. Song, Y. Zhao, A. Redo-Sanchez, C. Zhang, and X. Liu, "Fast continuous terahertz wave imaging system for security," *Optics Communications,* vol. 282, pp. 2019-2022, 2009.

[14] K. Kawase, Y. Ogawa, Y. Watanabe, and H. Inoue, "Non-destructive terahertz imaging of illicit drugs using spectral fingerprints," *Optics Express,* vol. 11, pp. 2549-2554, 2003/10/06 2003.

[15] M. Lu, J. Shen, N. Li, Y. Zhang, C. Zhang, L. Liang, and X. Xu, "Detection and identification of illicit drugs using terahertz imaging," *Journal of Applied Physics,* vol. 100, p. 103104, 2006.

[16] A. G. Davies, A. D. Burnett, W. Fan, E. H. Linfield, and J. E. Cunningham, "Terahertz spectroscopy of explosives and drugs," *Materials Today,* vol. 11, pp. 18-26, 2008.

[17] R. Appleby and H. B. Wallace, "Standoff Detection of Weapons and Contraband in the 100 GHz to 1 THz Region," *IEEE Transactions on Antennas and Propagation,* vol. 55, pp. 2944-2956, 2007.

[18] W. H. Taliaferro and L. G. Taliaferro, "Effect of X-rays on immunity: a review," *The Journal of Immunology,* vol. 66, pp. 181-212, 1951.

[19] R. M. Woodward, V. P. Wallace, R. J. Pye, B. E. Cole, D. D. Arnone, E. H. Linfield, and M. Pepper, "Terahertz Pulse Imaging of ex vivo Basal Cell Carcinoma," *Journal of Investigative Dermatology,* vol. 120, pp. 72-78, 2003.

[20] V. P. Wallace, A. J. Fitzgerald, S. Shankar, N. Flanagan, R. Pye, J. Cluff, and D. D. Arnone, "Terahertz pulsed imaging of basal cell carcinoma ex vivo and in vivo," *British Journal of Dermatology,* vol. 151, pp. 424-432, 2004.

[21] A. J. Fitzgerald, V. P. Wallace, M. Jimenez-Linan, L. Bobrow, R. J. Pye, A. D. Purushotham, and D. D. Arnone, "Terahertz Pulsed Imaging of Human Breast Tumors," *Radiology,* vol. 239, pp. 533-540, 2006.

[22] F. Wahaia, G. Valusis, L. M. Bernardo, A. Almeida, J. A. Moreira, P. C. Lopes, J. Macutkevic, I. Kasalynas, D. Seliuta, R. Adomavicius, R. Henrique, and M. Lopes, "Detection of colon cancer by terahertz techniques," *Journal of Molecular Structure,* vol. 1006, pp. 77-82, 2011.

[23] K. c. Huang and Z. Wang, "Terahertz Terabit Wireless Communication," *IEEE Microwave Magazine,* vol. 12, pp. 108-116, 2011.

[24] T. Löffler, T. Bauer, K. J. Siebert, H. G. Roskos, A. Fitzgerald, and S. Czasch, "Terahertz dark-field imaging of biomedical tissue," *Optics Express,* vol. 9, pp. 616-621, 2001/12/03 2001.

[25] J. Ryu, Y. Jung, S. Baek, J. Lee, S. Kim, S. Kwon, and J. Kim, "Diagnosis of Dental Cavity and Osteoporosis Using Terahertz Transmission Images," in *Ultrafast Phenomena XII: Proceedings of the 12th International Conference, Charleston, SC, USA, July 9-13, 2000*, ed Berlin, Heidelberg: Springer Berlin Heidelberg, 2001, pp. 265-267.

[26] T. Kleine-Ostmann and T. Nagatsuma, "A Review on Terahertz Communications Research," *Journal of Infrared, Millimeter, and Terahertz Waves,* vol. 32, pp. 143-171, 2011.

[27] G. J. Wilmink and J. E. Grundt, "Invited Review Article: Current State of Research on Biological Effects of Terahertz Radiation," *Journal of Infrared, Millimeter, and Terahertz Waves,* vol. 32, pp. 1074-1122, 2011.

[28] J. El Haddad, B. Bousquet, L. Canioni, and P. Mounaix, "Review in terahertz spectral analysis," *TrAC Trends in Analytical Chemistry,* vol. 44, pp. 98-105, 2013.

[29] P. Dean, A. Valavanis, J. Keeley, K. Bertling, Y. Lim, R. Alhathlool, A. Burnett, L. Li, S. Khanna, and D. Indjin, "Terahertz imaging using quantum cascade lasers—a review of systems and applications," *Journal of Physics D: Applied Physics,* vol. 47, p. 374008, 2014.

[30] J. Lloyd-Hughes and T.-I. Jeon, "A review of the terahertz conductivity of bulk and nano-materials," *Journal of Infrared, Millimeter, and Terahertz Waves,* vol. 33, pp. 871-925, 2012.

[31] M. Perenzoni and D. J. Paul, *Physics and applications of terahertz radiation*: Springer, 2014.

[32] Y.-S. Lee, *Principles of terahertz science and technology* vol. 170: Springer Science & Business Media, 2009.

[33] K. Sakai, M. Tani, and K. Sakai, "Terahertz optoelectronics," 2005.

[34] D. Mittleman, *Sensing with terahertz radiation* vol. 85: Springer, 2013.

[35] D. Saeedkia and S. Safavi-Naeini, "Terahertz Photonics: Optoelectronic Techniques for Generation and Detection of Terahertz Waves," *Lightwave Technology, Journal of,* vol. 26, pp. 2409-2423, 2008.

[36] L. Lianhe, C. Li, Z. Jingxuan, J. Freeman, P. Dean, A. Valavanis, A. G. Davies, and E. H. Linfield, "Terahertz quantum cascade lasers with >1 W output powers," *Electronics Letters,* vol. 50, pp. 309-311, 2014.

[37] C. W. Berry, M. R. Hashemi, and M. Jarrahi, "Generation of high power pulsed terahertz radiation using a plasmonic photoconductive emitter array with logarithmic spiral antennas," *Applied Physics Letters,* vol. 104, p. 081122, 2014.

[38] E. Nichols and J. Tear, "Joining the infra-red and electric wave spectra," *The Astrophysical Journal,* vol. 61, p. 17, 1925.

[39] S. H. Gold and G. S. Nusinovich, "Review of high-power microwave source research," *Review of Scientific Instruments,* vol. 68, pp. 3945-3974, 1997.

[40] V. L. Granatstein, R. K. Parker, and C. M. Armstrong, "Vacuum electronics at the dawn of the twenty-first century," *Proceedings of the IEEE,* vol. 87, pp. 702-716, 1999.

[41] W. He, C. R. Donaldson, L. Zhang, K. Ronald, P. McElhinney, and A. W. Cross, "High Power Wideband Gyrotron Backward Wave Oscillator Operating towards the Terahertz Region," *Physical Review Letters,* vol. 110, p. 165101, 2013.

[42] L. P. Schmidt, S. Biber, G. Rehm, and K. Huber, "THz measurement technologies and applications," in *Microwaves, Radar and Wireless Communications, 2002. MIKON-2002. 14th International Conference on*, 2002, pp. 581-587 vol.2.

[43] M. Y. Glyavin, A. Luchinin, and G. Y. Golubiatnikov, "Generation of 1.5-kW, 1-THz coherent radiation from a gyrotron with a pulsed magnetic field," *Physical Review Letters,* vol. 100, p. 015101, 2008.

[44] A. V. Raisanen, "Frequency multipliers for millimeter and submillimeter wavelengths," *Proceedings of the IEEE,* vol. 80, pp. 1842-1852, 1992.

[45] A. Maestrini, J. Ward, J. Gill, H. Javadi, E. Schlecht, G. Chattopadhyay, F. Maiwald, N. R. Erickson, and I. Mehdi, "A 1.7-1.9 THz local oscillator source," *IEEE Microwave and Wireless Components Letters,* vol. 14, pp. 253-255, 2004.

[46] N. Orihashi, S. Suzuki, and M. Asada, "One THz harmonic oscillation of resonant tunneling diodes," *Applied Physics Letters,* vol. 87, p. 233501, 2005.

[47] W. Shi, Y. J. Ding, N. Fernelius, and K. Vodopyanov, "Efficient, tunable, and coherent 0.18–5.27-THz source based on GaSe crystal," *Optics Letters,* vol. 27, pp. 1454-1456, 2002/08/15 2002.

[48] J. E. Schaar, K. L. Vodopyanov, P. S. Kuo, M. M. Fejer, X. Yu, A. Lin, J. S. Harris, D. Bliss, C. Lynch, V. G. Kozlov, and W. Hurlbut, "Terahertz Sources Based on Intracavity Parametric Down-Conversion in Quasi-Phase-Matched Gallium Arsenide," *IEEE Journal of Selected Topics in Quantum Electronics,* vol. 14, pp. 354-362, 2008.

[49] T. J. Edwards, D. Walsh, M. B. Spurr, C. F. Rae, M. H. Dunn, and P. G. Browne, "Compact source of continuously and widely-tunable terahertz radiation," *Optics Express,* vol. 14, pp. 1582-1589, 2006/02/20 2006.

[50] G. P. Williams, "FAR-IR/THz radiation from the Jefferson Laboratory, energy recovered linac, free electron laser," *Review of Scientific Instruments,* vol. 73, pp. 1461-1463, 2002.

[51] E. Bründermann and H. P. Röser, "First operation of a far-infrared p-germanium laser in a standard close-cycle machine at 15 K," *Infrared Physics & Technology,* vol. 38, pp. 201-203, 1997.

[52] Y. P. Gousev, I. V. Altukhov, K. A. Korolev, V. P. Sinis, M. S. Kagan, E. E. Haller, M. A. Odnoblyudov, I. N. Yassievich, and K.-A. Chao, "Widely tunable continuous-wave THz laser," *Applied Physics Letters,* vol. 75, pp. 757-759, 1999.

[53] D. H. Auston, K. P. Cheung, and P. R. Smith, "Picosecond photoconducting Hertzian dipoles," *Applied Physics Letters,* vol. 45, pp. 284-286, 1984.

[54] E. R. Brown, F. W. Smith, and K. A. McIntosh, "Coherent millimeter-wave generation by heterodyne conversion in low-temperature-grown GaAs photoconductors," *Journal of Applied Physics,* vol. 73, pp. 1480-1484, 1993.

[55] J. Faist, F. Capasso, D. L. Sivco, C. Sirtori, A. L. Hutchinson, and A. Y. Cho, "Quantum Cascade Laser," *Science,* vol. 264, pp. 553-556, 1994-04-22 00:00:00 1994.

[56] R. Kohler, A. Tredicucci, F. Beltram, H. E. Beere, E. H. Linfield, A. G. Davies, D. A. Ritchie, R. C. Iotti, and F. Rossi, "Terahertz semiconductor-heterostructure laser," *Nature,* vol. 417, pp. 156-159, 2002.

[57] T. H. Maiman, "Stimulated Optical Radiation in Ruby," *Nature,* vol. 187, pp. 493-494, 1960.

[58] R. N. Hall, G. E. Fenner, J. D. Kingsley, T. J. Soltys, and R. O. Carlson, "Coherent Light Emission From GaAs Junctions," *Physical Review Letters,* vol. 9, pp. 366-368, 1962.

[59] M. I. Nathan, W. P. Dumke, G. Burns, F. H. Dill, and G. Lasher, "Stimulated emission of radiation from GaAs pn junctions," *Applied Physics Letters,* vol. 1, pp. 62-64, 1962.

[60] J. P. van der Ziel, R. Dingle, R. C. Miller, W. Wiegmann, and W. A. Nordland, "Laser oscillation from quantum states in very thin GaAs−Al0.2Ga0.8As multilayer structures," *Applied Physics Letters,* vol. 26, pp. 463-465, 1975.

[61] F. P. Schäfer, W. Schmidt, and J. Volze, "Organic dye solution laser," *Applied Physics Letters,* vol. 9, pp. 306-309, 1966.

[62] H. G. Heard, "Ultra-violet Gas Laser at Room Temperature," *Nature,* vol. 200, pp. 667-667, 1963.

[63] Y. Arakawa and A. Yariv, "Quantum well lasers--Gain, spectra, dynamics," *IEEE Journal of Quantum Electronics,* vol. 22, pp. 1887-1899, 1986.

[64] K. RF and R. Suris, "Possibility of amplication of electromagnetic waves in a semiconductor with a superlattice," vol. 5, ed: Amer Inst Physics Circulation Fulfillment Div, 500 Sunnyside BLVD, Woodbury, NY 11797-2999, 1971, pp. 707-&.

[65] C. Gmachl, F. Capasso, D. L. Sivco, and A. Y. Cho, "Recent progress in quantum cascade lasers and applications," *Reports on Progress in Physics,* vol. 64, p. 1533, 2001.

[66] J. Faist, F. Capasso, C. Sirtori, D. L. Sivco, A. L. Hutchinson, S.-N. G. Chu, and A. Y. Cho, "Continuous wave operation of quantum cascade lasers based on vertical transitions at λ=4.6μm," *Superlattices and Microstructures,* vol. 19, pp. 337-345, 1996.

[67] C. Sirtori, J. Faist, F. Capasso, D. L. Sivco, A. L. Hutchinson, and A. Y. Cho, "Mid-infrared (8.5 um) semiconductor lasers operating at room temperature," *Photonics Technology Letters, IEEE,* vol. 9, pp. 294-296, 1997.

[68] R. Manijeh, S. Steven, B. Yanbo, G. Burc, and D. Shaban Ramezani, "High power quantum cascade lasers," *New Journal of Physics,* vol. 11, p. 125017, 2009.

[69] B. S. Williams, "Terahertz quantum-cascade lasers," *Nat Photon,* vol. 1, pp. 517-525, 2007.

[70] Q. Hu and S. Feng, "Feasibility of far-infrared lasers using multiple semiconductor quantum wells," *Applied Physics Letters,* vol. 59, pp. 2923-2925, 1991.

[71] A. G. Davies, E. H. Linfield, and M. B. Johnston, "The development of terahertz sources and their applications," *Physics in Medicine and Biology,* vol. 47, p. 3679, 2002.

[72] J. Faist, M. Beck, T. Aellen, and E. Gini, "Quantum-cascade lasers based on a bound-to-continuum transition," *Applied Physics Letters,* vol. 78, pp. 147-149, 2001.

[73] B. S. Williams, H. Callebaut, S. Kumar, Q. Hu, and J. L. Reno, "3.4-THz quantum cascade laser based on longitudinal-optical-phonon scattering for depopulation," *Applied Physics Letters,* vol. 82, pp. 1015-1017, 2003.

[74] I. A. Maria, S. Giacomo, T. Romain, F. Milan, B. Mattias, F. Jérôme, R. Alok, G. Pascal, and K. Eli, "Bound-to-continuum terahertz quantum cascade laser with a single-quantum-well phonon extraction/injection stage," *New Journal of Physics,* vol. 11, p. 125022, 2009.

[75] S. Kumar, C. W. I. Chan, Q. Hu, and J. L. Reno, "A 1.8-THz quantum cascade laser operating significantly above the temperature of [planck][omega]/kB," *Nat Phys,* vol. 7, pp. 166-171, 2011.

[76] H. Qing, S. W. Benjamin, K. Sushil, C. Hans, K. Stephen, and L. R. John, "Resonant-phonon-assisted THz quantum-cascade lasers with metal–metal waveguides," *Semiconductor Science and Technology,* vol. 20, p. S228, 2005.

[77] A. B. Mikhail and C. Federico, "New frontiers in quantum cascade lasers: high performance room temperature terahertz sources," *Physica Scripta,* vol. 90, p. 118002, 2015.

[78] B. S. Williams, S. Kumar, H. Callebaut, Q. Hu, and J. L. Reno, "Terahertz quantum-cascade laser operating up to 137 K," *Applied Physics Letters,* vol. 83, pp. 5142-5144, 2003.

[79] S. Barbieri, J. Alton, H. E. Beere, J. Fowler, E. H. Linfield, and D. A. Ritchie, "2.9THz quantum cascade lasers operating up to 70K in continuous wave," *Applied Physics Letters,* vol. 85, pp. 1674-1676, 2004.

[80] S. Kumar, B. S. Williams, S. Kohen, Q. Hu, and J. L. Reno, "Continuous-wave operation of terahertz quantum-cascade lasers above liquid-nitrogen temperature," *Applied Physics Letters,* vol. 84, pp. 2494-2496, 2004.

[81] B. S. Williams, S. Kumar, Q. Hu, and J. L. Reno, "Operation of terahertz quantum-cascade lasers at 164 K in pulsed mode and at 117 K in continuous-wave mode," *Optics Express,* vol. 13, pp. 3331-3339, 2005/05/02 2005.

[82] S. Kumar, Q. Hu, and J. L. Reno, "186 K operation of terahertz quantum-cascade lasers based on a diagonal design," *Applied Physics Letters,* vol. 94, pp. 131105-131105-3, 2009.

[83] A. Wei Min Lee, Q. Qin, S. Kumar, B. S. Williams, Q. Hu, and J. L. Reno, "High-power and high-temperature THz quantum-cascade lasers based on lens-coupled metal-metal waveguides," *Opt. Lett.,* vol. 32, pp. 2840-2842, 2007.

[84] S. Fathololoumi, E. Dupont, C. W. I. Chan, Z. R. Wasilewski, S. R. Laframboise, D. Ban, A. Mátyás, C. Jirauschek, Q. Hu, and H. C. Liu, "Terahertz quantum cascade lasers operating up to ~200 K with optimized oscillator strength and improved injection tunneling," *Opt. Express,* vol. 20, pp. 3866-3876, 2012.

[85] M. Wienold, B. Röben, L. Schrottke, R. Sharma, A. Tahraoui, K. Biermann, and H. T. Grahn, "High-temperature, continuous-wave operation of terahertz quantum-cascade lasers with metal-metal waveguides and third-order distributed feedback," *Optics Express,* vol. 22, pp. 3334-3348, 2014/02/10 2014.

[86] A. Wade, G. Fedorov, D. Smirnov, S. Kumar, B. Williams, Q. Hu, and J. Reno, "Magnetic-field-assisted terahertz quantum cascade laser operating up to 225 K," *Nature Photonics,* vol. 3, pp. 41-45, 2009.

[87] C. Walther, M. Fischer, G. Scalari, R. Terazzi, N. Hoyler, and J. Faist, "Quantum cascade lasers operating from 1.2THz to 1.6THz," *Applied Physics Letters,* vol. 91, pp. 131122-131122-3, 2007.

[88] C. W. I. Chan, Q. Hu, and J. L. Reno, "Ground state terahertz quantum cascade lasers," *Applied Physics Letters,* vol. 101, p. 151108, 2012.

[89] B. S. Williams, S. Kumar, Q. Hu, and J. L. Reno, "High-power terahertz quantum-cascade lasers," *Electronics Letters,* vol. 42, pp. 89-91, 2006.

[90] R. H. S. Alhathlool, "The development and applications of terahertz quantum cascade lasers," *University of Leeds Thesis,* 2014.

[91] I. Kundu, "Frequency tunable terahertz quantum cascade lasers," *University of Leeds Thesis,* 2014.

[92] J. Zhu, "MBE growth, fabrication, and electrical characterisation of terahertz frequency quantum cascade lasers," *University of Leeds Thesis,* 2015.

[93] M. Hatzakis, B. J. Canavello, and J. M. Shaw, "Single-Step Optical Lift-Off Process," *IBM Journal of Research and Development,* vol. 24, pp. 452-460, 1980.

[94] A. Fathimulla, "Single-step lift-off process using chlorobenzene soak on AZ4000 resists," *Journal of Vacuum Science & Technology B,* vol. 3, pp. 25-27, 1985.

[95] M. Heiblum, M. I. Nathan, and C. A. Chang, "Characteristics of AuGeNi ohmic contacts to GaAs," *Solid-State Electronics,* vol. 25, pp. 185-195, 1982/03/01 1982.

[96] D. Jucknischke, H. J. Buhlmann, M. Ilegems, B. Jeckelmann, and W. Schwitz, "Properties of alloyed AuGeNi-contacts on GaAs/GaAlAs-heterostructures," in *Precision Electromagnetic Measurements, 1990. CPEM '90 Digest., Conference on*, 1990, pp. 336-337.

[97] H. Goronkin, S. Tehrani, T. Remmel, P. L. Fejes, and K. J. Johnston, "Ohmic contact penetration and encroachment in GaAs/AlGaAs and GaAs FETs," *IEEE Transactions on Electron Devices,* vol. 36, pp. 281-288, 1989.

[98] A. Callegari, E. T. S. Pan, and M. Murakami, "Uniform and thermally stable AuGeNi ohmic contacts to GaAs," *Applied Physics Letters,* vol. 46, pp. 1141-1143, 1985.

[99] R. Köhler, A. Tredicucci, F. Beltram, H. E. Beere, E. H. Linfield, A. G. Davies, D. A. Ritchie, S. S. Dhillon, and C. Sirtori, "High-performance continuous-wave operation of superlattice terahertz quantum-cascade lasers," *Applied Physics Letters,* vol. 82, pp. 1518-1520, 2003.

[100] J. R. Freeman, O. Marshall, H. E. Beere, and D. A. Ritchie, "Improved wall plug efficiency of a 1.9THz quantum cascade laser by an automated design approach," *Applied Physics Letters,* vol. 93, p. 191119, 2008.

[101] S. Preu, G. H. Dohler, S. Malzer, L. J. Wang, and A. C. Gossard, "Tunable, continuous-wave Terahertz photomixer sources and applications," *Journal of Applied Physics,* vol. 109, pp. 061301-56, 2011.

[102] J. T. Darrow, X.-C. Zhang, D. H. Auston, and J. D. Morse, "Saturation properties of large-aperture photoconducting antennas," *Quantum Electronics, IEEE Journal of,* vol. 28, pp. 1607-1616, 1992.

[103] A. Dreyhaupt, S. Winnerl, T. Dekorsy, and M. Helm, "High-intensity terahertz radiation from a microstructured large-area photoconductor," *Applied Physics Letters,* vol. 86, p. 121114, 2005.

[104] M. Awad, M. Nagel, H. Kurz, J. Herfort, and K. Ploog, "Characterization of low temperature GaAs antenna array terahertz emitters," *Applied Physics Letters,* vol. 91, p. 181124, 2007.

[105] G. Matthäus, S. Nolte, R. Hohmuth, M. Voitsch, W. Richter, B. Pradarutti, S. Riehemann, G. Notni, and A. Tünnermann, "Microlens coupled interdigital photoconductive switch," *Applied Physics Letters,* vol. 93, p. 091110, 2008.

[106] G. Matthäus, S. Nolte, R. Hohmuth, M. Voitsch, W. Richter, B. Pradarutti, S. Riehemann, G. Notni, and A. Tünnermann, "Large-area microlens emitters for powerful THz emission," *Applied Physics B,* vol. 96, pp. 233-235, 2009.

[107] C. W. Berry, N. Wang, M. R. Hashemi, M. Unlu, and M. Jarrahi, "Significant performance enhancement in photoconductive terahertz optoelectronics by incorporating plasmonic contact electrodes," *Nat Commun,* vol. 4, p. 1622, 2013.

[108] M. Martin and E. R. Brown, "Critical comparison of GaAs and InGaAs THz photoconductors," in *Proc. SPIE 8261 Terahertz Technology and Applications V*, 2012, pp. 826102-826102-7.

[109] C. D. Wood, O. Hatem, J. E. Cunningham, E. H. Linfield, A. G. Davies, P. J. Cannard, M. J. Robertson, and D. G. Moodie, "Terahertz emission from metal-organic chemical vapor deposition grown Fe:InGaAs using 830 nm to 1.55 mu m excitation," *Applied Physics Letters,* vol. 96, pp. 194104-3, 2010.

[110] Y. C. Shen, P. C. Upadhya, H. E. Beere, E. H. Linfield, A. G. Davies, I. S. Gregory, C. Baker, W. R. Tribe, and M. J. Evans, "Generation and detection of ultrabroadband terahertz radiation using photoconductive emitters and receivers," *Applied Physics Letters,* vol. 85, pp. 164-166, 2004.

[111] Q. Wu and X. C. Zhang, "Free-space electro-optic sampling of terahertz beams," *Applied Physics Letters,* vol. 67, pp. 3523-3525, 1995.

[112] Y. Cai, I. Brener, J. Lopata, J. Wynn, L. Pfeiffer, J. B. Stark, Q. Wu, X. C. Zhang, and J. F. Federici, "Coherent terahertz radiation detection: Direct comparison between free-space electro-optic sampling and antenna detection," *Applied Physics Letters,* vol. 73, pp. 444-446, 1998.

[113] I. Wilke and S. Sengupta, "Nonlinear optical techniques for terahertz pulse generation and detection—optical rectification and electrooptic sampling," *Terahertz Spectroscopy: Principles and Applications, Optical Science and Engineering,* vol. 131, p. 41, 2008.

[114] S. Gupta, M. Y. Frankel, J. A. Valdmanis, J. F. Whitaker, G. A. Mourou, F. W. Smith, and A. R. Calawa, "Subpicosecond carrier lifetime in GaAs grown by molecular beam epitaxy at low temperatures," *Applied Physics Letters,* vol. 59, pp. 3276-3278, 1991.

[115] M. Kaminska, E. R. Weber, Z. Liliental-Weber, R. Leon, and Z. U. Rek, "Stoichiometry-related defects in GaAs grown by molecular-beam epitaxy at low temperatures," *Journal of Vacuum Science & Technology B,* vol. 7, pp. 710-713, 1989.

[116] E. R. Brown, K. A. McIntosh, F. W. Smith, K. B. Nichols, M. J. Manfra, C. L. Dennis, and J. P. Mattia, "Milliwatt output levels and superquadratic bias dependence in a low-temperature-grown GaAs photomixer," *Applied Physics Letters,* vol. 64, pp. 3311-3313, 1994.

[117] E. R. Brown, K. A. McIntosh, F. W. Smith, M. J. Manfra, and C. L. Dennis, "Measurements of optical-heterodyne conversion in low-temperature-grown GaAs," *Applied Physics Letters,* vol. 62, pp. 1206-1208, 1993.

[118] P. U. Jepsen and S. R. Keiding, "Radiation patterns from lens-coupled terahertz antennas," *Opt. Lett.,* vol. 20, pp. 807-809, 1995.

[119] E. R. Brown, K. A. McIntosh, K. B. Nichols, and C. L. Dennis, "Photomixing up to 3.8 THz in low-temperature-grown GaAs," *Applied Physics Letters,* vol. 66, pp. 285-287, 1995.

[120] S. Matsuura, M. Tani, and K. Sakai, "Generation of coherent terahertz radiation by photomixing in dipole photoconductive antennas," *Applied Physics Letters,* vol. 70, pp. 559-561, 1997.

[121] T. Hidaka, S. Matsuura, M. Tani, and K. Sakai, "CW terahertz wave generation by photomixing using a two-longitudinal-mode laser diode," *Electronics Letters,* vol. 33, pp. 2039-2040, 1997.

[122] S. Verghese, K. A. McIntosh, and E. R. Brown, "Highly tunable fiber-coupled photomixers with coherent terahertz output power," *Microwave Theory and Techniques, IEEE Transactions on,* vol. 45, pp. 1301-1309, 1997.

[123] S. Verghese, K. A. McIntosh, S. Calawa, W. F. DiNatale, E. K. Duerr, and K. A. Molvar, "Generation and detection of coherent terahertz waves using two photomixers," *Applied Physics Letters,* vol. 73, pp. 3824-3826, 1998.

[124] R. A. Cheville and D. Grischkowsky, "Far-infrared terahertz time-domain spectroscopy offlames," *Optics Letters,* vol. 20, pp. 1646-1648, 1995/08/01 1995.

[125] M. Usami, T. Iwamoto, R. Fukasawa, M. Tani, M. Watanabe, and K. Sakai, "Development of a THz spectroscopic imaging system," *Physics in Medicine and Biology,* vol. 47, p. 3749, 2002.

[126] J. S. Karsten, L. Torsten, Q. Holger, T. Mark, B. Tobias, L. Rainer, C. Stephanie, and G. R. Hartmut, "All-optoelectronic continuous wave THz imaging for biomedical applications," *Physics in Medicine and Biology,* vol. 47, p. 3743, 2002.

[127] K. J. Siebert, H. Quast, R. Leonhardt, T. Löffler, M. Thomson, T. Bauer, H. G. Roskos, and S. Czasch, "Continuous-wave all-optoelectronic terahertz imaging," *Applied Physics Letters,* vol. 80, pp. 3003-3005, 2002.

[128] I. S. Gregory, W. R. Tribe, B. E. Cole, C. Baker, M. J. Evans, I. V. Bradley, E. H. Linfield, A. G. Davies, and M. Missous, "Phase sensitive continuous-wave THz imaging using diode lasers," *Electronics Letters,* vol. 40, pp. 143-145, 2004.

[129] F. Hindle, A. Cuisset, R. Bocquet, and G. Mouret, "Continuous-wave terahertz by photomixing: applications to gas phase pollutant detection and quantification," *Comptes Rendus Physique,* vol. 9, pp. 262-275, 2008.

[130] I. S. Gregory, C. Baker, W. R. Tribe, I. V. Bradley, M. J. Evans, E. H. Linfield, G. Davies, and M. Missous, "Optimization of photomixers and antennas for continuous-wave terahertz emission," *Quantum Electronics, IEEE Journal of,* vol. 41, pp. 717-728, 2005.

[131] J. B. D. Soole and H. Schumacher, "Transit-time limited frequency response of InGaAs MSM photodetectors," *Electron Devices, IEEE Transactions on,* vol. 37, pp. 2285-2291, 1990.

[132] I. S. Gregory, "The development of a continuous-wave terahertz imaging system," *University of Cambridge,* 2004.

[133] I. Hiroshi, N. Fumito, F. Tomofumi, and I. Tadao, "Continuous THz-wave generation using antenna-integrated uni-travelling-carrier photodiodes," *Semiconductor Science and Technology,* vol. 20, p. S191, 2005.

[134] M. Barnoski, *Fundamentals of optical fiber communications*: Elsevier, 2012.

[135] D. Sands, *Diode lasers*: CRC Press, 2004.

[136] E. Bruce, "Tunable lasers," *Spectrum, IEEE,* vol. 39, pp. 35-39, 2002.

[137] E. Peytavit, P. Latzel, F. Pavanello, G. Ducournau, and J. F. Lampin, "CW Source Based on Photomixing With Output Power Reaching 1.8 mW at 250 GHz," *Electron Device Letters, IEEE,* vol. 34, pp. 1277-1279, 2013.

[138] W.-D. Zhang, J. R. Middendorf, and E. R. Brown, "Demonstration of a GaAs-based 1550-nm continuous wave photomixer," *Applied Physics Letters,* vol. 106, p. 021119, 2015.

[139] S. R. Forrest, O. K. Kim, and R. G. Smith, "Optical response time of In0.53Ga0.47As/InP avalanche photodiodes," *Applied Physics Letters,* vol. 41, pp. 95-98, 1982.

[140] S. Bandy, C. Nishimoto, S. Hyder, and C. Hooper, "Saturation velocity determination for In0.53Ga0.47As field-effect transistors," *Applied Physics Letters,* vol. 38, pp. 817-819, 1981.

[141] B. Tell, U. Koren, and B. I. Miller, "Metalorganic vapor-phase-epitaxial growth of Fe-doped In0.53Ga0.47As," *Journal of Applied Physics,* vol. 61, pp. 1172-1175, 1987.

[142] S. Adachi, "Refractive indices of III–V compounds: Key properties of InGaAsP relevant to device design," *Journal of Applied Physics,* vol. 53, pp. 5863-5869, 1982.

[143] B. R. Bennett, R. A. Soref, and J. A. del Alamo, "Carrier-induced change in refractive index of InP, GaAs and InGaAsP," *Quantum Electronics, IEEE Journal of,* vol. 26, pp. 113-122, 1990.

[144] M. Silver and E. P. O'Reilly, "Optimization of long wavelength InGaAsP strained quantum-well lasers," *Quantum Electronics, IEEE Journal of,* vol. 31, pp. 1193-1200, 1995.

[145] C. Wood-Hi, A. Mar, J. E. Bowers, R. T. Huang, and C. B. Su, "High speed 1.3 um InGaAsP Fabry-Perot lasers for digital and analog applications," *Quantum Electronics, IEEE Journal of,* vol. 29, pp. 1660-1667, 1993.

[146] S. Kristian, A. Masahiro, A. Shigehisa, and S. Yasuharu, "Spontaneous Recombination, Gain and Refractive Index Variation for 1.6 µm Wavelength InGaAsP/InP Lasers," *Japanese Journal of Applied Physics,* vol. 20, p. 1499, 1981.

[147] C. Baker, I. S. Gregory, W. R. Tribe, I. V. Bradley, M. J. Evans, E. H. Linfield, and M. Missous, "Highly resistive annealed low-temperature-grown InGaAs with sub-500fs carrier lifetimes," *Applied Physics Letters,* vol. 85, pp. 4965-4967, 2004.

[148] C. Y. Chen and G. C. Chi, "Low-noise Ga0.47In0.53As photoconductive detectors using Fe compensation," *Applied Physics Letters,* vol. 45, pp. 1083-1085, 1984.

[149] S. Gupta, J. F. Whitaker, and G. A. Mourou, "Ultrafast carrier dynamics in III-V semiconductors grown by molecular-beam epitaxy at very low substrate temperatures," *Quantum Electronics, IEEE Journal of,* vol. 28, pp. 2464-2472, 1992.

[150] S. M. Gulwadi, M. V. Rao, A. K. Berry, D. S. Simons, P. H. Chi, and H. B. Dietrich, "Transition metal implants in In0.53Ga0.47As," *Journal of Applied Physics,* vol. 69, pp. 4222-4227, 1991.

[151] C. Carmody, H. H. Tan, C. Jagadish, A. Gaarder, and S. Marcinkevicius, "Ion-implanted In0.53Ga0.47As for ultrafast optoelectronic applications," *Applied Physics Letters,* vol. 82, pp. 3913-3915, 2003.

[152] C. Baker, I. S. Gregory, W. R. Tribe, I. V. Bradley, M. J. Evans, M. Withers, P. F. Taday, V. P. Wallace, E. H. Linfield, A. G. Davies, and M. Missous, "Terahertz pulsed imaging with 1.06 µm laser excitation," *Applied Physics Letters,* vol. 83, pp. 4113-4115, 2003.

[153] M. Suzuki and M. Tonouchi, "Fe-implanted InGaAs terahertz emitters for 1.56 um wavelength excitation," *Applied Physics Letters,* vol. 86, pp. 051104-3, 2005.

[154] N. Chimot, J. Mangeney, L. Joulaud, P. Crozat, H. Bernas, K. Blary, and J. F. Lampin, "Terahertz radiation from heavy-ion-irradiated In0.53Ga0.47As photoconductive antenna excited at 1.55µm," *Applied Physics Letters,* vol. 87, p. 193510, 2005.

[155] J. Mangeney and P. Crozat, "Ion-irradiated In0.53Ga0.47As photoconductive antennas for THz generation and detection at 1.55 µm wavelength," *Comptes Rendus Physique,* vol. 9, pp. 142-152, 2008.

[156] A. Takazato, M. Kamakura, T. Matsui, J. Kitagawa, and Y. Kadoya, "Detection of terahertz waves using low-temperature-grown InGaAs with 1.56µm pulse excitation," *Applied Physics Letters,* vol. 90, p. 101119, 2007.

[157] A. Takazato, M. Kamakura, T. Matsui, J. Kitagawa, and Y. Kadoya, "Terahertz wave emission and detection using photoconductive antennas made on low-temperature-grown InGaAs with 1.56µm pulse excitation," *Applied Physics Letters,* vol. 91, p. 011102, 2007.

[158] D. C. Driscoll, M. P. Hanson, A. C. Gossard, and E. R. Brown, "Ultrafast photoresponse at 1.55 µm in InGaAs with embedded semimetallic ErAs nanoparticles," *Applied Physics Letters,* vol. 86, p. 051908, 2005.

[159] M. Guézo, S. Loualiche, J. Even, A. Le Corre, H. Folliot, C. Labbé, O. Dehaese, and G. Dousselin, "Ultrashort, nonlinear, optical time response of Fe-doped InGaAs/InP multiple quantum wells in 1.55-µm range," *Applied Physics Letters,* vol. 82, pp. 1670-1672, 2003.

[160] P. Gu, M. Tani, S. Kono, K. Sakai, and X.-C. Zhang, "Study of terahertz radiation from InAs and InSb," *Journal of Applied Physics,* vol. 91, pp. 5533-5537, 2002.

[161] V. Apostolopoulos and M. E. Barnes, "THz emitters based on the photo-Dember effect," *Journal of Physics D: Applied Physics,* vol. 47, p. 374002, 2014.

[162] M. Suzuki, M. Tonouchi, K.-i. Fujii, H. Ohtake, and T. Hirosumi, "Excitation wavelength dependence of terahertz emission from semiconductor surface," *Applied Physics Letters,* vol. 89, p. 091111, 2006.

[163] M. Sukhotin, E. R. Brown, A. C. Gossard, D. Driscoll, M. Hanson, P. Maker, and R. Muller, "Photomixing and photoconductor measurements on ErAs/InGaAs at 1.55 µm," *Applied Physics Letters,* vol. 82, pp. 3116-3118, 2003.

[164] C. Baker, I. Gregory, M. Evans, W. Tribe, E. Linfield, and M. Missous, "All-optoelectronic terahertz system using low-temperature-grown InGaAs photomixers," *Opt. Express,* vol. 13, pp. 9639-9644, 2005.

[165] N. Chimot, J. Mangeney, P. Crozat, J. Lourtioz, K. Blary, J. Lampin, G. Mouret, D. Bigourd, and E. Fertein, "Photomixing at 1.55 µm in ion-irradiated In(0.53)Ga(0.47)As on InP," *Opt. Express,* vol. 14, pp. 1856-1861, 2006.

[166] J. Mangeney, A. Merigault, N. Zerounian, P. Crozat, K. Blary, and J. F. Lampin, "Continuous wave terahertz generation up to 2THz by photomixing on ion-irradiated In0.53Ga0.47As at 1.55µm wavelengths," *Applied Physics Letters,* vol. 91, p. 241102, 2007.

[167] A. Fekecs, M. Bernier, D. Morris, M. Chicoine, F. Schiettekatte, P. Charette, and R. Arès, "Fabrication of high resistivity cold-implanted InGaAsP photoconductors for efficient pulsed terahertz devices," *Optical Materials Express,* vol. 1, pp. 1165-1177, 2011/11/01 2011.

[168] O. Hatem, J. Cunningham, E. H. Linfield, C. D. Wood, A. G. Davies, P. J. Cannard, M. J. Robertson, and D. G. Moodie, "Terahertz-frequency photoconductive detectors fabricated from metal-organic chemical vapor deposition-grown Fe-doped InGaAs," *Applied Physics Letters,* vol. 98, p. 121107, 2011.

[169] O. Hatem, J. R. Freeman, J. E. Cunningham, P. J. Cannard, M. J. Robertson, E. H. Linfield, A. G. Davies, and D. G. Moodie, "Generation of Terahertz Radiation from Fe-doped InGaAsP Using 800 nm to 1550 nm Pulsed Laser Excitation," *Journal of Infrared, Millimeter, and Terahertz Waves,* vol. 37, pp. 415-425, 2015.

[170] R. A. Mohandas, J. R. Freeman, M. C. Rosamond, O. Hatem, S. Chowdhury, L. Ponnampalam, M. Fice, A. J. Seeds, P. J. Cannard, M. J. Robertson, D. G. Moodie, J. E. Cunningham, A. G. Davies, E. H. Linfield, and P. Dean, "Generation of continuous wave terahertz frequency radiation from metal-organic chemical

vapour deposition grown Fe-doped InGaAs and InGaAsP," *Journal of Applied Physics,* vol. 119, p. 153103, 2016.

[171] TanotoH, J. H. Teng, Q. Y. Wu, SunM, Z. N. Chen, S. A. Maier, WangB, C. C. Chum, G. Y. Si, A. J. Danner, and S. J. Chua, "Greatly enhanced continuous-wave terahertz emission by nano-electrodes in a photoconductive photomixer," *Nat Photon,* vol. 6, pp. 121-126, 2012.

[172] A. M. Fox, *Optical properties of solids* vol. 3: Oxford university press, 2001.

[173] G. Mourou, C. V. Stancampiano, A. Antonetti, and A. Orszag, "Picosecond microwave pulses generated with a subpicosecond laser-driven semiconductor switch," *Applied Physics Letters,* vol. 39, pp. 295-296, 1981.

[174] L. Di and H. Yi, "Comparison of terahertz antennas," in *Antennas and Propagation, 2006. EuCAP 2006. First European Conference on*, 2006, pp. 1-5.

[175] J. Dyson, "The equiangular spiral antenna," *Antennas and Propagation, IRE Transactions on,* vol. 7, pp. 181-187, 1959.

[176] S. Chowdhury, "Development of terahertz systems using quantum cascade lasers and photomixers," *University of Leeds Thesis,* 2015.

[177] P. Notten, "The etching of InP in HCl solutions: a chemical mechanism," *Journal of The Electrochemical Society,* vol. 131, pp. 2641-2644, 1984.

[178] O. Hatem, J. R. Freeman, J. E. Cunningham, P. J. Cannard, M. J. Robertson, E. H. Linfield, A. G. Davies, and D. G. Moodie, "Generation of Terahertz Radiation from Fe-doped InGaAsP Using 800 nm to 1550 nm Pulsed Laser Excitation," *Journal of Infrared, Millimeter, and Terahertz Waves,* pp. 1-11, 2015.

[179] A. R. Clawson, D. P. Mullin, D. I. Elder, and H. H. Wieder, "Semi-insulating In0.53Ga0.47As by Fe doping," *Journal of Crystal Growth,* vol. 64, pp. 90-95, 1983/11/01 1983.

[180] A. K. Azad, R. P. Prasankumar, D. Talbayev, A. J. Taylor, R. D. Averitt, J. M. O. Zide, H. Lu, A. C. Gossard, and J. F. O'Hara, "Carrier dynamics in InGaAs with embedded ErAs nanoislands," *Applied Physics Letters,* vol. 93, p. 121108, 2008.

[181] P. G. Huggard, C. J. Shaw, J. A. Cluff, and S. R. Andrews, "Polarization-dependent efficiency of photoconducting THz transmitters and receivers," *Applied Physics Letters,* vol. 72, pp. 2069-2071, 1998.

[182] J. J. Kuta, H. M. van Driel, D. Landheer, and J. A. Adams, "Polarization and wavelength dependence of metal-semiconductor-metal photodetector response," *Applied Physics Letters,* vol. 64, pp. 140-142, 1994.

[183] S. M. Duffy, S. Verghese, K. A. McIntosh, A. Jackson, A. C. Gossard, and S. Matsuura, "Accurate modeling of dual dipole and slot elements used with photomixers for coherent terahertz output power," *Microwave Theory and Techniques, IEEE Transactions on,* vol. 49, pp. 1032-1038, 2001.

[184] I. S. Gregory, W. R. Tribe, B. E. Cole, M. J. Evans, E. H. Linfield, A. G. Davies, and M. Missous, "Resonant dipole antennas for continuous-wave terahertz photomixers," *Applied Physics Letters,* vol. 85, pp. 1622-1624, 2004.

[185] C. W. Berry, M. R. Hashemi, S. Preu, H. Lu, A. C. Gossard, and M. Jarrahi, "High power terahertz generation using 1550 nm plasmonic photomixers," *Applied Physics Letters,* vol. 105, p. 011121, 2014.

[186] D. Krökel, D. Grischkowsky, and M. B. Ketchen, "Subpicosecond electrical pulse generation using photoconductive switches with long carrier lifetimes," *Applied Physics Letters,* vol. 54, pp. 1046-1047, 1989.

[187] S. E. Ralph and D. Grischkowsky, "Trap-enhanced electric fields in semi-insulators: The role of electrical and optical carrier injection," *Applied Physics Letters,* vol. 59, pp. 1972-1974, 1991.

[188] U. D. Keil and D. R. Dykaar, "Ultrafast pulse generation in photoconductive switches," *Quantum Electronics, IEEE Journal of,* vol. 32, pp. 1664-1671, 1996.

[189] I. Brener, M. C. Nuss, D. Dykaar, A. Frommer, L. N. Pfeiffer, J. Lopata, J. Wynn, and K. West, "Terahertz emission from electric field singularities in biased semiconductors," *Optics Letters,* vol. 21, pp. 1924-1926, 1996/12/01 1996.

[190] C. W. Berry and M. Jarrahi, "Terahertz generation using plasmonic photoconductive gratings," *New Journal of Physics,* vol. 14, p. 105029, 2012.

[191] N. T. Yardimci, Y. Shang-Hua, C. W. Berry, and M. Jarrahi, "High-Power Terahertz Generation Using Large-Area Plasmonic Photoconductive Emitters," *Terahertz Science and Technology, IEEE Transactions on,* vol. 5, pp. 223-229, 2015.

[192] S.-H. Yang and M. Jarrahi, "Frequency-tunable continuous-wave terahertz sources based on GaAs plasmonic photomixers," *Applied Physics Letters,* vol. 107, p. 131111, 2015.

[193] H. Raether, *Surface plasmons on smooth surfaces*: Springer, 1988.

[194] B. H. Ong, X. Yuan, S. C. Tjin, J. Zhang, and H. M. Ng, "Optimised film thickness for maximum evanescent field enhancement of a bimetallic film surface plasmon resonance biosensor," *Sensors and Actuators B: Chemical,* vol. 114, pp. 1028-1034, 2006.

[195] Y. Suzaki and A. Tachibana, "Measurement of the μm sized radius of Gaussian laser beam using the scanning knife-edge," *Applied Optics,* vol. 14, pp. 2809-2810, 1975/12/01 1975.

[196] M. González-Cardel, P. Arguijo, and R. Díaz-Uribe, "Gaussian beam radius measurement with a knife-edge: a polynomial approximation to the inverse error function," *Applied Optics,* vol. 52, pp. 3849-3855, 2013/06/01 2013.

[197] G. Veshapidze, M. L. Trachy, M. H. Shah, and B. D. DePaola, "Reducing the uncertainty in laser beam size measurement with a scanning edge method," *Applied Optics,* vol. 45, pp. 8197-8199, 2006/11/10 2006.

[198] M. Born and E. Wolf, *Principles of optics: electromagnetic theory of propagation, interference and diffraction of light*: Cambridge university press, 1999.

[199] H. Tamada, T. Doumuki, T. Yamaguchi, and S. Matsumoto, "Al wire-grid polarizer using the s-polarization resonance effect at the 0.8-Ám-wavelength band," *Optics Letters,* vol. 22, pp. 419-421, 1997.

[200] J. Auton, "Infrared transmission polarizers by photolithography," *Applied Optics,* vol. 6, pp. 1023-1027, 1967.

[201] Q. Wu, M. Litz, and X. C. Zhang, "Broadband detection capability of ZnTe electro-optic field detectors," *Applied Physics Letters,* vol. 68, pp. 2924-2926, 1996.

[202] C. Winnewisser, P. U. Jepsen, M. Schall, V. Schyja, and H. Helm, "Electro-optic detection of THz radiation in LiTaO3, LiNbO3 and ZnTe," *Applied Physics Letters,* vol. 70, pp. 3069-3071, 1997.

[203] R. Adler, "A Study of Locking Phenomena in Oscillators," *Proceedings of the IRE,* vol. 34, pp. 351-357, 1946.

[204] H. L. Stover and W. H. Steier, "Locking of Laser Oscillators by Light Injection," *Applied Physics Letters,* vol. 8, pp. 91-93, 1966.

[205] C. Tamm, "Frequency locking of two transverse optical modes of a laser," *Physical Review A,* vol. 38, pp. 5960-5963, 1988.

[206] H. Statz and C. L. Tang, "Phase Locking of Modes in Lasers," *Journal of Applied Physics,* vol. 36, pp. 3923-3927, 1965.

[207] P. Khosropanah, A. Baryshev, W. Zhang, W. Jellema, J. N. Hovenier, J. R. Gao, T. M. Klapwijk, D. G. Paveliev, B. S. Williams, S. Kumar, Q. Hu, J. L. Reno, B. Klein, and J. L. Hesler, "Phase locking of a 2.7 THz quantum cascade laser to a microwave reference," *Optics Letters,* vol. 34, pp. 2958-2960, 2009/10/01 2009.

[208] M. S. Vitiello, L. Consolino, S. Bartalini, A. Taschin, A. Tredicucci, M. Inguscio, and P. De Natale, "Quantum-limited frequency fluctuations in a terahertz laser," *Nat Photon,* vol. 6, pp. 525-528, 2012.

[209] H. Andreas, M. Richard, and F. Jérôme, "External cavity quantum cascade laser," *Semiconductor Science and Technology,* vol. 25, p. 083001, 2010.

[210] B. S. Williams, S. Kumar, Q. Hu, and J. L. Reno, "Distributed-feedback terahertz quantum-cascade lasers with laterally corrugated metal waveguides," *Optics Letters,* vol. 30, pp. 2909-2911, 2005/11/01 2005.

[211] L. Consolino, S. Bartalini, H. E. Beere, D. A. Ritchie, M. S. Vitiello, and P. De Natale, "THz QCL-based cryogen-free spectrometer for in situ trace gas sensing," *Sensors,* vol. 13, pp. 3331-3340, 2013.

[212] D. Mittleman, "Terahertz Imaging," in *Sensing with Terahertz Radiation*, D. Mittleman, Ed., ed Berlin, Heidelberg: Springer Berlin Heidelberg, 2003, pp. 117-153.

[213] R. Kohler, A. Tredicucci, C. Mauro, F. Beltram, H. E. Beere, E. H. Linfield, A. G. Davies, and D. A. Ritchie, "Terahertz quantum-cascade lasers based on an interlaced photon-phonon cascade," *Applied Physics Letters,* vol. 84, pp. 1266-1268, 2004.

[214] A. Barkan, F. K. Tittel, D. M. Mittleman, R. Dengler, P. H. Siegel, G. Scalari, L. Ajili, J. Faist, H. E. Beere, E. H. Linfield, A. G. Davies, and D. A. Ritchie, "Linewidth and tuning characteristics of terahertz quantum cascade lasers," *Optics Letters,* vol. 29, pp. 575-577, 2004/03/15 2004.

[215] S. Barbieri, J. Alton, H. E. Beere, E. H. Linfield, D. A. Ritchie, S. Withington, G. Scalari, L. Ajili, and J. Faist, "Heterodyne mixing of two far-infrared quantum cascade lasers by use of a point-contact Schottky diode," *Optics Letters,* vol. 29, pp. 1632-1634, 2004/07/15 2004.

[216] A. L. Betz, R. T. Boreiko, B. S. Williams, S. Kumar, Q. Hu, and J. L. Reno, "Frequency and phase-lock control of a 3 THz quantum cascade laser," *Optics Letters,* vol. 30, pp. 1837-1839, 2005/07/15 2005.

[217] A. Baryshev, J. N. Hovenier, A. J. L. Adam, I. Kašalynas, J. R. Gao, T. O. Klaassen, B. S. Williams, S. Kumar, Q. Hu, and J. L. Reno, "Phase locking and spectral linewidth of a two-mode terahertz quantum cascade laser," *Applied Physics Letters,* vol. 89, p. 031115, 2006.

[218] D. Rabanus, U. U. Graf, M. Philipp, O. Ricken, J. Stutzki, B. Vowinkel, M. C. Wiedner, C. Walther, M. Fischer, and J. Faist, "Phase locking of a 1.5 Terahertz quantum cascade laser and use as a local oscillator in a heterodyne HEB receiver," *Optics Express,* vol. 17, pp. 1159-1168, 2009/02/02 2009.

[219] A. A. Danylov, T. M. Goyette, J. Waldman, M. J. Coulombe, A. J. Gatesman, R. H. Giles, W. D. Goodhue, X. Qian, and W. E. Nixon, "Frequency stabilization of a single mode terahertz quantum cascade laser to the kilohertz level," *Optics Express,* vol. 17, pp. 7525-7532, 2009/04/27 2009.

[220] A. A. Danylov, A. R. Light, J. Waldman, N. R. Erickson, X. Qian, and W. D. Goodhue, "2.32 THz quantum cascade laser frequency-locked to the harmonic of a microwave synthesizer source," *Optics Express,* vol. 20, pp. 27908-27914, 2012/12/03 2012.

[221] D. J. Hayton, A. Khudchenko, D. G. Pavelyev, J. N. Hovenier, A. Baryshev, J. R. Gao, T. Y. Kao, Q. Hu, J. L. Reno, and V. Vaks, "Phase locking of a 3.4 THz third-order distributed feedback quantum cascade laser using a room-temperature superlattice harmonic mixer," *Applied Physics Letters,* vol. 103, p. 051115, 2013.

[222] H. Richter, S. G. Pavlov, A. D. Semenov, L. Mahler, A. Tredicucci, H. E. Beere, D. A. Ritchie, and H.-W. Hübers, "Submegahertz frequency stabilization of a terahertz quantum cascade laser to a molecular absorption line," *Applied Physics Letters,* vol. 96, p. 071112, 2010.

[223] Y. Ren, J. N. Hovenier, M. Cui, D. J. Hayton, J. R. Gao, T. M. Klapwijk, S. C. Shi, T.-Y. Kao, Q. Hu, and J. L. Reno, "Frequency locking of single-mode 3.5-THz

quantum cascade lasers using a gas cell," *Applied Physics Letters,* vol. 100, p. 041111, 2012.

[224] S. Barbieri, P. Gellie, G. Santarelli, L. Ding, W. Maineult, C. Sirtori, R. Colombelli, H. Beere, and D. Ritchie, "Phase-locking of a 2.7-THz quantum cascade laser to a mode-locked erbium-doped fibre laser," *Nat Photon,* vol. 4, pp. 636-640, 2010.

[225] S. Barbieri, M. Ravaro, P. Gellie, G. Santarelli, C. Manquest, C. Sirtori, S. P. Khanna, E. H. Linfield, and A. G. Davies, "Coherent sampling of active mode-locked terahertz quantum cascade lasers and frequency synthesis," *Nat Photon,* vol. 5, pp. 306-313, 2011.

[226] M. Ravaro, C. Manquest, C. Sirtori, S. Barbieri, G. Santarelli, K. Blary, J. F. Lampin, S. P. Khanna, and E. H. Linfield, "Phase-locking of a 2.5 THz quantum cascade laser to a frequency comb using a GaAs photomixer," *Optics Letters,* vol. 36, pp. 3969-3971, 2011/10/15 2011.

[227] H. Nong, S. Pal, S. Markmann, N. Hekmat, R. A. Mohandas, P. Dean, L. Li, E. H. Linfield, A. Giles Davies, A. D. Wieck, and N. Jukam, "Narrow-band injection seeding of a terahertz frequency quantum cascade laser: Selection and suppression of longitudinal modes," *Applied Physics Letters,* vol. 105, pp. -, 2014.

[228] L. Siegman, "University science books," *Mill Valley, CA,* pp. 858-890, 1986.

[229] D. Oustinov, N. Jukam, R. Rungsawang, J. Madéo, S. Barbieri, P. Filloux, C. Sirtori, X. Marcadet, J. Tignon, and S. Dhillon, "Phase seeding of a terahertz quantum cascade laser," *Nat Commun,* vol. 1, p. 69, 2010.

[230] N. Vukovic, N. Healy, J. R. Sparks, J. V. Badding, P. Horak, and A. C. Peacock, "Tunable continuous wave emission via phase-matched second harmonic generation in a ZnSe microcylindrical resonator," *Scientific Reports,* vol. 5, p. 11798, 2015.

[231] P. Dean, Y. Leng Lim, A. Valavanis, R. Kliese, M. Nikoli, S. P. Khanna, M. Lachab, D. Indjin, Z. Ikoni, P. Harrison, A. D. Raki, E. H. Linfield, and A. G. Davies, "Terahertz imaging through self-mixing in a quantum cascade laser," *Opt. Lett.,* vol. 36, pp. 2587-2589, 2011.

[232] A. Valavanis, P. Dean, L. Yah Leng, R. Alhathlool, M. Nikolic, R. Kliese, S. P. Khanna, D. Indjin, S. J. Wilson, A. D. Rakic, E. H. Linfield, and G. Davies, "Self-Mixing Interferometry With Terahertz Quantum Cascade Lasers," *Sensors Journal, IEEE,* vol. 13, pp. 37-43, 2013.

[233] B. Razavi, "A study of injection locking and pulling in oscillators," *IEEE Journal of Solid-State Circuits,* vol. 39, pp. 1415-1424, 2004.